Fakultät für Physik

Fundamental physics with neutrons

Electric dipole moment searches using the isotope 129-xenon

Florian Kuchler

Vollständiger Abdruck der von der Fakultät für Physik der Technischen Universität München zur Erlangung des akademischen Grades eines

Doktors der Naturwissenschaften (Dr. rer. nat.)

genehmigten Dissertation.

Vorsitzende:		Univ.-Prof. Dr. Nora Brambilla
Prüfer der Dissertation:		
	1.	Univ.-Prof. Dr. Peter Fierlinger
	2.	Univ.-Prof. Dr. Elisa Resconi

Die Dissertation wurde am 03.11.2014 bei der Technischen Universität München eingereicht und durch die Fakultät für Physik am 13.11.2014 angenommen.

Abstract

The search for permanent electric dipole moments (EDM) of fundamental systems is motivated by their time-reversal and parity violating nature. A non-zero EDM implies a new source of $\mathcal{CP}$ violation, essential to explain the huge excess of matter over antimatter in our Universe. Moreover, an EDM is a clean probe of physics beyond the Standard Model (SM).

Besides other fundamental systems the diamagnetic atom ^{129}Xe is a particularly interesting candidate for an EDM search due to its unique properties. Considering semileptonic $\mathcal{CP}$ violating interactions, ^{129}Xe offers a higher sensitivity compared to ^{199}Hg when measured at the same level. Also, adding a new limit of the EDM of ^{129}Xe to superior result from ^{199}Hg can significantly improve existing constraints on hadronic $\mathcal{CP}$ odd couplings.

In this work two new complementary EDM experiments are discussed, which both introduce highly sensitive SQUID detection systems, but feature totally different systematics. A novel approach is based on sub-millimeter hyper-polarized liquid xenon droplets enclosed on a micro-fabricated structure. Implementation of rotating electric fields enables a conceptually new EDM measurement technique, potentially overcoming current sensitivity limitations while allowing thorough investigation of new systematic effects. However, an established "Ramsey-type" spin precession experiment with static electric field can be realized at similar sensitivity within the same setup. Employing superconducting pick-up coils and highly sensitive LTc-SQUIDs, a large array of independent measurements can be performed simultaneously with different configurations. With this new approach we aim to finally lower the limit on the EDM of ^{129}Xe by about three orders of magnitude. The method and new systematic effects are discussed limiting this approach to about 10^{-30} $e$cm. Operation of superconducting pickup coils mounted close to a high temperature sample in a cryogen-free environment as well as production and transport of polarized xenon is demonstrated.

In the second experiment a ^{3}He co-magnetometer is introduced in a newly developed EDM cell with silicon electrodes. Here, established techniques with well known systematics are improved and the experiment placed in a magnetically shielded environment, particularly developed for low energy precession experiments. Under these nearly perfect conditions and with high signal-to-noise ratio due to SQUID detection, it is demonstrated, that first successful measurements with applied high voltage yield competitive EDM sensitivity.

The two experiments feature different systematics and represent a balance between moderate short-term improvements and a long-term high gain in sensitivity involving extensive R&D work.

Contents

1 Introduction

Searches for electric dipole moments (EDM) are motivated by their symmetry-violating nature. An EDM of a fundamental system is a manifestation of time-reversal violation and hence also breaks $\mathcal{CP}$ symmetry[1]. The violation of $\mathcal{CP}$ symmetry is essential to explain the observed asymmetry of baryons to anti-baryons in the Universe. In the well established Standard model of particle physics (SM), $\mathcal{CP}$ violation occurs only through (i) $\overline{\theta}$ in quantum chromodynamics (QCD) and (ii) the complex phase δ in the CKM matrix. Experiments strongly limit $\overline{\theta}$ and determine δ very well. As a result only small $\mathcal{CP}$ violation is generated in the SM, which is far from being sufficient to account for cosmological observations of the baryon number to photon ratio. This poses one of the most important fundamental puzzles in physics:

How did baryon asymmetry emerge from the early Universe?

Models extending the SM try to solve this question (and others). In particular, Supersymmetry (SUSY) is very popular, but suffers from recent (non-)observations at the Large Hadron Collider (LHC), where as of yet no supersymmetric partner particles were found at the accessible energies. However, most extensions of the SM also require larger EDMs than the SM predicts. Hence, EDMs provide a probe for new physics and EDM searches help constrain parameters of the new physics models. In this regard an ultra-low energy EDM search is complementary to extremely high energy experiments at LHC.

Besides fundamental systems like neutrons, diamagnetic atoms, particularly ^{129}Xe and ^{199}Hg with nuclear spin 1/2, are interesting candidates for an EDM experiment. The current best limit on an EDM was obtained from ^{199}Hg, with sensitivity improvements published in recent years. Despite the more complicated internal structure the ^{199}Hg EDM limit is widely used to constrain many new physics parameters as it has even higher sensitivity than more fundamental systems, e.g. the neutron. In the evolution of new EDM limits, ^{129}Xe has fallen behind recently, with the last published result in 2001. However, the role of ^{129}Xe is special in the sense that some of the fundamental $\mathcal{CP}$ violating parameters can be better constrained by an (improved) EDM limit on ^{129}Xe, as I will point out in the first chapter, particularly in Sec. 2.6.

In this thesis I will introduce two new experiments at the TU München searching for an EDM of the diamagnetic atom ^{129}Xe in both gas and liquid phase using superconducting quantum interference devices (SQUIDs) for signal detection. The usually employed method looking for deviations in spin-precession frequency in applied parallel magnetic

---

[1] The $\mathcal{CP}$ operator describes subsequent application of charge-conjugation $\mathcal{C}$ and the parity operator $\mathcal{P}$.

and electric fields in the gas phase seems to get closer to a dead-end in sensitivity. To overcome these limitations, the development of new methods is highly motivated.
The R&D efforts towards a liquid xenon EDM experiment are presented in Sec. 5. It introduces a completely new measurement method with time-varying electric fields. The potential sensitivity of the novel method and the resulting new systematic effects are discussed in Sec. 5.1. In Sec. 5.2 the cryogenic setup for cooling and operating the SQUID sensors as well as details on the temperature control of the liquid xenon sample are presented. In subsequent sections supplemental information on the main components for production, accumulation and transfer of hyper-polarized xenon is given. The chapter concludes with remarks on the development of a micro-structured "EDM chip" in the EDM cryostat,where polarized xenon is liquefied for the future EDM measurement. In summary the evaluation of new effects due to time-varying electric fields reveals systematic uncertainties on a $10^{-30}\,e$cm level suggesting a potential improvement on the xenon EDM limit by more than two orders of magnitude. However the novel systematics of this approach have to be studied experimentally to quote reliable estimates. It is also demonstrated that the detection system of external superconducting pickup coils and SQUID current sensors can be operated in a cryogen-free setup at a magnetic flux noise level of 144 $\mathrm{fT}/\sqrt{\mathrm{Hz}}$ above 50 Hz with a close-by sample at 162 K. Along with successful production and accumulation of hyper-polarized xenon a comprehensive area rich of further physics studies for a high potential new xenon EDM search is now available for new graduate students.

In contrast to the long-term development for this novel approach a new EDM experiment using rather established well-known techniques is underway together with collaborators from the University of Michigan, Michigan State University, PTB Berlin and the Maier-Leibnitz Zentrum. This effort promises short-term results as a known "conventional" method is used basically improved by means of SQUID detection. At the TU München the best possible environment with lowest residual magnetic field and magnetic field gradients is available inside a state-of-the-art magnetically shielded room. By employing highly sensitive SQUID detection we demonstrated the new concept to improve the current EDM limit on xenon by at least an order of magnitude in the short-term.
The current status and progress in this He-Xe spin-clock comparison approach is presented in Sec. 6. The results of two test runs are discussed, including an already successful observation of simultaneous spin-precession of ^{3}He and ^{129}Xe in a prototype EDM cell with high voltage applied. The non-optimized EDM sensitivity of this measurement is already on the order of $10^{-23}\,e$cm. With several straightforward improvements we anticipate a sensitivity of $10^{-26}\,e$cm in a single run of 100 s.

The fast progress of the latter EDM search and the high potential gain of the novel time-varying electric field approach make both EDM experiments very valuable for the search of new physics.

2 Electric dipole moment (EDM): Motivation, theory and experiments

2.1 The matter-antimatter mystery

In many aspects predictions according to the SM have been experimentally confirmed with high precision. The signal of a Higgs-like particle measured at the LHC at a mass of about 125 GeV has been found recently [1, 2] and provides another important success of the SM[2].

Nevertheless there are many open questions and shortcomings in the SM. Besides the unsolved nature of Dark Matter, Mass Hierarchy and other fundamental problems, the SM can not sufficiently account for the huge excess of matter over antimatter observed in our Universe.

The strong matter-antimatter asymmetry in our local region up to the scale of galaxy clusters is evident from γ-ray observations and the absence of an excess of anti-particles in cosmic rays. Also, there are arguments that rule out domains of large abundances of antimatter on scales less than our visible Universe [3–5]. From precise measurements of the Cosmic Microwave Background Radiation, the ratio of the difference of baryon and anti-baryon number densities $n_\mathrm{B} = n_\mathrm{b} - n_{\overline{\mathrm{b}}}$ to photon number density n_γ in today's Universe is determined to [6, 7]

$$\eta = \frac{n_\mathrm{B}}{n_\gamma} = 6.1^{+0.3}_{-0.2} \times 10^{-10}. \tag{2.1}$$

A similar value of η can be deduced from ratios of light element abundances from Big Bang Nucleosynthesis [8]. As the present n_B evolved from a difference in number density of baryons and anti-baryons $n_b - n_{\overline{b}}$ in the early Universe, where at high temperatures $n_\mathrm{b} \approx n_{\overline{\mathrm{b}}} \approx n_\gamma$, a tiny baryon excess of 1 part in 10^{10} led to all of the ordinary matter in the Universe.

Today's baryon abundance predicted from symmetric cosmological models (with initially $n_\mathrm{b} = n_{\overline{\mathrm{b}}}$) is no where near the observed $\eta \approx 10^{-10}$. When in the early Universe the temperature was sufficiently high, a thermal equilibrium of annihilation and pair-production of nucleons N and anti-nucleons $\overline{N}$ is maintained: $N + \overline{N} \rightleftarrows \gamma + \gamma$. As the temperature decreases fewer baryon-anti-baryon pairs are generated and annihilation processes $N + \overline{N} \rightarrow \gamma + \gamma$ are favoured. With lower particle density annihilations cease and effectively stop at a freeze-out temperature $T_\mathrm{f} \approx 20\,\mathrm{MeV}$, when the expansion rate of the

---

[2] Although the nature the Higgs-like observation still has to be clarified. As yet the findings are consistent with a SM Higgs boson.

Universe becomes larger than the annihilation rate. From the temperature dependence of the baryon density to photon density one obtains at the freeze-out temperature [3, 9]

$$\frac{n_b}{n_\gamma} \approx 10^{-18}, \tag{2.2}$$

which is eight orders of magnitude smaller than the value determined from observations.

2.2 Baryon asymmetry and CP violation in the Standard Model (SM)

Several models are under discussion to generate baryonic matter during the early evolution of the Universe (for an overview, see [10, 11]). No matter which framework is used for baryogenesis, there are three conditions necessary to dynamically generate a baryon asymmetry (rather than assuming it to be an initial condition). In 1967 Sakharov [12] formulated these essential conditions:

- **Baryon number violation**
  To create an excess of baryons (B=1) over anti-baryons (B=-1) starting from B=0 (or $\eta = 0$) the baryon number B obviously has to be non-conserved.
- **$\mathcal{C}$ and $\mathcal{CP}$ violation**
  This condition concerns two fundamental symmetries:

  Charge-conjugation $\mathcal{C}$: The operator $\mathcal{C}$ converts particles to corresponding antiparticles by charge reversal

  Parity operation $\mathcal{P}$: The parity operator inverses a vector $\mathcal{P}\boldsymbol{x} = -\boldsymbol{x}$ (mirror reflection followed by 180°)

  To fulfill this condition, charge-conjugation $\mathcal{C}$ and the successive operation of parity and charge-conjugation $\mathcal{CP}$ need to be violated. Otherwise, the rates of processes generating baryon or anti-baryon excess are exactly equal.
- **Departure from thermal equilibrium**
  By definition, in thermal equilibrium every process $X \rightarrow Y + B$, creating a baryon excess B has an inverse process $Y + B \rightarrow X$ with an equal rate.

The most eminent classes of new physics models for generation of baryon asymmetry are electroweak baryogenesis, Grand Unified Theory (GUT) baryogenesis, leptogenesis and the Affleck-Dine mechanism. For reviews see [13–15].
The above prerequisites for baryogenesis can in principle be fulfilled in the framework of the SM. Here, the baryon number is conserved at low energies, but non-perturbative electroweak sphaleron (mass M_{sp}) processes at extreme temperatures ($T \approx M_{sp} \approx 7.2\,\mathrm{TeV}$) violate baryon number [16, 17][3]. Nevertheless, to avoid wash-out of a previously created baryon asymmetry and to account for processes out of thermal equilibrium, a fast first

---

[3] B+L is violated, B-L is strictly conserved (L being the lepton number)

order phase transition in the early Universe is essential. In the SM the electroweak phase transition is not of first order and can thus not adequately describe baryogenesis. At least minimal extensions to the SM are necessary to resolve these issues.[4]
Regarding the second condition the SM also doesn't provide sufficient $\mathcal{CP}$ violation. More detail on this particular issue will be given in the following as this is strongly related to the search for EDMs, see Sec. 2.3.

Parity and charge-conjugation in the SM

In electromagnetic and strong interactions of the SM, parity is conserved. However, parity violation in weak interactions was experimentally confirmed by Wu in 1957 [21] following a proposal from 1956 by Lee and Yang [22]. In Wu's experiment the direction of emitted electrons in the weak decay $^{60}\mathrm{Co} \rightarrow {}^{60}\mathrm{Ni}^* + \mathrm{e}^- + \overline{\nu} \rightarrow {}^{60}\mathrm{Ni} + 2\gamma + \mathrm{e}^- + \overline{\nu}$ was determined for the ^{60}Co nuclear spin aligned both up and down. Surprisingly, they observed all electrons being emitted to the direction opposite to the nuclear spin orientation. This implies, that parity is not only violated but that parity symmetry is maximally broken in weak interactions. This fact could be accounted for in the SM, by adding an axial vector $\propto \epsilon g_w \gamma^5$ to the Lagrangian of the weak interaction, with the weak coupling constant g_w and the Dirac matrix γ^5. As parity is maximally violated in weak interactions $\epsilon = -1$.
Charge conjugation is also strongly violated in the weak interaction, as only left-handed neutrinos and right-handed anti-neutrinos are observed.

$\mathcal{CP}$ violation in the weak sector

The symmetry of the operator $\mathcal{CP}$ in the SM was assumed to hold [23], before Cronin and Fitch observed $\mathcal{CP}$ violation in the weak decay of neutral kaons [24]. In a "pure" beam of a superposition state of the neutral kaon and it's anti-particle two-pion decays on the order of 10^{-3} were observed, which are forbidden by $\mathcal{CP}$ symmetry. Later $\mathcal{CP}$ violation was also found in the $\mathrm{B}^0 \rightleftarrows \overline{\mathrm{B}}^0$ system [25, 26].

Including this small effect of non-conservation of $\mathcal{CP}$ in the SM lead to the predicting of a third quark generation. Cabibbo's [27] theory of mixing of two quark generations, described by a single (real) mixing angle (Cabbibo angle) was extended by Kobayashi et al. [28]. The parametrization of the resulting Cabibbo-Kobayashi-Maskawa (CKM) matrix now describes the quark mixing by three generalized Cabibbo angles $\theta_{12}, \theta_{23}, \theta_{13}$ and a complex phase δ, which accounts for observed $\mathcal{CP}$ violation.

$\mathcal{CP}$ violation in the strong interaction

In QCD, $\mathcal{CP}$ violation is in principal possible via the $\overline{\theta}$-term in the SM Lagrangian. But, the experimental limit on the EDM of the neutron already strongly constraints

---

[4] An extension of the SM actually has been found by the observation of neutrino oscillations [18–20], which confirm non-zero neutrino masses. This allows for a leptonic flavor mixing matrix required for baryogenesis via leptogenesis. It is still under discussion whether the observed baryon asymmetry can be accounted for by leptogenesis.

	$\boldsymbol{B}$	$\boldsymbol{S}$	$\boldsymbol{E}$	$\boldsymbol{B}.\boldsymbol{S}$	$\boldsymbol{E}.\boldsymbol{S}$
Parity	+1	+1	-1	+1	-1
Time reversal	-1	-1	+1	+1	-1

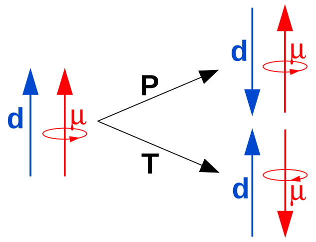

Fig. 1: Under the parity and time-reversal operation polar (electric field $\boldsymbol{E}$) and axial (magnetic field $\boldsymbol{B}$, spin $\boldsymbol{S}$) vectors transform differently. Hence, a term $d\boldsymbol{E}.\boldsymbol{S}$ in the Hamiltonian is parity and time-reversal violating, unless $d = 0$.

$\mathcal{CP}$ violation from the $\overline{\theta}$-term to be extremely small (cf. Sec. 2.5).

In summary, the SM - although being largely successful - can not provide sufficient mechanisms for B-violation, $\mathcal{C}$ and $\mathcal{CP}$ violation and processes out of thermal equilibrium. Models beyond the SM, e.g. supersymmetric models, often provide mechanisms for additional $\mathcal{CP}$ violation. Searching for observable properties generated by these mechanisms is highly motivated to constrain model parameters.

2.3 Permanent electric dipole moments as probes of CP violation

An unmistakable manifestation of $\mathcal{CP}$ violation is a permanent EDM of an elementary system. In this section I will introduce the properties of EDMs, mechanisms that generate EDMs and discuss the sensitivity to new physics of various EDM measurements. Finally, the current status of EDM searches in different systems (neutrons, electrons and atoms) and perspectives of future improvements will be discussed.
The $\mathcal{T}$ and $\mathcal{P}$ violating nature of an EDM can be understood by the different properties of transformations of axial and polar vectors under coordinate inversion and time reversal, see Fig. 1. Assuming $\mathcal{CPT}$ symmetry[5] a non-zero EDM implies also $\mathcal{CP}$ violation. Moreover, the $\mathcal{P}$ odd property makes an EDM a very clean probe of new physics.

The Hamiltonian of a spin-$\frac{1}{2}$ particle with spin $\boldsymbol{S}$, electric dipole moment d and magnetic moment μ in both a magnetic field $\boldsymbol{B}$ and an electric field $\boldsymbol{E}$

$$\mathcal{H} = -\mu\boldsymbol{B}.\frac{\boldsymbol{S}}{S} - d\boldsymbol{E}.\frac{\boldsymbol{S}}{S} \tag{2.3}$$

is only invariant under P and T for $d = 0$.
EDMs are sensitive probes for new $\mathcal{CP}$ odd interactions as well as tests of $\mathcal{T}$ symmetry. A non-zero EDM would provide strong evidence for new physics beyond the SM. In the following mechanisms generating EDMs from $\mathcal{P}$ and $\mathcal{T}$ symmetry violating mechanisms will be discussed.

---

[5] This symmetry is expected to be valid, as violation of the $\mathcal{CPT}$ theorem has very profound consequences, like Lorentz invariance violation [29].

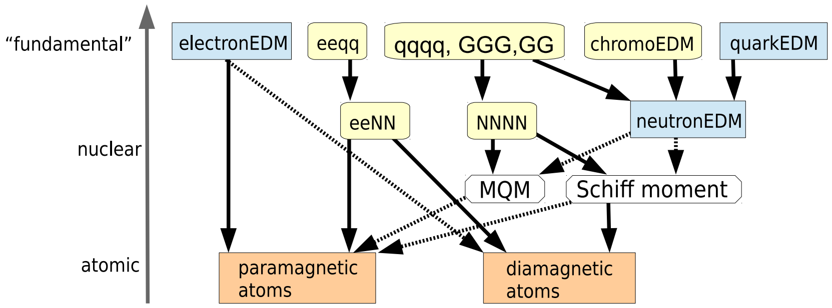

Fig. 2: Shown are sources contributing to EDMs of elementary particles d_n, d_e, paramagnetic atoms, molecules and diamagnetic atoms on different energy scales. To pin down underlying dominant (solid) and higher order (dashed) contributions information from several fundamental systems is absolutely necessary.

2.4 Mechanisms generating EDMs of atoms

The physics underlying the generation of an observable EDM is currently not conclusively understood and the exact mechanisms need to be clarified by experiments. Nevertheless, for different fundamental systems like elementary particles, diamagnetic and paramagnetic atoms or molecules, the physics inducing EDMs can be categorized.

Fig. 2 shows an overview depicting the sources contributing to various systems. References [30–33] give reviews on EDM inducing mechanisms focusing mostly on the neutron and atom EDMs. In the neutron as an elementary system sources of an EDM are intrinsic EDMs of the constituent quarks d_q and various interactions between quarks ($\overline{q}q\overline{q}q$), quarks and gluons (the so called chromo-EDMs $\widetilde{d}_q$) or couplings of gluons ($G\widetilde{G}, GG\widetilde{G}$), where the two-gluon term leads to the famous $\overline{\theta}$ term in QCD.

In more complex systems also electron interactions and an electron EDM contributes to the atomic EDM. The contributions to an atomic EDM at the nuclear level (<1 GeV) can be categorized as

- the intrinsic EDM of an electron d_e,
- the intrinsic EDM of a valence nucleon $d_\mathrm{n}, d_\mathrm{p}$.
- $\mathcal{P}$,$\mathcal{T}$ odd electron-nucleon interactions and
- $\mathcal{P}$,$\mathcal{T}$ odd nucleon-nucleon interactions.

As discussed in the following an EDM of diamagnetic atom mainly arises from an intrinsic nucleon EDM and $\mathcal{T},\mathcal{P}$ odd nucleon-nucleon interactions. Effects on atom EDMs by an electron EDM and $\mathcal{T},\mathcal{P}$ odd electron-nucleon interactions will also be adressed.

Naively, an EDM of a nucleus is supposed to be screened by the electron cloud and hence is not observable[6]. This so called Schiff screening was shown to be complete for a quantum system of point-like electric dipoles in an external electric field of arbitrary shape by Schiff [34]. However, this so-called Schiff shielding is suppressed by relativistic effects[7] in paramagnetic atoms [35, 36] and finite size effects in diamagnetic atoms [34]. In a simple picture the electric field is only canceled on average inside the nucleus, but not necessarily at the location of an unpaired valence nucleon. On an atomic level this effect can be deduced by a multipole expansion of the electrostatic potential of the nucleus.

2.4.1 T, P odd nuclear moments

To account for Schiff screening the electrostatic potential $\varphi(\boldsymbol{R})$ of the nuclear charge density $\rho(\boldsymbol{r})$ implies an additional screening term, hence the potential reads [37]

$$\varphi(\boldsymbol{R}) = \int \frac{e\rho(\boldsymbol{r})}{|\boldsymbol{R}-\boldsymbol{r}|}\mathrm{d}^3r + \frac{1}{Z}(\boldsymbol{d}\cdot\boldsymbol{\nabla})\int\frac{\rho(\boldsymbol{r})}{|\boldsymbol{R}-\boldsymbol{r}|}\mathrm{d}^3r \tag{2.4}$$

with the charge of the nucleus Z ($\int \rho(\boldsymbol{r})\mathrm{d}^3r = Z$) and the the nuclear EDM

$$\boldsymbol{d} = \int e\,\boldsymbol{r}\rho(\boldsymbol{r})\mathrm{d}^3r = d\frac{\boldsymbol{I}}{I}. \tag{2.5}$$

Note, that the EDM vector points along the spin axis $\boldsymbol{I}/I$, as this is the only preferred direction available in an atom[8].

In the multipole expansion of (2.4) the nuclear electric dipole moment is canceled by the screening term (Schiff's screening theorem). The next order $\mathcal{T},\mathcal{P}$ odd term, which mixes states of different parity, in the expansion is[9]

$$\varphi^{(3)} = 4\pi\boldsymbol{S}\boldsymbol{\nabla}\delta(R) - \frac{1}{6}Q_{\alpha\beta\gamma}\nabla_\alpha\nabla_\beta\nabla_\gamma\frac{1}{R} = \varphi^{(3)}_{\text{Schiff}} + \varphi^{(3)}_{\text{octupole}}, \tag{2.6}$$

where $Q_{\alpha\beta\gamma}$ is the nuclear octupole moment and $\boldsymbol{S}$ is the Schiff moment

$$\boldsymbol{S} = \frac{1}{10}\left[\int e\rho(\boldsymbol{r})\boldsymbol{r}r^2\mathrm{d}^3r - \frac{5}{3}\boldsymbol{d}\frac{1}{Z}\int\rho(\boldsymbol{r})r^2\mathrm{d}^3r\right]. \tag{2.7}$$

Note, that Schiff moments and octupole moments only arise for nuclei with spin $I \geqslant \frac{1}{2}$ and $I \geqslant \frac{3}{2}$, respectively. To lowest order the atomic EDM is induced by the contact interaction with nuclear moments.

Analog to the $\mathcal{T},\mathcal{P}$ odd electric multipole moments also the $\mathcal{T},\mathcal{P}$ odd magnetic moments

---

[6] In a classical picture the electric field at the nucleus has to be zero, since otherwise it would be accelerated.

[7] Due to relativistic effects the atomic EDM is even enhanced relative to the an electron EDM.

[8] A non-degenerate quantum system is characterized by the only vector available, the internal angular momentum vector $\boldsymbol{j}$. If an additional direction, independent of $\boldsymbol{j}$, is introduced more quantum numbers are needed to specify the state, which makes the system degenerate.

[9] The electric quadrupole term $\varphi^{(2)}$ turns out to be $\mathcal{T},\mathcal{P}$ even.

Atom	^{129}Xe	^{199}Hg	^{133}Cs	^{203,205}Tl
Nuclear spin I	1/2+	1/2-	7/2+	1/2+
S [$e$fm$^3 \times 10^8$]	$1.75\eta_{np}$	$-1.4\eta_{np}$	$3.0\eta_p$	$-2\eta_p$
M [efm/$m_\mathrm{p} \times 10^7$]	-	-	$1.7\eta_p$	-

Tab. 2.1: Schiff moments (S) and magnetic quadrupole moments (M) induced by the nucleon-nucleon interaction, obtained from numerical calculations using a Woods-Saxon potential with spin-orbit interaction. Results for ^{129}Xe, ^{199}Hg with valence neutron from [43, 44] and for ^{133}Cs, ^{203,205}Tl with valence proton from [45].

induce EDMs in atoms. However, the magnetic quadrupole moment (MQM) can't contribute to EDMs of atoms with zero electron angular momentum[10]. In paramagnetic atoms the EDM from nuclear moments is induced mainly by the MQM, but there is also a strong contribution from an intrinsic EDM of the unpaired electron (cf. Sec. 2.4.3).
Diamagnetic atoms with closed electron shells (e.g. ^{129}Xe, ^{199}Hg) predominantly obtain an EDM from the Schiff moment, as the contribution from the electric octupole moment is significantly suppressed.
However, in the last years the electric octupole moment has attracted interest in the EDM community for it's potential to enhance the Schiff moment in heavy deformed ("pear-shaped") nuclei [38, 39]. Enhancements due to octupole vibrations or static deformations are expected to be on the order of 100-1000 compared to "spherical-shaped" atoms [40]. These findings triggered efforts on EDM searches with radioactive isotopes of Radium (^{225}Ra, $\tau_{1/2} = 14.9\,\mathrm{d}$) [41] and Radon (^{223}Rn, $\tau_{1/2} = 24.3\,\mathrm{min}$) [42].
The Schiff moment, electric octupole moment and MQM can be induced by either the nucleon-nucleon interaction or an intrinsic nucleon EDM. Here, the focus is on spherical nuclei with a single unpaired (or external) nucleon, either proton or neutron.

Inducing nuclear moments via the nucleon-nucleon interaction

The exchange of pions between core nucleons and an external nucleon can contribute to a nuclear moment by excitations of the unpaired nucleon [45] or excitations of the internal nucleons [44], both being of comparable strength. For a simple shell model only considering external nucleon excitations an analytical expression for the nuclear moments was derived in [45]. A summary of the derivation is given in Sec. A.1.
For a heavy nucleus, the $\mathcal{T},\mathcal{P}$ odd nucleon-nucleon interaction of an external nucleon with spin $\boldsymbol{\sigma}$ and the core with nuclear charge density $\rho(\boldsymbol{r})$ simplifies the effective Hamiltonian to

$$\mathcal{H}^{\cancel{T}\cancel{P}} = \frac{G_\mathrm{F}}{\sqrt{2}} \frac{\eta_a}{2m_\mathrm{p}} \boldsymbol{\sigma} \cdot \boldsymbol{\nabla} \rho(\boldsymbol{r}), \tag{2.8}$$

---

[10] In this case the electrons don't provide a magnetic field to interact with the MQM.

Atom	^{129}Xe	^{199}Hg	^{223}Rn	^{225}Ra
d [10^{-17} S/($e$fm^3)$\cdot e$cm]	0.38	-2.8	3.3	-8.5

Tab. 2.2: EDMs arising from the nuclear Schiff moments, calculated by ab initio many-body calculations respecting core polarizations and correlation corrections [46].

with the Fermi coupling constant G_F and the mass of the proton m_p.
The dimensionless interaction strength

$$\eta_a = \frac{Z}{A}\eta_{ap} + \frac{N}{A}\eta_{an} \tag{2.9}$$

includes the interaction of an external nucleon a with core protons η_{ap} and neutrons η_{an}. For the case of an external neutron in a s-state, the Schiff moment is related to η_a via

$$\begin{aligned} S^{\mathrm{Xe}} &\approx -\frac{e}{30}\eta_a\left(r_{\mathrm{ext}}^2 - r_{\mathrm{q}}^2\right) \times 10^{-21}\,\mathrm{cm} \\ S^{\mathrm{Hg}} &\approx -\frac{e}{30}\eta_a\left(\frac{9}{5}r_{\mathrm{ext}}^2 - r_{\mathrm{q}}^2\right) \times 10^{-21}\,\mathrm{cm}. \end{aligned} \tag{2.10}$$

The Schiff moment and hence the EDM arises from a difference of the mean square distance of the valence nucleon from the center of the nucleus r_ext^2 and the mean square radius of the charge distribution r_q^2. The analytic calculation with the usually assumed relation[11] $r_\mathrm{ext}^2 \approx r_\mathrm{q}^2 \approx \frac{3}{5}r_0^2A^{2/3}$ ($r_0 = 1.1\,\mathrm{fm}$) leads to a vanishing Schiff moment and numerical calculations are needed. The Schiff moments induced by the nucleon-nucleon interaction computed in the Woods-Saxon potential $U(\boldsymbol{r}) = \frac{-V_0}{1+e^{(r-R)/a}}$ including spin-orbit interaction are shown in Tab. 2.1 for ^{129}Xe, ^{199}Hg (external neutron) and ^{133}Cs, ^{203,205}Tl (external proton).
An interesting relation can be obtained with the relation $r_{ext}^2 \propto r_q^2 \propto A^{2/3}$. From Eq. 2.10 we can see that the Schiff moment scales as

$$S \propto A^{2/3}. \tag{2.11}$$

Heavy atoms are expected to yield larger EDMs due to an enhancement of the Schiff moment induced by nucleon-nucleon interactions.

Inducing nuclear moments via an EDM of an external nucleon

The second contribution to a nuclear Schiff moment arises directly from the EDM of the unpaired nucleon. Although the contribution from the external nucleon is a factor of 10-100 weaker than from the nucleon-nucleon interaction [45], improved limits on atomic EDMs can compete with direct constraints on the proton and neutron EDM.
The expression for the Schiff moment due to an external nucleon EDM obtained in [31,

---

[11] Justified by results from electron scattering on nuclei.

Atom	^{129}Xe	^{199}Hg	^{133}Cs	^{203,205}Tl
$d[10^{-18}\,C^{\mathrm{SP}}\,e\mathrm{cm}]$	-5.6×10^{-5}	-5.9×10^{-4}	0.7	-5.1
$d[10^{-23}\,C^{\mathrm{PS}}\,e\mathrm{cm}]$	1.2	6.0	2.2	1.5
$d[10^{-20}\,C^{\mathrm{T}}\,e\mathrm{cm}]$	0.52	2.0	0.92	0.5

Tab. 2.3: Atom EDMs d induced by the electron-nucleon interaction. Results are quoted from [31] and originate from various references therein. Note the units of atom EDMs given.

47] turns out to be very similar to Eq. (2.10), with the replacement $0.2e\eta_a \times 10^{-21}$ cm → d_{n} and yields

$$\begin{aligned} S^{\mathrm{Xe}} &= \frac{1}{6} d_{\mathrm{n}} \left[r_{\mathrm{ext}}^2 - r_{\mathrm{q}}^2\right] \\ S^{\mathrm{Hg}} &= \frac{1}{6} d_{\mathrm{n}} \left[\frac{9}{3} r_{\mathrm{ext}}^2 - r_{\mathrm{q}}^2\right]. \end{aligned} \tag{2.12}$$

With a comparison of the experimental value and the result from a simple shell model of the magnetic moment the contribution of the proton EDMs can be accounted for by replacing

$$d_n \rightarrow d_n + 0.1 d_p \tag{2.13}$$

The EDM values induced by the Schiff moment, predominantly by the nucleon-nucleon interaction, are shown in Tab. 2.2. For constraints on $\mathcal{T},\mathcal{P}$ odd nucleon-nucleon interactions ^{199}Hg is roughly a factor of ten more sensitive than ^{129}Xe. Octupole deformed nuclei can give a threefold improvement over ^{199}Hg at the same EDM sensitivity level.

2.4.2 Electron-nucleon interaction

Mixing of opposite parity states of electrons close to the nuclear core can lead to an atomic EDM. The $\mathcal{T},\mathcal{P}$ odd interaction generating the mixing of the state of an electron e can be written as [31]

$$\mathcal{H}_{\mathrm{eN}}^{\cancel{\mathcal{TP}}} = \frac{G_{\mathrm{F}}}{\sqrt{2}} \sum_N \left[C_N^{\mathrm{SP}} \underbrace{(\overline{N}N)(\overline{e}i\gamma_5 e)}_{\text{scalar-pseudoscalar}} + C_N^{\mathrm{PS}} \underbrace{(\overline{N}i\gamma_5 N)(\overline{e}e)}_{\text{pseudoscaler-scalar}} + C_N^{\mathrm{T}} \underbrace{(\overline{N}i\gamma_5\sigma_{\mu\nu}N)(\overline{e}\sigma_{\mu\nu}e)}_{\text{tensor}}\right], \tag{2.14}$$

with the sum running over all nucleons wave-functions N, the dimensionless constants C_N^{SP}, C_N^{PS} and C_N^{T} describing the interaction strength and $\sigma_{\mu\nu} = \frac{1}{2}(\gamma_\mu\gamma_\nu - \gamma_\nu\gamma_\mu)$. For an infinite mass of the nucleus, the pseudoscalar-scalar term can be neglected and

Atom	^{129}Xe	^{199}Hg	^{133}Cs	^{203,205}Tl
$K = d_{\mathrm{atom}}/d_e$	-0.0008	-0.014	114 to 115	-1041 to -179

Tab. 2.4: Enhancement factors for the electron EDM in paramagnetic and diamagnetic atoms, obtained from ab initio calculations [31].

the interaction with the nucleus containing Z protons and N neutrons is simplified to

$$\mathcal{H}_{\mathrm{eN}}^{\cancel{\mathrm{TP}}} = i\frac{G_{\mathrm{F}}}{\sqrt{2}}\rho(r)\Bigg[\underbrace{\left(ZC_p^{\mathrm{SP}} + NC_n^{\mathrm{SP}}\right)\gamma_0\gamma_5}_{\text{spin-indep.}} + \underbrace{2\Bigg(C_p^{\mathrm{T}}\sum_p \boldsymbol{\sigma}_p + C_n^{\mathrm{T}}\sum_n \boldsymbol{\sigma}_n\Bigg)\cdot\boldsymbol{\gamma}}_{\text{spin-dep.}}\Bigg], \tag{2.15}$$

where $\rho(r)$ is the normalized spin density in the nucleus ($\int \rho(r)dV = 1$) and $\boldsymbol{\sigma}_p$, $\boldsymbol{\sigma}_n$ are nuclear proton and neutron spins, respectively and $\boldsymbol{\gamma}$ the Dirac matrix of the electron. The spin-independent term arises from contributions of the nucleons in the core and the spin-dependent term emerges from the unpaired nucleon.

While in paramagnetic atoms both, C^{SP} and C^{T} can directly induce an atomic EDM, diamagnetic atoms only have direct contributions from the spin-dependent C^{T}. However, if the hyperfine interaction is taken into account as a perturbation, the nuclear spin-independent coefficients can also be constrained by EDM limits of diamagnetic atoms with the relations given in Sec. A.2. Tab. 2.3 quotes the EDM values induced by the various contributions of $\mathcal{H}_{\mathrm{eN}}^{\cancel{\mathrm{TP}}}$. Notably, an EDM limit on ^{129}Xe yields a fourfold to tenfold improved constrain on the electron-nucleon interaction compared to a ^{199}Hg limit of similar sensitivity.

2.4.3 Electron EDM

Sandars [36] pointed out that an atomic EDM arises from an electron EDM, if the problem is treated relativistically. Enhancement factors $K = d_{\mathrm{atom}}/d_{\mathrm{e}}$ ranging from 10^{-3} for lithium up to 10^{3} for francium emerge from two contributions:

(i) the intrinsic EDM of the electrons

(ii) the $\mathcal{T},\mathcal{P}$ odd interaction of the electron EDM with the (electric and magnetic) field of the nucleus.

Paramagnetic atoms obtain their atomic EDM predominantly from an enhanced electron EDM. The relativistic electron is subject to a strong motional magnetic field in the Coulomb potential of the nucleus. Due to the spin-orbit coupling, Schiff screening is partly balanced and the electron experiences an internal electric field. An order of magnitude estimate for the enhancement K is given by [31]

$$d_{\mathrm{para}}(d_e) \approx 10\alpha^2 Z^3 d_e. \tag{2.16}$$

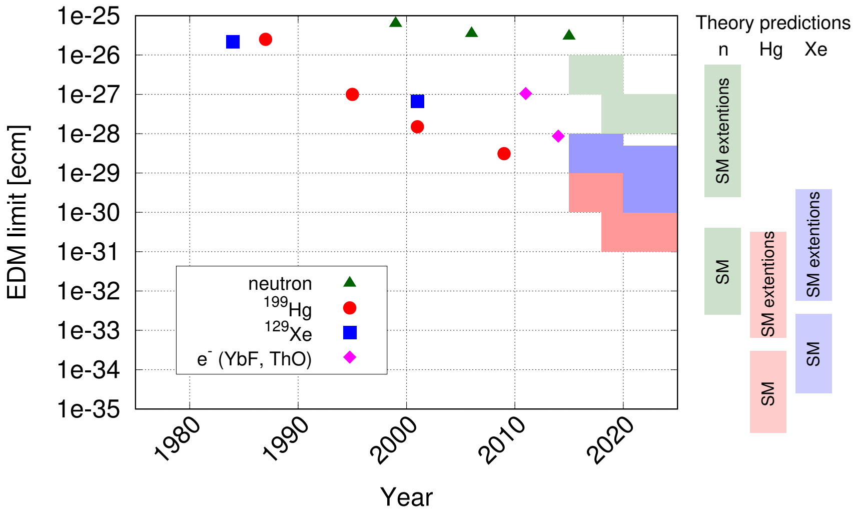

Fig. 3: Published limits on the EDM of the neutron, electron, ^{199}Hg and ^{129}Xe within the last three decades. Also shown are projected experimental sensitivities and ranges from theoretical predictons for the SM and extentions of the SM. The EDM sensitivity for ^{129}Xe has fallen behind that for ^{199}Hg, although ^{129}Xe offers a valuable probe for $\mathcal{CP}$ odd hadronic and semileptonic couplings.

Note, that the enhancement scales with the proton number Z^3.
Diamagnetic atoms are only weakly sensitive to an electron EDM mainly caused by two higher order effects [30]. The first arises in third order perturbation theory and takes into account polarization of the closed electron shells along the nuclear spin by the hyperfine interaction. The second, more important contribution emerges from a direct interaction of the electron EDM with the magnetic moment of the nucleus.
Although the sensitivity is negligible (Tab. 2.4) a relation between the electron EDM d_e and the electron-nucleon tensor coupling strength C^T can be obtained to set a limit to d_e from a EDM measurement of a diamagnetic atom, cf. Sec. A.3.

2.5 Sensitivity of EDMs to physics beyond the SM

As the sources of atomic EDMs have been discussed very generally on the atomic and nuclear level in the previous chapter now the implications of EDM limits on new physics and the sensitivity of diamagnetic atoms to higher energy parameters will be covered.
The search for an EDM is strongly related to physics beyond the SM, since models extending the SM usually predict larger EDM values. Limits on EDMs can strongly constrain models beyond the SM (e.g. SUSY, Multi-Higgs models [48], etc.).

An effective Lagrangian of $\mathcal{CP}$ odd operators up to dimension six including beyond-SM terms and normalized to 1 GeV[12] can be obtained in a model-independent way as

---

[12] All particles with higher mass are integrated out and need not be considered.

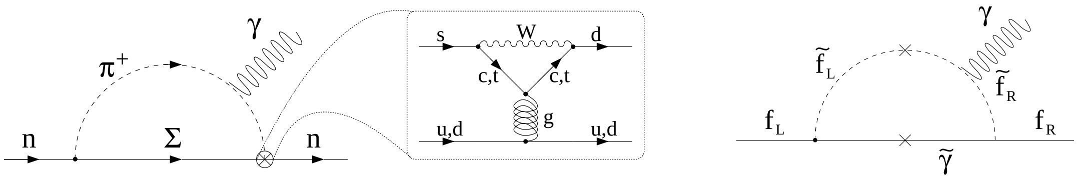

Fig. 4: (a) In the SM a contribution to an EDM (the neutron in the example diagram) can only be generated in higher order loops (Adapted from [32]). (b) Supersymmetric models allow these mechanisms at one-loop level.

(see [49] for a compact or [32] for a more extensive review)

$$\mathcal{L}^{\not{T}\not{P}} = \mathcal{L}_{\overline{\theta}} + \mathcal{L}_{\text{EDM}} + \mathcal{L}_{\text{3Gluon}} + \mathcal{L}_{\text{4Fermion}}. \tag{2.17}$$

The leading term of dimension four is called the $\overline{\theta}$-term

$$\mathcal{L}_{\overline{\theta}} = \frac{g_{\text{s}}^2}{32\pi}\overline{\theta}G\widetilde{G}, \tag{2.18}$$

with the dimensionless parameter $\overline{\theta}$ characterizing it's strength, the strong coupling constant g_{s}, the gluon field G and it's dual $\widetilde{G}$. The EDMs d_i and chromo-EDMs $\widetilde{d_i}$ of constituent particles arising from their coupling to the electromagnetic field F and the gluon field G, respectively, are represented as

$$\mathcal{L}_{\text{EDM}} = -\frac{i}{2}\sum_{i=e,\mu,u,d,s} d_i\overline{\psi}_i(F\sigma)\gamma_5\psi_i - \frac{i}{2}\sum_{u,d,s}\widetilde{d_i}\overline{\psi}_i g_s(G\sigma)\gamma_5\psi_i, \tag{2.19}$$

where ψ_i are the Dirac fields of the particles involved. The third term of dimension six is called the Weinberg term and denotes a three-gluon interaction

$$\mathcal{L}_{\text{3Gluon}} = \frac{1}{3}wf^{abc}GG\widetilde{G}. \tag{2.20}$$

It will not be considered further, since it has been shown that this term is not dominant in generating nucleon EDMs [50]. The last term considered in the effective $\mathcal{CP}$ odd Lagrangian allows for four-fermion couplings, where usually only hadronic and semi-leptonic ones are taken into account:

$$\mathcal{L}_{\text{4Fermion}} = \sum_{i,j=e,\mu,u,d,s} C_{ij}(\overline{\psi}_i\psi_i)(\psi_j i\gamma_5\psi_j). \tag{2.21}$$

EDMs in the Standard model

The SM only provides the QCD parameter $\overline{\theta}$ and the complex phase δ in the CKM matrix to allow for $\mathcal{CP}$ violating effects[13]. Calculations of EDMs of electrons, neutrons

---

[13] This assumes massless neutrinos in the SM. Since neutrino oscillations have been confirmed a lepton mixing matrix also provides a mechanism for $\mathcal{CP}$ violation. However, calculations of lepton EDMs show negligible contributions from neutrino masses and mixing [51].

and ^{199}Hg due to CKM phase contributions yield [49]

$$\begin{aligned} d_{\mathrm{e}}(J) &\lesssim 10^{-38} && (J/J_{\mathrm{exp}})\, e\mathrm{cm} \\ d_{\mathrm{n}}(J) &\lesssim 10^{-32} - 10^{-31} && (J/J_{\mathrm{exp}})\, e\mathrm{cm} \\ d_{\mathrm{Hg}}(J) &\lesssim 10^{-34} - 10^{-35} && (J/J_{\mathrm{exp}})\, e\mathrm{cm}, \end{aligned} \tag{2.22}$$

parametrized by the ratio of calculated Jarlskog invariant[14] J [52] to the experimentally determined value

$$J_{\mathrm{exp}} = Im[V_{\mathrm{us}} V_{\mathrm{cb}} V^*_{\mathrm{cs}} V^*_{\mathrm{ub}}] \approx 3 \times 10^{-5}. \tag{2.23}$$

As reviewed in [32] SM contributions to quark EDMs turn out to arise at three-loop level[15] and are of order $d_{\mathrm{q}} \approx 10^{-34}\, e\mathrm{cm}$. The contribution to the neutron EDM is dominated by a four-quark operator enhanced by a pion loop (Fig. 4).
An observable neutron EDM due to the $\overline{\theta}$ term in QCD was calculated in [53, 54]

$$d_{\mathrm{n}}(\overline{\theta}) \approx (10^{-16}\overline{\theta})\, e\mathrm{cm}. \tag{2.24}$$

With the current limit $d_{\mathrm{n}} < 3 \times 10^{-26}$ [55] the $\overline{\theta}$ term is constrained to $\overline{\theta} < 10^{-10}$, which implies a very unnatural fine-tuning, as $\overline{\theta} \approx \mathcal{O}(1)$ is expected.
This so called strong $\mathcal{CP}$ problem could in principal be solved by introducing a new particle, as suggested by Peccei and Quinn [56]. This pseudoscalar Goldstone boson, called axion arises from spontaneous symmetry breaking of $U_{\mathrm{PQ}}(1)$ at a high energy scale f_{a} and yields a shift of $\overline{\theta} \to \overline{\theta} + a/f_{\mathrm{a}}$, where a is the axion field, with the mass $m_{\mathrm{a}} = 0.60\,\mathrm{meV}/(f_{\mathrm{a}}/10^{10})\,\mathrm{GeV}$. But, no indications of the axion are found yet. For a recent review on axions, see [57].

EDMs in extensions of the SM

Extensions of the SM often include more $\mathcal{CP}$ odd phases, which are generated at lower loop level and hence lead to larger EDMs. For example, the SUSY prediction for the neutron EDM of $d_{\mathrm{n}}^{\mathrm{SUSY}} \approx 10^{-26} - 10^{-30}\ e\mathrm{cm}$ (cf. [58]) is several orders of magnitude larger than the SM prediction and within reach of upcoming experiments (cf. Sec. 2.6). In the minimal super-symmetric model (MSSM) a linear combination of two independent phases θ_μ and θ_{A} can generate $\mathcal{CP}$ violation. Both phases can be constrained by combining EDM limits, e.g. of the neutron, electron and atoms. Particularly the ^{199}Hg EDM limit can set tight constraints [59] of order $10^{-2} - 10^{-3}$ on these phases for a mass scale $M_{\mathrm{SUSY}} \lesssim 1\,\mathrm{Tev}$ (Fig. 5).

Parameter contraints from different systems

Reviews on the constraints from EDM limits on the nuclear and QCD level can be found in [31] and [33, 60], respectively. The model independent parameters in the $\mathcal{CP}$ odd Lagrangian (2.17) can only be sufficiently constrained from measurements in different systems (cf. Tab. 2.5).

---

[14] The Jarlskog invariant characterizes the $\mathcal{CP}$ violating phase δ in the CKM matrix.

[15] Contributions at two-loop level are exactly zero.

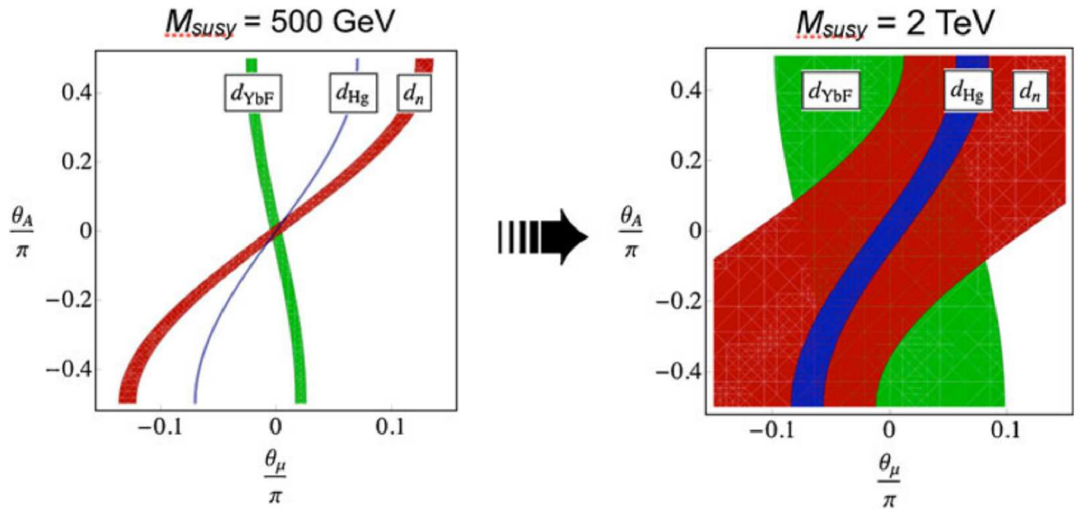

Fig. 5: Constraints on $\mathcal{CP}$ violating phases θ_μ and θ_A of minimal SUSY imposed by combined limits of the EDM of the neutron, YbF and ^{199}Hg. The tight constraints for MSSM mass scales $M_{\mathrm{SUSY}} < 1$ TeV, which are excluded by non-observation of new particles at the LHC, can only be relaxed by increasing $M_{\mathrm{SUSY}} > 1$ TeV (Reproduced from [49] with permission).

GeV scale		n,p-EDM	nucleon-nucleon				e$^-$-nucleon		
TeV scale	d_{e^-}	d_{q}	$\widetilde{d}_{\mathrm{q}}$	$\overline{\theta}$-QCD	$GG\widetilde{G}$	$q\widetilde{q}q\widetilde{q}$	C^{SP}	C^{PS}	C^{T}
neutron	-	++	++	++	+	+	-	-	-
param. atoms	++	o	o	o	o	o	++	o	o
diam. atoms	o	+	+	+	+	+	+	o	++

Tab. 2.5: Different systems need to be probed in EDM searches in order to constrain the underlying $\mathcal{CP}$ violating mechanisms, as their sensitivity to the $\mathcal{CP}$ odd operators varies. This table illustrates the sensitivities by high (++), good (+), low (o) and not sensitive (-).

As has been pointed out in [61] comparable constraints on the effective $\mathcal{CP}$ odd operators can be drawn by EDM limits from the neutron as from atomic systems, particularly considering the high sensitivity that has been achieved in the ^{199}Hg measurement.
From nuclear Schiff moment calculations (Tab. 2.2) the dimensionless nucleon-nucleon coupling η_{np} (Tab. 2.1) and the electron-nucleon tensor interaction (Tab. 2.3) can be constrained. The nucleon-nucleon coupling strength is related to the QCD coupling constant by[16] [31]

$$\eta_{np} \approx \frac{\sqrt{2}}{G_{\mathrm{F}} m_\pi^2} g\overline{g} = \frac{\sqrt{2}}{G_{\mathrm{F}} m_\pi^2} g(\overline{g}_\pi^{(0)} + \overline{g}_\pi^{(1)} - 2\overline{g}_\pi^{(2)}) \approx 7 \times 10^6 g(\overline{g}_\pi^{(0)} + \overline{g}_\pi^{(1)}), \tag{2.25}$$

---

[16] To first order only the contribution of the lightest meson π_0 needs to be considered.

with the strong coupling constant $g = 13.6$, the pion mass m_π and the isoscalar $\overline{g}_\pi^{(0)}$, isovector $\overline{g}_\pi^{(1)}$ and isotensor $\overline{g}_\pi^{(2)}$ couplings. The latter turns out to be suppressed [33]. Note, that $\overline{\theta}$ is related to $\overline{g}$ as [53]

$$|\overline{g}| \approx |\overline{g}_\pi^{(0)} + \overline{g}_\pi^{(1)}| \approx 0.027\,\overline{\theta}. \tag{2.26}$$

Constraints on the chromo EDMs of up- and down-quark can be obtained from [62]

$$\overline{g} = 2(\widetilde{d}_u - \widetilde{d}_d)/10^{-14}\,e\text{cm}. \tag{2.27}$$

For the description of four fermion interactions phenomenological parameters for quark-quark and semi-leptonic interactions are defined and respective limits extracted, cf. [31]. The neutron EDM sets a limit on the parameter $\overline{\theta}$ (cf. Eq. (2.24)) and the quark and chromo EDMs via [63]

$$d_\mathrm{n} = (1 \pm 0.5)[0.55e(\widetilde{d}_\mathrm{d} + 0.5\widetilde{d}_\mathrm{u}) + 0.7(d_\mathrm{d} - 0.25d_\mathrm{u})]. \tag{2.28}$$

The EDM limit obtained from paramagnetic atoms dominantly imposes constraints on an electron EDM d_e and the scalar-pseudoscalar coupling C^SP.

Diamagnetic atoms are particularly sensitive to hadronic sources and the spin-dependent electron-nucleon coupling (Eq. 2.15). In higher order also the electron EDM and C^SP contribute.

To disentangle the many $\mathcal{T}, \mathcal{P}$ odd parameters $d_\mathrm{e}, C^\mathrm{SP}, C^\mathrm{T}, \overline{g}_\pi^{(0)}, \overline{g}_\pi^{(1)}$ and the neutron and proton EDM $d_\mathrm{n}, d_\mathrm{p}$ various EDM limits on different systems are needed. A summary on improvements on the parameters from additional new EDM limits of ^{129}Xe, ^{225}Ra, the neutron and their combination is given in [60]. Adding an ^{129}Xe EDM limit of $\approx 10^{-29}\,e$cm to the current ^{199}Hg limit the constraints on $C^\mathrm{T}, \overline{g}_\pi^{(0)}, \overline{g}_\pi^{(1)}$ would be improved by factors of roughly 10, 3 and 2, respectively. The effective field theory [60] and nuclear calculations [31] identify the importance of new EDM limits of additional diamagnetic systems, even though the ^{199}Hg measurement already provides an excellent sensitivity.

2.6 Experimental status and prospects of EDM searches

In this section the basic experimental method used in state-of-the-art EDM searches will be introduced. A detailed discussion focused on the most recent measurement on ^{129}Xe is postponed to Sec. 4, where also new approaches to further improve the sensitivity are presented.

Various efforts of EDM searches have been undertaken after the possibility of non-zero EDMs was suggested about 60 years ago [64]. In the first EDM experiment Ramsey used the technique of separated oscillatory fields, which he developed and adapted to a neutron beam to search for an EDM [65] (for a recent review of the method, see [66]).

Most EDM experiments nowadays, no matter whether the system used is the neutron, para- or diamagnetic atoms are looking for a deviation of the Larmor precession frequency ω_L when applying an additional electric field $\boldsymbol{E}$ parallel to a magnetic field $\boldsymbol{B}$. The Zeeman splitting in a two-level system reads

$$\hbar\omega_\mathrm{L} = 2(\boldsymbol{\mu}.\boldsymbol{B} - \boldsymbol{d}.\boldsymbol{E}) \tag{2.29}$$

	Experiment [ecm]		SM pred.	References	
	Current	Proposed	[ecm]	exp.	theor.
n	3×10^{-26}	$\sim 10^{-28}$	$\sim 10^{-31} - 10^{-32}$	[55]	[68]
e^-	8.7×10^{-29}	$\sim 10^{-32}$	$\lesssim 10^{-38}$	[69]	[32, 70]
^{129}Xe	$0.7 \pm 3.3 \times 10^{-27}$	$\sim 10^{-29}$	$\sim 10^{-33} - 10^{-34}$	[71]	[45]
^{199}Hg	3.1×10^{-29}	$\lesssim 10^{-29}$	$\sim 10^{-34} - 10^{-35}$	[67]	[49]

Tab. 2.6: Current experimental limits, goals of next generation experiments and predicted values in the SM for the EDMs of neutrons, electrons and diamagnetic atoms. Experimental values for neutrons and electrons are 90% C.L. and for ^{199}Hg 95% C.L..

with the magnetic moment $\boldsymbol{\mu}$ and the electric dipole moment $\boldsymbol{d}$.
Some recent EDM measurements and their limits for elementary particles and diamagnetic atoms are listed in Tab. 2.6. For EDM measurements with diamagnetic atoms the highest sensitivity was achieved in the experiment with the stable isotope ^{199}Hg [67]. This actually leads to nearly competitive constraints even on parameters that ^{199}Hg is not particularly a very sensitive probe of. In Tab. 2.7 constraints deduced from the recent limit on the EDM of ^{199}Hg are compared to the current ^{129}Xe limit. The numbers are obtained from the results on atomic calculations previously presented in this section. In the last column a projected ^{129}Xe EDM limit at the current ^{199}Hg sensitivity is assumed, which shows that for the electron-nucleon couplings an EDM search with ^{129}Xe has significantly better sensitivity. However, for hadronic interactions and EDMs of elementary particles the ^{129}Xe sensitivity has to reach a level of 10^{-30} $e$cm to compete with ^{199}Hg.

Since work on diamagnetic atoms started in the 1980s limits and errors have been greatly improved, especially for measurements using ^{199}Hg. EDM searches on xenon still have to catch up on sensitivity and errors (cf. Fig. 3). Note, that a factor four improvement on the ^{129}Xe EDM published in 1984 [72] was achieved in 2001 [71], about 17 years later. Slow progress in ^{129}Xe compared to ^{199}Hg is mostly due to the fact, that the availability of UV lasers at 254 nm makes direct optical detection of mercury spin-precession viable. But, the option to liquefy polarized ^{129}Xe offers a very high potential of improving the xenon EDM limit not only statistically but also by applying a novel method, as will be discussed in detail in Sec. 5.
Many new EDM experiments on new systems are currently developed. The intrinsic high electric field available in polar molecules make these a perfect probe for an electron EDM. Octupole-deformed nuclei are promising new candidates for next generation EDM experiments, due to their strong enhancement of the Schiff moment. Besides, there are various efforts to improve the EDM limit of the neutron by about two orders of magnitude. Proposed storage ring EDM searches open up possibilities for charged particles and light atoms overcoming suppression due to Schiff screening. Sec. 4 is dedicated to a discussion of proposed improvements and new measurement methods in upcoming EDM searches, particularly using ^{129}Xe.

	^{199}Hg exp.	^{199}Hg /^{129}Xe exp.	^{199}Hg /^{129}Xe proj.
d_{n}	$(17 \pm 10) \times 10^{-26}$	n/a	n/a
d_{p}	$(1.7 \pm 1) \times 10^{-24}$	n/a	n/a
d_{e}	$(91 \pm 54) \times 10^{-28}$	0.0025	≈ 0.1
η	$(2.7 \pm 1.6) \times 10^{-4}$	0.0048	≈ 0.5
C^{SP}	$0.4C_p^{\mathrm{SP}} + 0.6C_n^{\mathrm{SP}} = 18 \pm 10.6) \times 10^{-8}$	0.47	≈ 47
C^{PS}	$C_n^{\mathrm{PS}} = (1.8 \pm 1.1) \times 10^{-6}$	0.22	≈ 22
C^{T}	$C_n^{\mathrm{T}} = 5.3 \pm 3.2 \times 10^{-9}$	0.17	≈ 17

Tab. 2.7: How does ^{129}Xe compete with ^{199}Hg? Constraints on atomic parameters deduced from current limits on the EDM of ^{199}Hg [31] are shown in the first column. The sensitivity on these parameters of the most recent ($\approx 10^{-27}\,e$cm) and projected limits for ^{129}Xe $\approx 10^{-29}\,e$cm is obtained from numerical results of atomic calculations.

In summary, searching for EDMs is becoming more and more challenging as the sensitivity gets pushed further, but nevertheless has gained a lot of interest due to the strong impact of EDM limits on new physics models. Limits obtained from EDM searches already now probe new physics at very high energy scales beyond the reach of particle colliders available in the near future.

3 Optimizing the parameter space for a new ^{129}Xe EDM search

A key to new EDM experiments, particularly using novel concepts, is evaluation of the parameter space. For that purpose the theoretical and experimental principles of atomic physics, spin precession and superconducting magnetometers are introduced in this section. The first part will be dedicated to some basic atomic physics, before advancing to optical pumping of alkali atoms and spin-exchange to the noble gas nuclei. A discussion of spin relaxation of ^{129}Xe and ^{3}He will be given in Sec. 3.3 with emphasis on the relaxation mechanisms in gas, liquid and solid phases of ^{129}Xe. A short introduction to superconductivity and the benefits of superconducting quantum interference devices (SQUIDs) for detection of spin-precession will conclude this section.

3.1 Atomic physics

For the course of this section on optical pumping and spin precession physics some fundamentals of atomic magnetic moments, level splitting and response to externally applied magnetic fields are needed. Most of this is treated in standard textbooks, e.g. [73].

3.1.1 Atomic magnetic moments and level splitting

The terminology characterizing electronic energy levels follows $n^{2S+1}L_{\mathrm{J}}$, with the principal quantum number n, the multiplicity $2S+1$, the orbital angular momentum L and the total angular momentum J. L represents the orbital angular momentum $l = 0, 1, 2, ...$, but for historic reasons $l = S, P, D, F, ...$ is commonly used.

The electronic magnetic moment $\boldsymbol{\mu}_{\mathrm{J}}$ of an atom has contributions from the electron's orbital angular momentum $\boldsymbol{L}$ and it's spin $\boldsymbol{S}$. The spin-orbit coupling leads to the total angular momentum $\boldsymbol{J} = \boldsymbol{L} + \boldsymbol{S}$ yielding the magnetic moment due to the electron cloud

$$\boldsymbol{\mu}_{\mathrm{J}} = -g_{\mathrm{J}} \frac{\mu_{\mathrm{B}}}{\hbar} \boldsymbol{J}, \text{ where } g_{\mathrm{J}} = 1 + \frac{\boldsymbol{J}^2 + \boldsymbol{S}^2 - \boldsymbol{L}^2}{2\boldsymbol{J}^2} \tag{3.1}$$

is the Landé factor and the Bohr magneton $\mu_{\mathrm{B}} = \frac{e\hbar}{2m_e}$. The total angular momentum takes on values of $L - S \leq J \leq L + S$ in integer steps.

The nuclear magnetic moment $\boldsymbol{\mu}_{\mathrm{I}}$ is determined by the sum of the combination of spins and orbital angular momenta of all nucleons $\boldsymbol{I} = \sum_i (\boldsymbol{s}_i + \boldsymbol{l}_i)$ as

$$\boldsymbol{\mu}_{\mathrm{I}} = g_{\mathrm{I}} \frac{\mu_{\mathrm{N}}}{\hbar} \boldsymbol{I}, \tag{3.2}$$

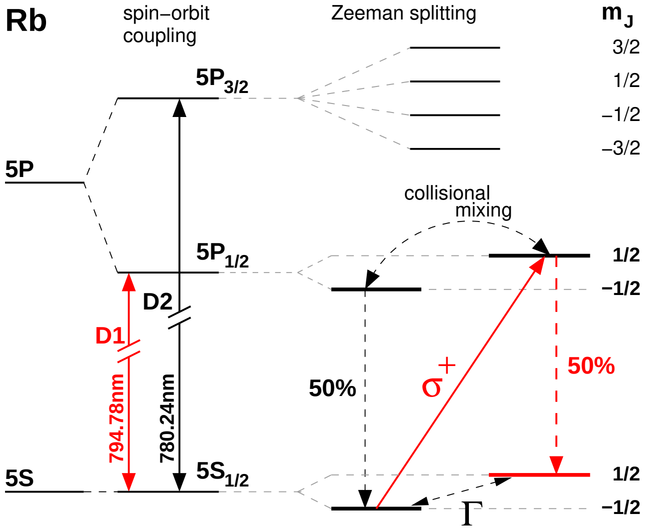

Fig. 6: Level splittings due to spin-orbit coupling (fine structure) and the weak field Zeeman effect of Rb. Also shown is the optical pumping scheme using the D1 transition ($5^1\mathrm{S}_{1/2} \rightarrow 5^1\mathrm{P}_{1/2}$) and circularly polarized light (e.g. σ^+) to populate the $m_\mathrm{J} = +1/2$ spin state in a magnetic field. The Zeeman levels of the S- and P-state are mixed by spin-destruction mechanisms (spin destruction rate Γ) and collisional mixing, respectively.

with the nuclear structure dependent “g-factor” g_I and the nuclear magneton $\mu_\mathrm{N} = \frac{e\hbar}{2m_p} \approx 10^{-3}\mu_B$. The total angular momentum of the atom $\boldsymbol{F} = \boldsymbol{J} + \boldsymbol{I}$ is obtained by coupling of the total angular momentum of the electron cloud $\boldsymbol{J}$ and the nuclear angular momentum $\boldsymbol{I}$ giving values $J - I \leq F \leq J + I$, with F taking integer values.

Level splitting in zero external magnetic field

The atomic “fine structure” is introduced by splitting degenerate energy levels according to their spin state (cf. Fig. 6). The spin-orbit interaction of the spin’s moment $\boldsymbol{\mu}_\mathrm{S} = g_\mathrm{e}\frac{\mu_\mathrm{B}}{\hbar}\boldsymbol{S}$ with the electron g-factor $g_\mathrm{e} \approx 2$ and the motional magnetic field $\boldsymbol{B} = -\frac{1}{c^2}\boldsymbol{v} \times \boldsymbol{E}_\mathrm{nuc}$ adds a potential energy $\Delta E^\mathrm{fine} = -\boldsymbol{\mu}_S.\boldsymbol{B}$, which is $\approx 0.03\,\mathrm{eV}$ for rubidium (cf. Fig. 6). Furthermore, fine structure levels are shifted by relativistic corrections and the Darwin term. The interaction of the nuclear magnetic moment $\boldsymbol{\mu}_\mathrm{N}$ with the magnetic field generated by the electrons $\boldsymbol{B}_\mathrm{elec}$ generates the atomic hyperfine structure ($\Delta E^\mathrm{hf} = -\boldsymbol{\mu}_\mathrm{N}.\boldsymbol{B}_\mathrm{elec} \approx 10^{-5}\,\mathrm{eV}$).
The properties of atoms relevant for this work can be found in Tab. A.1.

Atoms in static magnetic fields

For optical pumping, the Zeeman splitting due to static magnetic fields is most important. Manipulating spins in static fields with time-varying magnetic fields is of great significance for magnetic resonance techniques, particularly nuclear magnetic resonance (NMR) and will be treated in Sec. 3.1.2.
In the limits of weak ($\Delta E_\mathrm{B} \ll \Delta E_\mathrm{fine}, \Delta E_\mathrm{hf}$) and strong ($\Delta E_\mathrm{B} \gg \Delta E_\mathrm{fine}, \Delta E_\mathrm{hf}$) magnetic

fields the breaking of degeneracy is the Zeeman and Paschen-Back effect, respectively. An external magnetic field splits up the fine and hyperfine levels into $2J+1$ and $2F+1$ energy levels, respectively. Depending on the applied magnetic field the electron angular momenta $\boldsymbol{S}$ (spin) and $\boldsymbol{L}$ (orbit) are either coupled to $\boldsymbol{J} = \boldsymbol{S} + \boldsymbol{L}$ (weak field) or uncoupled (strong field). The level splittings due to angular momenta couplings are of order $10^{-2}\,\mathrm{eV}$ (spin-orbit) and $10^{-5}\,\mathrm{eV}$ (electron-nuclear angular momenta), hence magnetic fields $B \ll 0.1\,\mathrm{T}$ are considered weak.
For a magnetic field B in z direction (the quantization axis) the separation of the fine and hyperfine structure levels are

$$\Delta E_{\mathrm{B}}^{\mathrm{fine}} = g_{\mathrm{J}} m_{\mathrm{J}} \mu_{\mathrm{B}} B_z \quad \text{and} \quad \Delta E_{\mathrm{B}}^{\mathrm{hf}} = g_{\mathrm{F}} m_{\mathrm{F}} \mu_{\mathrm{B}} B_z. \tag{3.3}$$

The magnetic quantum numbers m_{J} and m_{F} take on integer values from $-J\hbar, ..., J\hbar$ and $-F\hbar, ..., F\hbar$, respectively. In (3.3) g_{J} is the Landé factor (Eq. (3.1)) and

$$g_{\mathrm{F}} = g_{\mathrm{J}} \frac{F(F+1) + J(J+1) - I(I+1)}{2F(F+1)} + g_{\mathrm{I}} \frac{F(F+1) + I(I+1) - J(J+1)}{2F(F+1)}, \tag{3.4}$$

where the second term is often negligible as $g_{\mathrm{I}} \approx 10^{-3} g_{\mathrm{J}}$.

In optical pumping techniques the Zeeman level splitting is utilized to populate one electronic spin state of an alkali metal, e.g. rubidium (cf. Fig. 6 and Sec. 3.2) in magnetic fields of $1-10\,\mathrm{mT}$. Under these conditions the hyperfine structure is not resolved.

3.1.2 Nuclear magnetic resonance

Here, I will only consider nuclear magnetic resonance of atoms with nuclear spin $I = \frac{1}{2}$ applying to $^{1}\mathrm{H}$, $^{3}\mathrm{He}$ and $^{129}\mathrm{Xe}$. Then, the nuclear Zeeman levels $(m_{-1/2}, m_{+1/2})$ are separated in a magnetic field B by

$$\Delta E = 2\mu_{\mathrm{I}} B = h\gamma_{\mathrm{I}} B = \hbar\omega_{\mathrm{L}}, \tag{3.5}$$

with the nuclear magnetic moment μ_{I}, the gyromagnetic ratio $\gamma_{\mathrm{I}} = \gamma$ and the definition of the Larmor frequency

$$\omega_{\mathrm{L}} = 2\pi\gamma B. \tag{3.6}$$

In nuclear magnetic resonance (NMR) the fundamental processes are absorption and stimulated emission arising from the transition between Zeeman energy levels. Selection rules imply $\Delta m_{\mathrm{I}} = \pm 1$. This quantum-mechanical two-level system with $I_z = \pm\frac{1}{2}\hbar$ and $\boldsymbol{I}^2 = I(I+1)\hbar^2 = \frac{3}{4}\hbar^2$ can be macroscopically described by the difference of level population $\Delta N = N^+ - N^-$. The polarization P of a sample is then defined as

$$P = \frac{N^+ - N^-}{N^+ + N^-}. \tag{3.7}$$

In thermal equilibrium the levels are populated according to the Boltzmann distribution $e^{\Delta E/k_\mathrm{B}T}$, yielding

$$P_\mathrm{therm} = \frac{1 - e^{\frac{2\mu B}{k_\mathrm{B}T}}}{1 + e^{\frac{2\mu B}{k_\mathrm{B}T}}} \approx \frac{\mu B}{k_\mathrm{B}T}. \tag{3.8}$$

The magnetization $\boldsymbol{M}$ is defined as the magnetic moment density and for a spin-polarized two-level system one obtains

$$\boldsymbol{M} = \frac{1}{V}\sum_N \boldsymbol{\mu} = \frac{\Delta N}{V}\boldsymbol{\mu} = \frac{NP}{V}\boldsymbol{\mu}, \tag{3.9}$$

with the sample volume V, the total number of magnetic moments N, the degree of polarization P and the magnetic moment of the constituents $\boldsymbol{\mu}$. A polarization vector can be defined as $\boldsymbol{P} = P\boldsymbol{M}/M$.

The dynamics of a macroscopic magnetization in a magnetic field can be understood in the following way. A magnetic moment initially not aligned with a static magnetic field axis feels a torque according to $\boldsymbol{\mu} \times \boldsymbol{B}$ and starts precessing around the holding field. The torque represents a change in total nuclear angular momentum $\boldsymbol{I} = \boldsymbol{\mu}/\gamma$, hence

$$\frac{d\boldsymbol{I}}{dt} = \frac{1}{\gamma}\frac{d\boldsymbol{\mu}}{dt} = \boldsymbol{\mu} \times \boldsymbol{B}. \tag{3.10}$$

Since the macroscopic magnetization is proportional to the expectation value $\langle\hat{\mu}\rangle$, we get an equation describing the precession of the magnetization $\boldsymbol{M}$ as

$$\frac{d\boldsymbol{M}}{dt} = \gamma\boldsymbol{M} \times \boldsymbol{B}. \tag{3.11}$$

Assume for simplicity, that the static magnetic field is applied in z direction $\boldsymbol{B} = (0, 0, B_z)$. Because the spin system can exchange energy with the surrounding (e.g. solid lattice, walls, etc.) the magnetization M_z along $\boldsymbol{B}$ is relaxing to it's thermal equilibrium value, cf. Eq. (3.8), in a characteristic time T_1, called spin-lattice, longitudinal or simply "T_1" relaxation time. Additionally, magnetization in the x,y plane M_x, M_y relaxes to thermal equilibrium within a characteristic time due to interactions of neighbouring spins. These locally generate magnetic fields making the spin precession frequencies diverge. The characteristic time of this spin-spin or transverse relaxation is called "T_2""relaxation time. In real world experiments the term "T_2^*" is often used including relaxation effects due to gradients of applied or residual magnetic fields: $\frac{1}{T_2^*} = \frac{1}{T_2} + \frac{1}{T_2^\mathrm{grad}}$.

Both longitudinal and transverse relaxation mechanisms were phenomenologically included in Bloch's equations [74] yielding the time evolution of a magnetization vector in a magnetic field B_z,

$$\begin{aligned}
\frac{dM_x}{dt} &= \gamma M_y B_z - \frac{M_x}{T_2} \\
\frac{dM_y}{dt} &= -\gamma M_x B_z - \frac{M_y}{T_2} \\
\frac{dM_z}{dt} &= -\frac{M_z - M_0}{T_1},
\end{aligned} \tag{3.12}$$

where M_0 denotes the equilibrium magnetization. The equations of Bloch were generalized by the inclusion of a diffusion term yielding the Bloch-Torrey equations [75].

3.1.3 Time-varying magnetic fields

To measure spin precession one needs to manipulate the polarization vector initially aligned along a magnetic field B_z. To detect the precession the polarization vector needs to be tipped by an angle θ, so that the precessing magnetization of the sample induces a voltage in a pickup loop.
One way to achieve the misalignment is using an oscillating RF field pulse of amplitude $2B_1$, frequency $\omega_\perp$ and duration τ, which is applied perpendicular to the B_z-axis. In the rotating frame it can be shown, that if $\omega_\perp$ equals the Larmor frequency the magnetic field in z-direction is zero and the magnetization is precessing away from B_z at the Rabi frequency γB_1 [76]. Hence, with a pulse of duration τ the tipping angle is

$$\theta = \gamma B_1 \tau. \tag{3.13}$$

From the usually neglected counter-rotating component of $\boldsymbol{B}_\perp$ the Bloch-Siegert shift of the Larmor precession frequency of $\frac{B_1^2}{4B_0^2}$ arises [77]. Choosing the amplitude of the oscillating field B_1 to be less than $< \frac{B_0}{10}$ limits the shift to less than $\approx 1\%$. The rotation of the magnetization under off-resonant conditions can be evaluated when introducing the oscillating magnetic field $B_\perp = B_{x,y}\sin(\omega_\perp t)$ in the Bloch equations (Eq. 3.12).
The polarization vector can also be misaligned from B_z by a non-adiabatic magnetic field change. The adiabatic condition assures that spins can follow a magnetic field change, e.g. the Larmor precession frequency ω_L must be much larger than rotation frequency of the total magnetic field $\omega_\mathrm{B}^\mathrm{rot}$, hence

$$\omega_\mathrm{L} \gg \omega_\mathrm{B}^\mathrm{rot}. \tag{3.14}$$

If the total field is changed fast enough to make the switching process non-adiabatic, the spins start precessing around the final magnetic field direction. In contrast to this the transport of polarized gas needs to be adiabatic to preserve polarization while spins move through different magnetic field regions.

3.2 Spin exchange optical pumping of ^{129}Xe and ^{3}He

The magnitude of the signal generated by a spin-polarized sample (e.g. by induction in a pickup loop) scales with the magnetization (3.9), hence with the number of polarized atoms or nuclei. The thermal polarization of a sample (Eq. (3.8)) described by the Boltzmann distribution is very small even at lowest temperatures and strongest magnetic fields. At room temperature the population difference is of order 10^{-9}/mT. The degree of polarization can be enhanced by several orders of magnitude by applying optical pumping techniques.
The nuclear spins of both ^{3}He and ^{129}Xe can be efficiently polarized by spin-exchange

optical pumping (SEOP)[17], which was first demonstrated for ^{3}He and ^{129}Xe by Bouchiat [79] and Grover [80], respectively. In SEOP electrons of an alkali vapor are polarized by circularly polarized light (cf. Fig. 6) and the electron polarization is transfered to noble gas nuclei by exchange collisions. A general review of optical pumping and SEOP can be found in [81] and [82], respectively. A more recent review particularly focusing on recent developments in SEOP of ^{3}He is given in [83].
Note, that the nuclear spin of ^{199}Hg can be more directly polarized by depopulation pumping of the ground state $^1S_0$ to the excited state $^3P_1$ using circularly polarized light with a wavelength of 254 nm. In a magnetic field the angular momentum of the photon is transfered to the nucleus due to the strong hyperfine coupling, hence populating the Zeeman state $m_{+1/2}$ ($m_{-1/2}$) by σ^+ (σ^-) photons, respectively. The availability of UV lasers of the required wavelength makes ^{199}Hg very attractive, particularly because the spin precession can also be read out optically in a pump-probe scheme. This is one of the many reasons for the superior sensitivity of the ^{199}Hg EDM measurement.

3.2.1 Optical pumping of alkali metals

The alkali metals rubidium and potassium are of relevance in SEOP of noble gas nuclei. Their binary spin-exchange rates with ^{129}Xe and ^{3}He and relevant alkali spin destruction rates are listed in Tab. 3.1. The energy levels and optical pumping scheme of Rb in a magnetic field is shown in Fig. 6. The $5P_{1/2}$ state has a lifetime of 27.7 ns [84], the inverse of the spontaneous emission rate. Excitation of the ground state electrons from $5S_{1/2}$ to $5P_{1/2}$ by absorption of circularly polarized $\sigma^+(\sigma^-)$ light at 794.78 nm is subject to the selection rule $\Delta l = +1$ ($\Delta l = -1$) and hence populates the $5S$ state with $m_J = 1/2$ ($m_J = -1/2$). By collisional mixing the Zeeman sublevels are equally populated very rapidly. De-excited electrons emit photons, which can be re-absorbed (Fig. 6) in the vapor. This process counteracts the optical pumping scheme as it is not subject to $\Delta m = \pm 1$. To avoid this "radiation trapping" the excited states need to be quenched by a buffer gas. Using di-atomic molecules the energy can be very efficiently transfered to vibrational and rotational states. Inert nitrogen gas has low spin-destruction rates (Tab. 3.1) and serves this purpose very well. It is usually introduced into the optical pumping cell at pressures of 50 to 200 mbar. This quenching occurs equally for both Zeeman $5P_{1/2}$ states, hence on average two photons are needed to polarize one Rb atom. Throughout this work only Rb is considered as it can exchange angular spin at reasonable rates for both ^{3}He and ^{129}Xe . However, for SEOP of ^{3}He a mixture of Rb-K or pure K was demonstrated more effective [85, 86].
In the following some practically important effects for light absorption are considered.

---

[17] Another technique successfully applied to ^{3}He is metastable exchange optical pumping (MEOP) [78], where a discharge excites the ground state electrons to the metastable state 2^3S_1 optically pumped to 2^3P_0 with 1083 nm light. The polarization is very efficiently transfered to the nuclei in the metastable state via the hyperfine interaction and to the ground state nuclei by exchange collisions. Very high nuclear polarization can be achieved, but only at low pressures $\mathcal{O}(1\,\mathrm{mbar})$.

	Rb		K	
Spin-exchange rates s^{-1}				
$k_{\text{He-Alk}}$	$6.8 \times 10^{-20}[\text{Rb}]$	[86]	$5.5 \times 10^{-20}[\text{K}]$	[86]
$k_{\text{Xe-Alk}}$	$1.0 \times 10^{-15}[\text{Rb}]$	[87]	$6.3 \times 10^{-17}[\text{K}]$	[87]
Spin-destruction rates ($T = 140\,°\text{C}$) s^{-1}				
$\Gamma_{\text{Alk-He}}$	$1.4 \times 10^{-18}[\text{He}]$	[86]	$1.4 \times 10^{-19}[\text{He}]$	[86]
$\Gamma_{\text{Alk-Xe}}$	$3.7 \times 10^{-16}[\text{Xe}]$	[88]		
$\Gamma_{\text{Alk-Alk}}$	$4.2 \times 10^{-13}[\text{Rb}]$	[86]	$9.6 \times 10^{-14}[\text{K}]$	[86]
$\Gamma_{\text{Alk-N2}}$	$9.2 \times 10^{-18}[\text{N}_2]$	[86]	$4.9 \times 10^{-18}[\text{N}_2]$	[86]

Tab. 3.1: Upper part: Spin-exchange rates for ^{129}Xe and ^{3}He polarized by optically pumped alkali atoms Rb and K. Lower part: Spin-destruction rates $\Gamma_{\text{Alk}-i}$ for the alkali metals and the usually used gases in SEOP. The brackets [..] denote the number densities in cm^{-3}.

Natural linewidth

Electric dipole transitions of the electron shell in an atom lead to the phenomena of absorption, spontaneous emission and stimulated emission. A dipolar transition can be treated classically as a damped oscillator with a temporal damping term $e^{-\frac{1}{2}\Gamma t}$. This yields the Lorentzian function describing the natural lineshape. Thus the intensity distribution $I(\omega)$ of a atomic dipolar transition is

$$I(\omega) = \frac{I_0}{\pi} \frac{\frac{\Gamma}{2}}{(\omega - \omega_0)^2 + \left(\frac{\Gamma}{2}\right)^2}, \tag{3.15}$$

where ω_0 is the central frequency and $I_0 = \int_0^\infty I(\omega)d\omega$ is the total intensity. The full width at half maximum (FWHM) Γ relates to the lifetime of the transition as $\frac{\Gamma}{2} = \tau^{-1}$. The D1 line of rubidium has a natural linewidth of

$$\Delta\nu^{\text{nat}} = 2\frac{1}{27.7\,\text{ns}}\frac{1}{2\pi} \approx 11.5\,\text{MHz}\,(\Delta\lambda \approx 10^{-5}\,\text{nm}). \tag{3.16}$$

Hence, a line-narrowed laser is advised to use most of the available photons. However, diode lasers nowadays provide inexpensive sources of high output power, but with broad emission lines ($\Delta\lambda \approx 1\,\text{nm}$). They can be used quite efficiently considering broadening effects.

Pressure broadening

Collisions with other atoms shorten the phase coherence lifetime, hence broaden the transition line. This collisional broadening is again described by a Lorentzian lineshape, but $\frac{\Gamma}{2}$ replaced by $nv\sigma$, where n is the number density, v the mean velocity and σ the effective cross-section. The dependence on the pressure is of particular importance for SEOP using inexpensive high-power diodes. The D1 line of rubidium is broadened by[18]

---

[18] $1\,\text{amg} = 2.687 \times 10^{19}\,\text{cm}^{-3}$, the number density at STP conditions.

$\approx 20\,\frac{\text{GHz}}{\text{amg}}$ ($0.04\,\frac{\text{nm}}{\text{amg}}$) at 80 °C for collisions with helium, xenon and nitrogen [89]. The broadening scales with temperature as $T^{0.3}$. At optical pumping conditions of 140 °C and 4 bar the pressure broadening is

$$\Delta\nu^{\text{press}} = 20\,\frac{\text{GHz}}{\text{amg}}\,\frac{4\,\text{bar}}{1\,\text{bar}}\,\frac{273\,\text{K}}{413\,\text{K}}\left(\frac{413\,\text{K}}{353\,\text{K}}\right)^{0.3} \approx 55\,\text{GHz} \gg \Delta\nu^{\text{nat}}\,(\Delta\lambda \approx 0.1\,\text{nm}), \tag{3.17}$$

which significantly increases absorption of light.

Other line broadening effects like Doppler broadening are very weak ($\Delta\lambda \approx 10^{-3}$ nm) under SEOP conditions. Note, that the Zeeman splitting of the Rb $5S_{1/2}$ levels in magnetic fields of order 1-10 mT is not resolved, as it is of order 100 MHz.

Predominantly, pressure broadening makes optical pumping of alkali metals much more efficient in pumping cells containing several atmospheres of total pressure. This broadening of the Rb absorption line is required in the liquid xenon experiment (cf. Sec. 5) as the laser diode linewidth is ≈ 500 GHz or ≈ 1 nm. However, narrowing of the laser line can additionally (or sufficiently) increase absorption even at lower pressures. In the He-Xe EDM experiment (cf. Sec. 6) a broad emission line is narrowed to ≈ 150 GHz or ≈ 0.3 nm by back-reflecting a selected wavelength off a grating to the laser cavity to increase photon absorption. In this experiment ^{3}He and ^{129}Xe are simultaneously polarized and due to the very different optimum conditions (cf. 3.1) absorption needs to be maximized. Generally, pressure to broaden the Rb absorption line can be provided inherently by the gas to be polarized as long as spin destruction with Rb collisions can be compensated. Hence, in SEOP of ^{3}He the ^{3}He itself can be at high pressure of several atmospheres, while in SEOP of ^{129}Xe an additional buffer gas is needed, usually ^{4}He.

Rate model for optically pumping rubidium

The buildup of the Rb polarization in a dense Rb vapor can be described by a rate model as first introduced in [90] or recently used in a slightly modified way [91].

Assume the populations of the groundstates $m_{\text{F}} = \pm 1/2$ are N_+ and N_-, with $N_+ + N_- = 1$. When pumping with σ^+ light (100% polarization) the rate equations are

$$\frac{dN_\pm}{dt} = \pm\left(\frac{\Gamma}{2} + \gamma_{\text{op}}\right)N_- \mp \frac{\Gamma}{2}N_+, \tag{3.18}$$

where $\Gamma = \sum [X]\Gamma_{\text{Rb-X}}$ is the total bulk spin-destruction rate mixing the $^5S_{1/2}, m_{\text{J}} = \pm 1/2$ states (cf. Fig. 6 and Tab. 3.1) via collisions with other gases of number density $[X]$ and γ_{op} is the optical pumping rate. The solution to (3.18) in a optically thick Rb vapor also depends on the depth z in the cell, yielding

$$P_{\text{Rb}}(t,z) = N_+ - N_- = \frac{\gamma_{\text{op}}(z)}{\gamma_{\text{op}}(z) + \Gamma}\left(1 - e^{-(\gamma_{\text{op}}(z)+\Gamma)t}\right). \tag{3.19}$$

Strickly speaking, a slowing down factor S needs to be included in the exponential, altering the argument to $-((\gamma_{\text{op}}(z) + \Gamma)t)/S$. This factor is of order 10 and accounts for the non-zero nuclear spin of Rb, which represents a reservoir of angular momentum, that also needs to be polarized via the hyperfine coupling to the electron spin.

Optical pumping rate

The optical pumping rate is defined as the overlap of the laser intensity profile $\Phi(\nu, z)$ with the photon absorption cross-section $\sigma(\nu)$

$$\gamma_{\mathrm{op}}(z) = \int_0^\infty \Phi(\nu, z)\sigma(\nu)d\nu. \tag{3.20}$$

The absorption cross-section is assumed to be a Lorentzian of (pressure-broadened) width Γ_{FWHM} and peak cross-section $\sigma_0 = \pi r_e c f_{\mathrm{osc}}$, with the classical electron radius r_e, the speed of light c and the D1 transition oscillator strength $f_{\mathrm{osc}} = 0.342$ [84], yielding

$$\sigma(\nu) = \frac{\pi r_e c f_{\mathrm{osc}}}{\Gamma_{\mathrm{FWHM}}} \frac{1}{1 + 4(\nu - \nu_0)^2/\Gamma_{\mathrm{FWHM}}^2}. \tag{3.21}$$

The photon-flux of a Gaussian laser beam can be described at the front of the pumping cell, where $\Phi(\nu, z) = \Phi(\nu)$ as

$$\Phi(\nu) = \frac{P_{\mathrm{L}}}{h\nu_0 A_{\mathrm{beam}} \delta\nu} \sqrt{\frac{4\ln 2}{\pi}} e^{-4\ln 2 \frac{(\nu-\nu_0)^2}{\delta\nu^2}}, \tag{3.22}$$

where P_{L} is the laser power, A_{beam} the cross-sectional area of the laser and $\delta\nu$ the FWHM of the laser spectrum.
A typical value for the optical pumping rate (3.20) in a cell of 2 bar total pressure, a laser line of 1 nm width and $1\,\mathrm{cm}^2$ of beam cross-sectional area is $\gamma_{\mathrm{op}} \approx 10^5\,\mathrm{s}^{-1}$ per Watt of laser power. According to Eq. (3.19) a Rb polarization of nearly 100% can be achieved if $\gamma_{\mathrm{op}} \gg \Gamma$. The most significant alkali relaxation arises from Rb-Xe collisions. In typical SEOP conditions at 140° C where $[\mathrm{Rb}] \approx 6 \times 10^{13}\,\mathrm{cm}^{-3}$ (cf. Fig. A.3) and a gas mixture of 300 mbar ^{129}Xe, 100 mbar N_2 and 2 bar of ^{4}He, the Rb spin destruction rates due to Rb, Xe, N_2 and ^{4}He are $25\,\mathrm{s}^{-1}$, $2700\,\mathrm{s}^{-1}$, $23\,\mathrm{s}^{-1}$ and $69\,\mathrm{s}^{-1}$, respectively (Tab. 3.1). Already at several W of laser power the condition $\gamma_{\mathrm{op}} \gg \Gamma$ can be achieved. With diode array bars available of up to 100 W laser power even in large cells a polarization of the Rb vapor of nearly 100% can be maintained, which is essential for high noble gas polarization.
However, at a high photon flux it is possible to operate at higher temperatures, which speeds up ^{3}He polarization as more Rb is available.

3.2.2 Alkali-noble gas collisions

In SEOP the polarization of Rb electrons is transfered to the noble-gas nuclei by spin-exchange collisions. Atomic collisions are described by their cross-section σ. The characteristic exchange time T^{ex} is defined as the inverse of the collision rate $\gamma = \sigma\bar{v}n$, with the average velocity $\bar{v}$ and the atomic number density n, hence

$$T^{\mathrm{ex}} = \gamma^{-1} = (\sigma\bar{v}n)^{-1}. \tag{3.23}$$

Assuming a Maxwell-Boltzmann distribution of velocities the average is $\bar{v} = \sqrt{\frac{8k_{\mathrm{B}}T}{\pi M}}$, with the reduced mass $M = \frac{m_{\mathrm{alk}} m_{\mathrm{ng}}}{m_{\mathrm{alk}} + m_{\mathrm{ng}}}$.

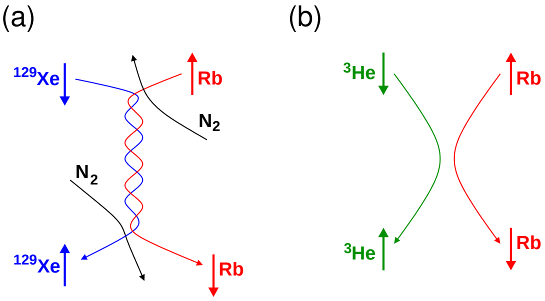

Fig. 7: The alkali electron spin is transfered to nuclear spin of noble gases via van-der-Waals (a) and binary (b) collisions. Usually the van-der-Waals type dominates spin exchange to ^{129}Xe nuclei, whereas binary collisions dominate for spin-exchange to ^{3}He (Reproduced from [82]).

3^{rd} body	ζ [s^{-1}]	$\frac{\zeta}{\text{amg}}$ [s^{-1}]
Xe	5230	1.95×10^{-16}[Rb]
N_2	5700	2.12×10^{-16}[Rb]
He	17000	6.33×10^{-16}[Rb]

Tab. 3.2: Spin exchange rates of ^{129}Xe and Rb due to the hyperfine interaction during the lifetime of weakly bound van-der-Waals molecules. The formation and lifetime depends on the third body (for references, see [92]). For comparison to the rates of Tab. 3.1 the molecular spin-exchange rate normalized to 1 amg of the third body is also given, with the Rb number density [Rb] in cm^3.

Two types of collisions between alkali and noble gas atoms can be distinguished. Van-der-Waals molecules (Fig. 7 (a)) form with help of a third body and transfer angular momentum during their long lifetime ($\gtrsim 10^{-9}$ s) before they break up again with support of a third body. These weakly bound molecules were investigated by Happer [93] and Zeng [94] using low pressures of Xe (≈ 1.3 mbar) and N_2 (≈ 100 mbar). In this regime the other process, binary collisions (Fig. 7 (b)), can be neglected. Generally, binary collisions dominate the spin-exchange with the light noble gas ^{3}He. For ^{129}Xe the specific gas pressures determine the dominating process, as the molecular lifetime strongly changes with the density of xenon and buffer gases.

The spin-exchange process is well described by a spin-dependent perturbation

$$\mathcal{H}_{\text{SE}} = \gamma(\boldsymbol{r})\boldsymbol{N}.\boldsymbol{S} + A_b(r)\boldsymbol{I}^{\text{ng}}.\boldsymbol{S}, \tag{3.24}$$

with the respective interaction of the rotational angular momentum $\boldsymbol{N}$ (spin-rotation interaction) and the nuclear spin of the noble gas $\boldsymbol{I}^{\text{ng}}$ (hyperfine interaction) with the alkali spin $\boldsymbol{S}$. The spin-rotation interaction relaxes alkali polarization to translational motion and can be pictured as the coupling of the alkali electron spin $\boldsymbol{S}$ to a magnetic field generated by the relative motion of charges of the colliding atoms. For heavy noble gases the contributions arise mostly from the noble gas core, while for light noble gases magnetic fields in the alkali core dominate. The hyperfine interaction actually transfers polarization to the noble gas nucleus by coupling the spin $\boldsymbol{S}$ to the magnetic field inside the noble gas nucleus.

A total spin exchange rate was first determined by Cates [88] for cells containing Rb, Xe and N_2, but a very helpful general form given in subsequent publications [92, 95] as

$$\gamma^{\text{SE}} = \left(\sum_i \frac{\zeta_i}{[G_i]} + \sigma\bar{v} \right) [Rb]. \tag{3.25}$$

The two terms account for spin-exchange via weakly bound molecules with rates for specific gases ζ_i of number density $[G_i]$ and via binary collisions. Spin-exchange with ^{3}He is governed by binary collisions, so particularly $\gamma_{\mathrm{SE}}^{\mathrm{3He}} = \sigma^{\mathrm{RbHe}}\bar{v}$. Relevant spin-exchange rates for ^{129}Xe due to binary collisions and weakly bound molecules can be found in Tab. 3.1 and Tab. 3.2, respectively. In a typical gas mixture of 2.4 bar total pressure and ratios of ^{129}Xe:N$_2$:He=3:1:20 spin-exchange is about 50% due to binary collisions.

The time evolution of the noble gas nuclear polarization can be deduced in an analog way to Eq. (3.19) from the rate equation (see e.g. [83])

$$\frac{dP_{\mathrm{ng}}}{dt} = \gamma_{\mathrm{SE}}(P_{\mathrm{Rb}} - P_{\mathrm{ng}}) - \Gamma_{\mathrm{SD}} P_{\mathrm{ng}}, \tag{3.26}$$

where P_{Rb} and P_{ng} are the rubidium and noble gas polarizations, respectively and Γ_{SD} is the spin destruction rate of the noble gas mostly due to wall collisions in the pumping cell. The solution to (3.26) describes the buildup of noble gas nuclear polarization and is given by

$$P_{\mathrm{ng}}(t) = \frac{\gamma_{\mathrm{SE}}}{\gamma_{\mathrm{SE}} + \Gamma_{\mathrm{SD}}} P_{\mathrm{Rb}} \left(1 - e^{-(\gamma_{\mathrm{SE}}+\Gamma_{\mathrm{SD}})t}\right). \tag{3.27}$$

Maximum polarization is achieved by both high Rb polarization and low spin destruction rate. The time scales of polarization built-up for ^{3}He and ^{129}Xe vary by more than three orders of magnitude (cf. Tab. 3.1 and Fig. 8), but also the maximum polarization achievable is higher for ^{3}He as the interaction with Rb causing spin-destruction is much weaker. There is discussion in the literature about a yet unknown source of ^{3}He relaxation limiting the maximum achievable polarization [96]. This is accounted for by an additional factor $X \approx 0.33$ in Eq. (3.27) giving the maximum achievable ^{3}He polarization

$$P_{\mathrm{3He}} = \frac{\gamma_{\mathrm{SE}}}{\gamma_{\mathrm{SE}}(1+X) + \Gamma_{SD}} P_{\mathrm{Rb}}. \tag{3.28}$$

Flow-through production of hyper-polarized xenon

The maximum noble gas polarization (Eq. (3.27)) requires nearly total spin-polarization of the rubidium vapor in an optical pumping cell. Additionally, this needs to be maintained in the whole volume, hence layers of smaller rubidium polarization need to be avoided, particularly far away from the front window. Although high power lasers are available this still limits the size of the optically pumped volume, hence the production rate. Especially ^{129}Xe can only be effectively polarized at low xenon pressures.

For medical applications or experiments using liquid hyper-polarized xenon the need for polarized gas is higher than can be achieved by static pumping. Already in the mid-90s limitations on the amount of polarized xenon have been overcome by using flow-through optical pumping schemes and subsequent accumulation [95]. Here, the gas mixture is flown through the optical pumping cell and passes a trap, usually cooled by liquid nitrogen. The very long spin-relaxation times of ^{129}Xe ($\approx 10^4$ s) at cryogenic temperatures (≈ 70 K) in high magnetic fields $\gtrsim 20$ mT (cf. Sec. 3.3.2) allow accumulation of significant amounts of hyper-polarized gas.

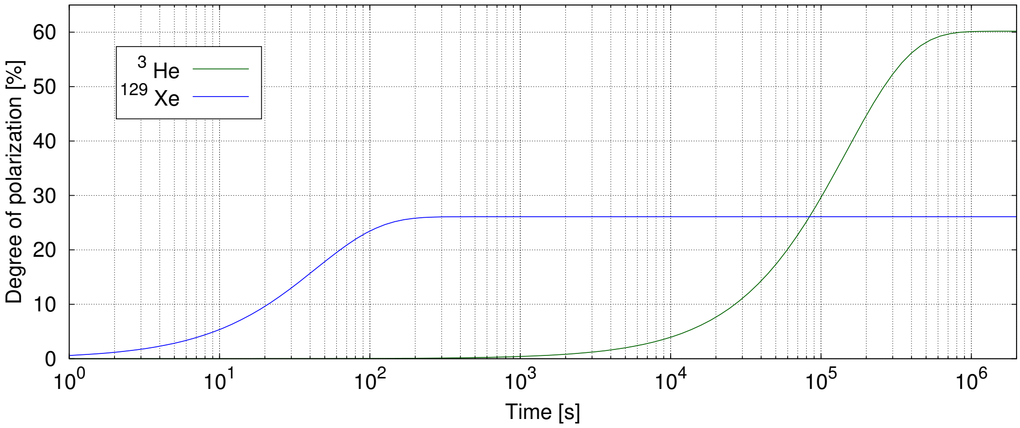

Fig. 8: Typical time-dependent buildup of ^{3}He and ^{129}Xe polarization plotted according to the rate model (Eq. (3.27) and Eq. (3.28)). For spin-exchange rates see Tab. 3.1. Spin-destruction rates are deduced from typical T_1 times, e.g. 100 h and 60 s for ^{3}He and ^{129}Xe, respectively. The variation of spin-exchange rates of ^{3}He and ^{129}Xe with Rb of more than three orders of magnitude impose experimental subtleties in realizing a repetitive clock-comparison experiment.

The remaining polarization P_{Xe} after accumulation in a cold trap for a time t_{acc} is [95]

$$P_{\mathrm{Xe}}(t_{\mathrm{acc}}) = P_{\mathrm{Xe}}(0)\frac{T_1}{t_{\mathrm{acc}}}\left(1 - e^{-t_{\mathrm{acc}}/T_1}\right), \tag{3.29}$$

with the polarization leaving the optical pumping cell $P_{\mathrm{Xe}}(0)$ and the longitudinal relaxation time T_1 in the trap.

3.3 Relaxation mechanisms of polarized ^{129}Xe and ^{3}He

Longitudinal relaxation is due to the tendency of the spin system to (re-)establish thermal equilibrium by repopulation of the Zeeman levels. In SEOP the polarizations generated are orders of magnitude larger than the thermal polarization (Eq. (3.8)). The energy transfer to the surrounding (or lattice) is induced by stimulated emission[19]. The processes causing de-excitation by time varying magnetic fields or electric field gradients are [76] relaxation at (para)magnetic impurities, spin-rotation interactions, dipole-dipole interactions, scalar relaxation of first and second kind, quadrupolar relaxation due to electric field gradients and relaxation due to the chemical shift. Additionally, the longitudinal relaxation can also be due to diffusion in magnetic field gradients [97].
Transverse relaxation is caused by dephasing of spins precessing in locally varying magnetic fields. These field deviations can be due to close-by spins (T_2) and external field gradients (T_2^{grad}). Both are included in the experimentally relevant

$$\frac{1}{T_2^*} = \frac{1}{T_2} + \frac{1}{T_2^{\mathrm{grad}}} \tag{3.30}$$

---

[19] The probability of spontaneous emission is negligibly small at the energy separations considered.

For an actual EDM measurement longitudinal relaxation during SEOP, transfer and delay times limits the sensitivity due to the signal-to-noise ratio. The transverse relaxation time determines the maximum observation time of a single run and possibly the number of measurements per time, depending on the time needed for preparation.
First, the dominant longitudinal relaxation mechanisms for ^{129}Xe and ^{3}He in the gas phase will be introduced, which is most important for the ^{129}Xe EDM search using the He-Xe clock comparison approach (Sec. 6). The relaxation in liquid and solid xenon are relevant for the presented novel approach of an EDM search in liquid xenon (Sec. 5), particularly for accumulation of hyper-polarized ^{129}Xe in a cold trap and subsequent thawing of the solid.

3.3.1 Gas phase relaxation of ^{129}Xe and ^{3}He

Due to the fact that both ^{3}He and ^{129}Xe have a nuclear spin of $I = 1/2$ and hence zero quadrupole moment to interact with varying electric field gradients long relaxation times can be expected. Note that nuclei with $I = 3/2$ usually relax very quickly with $T_1 < 1\,\mathrm{s}$. Natural xenon contains 21,3% of ^{131}Xe which has a quadrupole moment and provides a channel for quick relaxation of ^{129}Xe, particularly in the solid phase.

Intrinsic relaxation

In samples of ^{3}He very long spin-lattice relaxation times have been observed. The dipole-dipole interaction for identical nuclear spins I with gyromagnetic ratio γ, separated by r_{ij} and subject to Brownian motion (in liquid or gas) gives [98]

$$\frac{1}{T_1^{\mathrm{dip}}} = \frac{3}{2}\gamma^4\hbar^2 I(I+1)\left[J_1(\nu_0) + \frac{1}{2}J_2(2\nu_0)\right] \propto \gamma^4 \frac{1}{r_{ij}^6}, \tag{3.31}$$

with $J_i(\nu)$ describing the intensity spectra of local field fluctuations (see [98, 99]). The interaction of Eq. (3.31) dominates ^{3}He spin-lattice relaxation and at room temperature yields [100]

$$\Gamma_{\mathrm{He}}^{\mathrm{int}} = \frac{p[\mathrm{bar}]}{744}\,\mathrm{h}^{-1}. \tag{3.32}$$

In the early 60s Streever and Carr [101] found that the dipole-dipole interaction can not be the relaxation mechanism for ^{129}Xe and later Torrey [102] identified the spin-rotation interaction ($\propto \boldsymbol{I}.\boldsymbol{N}$) during binary collisions or transient existence of diatomic molecules as the appropriate process. The deduced $T_1 = 56\,\frac{\mathrm{h}}{\mathrm{amg}}$ proportional to the pressure, but independent of magnetic field strength was in very good agreement with the T_1 measurements of Hunt and Carr [103]. However, these measurements were done at high xenon densities ($\approx 50\,\mathrm{amg}$). About 40 years later Chann et al. [104] found, that the spin-rotation coupling is mediated by long-lived persistent dimers, with breakup times depending on a third body and hence relaxation varies with gas composition. A revised relaxation rate for xenon was obtained by Anger et al [105] by including gas composition and the magnetic field dependence. Their semi-empirical formula for the relaxation rate due to transient Γ^{t} and persistent dimers Γ^{p} is valid at room temperature and xenon densities below 1 amg, as long as $B_0 \lesssim 1\,\mathrm{T}$. With an uncertainty of 10% the relaxation rate is

$$\Gamma^{\mathrm{int}}_{\mathrm{Xe}} = \Gamma^{\mathrm{t}} + \Gamma^{\mathrm{p}} = \frac{[\mathrm{Xe}]}{56.1\,\mathrm{h}} + \frac{1}{4.59\,\mathrm{h}}[1 + (3.65 \times 10^{-3} B_0^2] \left(1 + r\frac{[B]}{[Xe]}\right)^{-1}, \qquad (3.33)$$

with the density of xenon $[Xe]$ and the density of a second gas $[B]$ is in amagats. The ratio of the persistent dimer breakup coefficient of B to that for xenon r equals 0.51 and 0.25 for N_2 and He, respectively.
The total relaxation rate of ^{129}Xe and ^{3}He needs to include effects due to the cell walls and magnetic field gradients

$$\Gamma = \Gamma^{\mathrm{wall}} + \Gamma^{\mathrm{grad}} + \Gamma^{\mathrm{int}}, \qquad (3.34)$$

with the wall relaxation rate Γ^{wall}, the relaxation due to diffusion in field gradients Γ^{grad} and the intrinsic relaxation Γ^{int}, which is dominated by the spin-rotation and dipole-dipole interaction for ^{129}Xe and ^{3}He , respectively.

Wall relaxation

Relaxation can also be due to complex interactions taking place during wall collisions, e.g. the noble gas atom sticks on the wall (adsorption) or permeates the wall or coating (absorption). It's commonly accepted that the relaxation is due to dipolar couplings to paramagnetic impurities or to nuclei/electrons with high gyromagnetic ratio. In pyrex cells Fitzsimmons et al. [106] found, that ^{3}He absorption dominates for $T > 130\,\mathrm{K}$, while ^{3}He relaxation is due to adsorption on the surface below 130 K. Starting from rate equations, they give a very general phenomenological expression for the mechanism independent wall relaxation time

$$\frac{1}{T_1} = \frac{N_{\mathrm{S}}}{N_{\mathrm{V}}} \frac{1}{t_{\mathrm{s}} + T_{\mathrm{S}}}, \qquad (3.35)$$

where N_{S} and N_{V} are the numbers of atoms on the surface and in the cell volume V, respectively, t_{s} is the sticking time and T_{s} is the relaxation time of atoms on the surface. Breeze et al. [107] adapted this to derive the pressure dependence of ^{129}Xe wall relaxation. The Langmuir equation gives the adsorbed fraction of atoms $\theta = \frac{k_2 p}{k_1 + k_2 p}$, with the adsorption rate k_2, the desorption rate k_1 and the pressure p. By also expressing $\theta = \frac{N_{\mathrm{s}}\sigma}{A}$ through the number of adsorbed atoms N_{s}, the cross-sectional area σ and the surface area A the pressure dependence of wall relaxation due to adsorption is obtained for low pressures ($\lesssim 3\,\mathrm{bar}$) as

$$\Gamma^{\mathrm{ads}} = \frac{A}{V} \frac{k_2}{k_1 + k_2 p} \frac{k_{\mathrm{B}} T}{\sigma (t_{\mathrm{s}} + T_{\mathrm{S}})}. \qquad (3.36)$$

Note that the wall relaxation rate increases with increasing surface-to-volume ratio A/V and with decreasing pressure. Zeng et al. [108] were the first to show an increase of typical T_1 times of several tens of s for uncoated cells to more than 1000 s with a

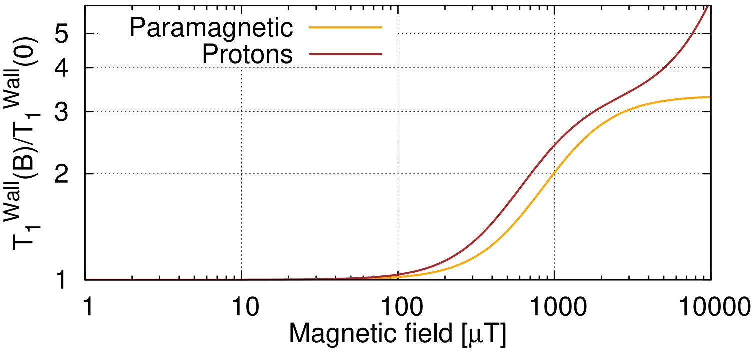

Fig. 9: The wall relaxation time of ^{129}Xe depending on magnetic field according to Eq. (3.38). Shown is the relaxation time normalized to the zero field wall relaxation time $T_1^{\mathrm{Wall}}(0)$ (cf. Eq. (3.37)) for interaction with paramagnetic glass impurities (orange) and protons (brown) usually found in coatings. Values for the correlation time of the fluctuations are taken from [109] for protons and electrons, yielding $\tau_{\mathrm{c}} = 8\,\mu\mathrm{T}$ and $\tau_{\mathrm{c}} = 8\,\mathrm{nT}$, respectively.

silicone coating. Various coatings (e.g. SurfaSil, OTS) have been shown to suppress wall relaxation by about one order of magnitude [107]. However, Driehuys et al. [109] found that trapping for times $\gtrsim 10\,\mu$s occurs in silicone coated cell walls and ^{129}Xe relaxes due to dipolar couplings to protons in the coating, which indicates further possible improvements. In the limit of zero magnetic field the relaxation rate due to dipolar fluctuations with characteristic time τ_c can be written [109]

$$\Gamma_0^{\mathrm{ads}} = \frac{4}{3}\theta S(S+1)\gamma_{\mathrm{I}}^2\gamma_{\mathrm{S}}^2\tau_c\sum_i\frac{1}{r_i^6}, \tag{3.37}$$

with the fraction of noble gas atoms sitting on the surface θ, the spin S on the surface with gyromagnetic ratio γ_{S}, the noble gas gyromagnetic ratio γ_{I} and the sum over the distances to the neighbouring spins r_i. As seen from Eq. (3.37) atoms of low gyromagnetic ratio should be favoured as well as thick coatings containing molecules with low gyromagnetic ratio.

A dependence of wall relaxation on the magnetic field B_0 seems evident for interacting dipoles of different gyromagnetic ratios and was determined also in [109] as

$$\Gamma^{\mathrm{ads}} = \frac{\Gamma_0^{\mathrm{ads}}}{10}\left(\frac{1}{1+(\gamma_{\mathrm{I}}-\gamma_{\mathrm{S}})^2B_0^2\tau_c^2}+\frac{3}{1+\gamma_{\mathrm{I}}^2B_0^2\tau_c^2}+\frac{6}{1+(\gamma_{\mathrm{I}}+\gamma_{\mathrm{S}})^2B_0^2\tau_c^2}\right). \tag{3.38}$$

Magnetic field dependence is only significant above $100\,\mu$T and may be relevant in SEOP but not for spin precession at low fields (cf. Fig. 9).
Wall relaxation is generally caused by adsorbing ^{129}Xe atoms for times $t_{\mathrm{s}} = t_0 e^{-E_{\mathrm{s}}/k_{\mathrm{B}}T}$, with $t_0 \approx 10^{-12}$ ps and the binding energy E_{s}. Hence, the fraction of adsorbed atoms is proportional to $e^{-E_S/(k_{\mathrm{B}}T)}$, which yields the temperature dependence of wall relaxation. Wall relaxation measurements of ^{3}He have reported T_1 times of several hours for uncoated borosilicate glass cells of 2.3 mbar [110], with an increase of at least an order of magnitude

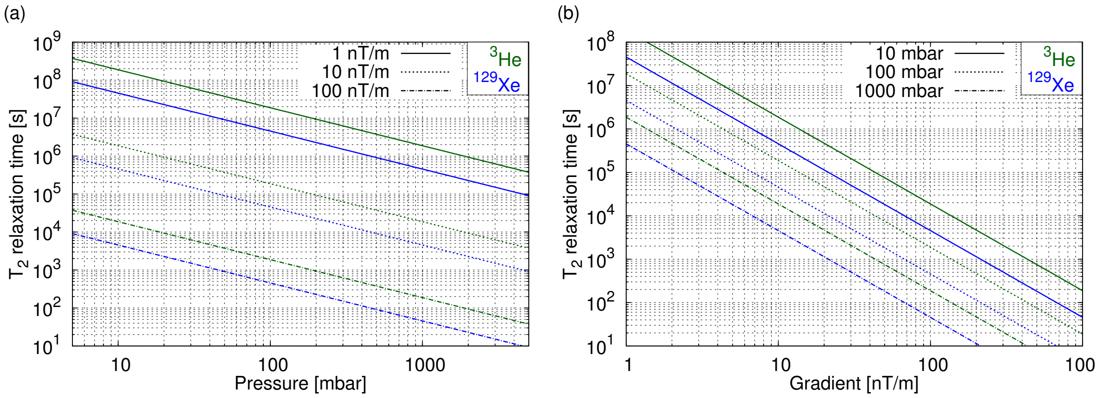

Fig. 10: Transverse spin relaxation due to diffusion in magnetic field gradients (cf. Eq. (3.41)) in a spherical cell of 30 mm diameter. The attainable T_2 times for ^{3}He (green) and ^{129}Xe (blue) strongly vary with gas pressure (a) and magnetic field gradients (b) and are very long in low pressure samples and absolutely non-magnetic environments.

using metal-coatings. However usually there is high fluctuation in the wall relaxation of similarly prepared uncoated cells. The experiments suggest longer T_1 times, when permeation into the glass is inhibited. Also, degradation of T_1 after exposing cells to high magnetic fields and recovered long T_1 times after subsequent degaussing [111] suggests dipolar interaction with paramagnetic impurities during permeation in the wall as the main relaxation mechanism. In low paramagnetic impurity cells made of GE180 hundreds and tens of hours of T_1 time due to wall relaxation were reported for ^{3}He and ^{129}Xe, respectively (e.g. [112]).

Diffusion in magnetic field gradients

Already in the 60s Colegrove et al. [78] found longitudinal relaxation times of ^{3}He of 600 s in 24 mT fields, while they observed $T_1 \approx 4000\,\mathrm{s}$ in more homogeneous fields of $400\,\mu$T. The faster relaxation was attributed to diffusion of the atoms in magnetic field gradients. Gamblin et al. [113] and also Schearer et al. [114] developed a theoretical model, which was later revised by Cates et al. [97]. Cates et al. showed, that the previously derived relaxation rate

$$\frac{1}{T_1} = D\frac{|\boldsymbol{\nabla} B_x|^2 + |\boldsymbol{\nabla} B_y|^2}{B_0^2}, \tag{3.39}$$

with the diffusion constant D and the gradients $|\boldsymbol{\nabla} B_x|$ and $|\boldsymbol{\nabla} B_y|$ transverse to the holding field direction, is only valid in the pressure range, where the parameter

$$\frac{\omega_\mathrm{L} R^2}{D} = \frac{\tau_\mathrm{d}}{\tau_\mathrm{L}} \gg 1 \tag{3.40}$$

for a spherical cell of radius R. The crucial figure is the ratio of characteristic diffusion time $\tau_\mathrm{d} = R^2/D$ across a cell and characteristic Larmor precession time $\tau_\mathrm{L} = \omega_\mathrm{L}^{-1}$. With the diffusion constants at 300 K [115] $D^{\mathrm{Xe}}_{1\mathrm{bar}} = 0.0576\,\mathrm{cm}^2\mathrm{s}^{-1}$ and $D^{\mathrm{He}}_{1\mathrm{bar}} = 1.8\,\mathrm{cm}^2\mathrm{s}^{-1}$, typical cell dimensions of several cm and μT magnetic fields, Eq. (3.39) is valid in the parameter range of interest in this work ($p^{\mathrm{Xe}} \gg 0.5\,\mathrm{mbar}, p^{\mathrm{He}} \gg 5\,\mathrm{mbar}$).[20]

In this high pressure regime an approximate expression for transverse relaxation due to diffusion in the gradient of the holding field is also derived in [97] as

$$\frac{1}{T_2} \approx \frac{8R^4\gamma^2|\boldsymbol{\nabla} B_z|^2}{175D}. \tag{3.41}$$

Note that $D \propto p^{-1}$ and the T_2 time increases with decreasing pressure, while T_1 in the high pressure limit is proportional to the pressure. Fig. 10 shows the pressure and gradient dependence of transverse relaxation times for ^{3}He and ^{129}Xe assuming a spherical cell of 30 mm diameter. The increased T_2 time at lower pressures is due to the atomic motion averaging the inhomogeneous magnetic fields in the cell during one Larmor period and is known as motional narrowing.

3.3.2 Solid phase relaxation of ^{129}Xe

Freezing hyper-polarized xenon gas is an attractive method of producing large amounts of polarized atoms as at temperatures of 77 K the longitudinal spin-relaxation time approaches several thousand seconds [116, 117]. At 4.2 K a T_1 time of hundreds of hours has been observed in 100 mT fields [117]. In solid xenon several mechanisms of spin relaxation have been studied in the last decades, clarifying the dominating temperature and magnetic field depending effects. Particularly vacancy diffusion as the dominating relaxation effect above about 120 K is very important for trapping and subsequent thawing of polarized xenon.

In the low temperature range ($< 20\,\mathrm{K}$) the ^{129}Xe polarization is mostly lost to quickly decaying ^{131}Xe, which has a magnetic quadrupole moment interacting with electric field gradients [118]. At very low temperatures a strong magnetic field dependence of this cross relaxation originates from the overlap of resonances of ^{129}Xe and ^{131}Xe. The electric field gradients develop at defects in the crystal, hence it is believed that different results of T_1 are due to crystal quality [119].

Raman scattering via the spin-rotation interaction

Between 20 K and 120 K additional scattering of phonons via the spin-rotation interaction dominates the longitudinal relaxation [116, 117, 120]. The spin-rotation interaction has the form

$$\mathcal{H}^{\mathrm{SR}} = \xi \boldsymbol{I}.\boldsymbol{N}, \tag{3.42}$$

with the spin I of the ^{129}Xe nucleus, the relative angular momentum $\boldsymbol{N}$ of a pair of atoms and a coupling strength ξ. For Raman scattering of phonons Fitzgerald et al.

---

[20] Cates et al. [97] also obtained the expression for T_1 for the case $\tau_{\mathrm{d}}/\tau_{\mathrm{L}} \ll 1$ as $\frac{1}{T_1} \approx \frac{8R^4\gamma}{175D}\left(|\boldsymbol{\nabla} B_x|^2 + |\boldsymbol{\nabla} B_y|^2\right)$.

[120] give an expression for the generated relaxation rate as

$$\left(\frac{1}{T_1}\right)_{\mathrm{SR}} = \frac{9\pi\xi_0^2(T^*)^2}{4\hbar^2\omega_\mathrm{D}}\eta(\epsilon_0, T^*) \overset{T>T_\mathrm{D}}{\approx} \frac{\xi_0^2(T^*)^2}{\hbar^2\omega_\mathrm{D}} \cdot 2 \times 10^4, \tag{3.43}$$

where $T^* = T/T_\mathrm{D} = T/55\,\mathrm{K}$ with the Debye temperature T_D of solid xenon, the Debye frequency $\omega_\mathrm{D} = k_\mathrm{B}T_\mathrm{D}/\hbar$, the efficiency function η and the spin-rotation coupling strength $\xi_0 = \xi(r_0)$ at one lattice spacing $r_0 = 4.4\,\text{Å}$. The function η accounts for phonon freeze-out at temperatures below T_D and approaches the value $\eta_0 = 2867$ for $T > T_\mathrm{D}$[21]. The spin-rotation coupling strength can be related to the chemical shift difference of gaseous and crystalline xenon and is determined to be [120] $\frac{\xi_0}{h} = -27\,\mathrm{Hz}$, with Planck's constant h.

Dipole-dipole coupling due to vacancy diffusion

Above 120 K to the melting point of about 160 K the relaxation rate is dominated by dipole-dipole interactions modulated by vacancy diffusion [121]. Very briefly I want to summarize the formulas needed to relate this longitudinal relaxation mechanism to temperature and magnetic field strength. The rates for relaxation due to dipole-dipole interactions are [121, 122]

$$\left(\frac{1}{T_1}\right)_{\mathrm{dip}}^{129\mathrm{Xe}} = f^{129}\frac{\hbar^2\gamma_\mathrm{I}^4 t_0 I(I+1)}{5b^6}\left[g\left(\frac{\omega_\mathrm{I}t_0}{2}\right) + 4g(\omega_\mathrm{I}t_0)\right] \tag{3.44}$$

for ^{129}Xe -^{129}Xe coupling and

$$\begin{aligned}\left(\frac{1}{T_1}\right)_{\mathrm{dip}}^{131\mathrm{Xe}} = f^{131}\frac{\hbar^2\gamma_\mathrm{I}^2\gamma_\mathrm{S}^2 t_0 S(S+1)}{15b^6}&\left[6g\left(\frac{(\omega_\mathrm{I}+\omega_\mathrm{S})t_0}{2}\right)\right.\\ &\left.+4g\left(\frac{(\omega_\mathrm{I}-\omega_\mathrm{S})t_0}{2}\right) + 3g\left(\frac{\omega_\mathrm{I}t_0}{2}\right)\right]\end{aligned} \tag{3.45}$$

due to ^{129}Xe -^{131}Xe coupling.

In the above equations γ_I $(I = 1/2)$ and γ_S $(S = 3/2)$ are the gyromagnetic ratios of ^{129}Xe and ^{131}Xe, respectively. $\omega_i = \gamma_i B$ denotes the Larmor frequency and f^i the isotopic abundances. The lattice parameter b depends on temperature via an empirical formula [123]

$$b(T) = 6.276416 + 0.00180771(T-125) + 4.57633 \times 10^{-6}(T-125)^2. \tag{3.46}$$

The hopping rate $1/t_0$ is extrapolated from T_2 measurements of Yen and Norberg [124] yielding

$$t_0 = 8.8 \times 10^{-17} e^{\frac{3604\,\mathrm{K}}{T}}\,\mathrm{s}. \tag{3.47}$$

---

[21] The efficiency function depends on a dimensionless function $\epsilon(r) = (r/\xi)d\xi/dr$ describing the variation of the coupling strength ξ with distance between nuclei r. In Eq. (3.43) ϵ is evaluated at the lattice spacing $r_0 = 4.4\,\text{Å}$, giving $\epsilon_0 = \epsilon(r_0) = -11.8$

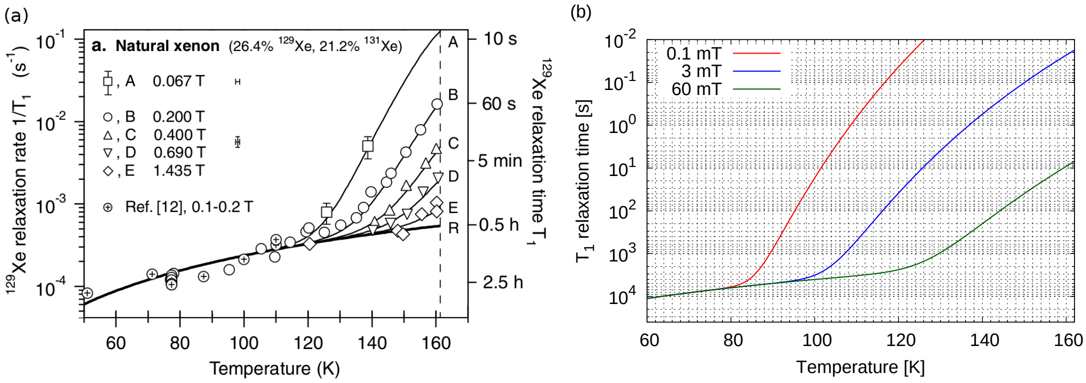

Fig. 11: Longitudinal relaxation of frozen ^{129}Xe: (a) temperature dependence of relaxation rates measured by Kuzma et al.[22]in magnetic fields between 67 mT and 1.4 T. The solid lines are the calculated rate taking into account photon scattering (spin-rotation interaction) and vacancy diffusion (dipole-dipole interaction). (b) T_1 relaxation at low magnetic field using the same model of phonon scattering and vacancy diffusion.

The function $g(y)$ can be given analytically in the monovacancy limit as [125]

$$g(y) = \frac{55.5}{0.169 + 0.128\sqrt{y} + y^2}. \tag{3.48}$$

In the case of temperatures approaching the melting point of 160 K Kuzma et al. [121] account for the chemical shift dependence on density by scaling the spin-rotating coupling strength according to

$$\xi(T) = \xi_0 \left[1 + 300\,\text{Å}^3 \left(\frac{1}{b^3} - \frac{1}{b_0^3}\right)\right], \tag{3.49}$$

where $b_0 = 6.2\,\text{Å}$ is the lattice spacing at 77 K.
In Fig. 11 the temperature and magnetic field dependence of the total longitudinal relaxation time

$$\frac{1}{T_1} = \left(\frac{1}{T_1}\right)_{\text{SR}} + \left(\frac{1}{T_1}\right)_{\text{dip}}^{\text{129Xe}} + \left(\frac{1}{T_1}\right)_{\text{dip}}^{\text{131Xe}} \tag{3.50}$$

is shown for the valid temperature range ($20\,\text{K} < T < 160\,\text{K}$) in high fields adopted from [121] (Fig. 11, a) and extrapolated to lower magnetic fields (Fig. 11, b). Fast relaxation at temperatures $\gtrsim 120\,\text{K}$ strongly affects preservation of polarization in low field environments. Xenon needs to be thawed quickly $\lesssim 60\,\text{s}$ in high magnetic fields $\gtrsim 200\,\text{mT}$ to avoid severe losses of polarization. This strongly constraints accumulation and subsequent thawing in magnetically shielded environments. In low magnetic fields $T_1 \ll 1\,\text{s}$ close to liquid temperatures. Thawing a frozen sample while preserving polarization is nearly impossible under these circumstances.

---

[22] Reprinted figure from [121, p. 3] with permission. Copyright 2002 by the American Physical Society.

Transverse spin relaxation has been extensively studied by Yen and Norberg [124]. At temperatures below 117 K the linewidth corresponds to $T_2 \approx 1\,\mathrm{ms}$ due to dipolar interactions. From $117 - 164\,\mathrm{K}$ motional narrowing occurs due to diffusion and the T_2 times increase exponentially from 1 ms to 2000 ms.

3.3.3 Liquid phase relaxation of ^{129}Xe

Longitudinal relaxation

First measurements of thermally polarized liquid xenon samples by Streever and Carr [101] were revised by Hunt and Carr [103] and they obtained T_1 relaxation times of order of 1000 s. These were not in agreement with predictions according to the dipole-dipole coupling theory [98] yielding both orders of magnitude longer T_1 times and an activation-like temperature dependence. A relation of chemical shifts $\Delta\sigma$ measured by Streever [101] to the relaxation (based on work by Torrey [102]) gave a well enough explanation of the T_1 times in high density liquid samples

$$\frac{1}{T_1} \approx 36 \left(\frac{\gamma mc}{e}\right)^2 \frac{D\langle\Delta\sigma\rangle_t^2}{R^2}, \tag{3.51}$$

with the gyromagnetic ratio γ, the electron mass m, electron charge e, the speed of light c, the diffusion constant D and $R \approx 10^{-8}$ the rigid sphere diameter of Torrey's model. The observed instantaneous chemical shift is averaged over all time. The relaxation mechanism is identified as a spin-rotation interaction: the charge clouds are distorted during collisions and induce both the chemical shift $\Delta\sigma$ and a time-varying field B_r due to the rotating charge distribution, with $B_r = (3mc/e)\omega\Delta\sigma$ [102]. Nearly 40 years later Sauer et al. [126] published new measurements extending the temperature down to the triple point close to 160 K where $T_1 > 1800\,\mathrm{s}$ was observed in a pyrex cell at 1.4 T. At low magnetic field of 50 μT the longitudinal relaxation time was determined only at a temperature of 200 K and showed a decrease to 1230 s from 1500 s measured at 1.4 T. The quicker relaxation in low fields was attributed to impurities in the glass which are more pronounced at lower fields.

Transverse relaxation and non-linear effects

Transverse relaxation in liquid xenon has been more extensively studied, particularly because there are interesting non-linear effects in highly polarized samples. Historically Yen and Norberg [124] published values of several seconds above the melting point already in 1963 using thermally (weakly) polarized samples. It's expected that in a liquid T_2 should be equal to T_1 in the regime of motional narrowing[23].
The implications on transverse relaxation due to slow diffusion in different magnetic field gradients are show in Fig. 12.

In more recent work of Romalis and Ledbetter [127] long transverse relaxation times of up to 1300 s have been reported. The extremely long T_2 were observed using spin-echo pulse sequences suppressing relaxation due to external magnetic field gradients.

---

[23] The correlation time τ_c of the spin-rotation interaction should be short, hence $\tau_c\omega_L \ll 1$

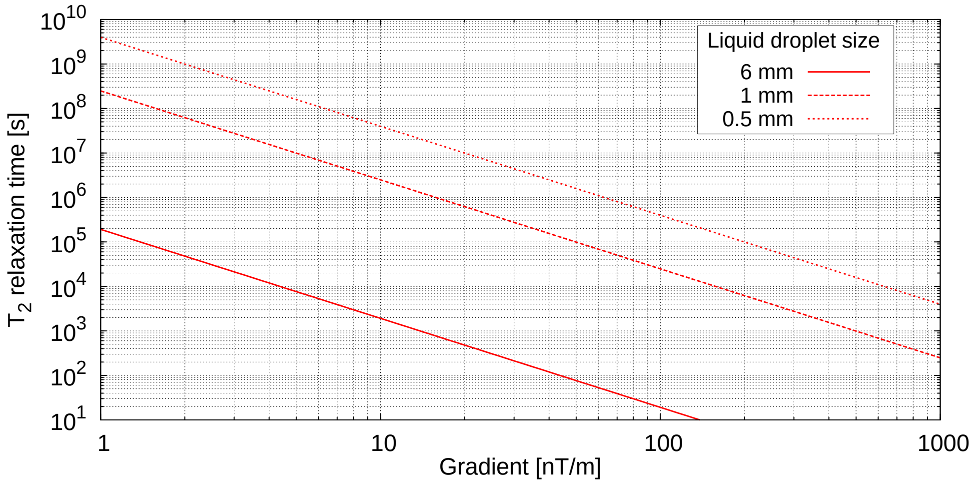

Fig. 12: Transverse relaxation due to magnetic field gradients in a liquid xenon droplet ($D = 3.9 \times 10^{-5}\,\mathrm{cm}^2/\mathrm{s}$, Tab. A.2) of variable diameter (cf. Eq. (3.41)).

However, effects due to long-range dipolar interactions in highly polarized samples that are not averaged out can lead to instabilities and spectral clustering [128, 129]. Ledbetter and Romalis [130] studied these non-linear effects in more detail employing two SQUIDs to directly observe the magnetization gradient in a spherical sample. For tip angles of $\theta > 35°$ away from the longitudinal direction they observe an exponential amplification of magnetization gradients while for $\theta < 35°$ oscillating magnetization gradients are generated which resulted in a fivefold increase of T_2^*.

A perturbative model accounts for linear gradients in dipolar fields and a longitudinal external gradient and solves the Bloch equations (Eq. 3.12) in the rotating frame. The magnetic field and magnetization in the Bloch equations modified by the linear magnetization gradient, hence the magnetization reads

$$\boldsymbol{M}(\boldsymbol{r},t) = \boldsymbol{M_0} + \boldsymbol{m}(t) M_0 \frac{z}{R}, \tag{3.52}$$

where R is the spherical cell radius and $\boldsymbol{M_0}$ is the initial magnetization. The dimensionless parameter describing the linear magnetization gradient is

$$\begin{aligned} m(t) &= -\frac{\gamma_{\mathrm{Xe}} g R}{\beta} \sin(\alpha)\sinh(\beta t) \\ \text{with}\,\beta &= \frac{4\sqrt{2}\pi}{15} M_0 \gamma_{\mathrm{Xe}} \sqrt{1-\cos(2\alpha)}, \end{aligned} \tag{3.53}$$

with the magnetic field gradient g and the tip angle α.

The non-linear effects strongly amplify gradients in a highly polarized (liquid) sample when spins are tipped by more angles more than 35°. However, at flip angles of 35° the dominant part (neglecting higher order terms) can be turned off and $m(t) = \gamma_{\mathrm{Xe}} g R t$ only grows linearly in time. At smaller flip angles ($< 35°$) the nonlinear effects even

suppress the growth of the magnetization gradients and lead to spectral narrowing.
The non-linear effects basically depend on the ambient external gradient, the sample size and sample magnetization and their implications on the liquid xenon EDM measurement need to be studied under existing experimental conditions.

3.4 SQUID detection

A highly sensitive detection of nuclear spin precession is a main challenge in atomic EDM experiments, as the ratio of observed signal to detection noise is substantially determining the EDM senstivity (cf. Sec. 4.2). Optical detection of spin precession has been employed in the ^{199}Hg EDM measurement [67, 131] giving an intrinsically very low noise level. In a search for a ^{129}Xe EDM optical detection is not as straight forward and currently not the preferred detection technique. However, EDM searches are currently planned with an improved spin maser concept. The ^{129}Xe precession is detected via optical absorption of 794.8 nm light in a rubidium vapor due to a small transverse magnetization of ^{129}Xe [132]. The drawback here is, that the rubidium vapor in the EDM cell potentially limits the breakdown voltage and causes unwanted frequency shifts. Nevertheless, an improvement of the noise level due to optical detection can still increase the EDM sensitivity.
In the efforts presented in this work the precessing nuclear spins in very low magnetic fields are detected using SQUIDs. SQUIDs provide a very sensitive probe of magnetic flux changes as the intrinsic noise density of commercially available SQUID sensors is on the order of several $\mathrm{fT}/\sqrt{\mathrm{Hz}}$ even at frequencies down to a few Hz. Reviews of SQUIDs and applications can be found in [133, 134] and the comprehensive SQUID handbook [135]. Operation of SQUIDs is based on the phenomena of superconductivity presented in various textbooks, e.g. [136, 137].

3.4.1 Superconductivity and the Josephson effect

In the superconducting state single electron scattering is eliminated as phonon exchange between two electrons leads to an attractive long-range interaction. The paired electrons, called Cooper pairs, have opposite spins, hence they are subject to Bose-Einstein statistics and tend to occupy a single ground state. The distance of two weakly bound electrons is specified by the coherence length $\zeta \approx 100\,\mathrm{nm}$, which is much larger than the average cooper pair distance $\bar{r} = 1\,\mathrm{nm}$. The strong overlap of the wave-functions allows a phase-coherent description of the superconducting state by a single many-body wave-function

$$\Psi(\boldsymbol{r}) = |\Psi(\boldsymbol{r})| e^{i\varphi(\boldsymbol{r})}. \tag{3.54}$$

To break up a Cooper pair and create two quasi-particle excitations an energy of $2\Delta \approx 10^{-3}\,\mathrm{eV}$ is necessary, which can be added thermally (critical temperature T_c), kinetically (critical current j_c) or magnetically (critical field H_c). As the binding of the Cooper pairs establishes an energy gap Δ at the Fermi level, the lack of available electron states makes the electron pairs propagate unscattered. This phenomenon of superconductivity brings along several new effects, like flux expulsion in superconductors (Meissner effect) [138], flux quantization ($\Phi_0 = 2.068 \times 10^{-15}\,\mathrm{Wb},\ 1\,\mathrm{Wb} = 1\,\mathrm{Tm}^2$) or the Josephson effect [139], particularly important for understanding the operational principle of SQUIDs and explained in the following.

In 1962 Josephson predicted a supercurrent arising from Cooper pairs tunneling through a weak link between two superconductors, that can be a insulating or normal conducting layer of thickness $d \ll \zeta$. Assume the two superconductors on either side of the weak link are described by two wave-functions $\Psi_1 = |\Psi_1|e^{i\varphi_1}$ and $\Psi_2 = |\Psi_2|e^{i\varphi_2}$. Then the gauge invariant phase difference reads

$$\Delta\varphi = \varphi_2 - \varphi_1 - \frac{2\pi}{\phi_0}\int \boldsymbol{A} d\boldsymbol{l}. \tag{3.55}$$

The first Josephson relation (Feynman [140] gives a derivation for the case without magnetic fields, $\boldsymbol{A} = 0$) relates the supercurrent I_s at zero voltage difference to the phase difference $\Delta\varphi$ as

$$I_\mathrm{s} = I_\mathrm{c} \sin \Delta\varphi, \tag{3.56}$$

where I_c is the critical current determined by the weak link, typically of order $10^2 - 10^4\,\mathrm{A/cm}^2$. The second Josephson relation arises from the time-derivative of the phase difference $\Delta\varphi$ as

$$\frac{d\Delta\varphi}{dt} = \frac{2e}{\hbar}V = \frac{2\pi}{\Phi_0}V, \tag{3.57}$$

with the fluxoid $\Phi_0 = \frac{h}{2e}$ and the voltage difference V across the junction. For a constant potential across the junction $V \neq 0$ the supercurrent (3.56) starts oscillating at a frequency $\nu = \frac{2eV}{h}$, typically in the GHz range.

3.4.2 SQUIDs and the flux-locked loop

With Josephson junctions in superconducting loops an extremely sensitive flux to voltage converter can be set up making use of interference of the coherent wave-functions[24]. Assume a magnetic flux Φ_a penetrates the loop and two Josephson junctions J1, J2 link the input and output terminals of the SQUID device (Fig. 13). The two wave-functions traveling across different Josephson junctions interfere at the output terminal. A magnetic flux Φ_a through the SQUID loop causes a circular current I^cir differently affecting the phase changes at the two Josephson junctions. Hence the interference of both wave-functions yields a modulation of the maximum supercurrent according to the magnetic flux. The resulting pattern is well known from two-slit interference in optics and can be derived with the Josephson equations.

Integration of the wave vector $\boldsymbol{k} = \frac{m\boldsymbol{v} - q\boldsymbol{A}}{\hbar}$ along a circular closed path within the loop (dashed line in Fig. 13) yields a relation between the flux $\Phi_\mathrm{a} = \oint \boldsymbol{A} d\boldsymbol{l}$ through the loop

---

[24] In a dc SQUID two Josephson junctions are used and the device can be directly read out electronically, while rf SQUIDs use only on junction, but need a tank circuit for read out. Rf SQUIDs were not of interest in this work as they usually have less sensitivity.

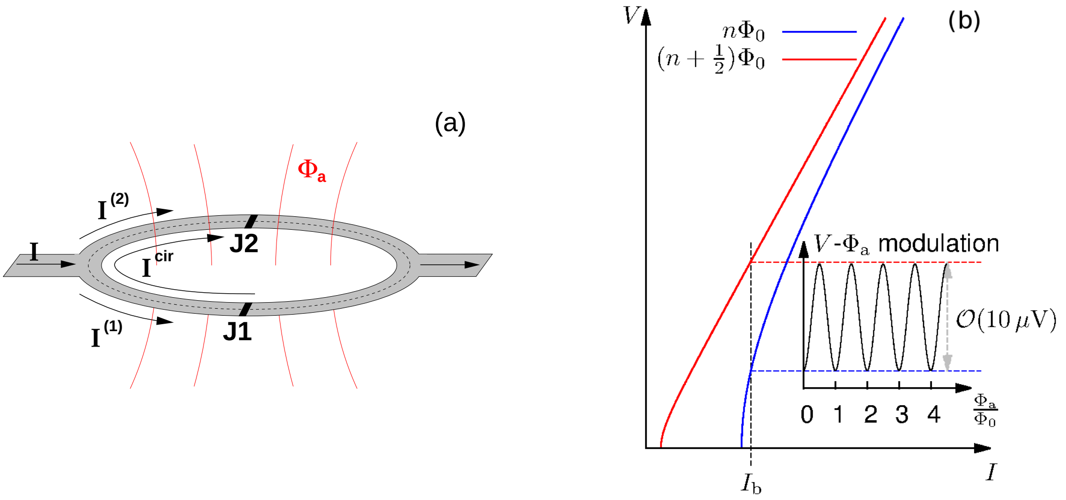

Fig. 13: The SQUID operation principle: A magnetic flux Φ_a penetrating a superconducting loop with two Josephson junctions (a) generates a screening current I^{cir} adding to $I^{(i)}$, which is eventually exceeding the critical current I_c. Due to the established voltage drop the maximum supercurrent across the junction is modulated with a period of $\Phi_0 = \frac{h}{2e}$. A bias current I_b applied across the SQUID loop generates a modulation of the average voltage according to the penetrating flux Φ_a (b). An appropriate choice of I_b maximizes the modulation height.

and the gauge invariant phase differences (3.55) along both paths

$$\Delta\varphi^{(2)} - \Delta\varphi^{(1)} = \frac{2\pi}{\Phi_0}(\Phi_a + LI^{cir}), \tag{3.58}$$

where Φ_0 is the flux quantum, L is the inductance of the SQUID loop and I^{cir} is the circular current in the loop. As $I^{cir} < I_c$ the maximum self-induced flux can be due to the critical current and by requiring the inductance of the loop $LI_c < \Phi_0/2$, one can neglect the self-inductive flux. With expressions for the half-circle currents $I^{(1)} = \frac{I}{2} + I^{cir}$, $I^{(2)} = \frac{I}{2} - I^{cir}$ and the Josephson equation for the supercurrent Eq. (3.56) one obtains

$$I = I_c \sin\left(\Delta\varphi^{(1)} + \pi\frac{\Phi_a}{\Phi_0}\right)\cos\left(\pi\frac{\Phi_a}{\Phi_0}\right). \tag{3.59}$$

With the phase $\Delta\varphi^{(1)}$ adjusting accordingly to fulfill (3.59), but the sine limited to $[-1, 1]$ the modulation of the maximal supercurrent through the SQUID depending on the magnetic flux Φ_a is

$$I^{max} = 2I_c\left|\cos\left(\pi\frac{\Phi_a}{\Phi_0}\right)\right|. \tag{3.60}$$

If the magnetic flux Φ_a is an integer multiple of Φ_0 the highest maximum supercurrent of $2I_c$ can run through the dc SQUID loop while $I^{cir} = 0$. For $\Phi_a = \left(n + \frac{1}{2}\right)\Phi_0$, with integer n the maximal supercurrent is zero and $|I^{cir}| = I_c$.
To avoid hysteresis in the I-V characteristic the Josephson junctions in a real dc SQUID

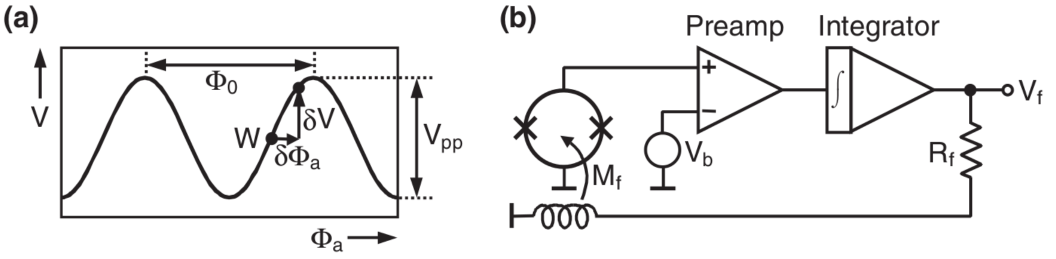

Fig. 14: (a) SQUID voltage modulation with period Φ_0 and modulation depth V_{pp}. At the working point a flux change $\delta\Phi_{\mathrm{a}}$ corresponds to a voltage change δV. (b) The FLL circuit feeds a current to a feedback coil coupled to the SQUID loop via the mutual inductance M_{f}. The voltage drop at the feedback resistor gives the signal at the FLL output.[26]

have a shunt resistor in parallel. In the resistively shunted junction (RSJ) model[25] the observed time-averaged voltage is (see [135, 136])

$$\begin{aligned} V &= 0 && I < I_{\mathrm{c}} \\ V &= \frac{R}{2}\sqrt{I^2 - I_{\mathrm{c}}^2} && I > I_{\mathrm{c}}. \end{aligned} \tag{3.61}$$

Here, thermal noise currents resulting in rounding the I-V curve are neglected. The I-V plots of Fig. 13 show the voltage modulation according to Eq. (3.61).

A practical dc SQUID is operated in a regime above the critical current by applying a bias current $I_{\mathrm{b}} > I_{\mathrm{c}}$ to the SQUID loop. Above the critical current an average voltage drops across the loop and is modulated by the magnetic flux Φ_{a}, see Fig. 13(c). The peak-to-peak value of this modulation can be determined in this ideal case of exactly symmetric junctions and negligible SQUID inductance L from Eq. (3.61) to be

$$V_{\mathrm{pp}} = V(\Phi_0/2) - V(0) = I_0 R \left[\frac{I}{2I_{\mathrm{c}}} - \sqrt{\left(\frac{I}{2I_{\mathrm{c}}}\right)^2 - 1} \right], \tag{3.62}$$

which is maximized at a bias current $I_{\mathrm{b}} = 2I_0$.

As the voltage response of the SQUID loop is only linear (e.g. $\approx 1\%$) in a small magnetic flux range ($\approx 0.1\Phi_0$) [135] a flux-lock-ing circuit is usually implemented, called the flux locked loop (FLL). In FLL mode the flux is locked on the linearly rising (or falling) slope and the SQUID responds to small flux changes $\delta\Phi_{\mathrm{a}}$ with a linearized voltage according to the transfer function $V_\Phi = \frac{\partial V}{\partial \Phi_{\mathrm{a}}}$ (Fig. 14 (a)). The fundamental scheme of an FLL circuit is shown in Fig. 14 (b). Any deviation δV across the SQUID loop from the working point at the bias voltage V_{b} is amplified and integrated. The obtained signal proportional to the total flux change in the SQUID loop is fed back into the SQUID loop

---

[25] A simplification of the very well justified resistively- and capacitively shunted junction (RCSJ) model, where the shunt capacitance is neglected

[26] Copyright Wiley-VCH Verlag GmbH & Co. KGaA. Reproduced from [135, p. 129] with permission.

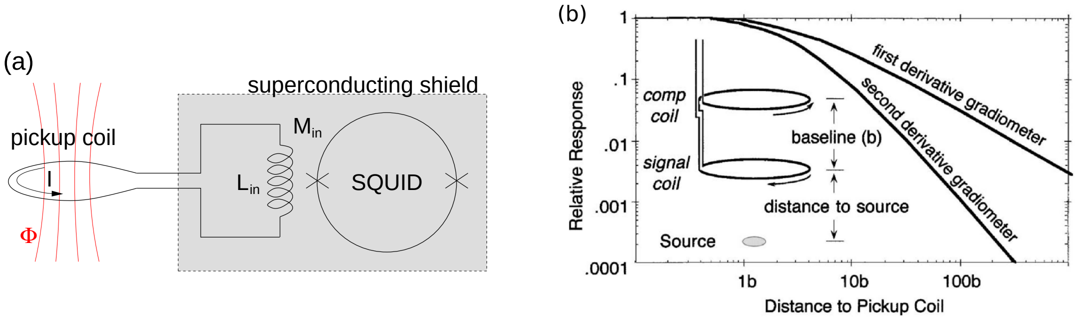

Fig. 15: (a) Superconducting flux transformer: the magnetic flux in a wire-wound pickup coil is transformed and coupled to the SQUID loop via the mutual inductance M_{in}. (b) The relative response of a gradiometer (first order) pickup coil depending on the distance to the signal source, which is normalized to the baseline. Also shown is the response for a second order gradiometer featuring four pickup loops (Reproduced from [134] with permission).

as a current through a feedback coil coupled to the SQUID via the mutual inductance M_{f}. With the feedback current running through a (variable) feedback resistor ($R_{\mathrm{f}} \approx \mathrm{k}\Omega$) the voltage drop can be digitized as the magnetic flux change in the SQUID loop.

The transfer function of the FLL only depends on the circuit parameters R_{f} and M_{f}, but not on the particular working point. The bandwidth of the FLL circuit is usually in the 10 MHz range and limited by the circuit parameter R_{f} and M_{f}[27]. For the detection of the low precession frequencies in this work the system bandwidth is of no further concern.

SQUIDs are extremely sensitive devices and the art of making the sensitivity available for measurements is mostly designing low noise readout electronics. Suppression of the noise of the electronics below the SQUID intrinsic noise can be achieved by several techniques, e.g. by modulation of the feedback flux or additional positive feedback (APF). The effect that sets the limits on SQUID sensors is 1/f noise which usually sets in below a corner frequency of several Hz. The 1/f noise is caused by fluctuations of the critical current in the Josephson junctions and motion of trapped flux vortices. Critical current fluctuation can occur during the tunneling process by trapping and subsequent release at defects. Flux vortices trapped in the superconductor can contribute to 1/f noise by hopping between pinning sites, which are provided by defects. However, low T_{c} (LTC) SQUIDs as used in the presented experiments generally offer superior noise performance compared to high T_{c} (HTC) SQUIDs. Although the 1/f noise is orders of magnitude smaller in LTC SQUIDs, a SQUID is less suited for longterm drift or DC measurements than atomic magnetometers.

3.4.3 Practical SQUID magnetometers and gradiometers

The SQUID loop is rarely well suited for magnetic field measurements. The energy resolution of a resistively shunted dc SQUID under optimum conditions is $\epsilon(f) \approx 16k_{\mathrm{B}}T\sqrt{LC}$ [135], hence a SQUID loop should have very small inductance and capacitance. A small inductance corresponds to a small enclosed area, typically $A_{\mathrm{L}} < 10^{-2}\,\mathrm{mm}^2$. Athough, the SQUID is extremely flux sensitive $\approx 10^{-6}\,\Phi_0$, the field sensitivity $\delta B = \delta\Phi/A_{\mathrm{L}}$ turns out to be orders of magnitude worse. To overcome this a washer of large outer diameter D and very small hole d can be used to increase the effective area to $A_{\mathrm{eff}} = dD$ by focusing the field. Another now widely used approach is implementation of a multi-turn flux transformer. A superconducting pickup coil of experimentally favourable dimensions and turns picks up the magnetic flux, which is transformed to an input coil on the SQUID chip. The input coil is coupled to the SQUID loop via the mutual inductance M_{in}, see Fig. 15 (a). This gives the freedom of having the pickup coil on chip or have it self-made using niobium wire. In the latter case the coil can be external of a superconducting shield, which encloses the SQUID chip. The only constrain on the external pickup coil is matching it's inductance to the inductance of the input coil, usually hundreds of nH to some μH. The inductance of a (flat) superconducting loop is given by [134]

$$L = \mu_0 N^2 r_{\mathrm{coil}} \left[\ln\left(\frac{8r_{\mathrm{coil}}}{r_{\mathrm{wire}}}\right) - 2 \right], \tag{3.63}$$

with the number of turns N, the radius of the coil r_{coil} and the radius of the wire r_{wire}. For high magnetic flux sensitivity a large coil area is preferred. However, it is constrained experimentally by it's size, by the anticipated spatial resolution and the intrinsic magnetic field noise of the SQUID. Additionally, to benefit from a large pickup loop area the environmental magnetic field noise has to be lower than the loop sensitivity. A rule of thumb is the coil diameter should be at least the distance to the source.In the detection of nearby signal sources external niobium wire pickup coils are particularly helpful as the gradiometer configuration can greatly reduce the noise level. From the $1/r^3$ dependence of the fields the optimum baseline of a gradiometer can be determined (Fig. 15 (b)).

---

[27] The bandwidth can be estimated by $f_{3\mathrm{dB}} \approx \frac{V_\Phi M_{\mathrm{f}}}{R_{\mathrm{f}}} \cdot GBP$, where $\frac{V_\Phi M_{\mathrm{f}}}{R_{\mathrm{f}}}$ is the SQUID gain and GBP is the gain bandwidth product set in the SQUID software, typically 0.23 GHz.

4 Improving EDM measurements of ^{129}Xe

As already pointed out (Eq. (2.29)) the signature of an EDM in “conventional” searches is a shift of the Larmor frequency due to a coupling of the EDM to an additionally applied electric field. The source of a frequency shift $\delta\nu \neq 0$ can not easily be disentangled. In a measurement with electric field of $E = 10\,\mathrm{kV/cm}$ and assuming an EDM $d = 10^{-26}\,e\mathrm{cm}$ the obtained frequency shift $\delta\nu$ is

$$\delta\nu = \frac{2(\delta d)E}{h} \approx 4 \times 10^{-8}\,\mathrm{Hz}, \tag{4.1}$$

with Planck’s constant h. The same shift is generated by a magnetic field variation δB of order

$$\delta B = \frac{h(\delta\nu)}{2\mu} \approx 10^{-15}\,\mathrm{T}, \tag{4.2}$$

where the magnetic moment $\mu \approx 4 \times 10^{-27}\,\mathrm{J/T}$.
To account for this in the analysis a lot of effort needs to be put in precise monitoring of the magnetic field during an EDM measurement with parallel fields. Sensitivity can mostly be enhanced by (further) tuning of experimental parameters and a better understanding of systematic effects. To overcome general limitations of the parallel fields method new approaches are highly motivated.
In this chapter I will first discuss the experiment from which the most recent EDM limit on ^{129}Xe was obtained and the fundamental parameters determining the sensitivity of an EDM search. The section will be concluded by adressing possible improvements in parallel fields EDM searches in the gas phase and new concepts.

4.1 Background

For the isotope ^{129}Xe the most recent limit from an experiment at the University of Michigan [71] was measured with a spin-maser setup. The method allows observation of spin precession for arbitrarily long times not being limited by spin relaxation times. Next to ^{129}Xe a second species (^{3}He) in the EDM cell provides extremely useful information on magnetic field variations. The limit for ^{129}Xe that was determined with the spin maser technique is $d_{\mathrm{Xe}} = 0.7 \pm 3.3 \cdot 10^{-27}\,e\mathrm{cm}$.

The two maser species are polarized in a pumping cell by SEOP using Rb metal and constantly diffuse to the cylindrical EDM cell (Fig. 16). The spins in a gas mixture of 85 mbar ^{129}Xe , 860 mbar ^{3}He and 62 mbar of nitrogen precess in a magnetic field of 315 μT inside a magnetically shielded environment. The rotating magnetization induces currents in resonant circuits consisting of pickup coils and capacitors (C_{He} and C_{Xe}).

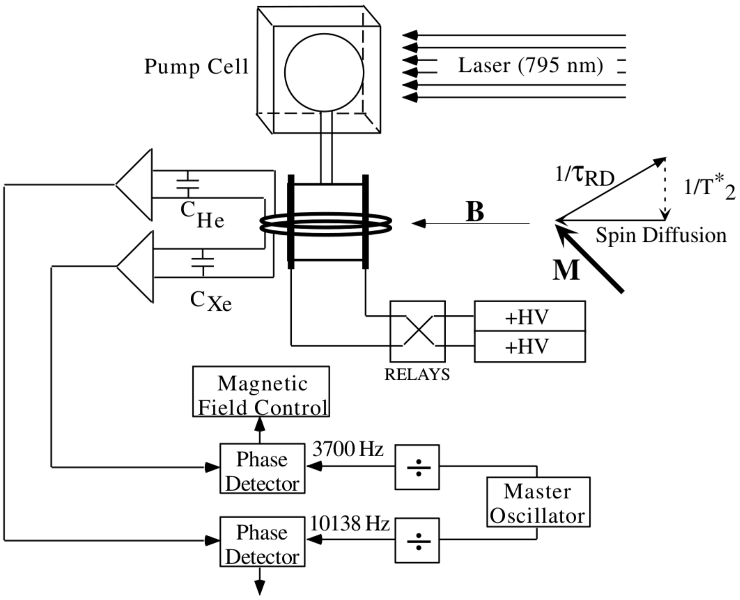

Fig. 16: Experimental setup of the He-Xe maser[28]. With steady state operation of the maser observation times much longer than T_2^* can be realized. The currently best published limit for the EDM of ^{129}Xe was measured with this technique in electric fields of 3.6 kV.

The oscillating magnetic fields induce torques on the magnetizations of the two species rotating them away from the magnetic field axis. However this also affects the induced current. Steady maser operation is sustained by equilibrium of the self-coupling, described by the radiation damping rate $1/\tau_{\mathrm{RD}}$, the transverse relaxation rate $1/T_2^*$ and the spin diffusion rate supplying magnetization in direction of B. Essentially a control loop changes the B_0 field current according to variations of the ^{129}Xe precession frequency, which leads to a frequency response of the ^{3}He with a gain of $\gamma_{\mathrm{He}}/\gamma_{\mathrm{Xe}} = 2.8$.

Many parameters, mostly temperatures and laser intensity, that affect the maser frequencies were found to be uncorrelated with the electric field or could be corrected for. Of the systematic effects the most dominant is a leakage current between the electrodes which in the worst case runs along a circular path generating an additional B_0 field. The measured leakage current of 20 pA at an applied electric field of 3.6 kV/cm would in that case produce a false EDM signal of $2 \times 10^{-27}\,e$cm. However the ^{3}He co-magnetometer helped to limit the leakage current systematic to below $10^{-28}\,e$cm. Other systematics, particularly frequency stability of electronics, effects quadratic in the electric field or magnetization of the magnetic shielding by the current charging the electrodes could be limited to $< 10^{-28}\,e$cm. The natural measurement procedure are runs with zero and reversed electric fields and with the magnetic field reversed.

According to the authors the ultimate sensitivity for an EDM search is about $5 \times 10^{-29}\,e\,\mathrm{cm}/\sqrt{\mathrm{day}}$ limited by the precision of the phase locked ^{129}Xe maser. A simi-

---

[28] Reprinted figure from [71, p. 2] with permission. Copyright 2001 by the American Physical Society.

lar maser technique improved by optical detection of the precession is planned to be used in a ^{129}Xe EDM search in Japan. The sensitivity to frequency measurements based on observed spin precession without electric field is quoted differently by the same group as $\approx 10^{-31}$ $e$cm within 10 days [141] and $\approx 10^{-28}$ $e$cm within 10000 s [142].

4.2 Fundamental limitations

In the following the sensitivity of the EDM d will be deduced depending on the relevant experimental parameters. Systematic effects are assumed to be zero, e.g. the magnetic field is known exactly or generally $\boldsymbol{\mu}.\boldsymbol{B}$ is known much better than $\boldsymbol{d}.\boldsymbol{E}$.

The fundamental uncertainty of a measurement of a single spin frequency running for a long time τ can be given according to Heisenberg's energy-time uncertainty principle as $\hbar(\delta\omega)\tau = \hbar$ and hence

$$\delta\omega = \frac{1}{\tau} \tag{4.3}$$

Assume the measurement is repeated N times at a signal-to-noise ratio S/n, then[29]

$$\delta\omega = \frac{1}{\tau(S/n)\sqrt{N}} = \frac{\epsilon\sqrt{f_{\mathrm{BW}}}}{\tau S\sqrt{N}}, \tag{4.4}$$

with the noise density ϵ and the bandwidth f_{BW}. The number of measurements in a total measurement time T is $N = T/\tau$ and the bandwidth can be assumed as $f_{\mathrm{BW}} \approx 1/\tau$. With Eq. (2.29) the fundamental sensitivity of an EDM determined from the uncertainty in the frequency measurement is

$$\sigma_{\mathrm{d}} = \frac{\hbar}{2E}\frac{\epsilon}{\tau^{3/2}S\sqrt{N}} = \frac{\hbar}{2E}\frac{\epsilon}{\tau S\sqrt{T}}. \tag{4.5}$$

The above derivation yields a very similar estimate as the frequency sensitivity according to the Cramer-Rao lower bound for an exponentiall decaying sine wave , see eg. [112].

4.2.1 Methods to improve EDM sensitivity

The fundamental sensitivity (Eq. (4.5)) reveals the obvious ways to go for an improved EDM limit.

Polar molecules are highly polarizable and hence offer very high internal electric fields of several tens of GV/cm in moderate laboratory fields, while EDM searches on particles and atoms are technically limited to tens of kV/cm. Several searches for the electron EDM with molecules (e.g. YbF, PbO, ThO,...) are currently on the way. Very recently the limit on the electron EDM has been improved to $< 9 \times 10^{-29}$ $e$cm [69] using the molecule ThO.

An increase in signal size corresponds to a higher density sample, e.g. high spin polarization. For EDM searches using particles or atomic/molecular beams an increase in signal

---

[29] The noise is assumed to be white noise.

size is not straightforward and limited by available facilities and upgrade progress. EDM searches with polarized noble gases are basically free to choose a gas density as desired. However, there is a trade off as the observation time τ of freely precessing spins, which in that case is T_2^*, is inversely proportional to the density.

In particular a long observation time significantly improves the sensitivity, which is harder to achieve by slowing atomic/molecular beams or by trapping of atoms in cavities. For the very promising radioactive isotopes with octupole deformation this is additionally limited by their lifetime, but for radium and radon this is sufficiently long $\tau_{1/2} > 1000\,\mathrm{s}$.

The noise density ϵ of the background also needs to be reduced for an enhanced sensitivity. Detection using a low-noise sensor is a challenging encounter, as the measurements are preferably done at very low frequencies of tens of Hz. The ^{199}Hg EDM experiment benefits from optical detection of the spin precession and quotes [131] a measured root mean square (rms) noise density of $30\,\mu$V. At a typical signal amplitude of 3 V this results in a signal-to-noise ratio of 3×10^4 (inferring a bandwidth of $f_{\mathrm{BW}} \approx 10\,\mathrm{Hz}$). Besides potentially useful atomic magnetometers with demonstrated sub-fT noise density [143] SQUIDs provide a relatively easy to use highly sensitive sensor for magnetic flux. The magnetic flux noise density of LTc SQUIDs is as low as $\lesssim 2\,\mathrm{fT}/\sqrt{\mathrm{Hz}}$ for frequencies down to several Hz. The possibility of using external superconducting pickup coils offers a variety of geometric shapes including gradiometer designs. A typical EDM cell with tens of mbar of ^{129}Xe polarized at 10% yields some nT magnetic flux in a few cm distance. Assuming only intrinsic SQUID noise, a signal-to-noise ratio of $\approx 10^5 - 10^6$ is expected, potentially at least an order of magnitude better than the currently available optical detection technique.

4.2.2 An improved conventional EDM search

Several EDM experiments try to exploit the fundamental sensitivity of Eq. (4.5) by further improving the established method of parallel electric and magnetic fields. The systematics are mostly well-known and new results can be obtained with moderate effort. However, the gain in sensitivity is less significant.

An effort of an EDM search using ^{129}Xe in a gas phase sample and using parallel fields is described in Sec. 6. Inside a magnetically shielded room with the best possible environment in terms of magnetic field gradients, homogeneity of the residual field and very low noise, we aim to observe ^{129}Xe spin-precession with very little magnetic and electric disturbance. A clock-comparison with a ^{3}He co-magnetometer and in a later stage the correlation of several external magnetometers compensate for magnetic field variations. With a SQUID based low-noise detection system a large signal-to-noise ratio greatly improves sensitivity.

The fundamental sensitivity of this approach with an applied electric field of $E = 10\,\mathrm{kV/cm}$ and assuming a $T_2^* \approx 200\,\mathrm{s}$ is estimated to be (Eq. (4.5))

$$\sigma_{\mathrm{d}} = \frac{\hbar}{2 \cdot 10\,\mathrm{kV/cm}} \frac{2\,\mathrm{fT}/\sqrt{\mathrm{Hz}}}{(200\,\mathrm{s})^{3/2} \cdot 1\,\mathrm{nT}} \frac{1}{\sqrt{N}} \approx 2 \times 10^{-29}\,\frac{e\mathrm{cm}}{\sqrt{N}}, \tag{4.6}$$

with the number of measurements N.

4.2.3 Next generation EDM search in liquid ^{129}Xe

Nevertheless the fundamental sensitivity limit is usually missed by at least an order of magnitude due to systematic effects. For significant progress towards new EDM limits new methods are strongly encouraged. Under development are EDM searches using protons, deuterons or muons in storage rings [144] and our novel approach aiming to use liquid hyper-polarized ^{129}Xe and time-varying electric fields. Superconducting pickup coils very close to the ^{129}Xe samples connected to SQUID current sensors with intrinsic noise $< 2\,\mathrm{fT}/\sqrt{\mathrm{Hz}}$ sense a magnetic flux due to Larmor precession of about 10 nT (at several % polarization). The method, setup and progress of this new effort is presented in Sec. 5. Implementation of rotating electric fields leads to decoupling of the rotation directions of the Larmor precession $\boldsymbol{\mu}.\boldsymbol{B}$ from the precession due to the term $\boldsymbol{d}.\boldsymbol{E}$, which relaxes magnetic field requirements and introduces totally different systematics not yet studied. The potential gain of this approach using very small, but high density samples is an EDM sensitivity on the order of $10^{-29}\,e\mathrm{cm}$ in a single measurement, but presumably limited by systematic effects from oscillating currents. Details on this future method of rotating electric fields and the obtained sensitivity are discussed in Sec. 5.1.

Nevertheless a parallel fields measurement has a similar fundamental sensitivity (Eq. (4.5)). Assuming $E = 50\,\mathrm{kV/cm}$ and $T_2^* \approx 500\,\mathrm{s}$ using a polarized liquid one obtains

$$\sigma_\mathrm{d} = \frac{\hbar}{2 \cdot 50\,\mathrm{kV/cm}} \frac{2\,\mathrm{fT}/\sqrt{\mathrm{Hz}}}{(500\,\mathrm{s})^{3/2} \cdot 10\,\mathrm{nT}} \frac{1}{\sqrt{N}} \approx 1.2 \times 10^{-31}\,\frac{e\mathrm{cm}}{\sqrt{N}}, \tag{4.7}$$

where N again denotes the total number of measurements.

The potential of an EDM search in a liquid is high, but experimentally very demanding. In this long-term effort a thorough study of a rich field of new systematic effects, their undertanding and control is of utterly importance.

5 Progress towards a liquid ^{129}Xe EDM experiment

This section is dedicated to a newly started xenon EDM experiment, which is designed to allow for implementation of novel methods in EDM searches. Building the experiment is a technically challenging task, but the potential gain of several orders of magnitude in EDM sensitivity is highly motivating the R&D work. With the end of this thesis the setup is in a status were succeeding graduate students can start physics measurements investigating the rich potential of the proposed method and study novel systematics in EDM searches. As a byproduct several effects regarding liquid NMR in ultra-low fields can be studied, e.g. the nonlinear effects.

The novel EDM measurement technique is discussed in detail in Sec. 5.1. It is based on sub-millimeter hyper-polarized liquid xenon droplets enclosed on a micro-fabricated structure. Implementation of rotating electric fields enables a conceptually new EDM measurement technique, potentially overcoming current sensitivity limitations while allowing thorough investigation of new systematic effects. An alternative new method with constant electric fields based on simulations of dipole couplings is also presented briefly.

The future EDM search is planned in a cryogen-free SQUID cryostat which was set up during this thesis. A paper prepared for publication describes the setup and measurements demonstrating a magnetic flux noise density on the order of 144 $\mathrm{fT}/\sqrt{\mathrm{Hz}}$ with a close-by sample at 161 K and the temperature control of the sample (Sec. 5.2). Some overlap mainly in the descriptions of the setup exists as both sections were prepared to be independently readable.

In the remainder of this chapter additional details are presented on the setup for production of hyper-polarized ^{129}Xe (Sec. 5.4), the xenon trap, polarized gas transfer system (Sec. 5.5), EDM chip development (Sec. 5.7) and magnetic field generation (Sec. 5.6).

To introduce the setup Fig. 17 shows a schematic overview of the liquid xenon EDM experiment. Polarized xenon gas from the polarizer is accumulated in a cold trap and subsequently transfered to the EDM chip inside a magnetic shield. It is liquefied at 163 K on the EDM chip and currents in superconducting pickup coils induced by spin precession are sensed with SQUID current sensors. The setup uses a cryo-cooler instead of a liquid helium dewar and is built to be fully automated for long-term operation. With our novel approach we aim to finally lower the limit on the EDM of ^{129}Xe by more than three orders of magnitude.

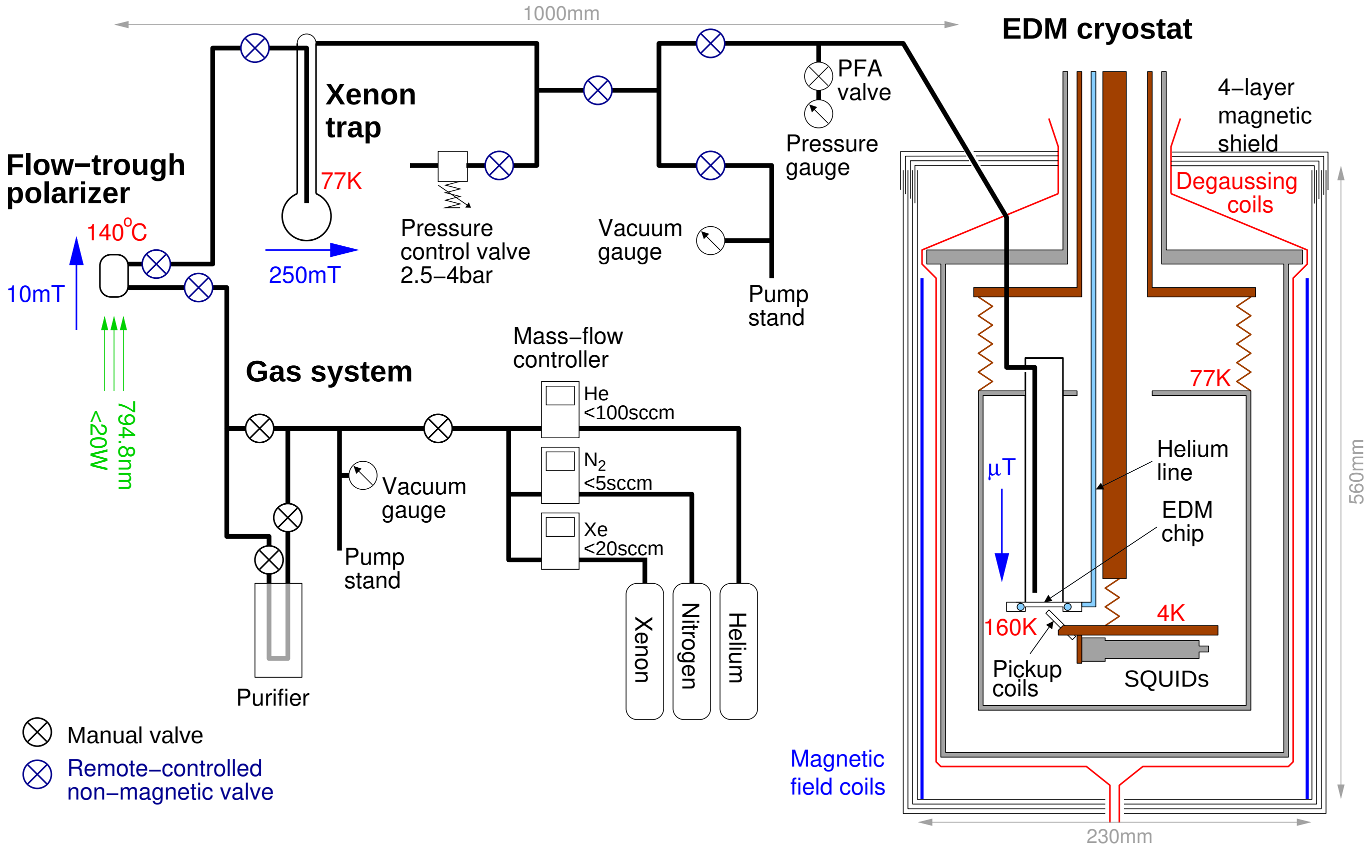

Fig. 17: Schematic overview of the liquid xenon EDM experimental setup. The gas mixture for SEOP is controlled via three mass-flow controllers, sent through a gas purifier and to the polarizing setup at pressures pf 2.5 to 4 bar. The polarized xenon is accumulated and separated from helium and nitrogen in a cold trap at high magnetic fields. A manifold of non-magnetic valves is used to evacuate the system and transfer polarized gas to the magnetically shielded EDM setup. The gas is diverted to the EDM chip attached to the bottom of a glass tube. The temperature can be controlled from 90 to 250 K. Homogeneous magnetic fields of up to 400 μT are generated by flexible circuits mounted on a cylindrical holder (blue). Currents induced in superconducting pickup coils below the “EDM chip” are detected by highly sensitive SQUID current sensors cooled to < 4.2 K.

5.1 A novel approach to measure the EDM of ^{129}Xe

In this section I mostly discuss the novel method of rotating electric fields we aim to implement in the xenon EDM setup. A large part will be dedicated to systematic effects that need to be considered. These effects are new to EDM searches as they arise from time-varying electric fields and need to be studied experimentally to be well understood.

5.1.1 Different ways to search for an EDM within this approach

"Ramsey-type" EDM search

In a typical EDM search a static electric field $\boldsymbol{E}$ is applied either parallel or anti-parallel to a magnetic holding field $\boldsymbol{B}_0$. A deviation in Larmor precession frequency ω_{L} for $E = 0$ and $E \neq 0$ can be attributed to an electric dipole moment (cf. Eqn. (2.29)):

$$\hbar\omega_{\mathrm{L}} = 2(\boldsymbol{\mu}.\boldsymbol{B}_0 - \boldsymbol{d}.\boldsymbol{E}), \tag{5.1}$$

where $\boldsymbol{E}$ can be aligned parallel and anti-parallel to $\boldsymbol{B}_0$, respectively. Using opposite polarities of the electric field the observed change in ω_{L} is $\delta\omega_{\mathrm{L}} = 4Ed/\hbar$ and directly translates to an EDM d.

This method strongly relies on highly stable (or precisely known) magnetic fields to disentangle false EDM effects due to magnetic field deviations. Accordingly, the stability of B_0 already limits the EDM sensitivity and highly sensitive magnetic field monitoring is essential.

Rotating electric fields

We aim to employ a novel EDM measurement technique introducing rotating electric fields rather than static electric fields to overcome current sensitivity limitations. In this approach the electric field $\boldsymbol{E}$ is applied perpendicular to $\boldsymbol{B}_0$ and co-rotating with the polarization $\boldsymbol{P}$ at a constant phase φ (cf. Fig. 18). The interaction of a non-zero EDM with the electric field causes a rotation of the polarization vector $\boldsymbol{P}$ according to $\boldsymbol{P} \times \boldsymbol{E}$ at a frequency $\omega_{\mathrm{d}} = dE/\hbar$, orthogonal to ω_{L}. Hence, in our approach B_0 fluctuations or drifts do not cause false EDM effects and constrictions on the knowledge of B_0 are less severe.

An EDM measurement starts by applying a highly accurate oscillating (or rotating) B_1 pulse to flip the polarization $\boldsymbol{P}$ (initially aligned along $\boldsymbol{B}_0$) by an (arbitrary) angle θ_1. Alternating voltages applied to eight electrodes embedded around each droplet can generate individually rotating electric fields. Phase-locked to the free precession signals the electric fields of e.g. three simultaneous experiments can be rotating (i) with a phase $\varphi = \frac{\pi}{2}$, (ii) in phase $\varphi = 0$ and (iii) with a phase $\varphi = -\frac{\pi}{2}$ with respect to $\boldsymbol{P}$ (cf. Fig. 18). After a free precession period τ a second B_1 pulse flips $\boldsymbol{P}$ by an angle $\theta_2 = \pi - \theta_1$. In case of a finite permanent EDM the polarization is rotated out of the precession plane during a free precession period τ accumulating an angle $\theta_d^{(i)} = \omega_{\mathrm{d}}\tau = \frac{dE\tau}{\hbar} = -\theta_d^{(iii)}$, where $\theta_d^{(i)}$ and $\theta_d^{(iii)}$ denote the angle in droplets with opposite electric field directions. An accumulated phase causes a misalignment of $\boldsymbol{P}$ and $\boldsymbol{B}_0$ after the second spin-flip pulse,

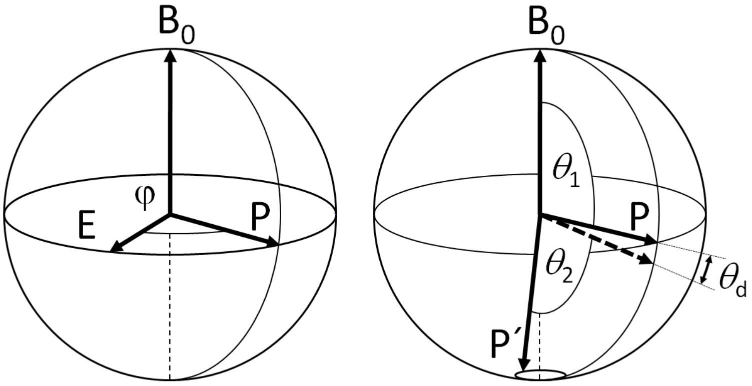

Fig. 18: Left: precession of electric field $\boldsymbol{E}$ ($\boldsymbol{E} \perp \boldsymbol{B}_0$) with constant phase φ to the polarization vector $\boldsymbol{P}$. Right: EDM measurement: (i) spin-flip by an angle θ_1 ($\theta_1 = \pi/2$ for illustration), (ii) accumulation of a possible phase $\theta_d = \frac{dE}{\hbar}\tau$ during the free precession time τ and (iii) spin-flip by an angle θ_2 with $\theta_1 + \theta_2 = \pi$. A potential misalignment ($\theta_1 + \theta_2 + \theta_d \neq \pi$) can be observed as precession with amplitude $P\theta_d$ of $\boldsymbol{P}$ around $\boldsymbol{B}_0$. This precession signal is phase-shifted by π for opposite polarities of E.

cf. Fig. 18. The resulting precession of $\boldsymbol{P}$ around $\boldsymbol{B}_0$ at a small tip angle $\theta_d = \frac{dE\tau}{\hbar}$ yields a possible EDM signal. Precession signals due to a misaligned polarization vector in experiments (i) and (iii) will be phase-shifted by π. Note, that instead of a forward spin-flip following the free precession an identical pulse can also be used flipping the polarization backward by $-\theta_1$.

Systematic effects caused by implementation of rotating (or oscillating) electric fields can be accounted for by monitoring the signal of a droplet where $\varphi = 0$, since there will be no effect due to an EDM ($\boldsymbol{P} \times \boldsymbol{E} = 0$).

Since individually rotating electric fields are implemented for each droplet a variety of effects not only regarding dynamic electric fields can be studied. The phase of the applied field to the (monitored) polarization can be adjusted anytime during a measurement allowing e.g. online field reversal or switching reference droplets. Further effects to investigate are particularly related to cross-talk between droplets. Changing the geometry (distance, size, quantity) the coupling strength can be strongly varied and potentially also lead to new EDM measurement schemes similar to the amplification of gradients due to non-linear effects [127].

The isotope ^{129}Xe is the ideal candidate for an EDM search with our novel method, as in liquid it has a high dielectric strength of 400 kV/cm [145] and long transverse spin-relaxation times $T_2 > 1000\,\mathrm{s}$ were observed previously [127]. Strong non-linear effects at tip angles $> 35°$ in large ($\approx 1\,\mathrm{cm}^3$) liquid ^{129}Xe samples have been reported in [127], which cause rapid depolarization due to amplification of external magnetic field gradients. In our approach the sample size, the magnetization and the expected ambient gradients are each an order of magnitude smaller. Non-linear effects and their implications need to be studied individually. However, the sensitivity to an EDM is similar for smaller tip angles $< 35°$, for which even prolonged relaxation times were observed.

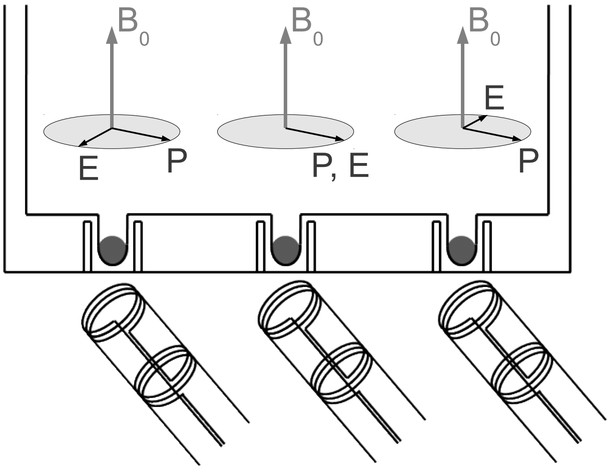

Fig. 19: Pickup coils mounted below three ^{129}Xe droplets with an example of different electric field configurations: (i) $+\boldsymbol{E} \perp \boldsymbol{P}$, (ii) $\boldsymbol{E} \parallel \boldsymbol{P}$ and (iii) $-\boldsymbol{E} \perp \boldsymbol{P}$. The filled grey circles represent the sub-millimeter liquid ^{129}Xe samples enclosed in a spheric cavity by means of a pressure actuated piston. The droplets are surrounded by eight electrodes, cf. Fig. 20 (b).

Currently the EDM experiment is designated to accommodate an array of three enclosed sub-millimeter droplets of highly polarized liquid ^{129}Xe. Implementing each with different electric field configurations allows for thorough studies of the qualitatively new systematic effects. The small size of the individual experiments in principal even allows for an upgrade with more droplets.

5.1.2 Experimental realization

Employing a high-density liquid sample reduces the volume by a factor $\approx 10^4$ (compared to gas-phase EDM searches) while even enhancing the precession signal. Consequently it faciliates generation of highly homogeneous constant B_0 and oscillating B_1 fields in the sample volume. The samples are placed inside a cylindrical multi-layer magnetic shield in the center of a field-compensation coil system to minimize existent external fields and gradients. Magnetic fields are generated by coils of much larger size ($\approx 20\,\mathrm{cm}$) printed on flexible circuit boards, which assures high geometric accuracy and makes possible implementation of correction coils of (nearly) arbitrary shape. Simulations of cylindrical cosine theta coils with correction currents show that relative homogeneities of $10^{-5} - 10^{-6}$ are accessible. Small sample volumes ($\approx 1\,\mathrm{mm}$) also allow high electric fields using moderate potentials ($\approx 10\,\mathrm{kV}$). In a magnetically shielded environment a low magnetic holding field of ($\approx \mu$T), where $\omega_\mathrm{L} \approx 10$Hz, permits application of time-varying (rotating or oscillating) electric fields.
Large amounts of hyper-polarized ^{129}Xe can be produced in the gas-phase via spin-exchange optical pumping (SEOP) [82] and subsequent accumulation in a cold-trap [95]. To prepare the sample xenon gas is polarized in a SEOP flow-through setup and accumulated in a cold trap at liquid nitrogen temperatures in magnetic fields of 250 mT,

where longitudinal spin-relaxation is slow [117]. The maximum polarization of 400 mbar of natural xenon in a 20 cm^3 cell determined by calibration with protons is $\approx$ 20% and builds up in about 100 s. After accumulation for about 20 min ^{129}Xe is transfered through PFA and glass tubing to a glass tube of 20 mm diameter mounted in the EDM setup. A micro-structured plate ("EDM chip") of 35 mm diameter and 2.5 mm thickness made of machinable ceramics or quartz is attached to the glass tube, where the polarized gas liquefies at $\approx 163\,\mathrm{K}$. The "EDM chip" is micro-structured to provide three cylindrical or (preferably) spherical cavities, aligned in a line and separated by about 5 mm. A pressure actuated piston is used to encapsulate separated samples of liquified xenon in the embedded microstructures. Depolarization effects in this volume can be minimized by appropriate surface treatment and coatings [107, 108]. The temperature of the "EDM chip" can be controlled between 90 K to 250 K by means of helium gas, which enables us to freeze, liquefy and evaporate xenon ($161.4\,\mathrm{K} < T_{\mathrm{liquid}} < 165.2\,\mathrm{K}$).
The precession of $\boldsymbol{P}$ around the $\boldsymbol{B}_0$ axis in each experiment is detected by superconducting gradiometer pickup coils mounted just below the downside of the "EDM chip" and tilted at a large angle of 45° to also be sensitive to transverse fields. The gradiometers are made of twelve turns of niobium wire ($T_c = 9.2\,\mathrm{K}$) on a 2 mm diameter sapphire rod. Magnetic induction is measured by connecting the coils to highly sensitive LTc SQUID current sensors. Both the SQUID current sensors and the niobium pickup coils are thermally anchored to the 4.2 K stage of a dry helium cooling machine. A vacuum gap of $\approx 1\,\mathrm{mm}$ maintains thermal insulation and an aluminum coating on the downside of the "EDM chip" reduces heat radiation from the "EDM chip". The SQUID sensors have a design noise level of $< 2\,\mathrm{fT}/\sqrt{\mathrm{Hz}}$ at frequencies above 3 Hz. The Larmor frequency for the EDM measurement can be chosen accordingly to minimize noise mostly caused by mechanical vibrations and the power line frequency ($\gamma_{\mathrm{Xe}} = 11.777\,\mathrm{Hz}/\mu\mathrm{T}$).

Static electric field sensitivity

The primary goal of our EDM search is to introduce the novel method of rotating electric fields and investigation of the expected new systematic effects to determine the ultimate potential of this approach. On the way the setup can be easily adapted to employ the standard EDM measurement technique with a static electric field applied in parallel to the magnetic field. This can be accomplished by metallization of the piston used for droplet enclosure. This layer in conjunction with the aluminum layer on the downside of the "EDM chip" can be used to apply potentials of order 10-15 kV over 1-2 mm. Hence, a liquid xenon sample (whether enclosed or not) can be exposed to electric fields of order 50 kV/cm.
Most dominantly magnetic field stability and leakage currents limit "Ramsey-type" EDM searches. Highly stable, low-noise magnetic fields of $\mathcal{O}(\mu\mathrm{T})$ can be generated by ultra-low noise current sources [131, 146]. Leakage currents of order 0.5 pA [67] and 20 pA [71] are considerably limiting the EDM searches using ^{199}Hg ($\approx 10^{-30}$ ecm) and of ^{129}Xe ($\approx 10^{-27}$ ecm), respectively. In an effort for a "Ramsey-type" EDM search with liquid xenon direct leakage currents through the sample and the high-resistivity "EDM chip" ($> 10^{16}\,\Omega\mathrm{cm}$) can be neglected. The top electrode on the piston has no direct contact

to the glass tube and the glass is at low temperatures ($< 200\,\mathrm{K}$). Leakage currents following helical paths along the inner glass wall are expected to be extremely small. In the case of a one-turn helical current of 0.01 pA ($d = 18\,\mathrm{mm}$) along the inner wall of the glass tube, the magnetic field ($\approx 0.7 \times 10^{-18}\,\mathrm{T}$) alternating with the electric field of 50 kV/cm would mimic an EDM of order $10^{-31}\,e\mathrm{cm}$ (cf. Eqn. (4.2)).

For false EDM effects due to accumulation of geometric phases [147] using a liquid sample is particularly advantageous over gas phase EDM searches. Diffusion in the liquid is many orders of magnitude slower resulting in a short mean free path and slow diffusive motion of order $\approx 100\,\mu\mathrm{m/s}$ [124]. Transverse motional magnetic fields $B_\mathrm{m} = c^{-2}\boldsymbol{v} \times \boldsymbol{E}$ contribute to geometric phase induced false effects but are suppressed by many orders of magnitude in a liquid sample[30].

The statistical sensitivity (Eqn. (4.7)) of this "Ramsey-type" EDM search gives $d \approx 1.2 \times 10^{-31}\,e\mathrm{cm}$ in a single measurement.

Rotating electric field sensitivity

In a configuration with time-varying electric fields of $50\,\frac{\mathrm{kV}}{\mathrm{cm}}$ and a spin precession time $\mathrm{T}_2 \approx 1000\,\mathrm{s}$ an EDM of $d = 1.4 \times 10^{-30}\,e\mathrm{cm}$ gives rise to an accumulated angle during free precession of

$$\theta_\mathrm{d} = \frac{dE\tau}{\hbar} \approx 1 \times 10^{-7}. \tag{5.2}$$

Keep in mind, that the angle due to the precession of the EDM in the electric field of 50 kV/cm accumulates at a rate of only $\approx 10^{-10}\,\mathrm{s}^{-1}$, which is the figure of merit used in the systematics discussion.

Arbitrarily assuming a droplet diameter of 1 mm containing about 8×10^{18} atoms and a polarization of 10% the precession signal amplitude at 1 mm distance of the pickup loops at 45° is $\approx 220\,\mathrm{nT}$, cf. Eqn. (6.2). The difference of signals from experiments (*i*) and (*iii*) (Fig. 19) arising from the accumulated angle θ_d gives the EDM signal size $\approx 40\,\mathrm{fT}$. With the intrinsic noise level of the SQUID current sensors of $2\,\mathrm{fT}/\sqrt{\mathrm{Hz}}$ we get a signal-to-noise ratio on the order of 10. Statistically the experiment can be repeated 10^4 times in ≈ 150 days and potentially improve the statistical sensitivity to $\lesssim 10^{-32}\,e\mathrm{cm}$.

However many new systematics of the rotating electric field method need to be well studied and understood in detail. In the following section I will discuss these systematic effects and give order of magnitude estimates of their relevance.

5.1.3 New systematic effects due to rotating electric fields

On account of the liquid sample effects of motional magnetic fields are strongly suppressed. The electric field is aligned normal to the B_0 direction, hence systematic effects concerning magnetic field stability are not limiting the sensitivity as severely as in "conventional" EDM experiments with $\boldsymbol{E} \parallel \boldsymbol{B}_0$. Although the tip angle θ_1 is generally arbitrary the droplet (*ii*) (Fig. 19) can be best used as a reference in the special case of $\theta_1 = \frac{\pi}{2}$. The signal will not show any rotation out of the precession plane due to

---

[30] The motional magnetic field contributes transverse components of order $c^{-2} \cdot 100 \times 10^{-6}\,\mathrm{m/s} \cdot 50\,\mathrm{kV/cm} \approx 5\,\mathrm{fT}$.

an EDM when $E \neq 0$ is co-rotating with the polarization vector ($\boldsymbol{P} \times \boldsymbol{E} = 0$). Not yet studied systematic effects in regard to the time-varying electric field can be thoroughly investigated with the reference experiment. In principal any (or several) of the three droplets can be used as references by adjusting the electric field phases on-line during free precession, which offers a very versatile tool for a systematics survey. The following discussion of expected systematic effects will focus on effects introduced by the time-varying electric fields and assume a tip angle of $\pi/2$.

Motional magnetic fields

In the liquid phase the ^{129}Xe atoms are moving with velocities on the order of self-diffusion ($v \approx 100\,\mu$m/s) and therefore experience a motional magnetic field of

$$\boldsymbol{B}_\mathrm{m} = -\frac{1}{c^2}\boldsymbol{v} \times \boldsymbol{E}. \tag{5.3}$$

The radial component v_r of the atomic motion perpendicular to $\boldsymbol{B}_0$ effectively causes modulation of the B_0 field and hence the precession frequency by $\delta\omega_\mathrm{L} = \pm\gamma_\mathrm{Xe}c^{-2}v_\mathrm{r}E$. For $E = 50\,$kV/cm and the velocity of self diffusion this effect accounts for a modulation of $\delta B_0 \approx 5\,$fT. The effect causes a frequency broadening on the 10^{-9} level for a 1μT holding field but no false EDM ($\omega_\mathrm{L} \perp \omega_\mathrm{d}$).
Atoms moving with an axial component v_z experience a motional magnetic field $\boldsymbol{B}_\mathrm{m,r}$ along the polarization vector ($\boldsymbol{v} \times \boldsymbol{E} \parallel \boldsymbol{P}$), therefore motion along the B_0 axis yields no effect $\boldsymbol{P} \times \boldsymbol{B}_\mathrm{m,r} = 0$. These considerations assume a perfectly aligned electric field with an exact phase angle of $\varphi = \pi/2$ to the polarization vector. Let's see what an electric field misalignment implicates.

Electric field misalignment

First of all consider the case where the electric field is misaligned in the precession plane and the phase angle between $\boldsymbol{E}$ and $\boldsymbol{P}$ is $\varphi = \frac{\pi}{2} \pm \delta\varphi$ (cf. Fig. 20). For atoms moving radially to $\boldsymbol{B}_0$ with $\boldsymbol{v}_r$ this only causes a negligible change in the mentioned modulation of $\boldsymbol{B}_0$ ($\boldsymbol{v}_r \times \boldsymbol{E} \parallel \boldsymbol{B}_0$).
Atoms moving in vertical direction in an electric field of $E = 50\,$kV/cm with velocity $v_z \approx 100\,\mu$m/s experience a motional magnetic field of order 5 fT. For a misalignment of the phase angle $\delta\varphi = 0.02$ ($\approx 1°$) this radial field is not parallel to $\boldsymbol{P}$ and $\boldsymbol{P} \times \boldsymbol{B}_\mathrm{m,r} \neq 0$. The nuclear spin precesses slowly about the motional field component of size 0.1 fT accumulating a false EDM angle at a rate of

$$2\pi\gamma_\mathrm{Xe} \cdot 0.02 \cdot B_\mathrm{m,r} \approx 10^{-8}\,\mathrm{s}^{-1}. \tag{5.4}$$

However, the time between collisions in the liquid is on the order of $\tau = (\sigma n v)^{-1} \approx 10^{-5}\,$s, where the cross-section σ is taken as roughly the square of the van-der-Waals radius $r^2 = (216\,\mathrm{pm})^2$ and the number density $n \approx 10^{22}\,\mathrm{cm}^{-3}$. Between collisions an angle of $\theta_d \approx 10^{-13}$ can be accumulated corresponding to $d \approx 10^{-36}\,e$cm. Additionally, to first order the effect is expected to cancel, as electric field rotation is much faster compared to atomic diffusion.

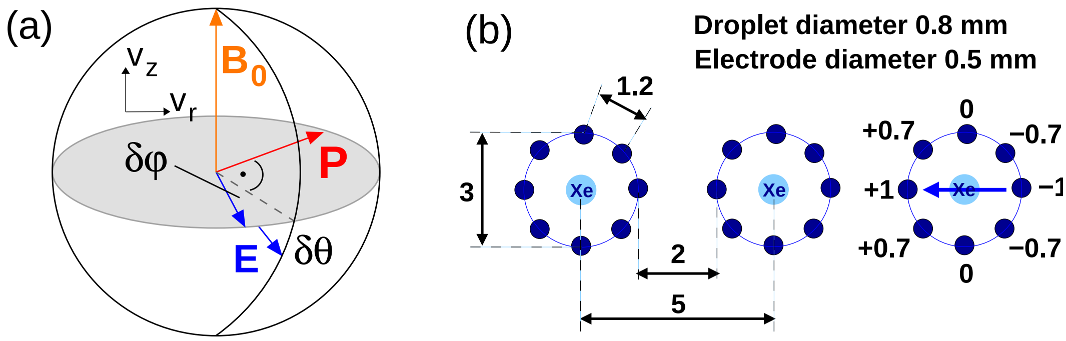

Fig. 20: (a) Misalignment of the electric field $\boldsymbol{E}$ in phase angle $\delta\varphi$ to the polarization vector $\boldsymbol{P}$ and in azimuthal angle $\delta\theta$ to the Larmor precession plane. (b) Example of the droplet and electrode geometry with measures in mm. The electrodes surrounding the right droplet indicate relative voltages applied and the electric field (blue arrow).

A similar effect is caused by a misalignment of the $\boldsymbol{E}$-field precession plane to the Larmor precession plane, e.g. $\delta\theta \neq 0$ (cf. Fig. 20). In this case the radial velocity component v_r generates a radial field $B_{\mathrm{m,r}} \approx 0.1\,\mathrm{fT}$ for a misalignment of $\delta\theta = 1°$. The cross product of a out-of-plane misaligned $\boldsymbol{E}$ and the vertical component of atomic motion only changes the magnitude but not orientation of the motional field, still $\boldsymbol{B}_{\mathrm{m,z}} || \boldsymbol{P}$ and $\boldsymbol{P} \times \boldsymbol{B}_{\mathrm{m,z}} = 0$. The misalignment of $\boldsymbol{E}$ can be well tested with the reference experiment where $\boldsymbol{P}$ is supposed to be parallel to $\boldsymbol{E}$. In general all false EDM effects due to atomic motion cancel to first order as a result of fast electric field rotation compared to diffusion.

Circular leakage currents

Leakage currents are predominantly limiting the sensitivity in previous EDM searches on diamagnetic atoms. The currents between high-voltage electrodes are minimized by the choice of materials with high volume resistivity and dielectric strength. Suitable for our approach are for example Macor ceramics or fused quartz with room temperature resistivity and dielectric strength of $> 10^{16}\,\Omega\mathrm{cm}$ and $> 100\,\mathrm{kV/cm}$, respectively.
Nevertheless, an effective ring current is created by currents between adjacent electrodes, which have a DC and a AC contribution. To generate an electric field of $50\,\mathrm{kV/cm}$ over 3 mm distance a voltage of 15 kV is needed across opposite electrodes. Hence the maximum potential difference of $0.7 \cdot 7.5\,\mathrm{kV}$ determines the maximum leakage current between adjacent electrodes. With the dimensions of Fig. 20 the DC and AC contributions for currents between neighbouring electrodes of height 1 mm are

$$\begin{aligned} I_{\mathrm{DC}}^{\mathrm{circ}} &= \frac{0.7 \cdot 7.5\,\mathrm{kV} \cdot 0.5\,\mathrm{mm}^2}{10^{16}\,\Omega\mathrm{cm} \cdot 1.2\,\mathrm{mm}} \approx 0.02\,\mathrm{pA} \\ I_{\mathrm{AC}}^{\mathrm{circ}} &= 0.7 \cdot 7.5\,\mathrm{kV} \cdot 2\pi \cdot 10\,\mathrm{Hz} \cdot \frac{5 \cdot \epsilon_0 \cdot 0.5\,\mathrm{mm}^2}{1.2\,\mathrm{mm}} \approx 6\,\mathrm{nA}. \end{aligned} \tag{5.5}$$

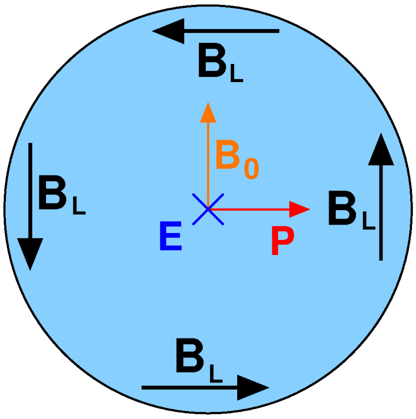

Fig. 21: Leakage currents between opposite electrodes generate a magnetic field $\boldsymbol{B}_{\mathrm{L}}$ transverse to the rotating electric field. The field is strongest at the droplet fringe and linearly decreases to zero in the center.

These circulating currents due to the potentials oscillating at the Larmor frequency generate a magnetic field $B_{\mathrm{L}} = \mu_0 I/2r$ in B_0 direction of order $\approx 3\,\mathrm{pT}$ with a very small contribution from the DC component $\approx 10^{-17}\,\mathrm{T}$. For $B_0 = 1\,\mu\mathrm{T}$ this modulates ω_{L} on a 10^{-6} level.

Leakage currents between opposite electrodes

The maximum current between electrodes of 1 mm height and 0.5 mm width at a potential difference of 15 kV over 3 mm separation (cf. Fig. 20) is

$$I_{\mathrm{DC}}^{\mathrm{opp}} = \frac{15\,\mathrm{kV}\cdot 0.5\,\mathrm{mm}^2}{10^{16}\,\Omega\mathrm{cm}\cdot 3\,\mathrm{mm}} \approx 0.03\,\mathrm{pA}. \tag{5.6}$$

Assume the current I^{tot} flows through the droplet cross-section with a constant current density. Currents on the outer fringe of the droplet don't generate magnetic fields inside the fringe. The current flowing inside the cross-section of radius r is $I^{\mathrm{tot}}\cdot(r^2/R^2)$ with the droplet radius R. This current creates a magnetic field zero in the center and linearly rising to the droplet fringe as

$$B_{\mathrm{L}}(r) = \frac{\mu_0}{2\pi}\cdot I^{\mathrm{tot}}\cdot\frac{r}{R^2}. \tag{5.7}$$

Hence the maximum field generated by a DC current at the fringe of the droplet is of order $0.01\,\mathrm{fT}$ decreasing linearly to zero in the droplet center.
Now consider the AC contribution. The capacitance of two opposed electrodes approximated by a plate capacitor is

$$C = \epsilon\epsilon_0\frac{A}{d} \approx 5\epsilon_0\frac{0.5\,\mathrm{mm}^2}{3\,\mathrm{mm}} \approx 7\,\mathrm{fF}. \tag{5.8}$$

Hence the AC current between opposing electrodes gives

$$I_{\mathrm{AC}}^{\mathrm{opp}} = 15\,\mathrm{kV}\cdot 2\pi\cdot 10\,\mathrm{Hz}\cdot 7\,\mathrm{fF} \approx 7\,\mathrm{nA} \tag{5.9}$$

and generates a magnetic field (Eqn. (5.7)) of order $B_\mathrm{L} \approx 3\,\mathrm{pT}$ at the droplet fringe, decreasing linearly to zero at the center. The gradients $\partial B_{x,y}/\partial z$ and $\partial B_z/\partial x, y$ introduced by the radial fields are of order $10\,\mathrm{nT/m}$ and are not limiting the anticipated observation time of 1000 s.

What are the consequences of the leakage currents between opposite electrodes?
Components of $\boldsymbol{B}_\mathrm{L}$ that are parallel to $\boldsymbol{P}$ have no effect ($\boldsymbol{B}_\mathrm{L} \times \boldsymbol{P} = 0$). But, they account for a false EDM if the angle between $\boldsymbol{E}$ and $\boldsymbol{P}$ deviates from $\pi/2$, similar to the case of motional fields in a misaligned $\boldsymbol{E}$. Note that the effect is of opposite sign at the top and bottom of a droplet (cf. Fig. 21).
Assume a misalignment of $\delta\varphi \approx 0.02$ ($\approx 1°$). Then the opposed rotations of spins at top and bottom that locally mimic an EDM effect occur at rates $1.5 \times 10^{-11}\,\mathrm{s}^{-1}$ and $4 \times 10^{-6}\,\mathrm{s}^{-1}$ for DC and effective AC leakage currents, respectively. Particularly the latter effect is of concern as it is much faster than the accumulation rate of θ_d.
The atoms take about eight seconds to diffuse from one side of the droplet to the opposing side. Many will spend a significant amount of time in the top or bottom half sphere where this false EDM effect can accumulate at the above rates. A pickup coil placed 1.5 mm below the droplet will mostly see the bottom half sphere (only $\approx 20\%$ of the top half-sphere contribute to the signal) so only weak cancellation is expected. In a long measurement run of thousand seconds some averaging is expected since then the atoms will cross the droplet volume about 100 times. In that case the false EDM phase angle due to the leakage current can only accumulate for about 5 s (compared to θ_d accumlating for 1000 s). The false EDM signal is suppressed by about two orders of magnitude, but for the above misalignment of $\delta\varphi \approx 1°$ this systematic limits the sensitivity to $\approx 3 \times 10^{-28}\,e\mathrm{cm}$.
However, this dominant systematic effect can be tested with the reference experiment, where it is maximal ($\boldsymbol{E} || \boldsymbol{P} \perp \boldsymbol{B}_\mathrm{L}$). If well understood it can probably be accounted for in the analysis. Also deliberate misalignment of $\boldsymbol{E}$ will help to understand and quantify it. With diffusive suppression and a phase angle $\delta\varphi$ accurate to 0.01° the false EDM phase limits a measurement to $d \approx 10^{-30}\,e\mathrm{cm}$.
Under these assumptions the false EDM phase due to the DC current with a rate of $10^{-11}\,\mathrm{s}^{-1}$ limits the EDM sensitivity to $d \approx 10^{-35}\,e\mathrm{cm}$.
The components perpendicular to $\boldsymbol{P}$ change the holding field strength and therefore the precession frequency directly. DC and AC currents cause a $B_0(1\,\mu\mathrm{T})$ field modulation on the 10^{-11} and 10^{-5} level, respectively. If the rotation frequency of the co-rotating electric field is static at ω_L the phase angle between $\boldsymbol{P}$ and $\boldsymbol{E}$ is modulated with a maximum amplitude of $\approx 10^{-5}$ due to the AC current. The modulation in the left and right half-sphere of the droplet is phase-shifted by π and the effect is to first order suppressed by cancellation in the pickup loop below the droplet.

Crosstalk between droplets

Another systematic effect unique for our EDM experiment is cross-talk between the three droplets each representing a rotating dipole field. For the polarization precessing perpendicular to B_0 a neighbouring droplet sees a magnetic field of order 10^{-11} T oscillating with a frequency of $2\omega_\mathrm{L}$, if the droplets are along a line perpendicular to B_0. This results in an oscillating angle θ with amplitude depending on the tip angle. However, if B_0 points along the connecting line of the droplets the cross-talk is zero, since dipolar fields generated by one droplet are parallel to the polarization vector of the neighbouring droplet. These effects can be well studied, but suggest an alignment of the holding field along the droplets to minimize the oscillation amplitude in θ. Details on these effects have been studied in [148].

Interesting effects arise, when B_0 is parallel to the connecting line of the droplets, but inhomogeneous. The presence of the gradient leads to slightly different precession frequencies and polarization vectors are no longer aligned. In that case the polarization vectors of the droplets start precession around the dipolar field of the neighbour droplet, which results in oscillations phase-shifted by π in both θ and ϕ. The amplitude of these oscillations depend on the strength of the gradient and distance of the droplets, while the frequency is determined by the generated dipolar fields, e.g. the magnetization. However, droplet distance also affects the magnetic field difference due to the gradient. The described small precession around each other might offer another novel method to look for an EDM. Instead of a gradient, the precession frequencies of both droplets could be misaligned by a coupling of an EDM to applied opposite electric fields parallel to the B_0 direction. This competes with the same effect due to magnetic field gradients. However, when using small tip angles the effect from the magnetic gradients is suppressed. Moreover, the amplitude of the induced precession grows with droplet distance. Details on the simulated results of these effects are found in [148].

Summary of systematics

Tab. 5.1 shows a summary of the discussed systematic effects. Note that some of the estimates are rather conservative, e.g. the resistivity is taken at room temperature and is expected to be about two orders of magnitude higher at the melting point of xenon.

The most severe systematic is a result from the AC currents due to the rotating (or oscillating) electric field. The only strategy for this false EDM phase is an extremely accurate alignment of the $\pi/2$ phase between $\boldsymbol{E}$ and $\boldsymbol{P}$. For the fundamental sensitivity level of 10^{-30} $e$cm this needs to be accomplished at a level $< 0.01°$. The reference droplet where this effect is maximal and studies with various deliberate misalignments can be used to account for this effect in the analysis.

Several effects cause a modulation or variation of the B_0 field. In general this is not causing significant effects on an EDM signal, but frequency shifts and modulations of 0.1 mHz to 0.1 nHz. Predominantly this induces misalignment of the co-rotating electric field vector if the phase is not adjusted.

Source	Magn. field [T]	d [$e$cm]
Electric field		
$v_\mathrm{r} \times E$	$\lvert\delta B_0\rvert \lesssim 5 \times 10^{-15}$	
$v_\mathrm{z} \times E$	$B_{\mathrm{m,r}} \parallel P$	
Motional fields $\boldsymbol{B}_\mathrm{m}$ due to electric field misalignment		
$v_\mathrm{r} \times E\ (\delta\varphi \neq 0)$	$\lvert\delta B_0\rvert \lesssim 5 \times 10^{-15}$	-
$v_\mathrm{z} \times E\ (\delta\varphi = 1^\circ)$	$B_{\mathrm{m,z}} \approx 10^{-16}$	10^{-36}
$v_\mathrm{r} \times E\ (\delta\theta = 1^\circ)$	$B_{\mathrm{m,r}} \approx 10^{-16}$	10^{-36}
$v_\mathrm{z} \times E\ (\delta\theta \neq 0)$	$\delta B_{\mathrm{m,z}} \parallel P$	-
Leakage currents generating $\boldsymbol{B}_\mathrm{L}$		
DC currents $\boldsymbol{B}_\mathrm{L} \perp \boldsymbol{P}$	$\lvert\delta B_0\rvert \lesssim 10^{-17}$	
DC currents $\boldsymbol{B}_\mathrm{L} \vert\vert \boldsymbol{P}\ (\delta\varphi = 1^\circ)$	$B_\mathrm{r} \approx 10^{-19}$	10^{-35}
AC currents $\boldsymbol{B}_\mathrm{L} \perp \boldsymbol{P}$	$\lvert\delta B_0\rvert \lesssim 10^{-11}$	-
AC currents $\boldsymbol{B}_\mathrm{L} \vert\vert \boldsymbol{P}\ (\delta\varphi = 0.01^\circ)$	$B_\mathrm{r} \approx 3 \times 10^{-12}$	10^{-30}
Circular leakage currents		
DC contribution	$\lvert\delta B_0\rvert \approx 10^{-17}$	-
AC contribution $(1/\omega C)$	$\lvert\delta B_0\rvert \approx 10^{-11}$	-

Tab. 5.1: Systematic effects due to co-rotating electric fields in the liquid xenon EDM experiment. The given values are for a holding field $B_0 = 1\,\mu\mathrm{T}$, hence $\omega_\mathrm{L}/2\pi \approx 10\,\mathrm{Hz}$ and an electric field of $E = 50\,\mathrm{kV/cm}$. Geometric dimensions as in Fig. 20.

An on-line adjustment can be implemented in the experiment as the free precession signal is monitored and available to be used as a feedback signal.

5.1.4 Conclusion

The liquid xenon EDM experiment is based on a new approach with several sub-millimeter liquid ^{129}Xe samples and electric fields rotating in the Larmor precession plane. This method potentially improves current EDM limits by several orders of magnitude. An implementation of this novel method inside a cryogen-free SQUID cryostat described in the following is underway at the TU München. The introduced systematic effects new to EDM searches arising from the time-varying nature of the electric field offer a rich field of studies to quantify their significance. The systematics discussed in this scope can be controlled on a level close to the fundamental sensitivity of 5×10^{-30} ecm. Multiple simultaneous experiments employing different field configurations allow for in detail understanding of systematic effects, which is different from all other EDM experiments. Particular focus needs to be put on errors in the phase angle between the electric field and the precessing polarization vector. The small liquid samples offer straightforward scaling to many simultaneous experiments.

Still, by implementing electrodes above and below the liquid ^{129}Xe droplets the setup allows for a “conventional” EDM experiment with $E \parallel B_0$ giving similar statistic sensitivity, but different systematic effects.

5.2 A cryogen-free SQUID cryostat with variable sample temperature

Abstract Operation of LTc SQUIDs with external pickup coils as highly sensitive current sensors is demonstrated in a cryogen-free environment allowing for unattended long-term operation. Multiple external superconducting pickup coils of two millimeter diameter detect local magnetic flux changes with small spacial resolution. The bottom end of a glass tube is mounted close to the pickup coils and is used to fill gaseous samples that can be studied in a temperature range between 90 K to 165 K at a noise floor density of $< 144\,\mathrm{fT}/\sqrt{\mathrm{Hz}}$ above 50 Hz. Mixing of a controlled flow of helium gas at the coldhead allows for sample temperature control.

5.2.1 Introduction

For the detection and investigation of magnetic sample structure superconducting quantum interference devices (SQUIDs) are of great interest, since they provide extremely high sensitivity to relative changes of magnetic flux well below 10^{-15} T. With the availability of superconductors with critical temperatures $T_c > 77\,\mathrm{K}$ SQUIDs can be operated even in liquid nitrogen. Nevertheless, high-T_c (HTc) SQUIDs have disadvantages over devices made of low critical temperature superconductors, e.g. LTc SQUIDs. HTc SQUIDS show significantly higher white and 1/f noise and ,due to their short coherence length, can only be fabricated in one-dimensional structures. To fully use the superior noise performance of LTc SQUIDs they need to be operated at or below half of the transition temperature (cf. [135]). Hence, for widely used niobium the operating temperature should be below 4.6 K. A bath of liquid helium (LHe) at 4.2 K provides perfect conditions for SQUID sensors of the LTc type. But, this experimental approach brings along challenges in dewar construction and operational drawbacks for highly sensitive long-term measurements in low magnetic fields. In particular, measurements of spin-precession require not only non-metallic (low magnetic noise) but also non-magnetic (small magnetic gradient) environments. These types of measurements with SQUIDs emerged in liquid helium require magnetically shielded rooms of significant size.

Measurements at a short distance ($< 1\,\mathrm{mm}$) of the superconducting pickup coils to samples at much higher temperature is experimentally very difficult. Hence, a liquid helium bath for the SQUID sensor is often combined with a thermal connection to an external pickup coil.. In the “SQUID microscopes” usually a high spatial resolution is aspired for magnetic scanning of samples. As an example Baudenbacher et al. [149] demonstrated a “SQUID microscope” with a pickup loop distance on the order of 100 μm to a room-temperature sample. In their dewar with 24 h hold time they also introduced a liquid nitrogen shield which complicates operation and refilling even further. The noise level achieved is on the order of $300\,\mathrm{fT}/\sqrt{\mathrm{Hz}}$.

In this paper we demonstrate operation of LTc SQUIDs cooled by a closed-cycle cooling machine (Gifford-MacMahon type) without the need of cryogens in the SQUID setup, while a sample of variable temperature can be studied. The setup enables unattended long-term operation of SQUIDs kept in vacuum, while a magnetic flux noise density of

49 fT/$\sqrt{\text{Hz}}$ and 165 fT/$\sqrt{\text{Hz}}$ is demonstrated for gradiometer and magnetometer pickup coils, respectively. These levels of the noise floor were measured in the frequency range above 50 Hz.

A drawback of using a coldhead and conductive cooling is certainly the vibrations caused by the moving parts and low frequency noise due to inevitable use of metallic parts in the setup. Several noise peaks are detected in the setup that are mostly related to these effects. However, this strongly depends on the purpose of the system and low frequency noise might be less of a concern.

In the setup highly sensitive measurements of magnetic flux changes can be taken out in a homogeneous small residual magnetic field without the need of large helium dewars or even magnetically shielded rooms. The non-magnetic vacuum and cryogenic part of the SQUID system is fed through a hole of less than 80 mm diameter in the magnetic shielding.

The presented SQUID cryostat is intended to be used for fundamental measurements using ultra low-field nuclear magnetic resonance (NMR) in magnetic fields of the order of $0.1 - 10\ \mu$T. Of special interest is a measurement of the electric dipole moment (EDM) of the isotope ^{129}Xe. A non-zero EDM is a strong manifestation of physics beyond the standard model violating fundamental symmetries [31, 33]. Furthermore, studies of solid and liquid polarized xenon in very low fields as well as a search of (more exotic) spin-matter couplings are anticipated.

5.2.2 Apparatus

Overview

The apparatus is mounted in a vertically hanging position with the coldhead on top. Two mechanically independent holding structures made of massive aluminum profiles carry both the vacuum vessel housing the coldhead in a height of 2.5 m and fix the non-magnetic vacuum system. Rectangular coils with 2 m side length are mounted for each spacial axis to compensate the earth's magnetic field and external gradient fields, but are not yet used. The whole setup is enclosed by a 3.5 m x 3.5 m x 3.5 m styrofoam cube for thermal stabilization of the magnetic shield and damping of external vibrations. Most electrical devices and the compressor unit for the coldhead are placed at a distance of several meters outside the styrofoam housing.

Electrical radio-frequency shielding is provided by the grounded vacuum system. Four layers of μ-metal (a high magnetic permeability nickel-iron alloy) enclose the vacuum system (Fig. 17) for magnetic shielding. The layers are made of top caps fixed on the top vacuum lid and cylinders with closed bottom ends which have a thickness of 1 mm but the second layer is of 2 mm thickness. The magnetically shielded volume for ultra low-field experiments is about 1 m below the coldhead and of dimensions of 560 mm height and 230 mm diameter. The μ-metal shield only has several small holes on the cylinder surface (5 mm and 8 mm diameter) and the center of the cylinder bottom (20 mm diameter). A 80 mm hole in the top caps is needed to feed-through the vacuum vessel including wiring, thermal shield and connection to the 4 K stage of the coldhead.

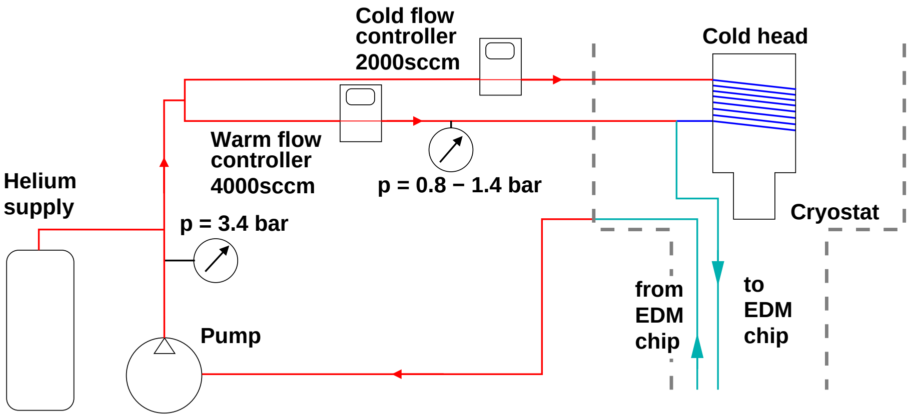

Fig. 22: Scheme of the closed-cycle cooling system for the "EDM chip". A helium supply bottle compensates for helium losses to the vacuum and keeps the pressure at 3.4 bar. Two mass flow controllers of 2000 sccm and 4000 sccm maximum flow control cold ($\sim$ 50K) and warm ($\sim$ 300K) helium flows mixed and diverted to the "EDM chip". A membrane pump maintains a pressure difference of about 2 bars.

Cryogenics

Cooling is provided by a two-stage closed-cylce cryocooler of the Gifford-McMahon type (Sumitomo RDK-415D) with a cooling power of 35 W at 50 K and 1.5 W at 4.2 K. In the central axis a massive copper (E-Cu) rod of 15 mm diameter is thermally anchored to the 2nd stage of the coldhead. In the bottom third of it's length half of the rod is milled off to provide some space for wiring running inbetween the rod and the thermal shield.

The thermal shield anchored at the first stage of the coldhead completely encloses the inner rod with a copper (E-Cu) tube of 45 mm outer diameter and 5 mm thickness. At the end a small aluminum shield and an aluminum cylinder of 197 mm height and 142 mm diameter extend the thermal shield. The cylinder is hanging freely to damp vibrations of metallic parts. This is accomplished by using eight copper straps of 80 mm length as thermal connection.

Three SQUID current sensors and the pickup coil sapphire rods are attached to a copper plate, which is cooled through the central rod and also anchored with flexible copper braides.

The sample stage and sample temperature control

For magnetic flux detection the pickup loops can be positioned as close as 1 mm below the bottom of a plate, which is closing the bottom head end of a sample glass tube. This glass tube has 18 mm inner diameter with 1.8 mm wall thickness and can accommodate gaseous, liquid or solid samples, see Fig. 23 (a). The sample volume is separated from the isolation vacuum and can be accessed via a 1/8″ PFA tube for filling or depleting a gaseous or liquid sample substance from outside the magnetic shield. The "EDM chip" material (e.g. Macor, quartz,...) is chosen for machinability, spin-relaxation properties

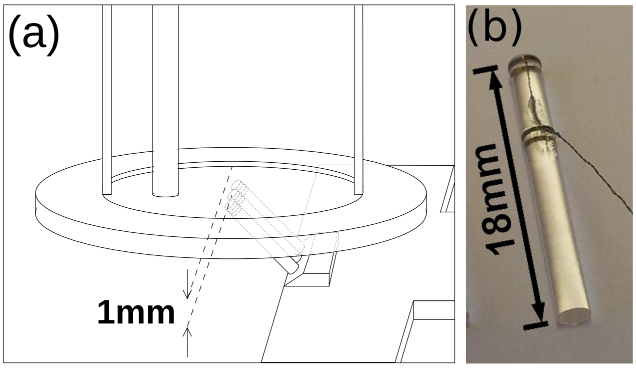

Fig. 23: (a) The lower end of the sample glass tube with a ceramics or quartz plate attached ("EDM chip"). The three pickup coils mounted at an angle of 45° are just 1 mm below. The coils are made of 12 total turns in either magnetometer or gradiometer configuration. (b) Picture of a gradiometer pickup coil made of 50μm thick niobium wire on 2 mm diameter sapphire of 18 mm length. The gradiometer has six turns at the head end and six counter-turns in about 5 mm distance and meets the input inductance of the SQUID current sensors of 400 nH to $< 25\%$.

and its high resistivity, which is important for reduction of Johnson-Nyquist noise and systematic effects due to electric field induced currents in a proposed EDM measurement.

The ceramics plate is thermally connected to a $1/8''$ copper tube ring which is used to guide the helium gas coolant. The temperature of the cooling gas can be adjusted to provide a sample temperature between 90 K and 250 K. For this temperature control warm (room temperature) and cold ($\approx 50\,\mathrm{K}$) helium gas is mixed at the top of the setup. This closed-cycle cooling system is able to deliver 2000 sccm of cold and 4000 sccm of warm gas (for fast warming). The helium is guided in glass tubes mounted outside of the thermal shield. On the bottom the tubes enter the inside of the thermal shield. Special care had to be taken for additional thermal shields to avoid radiation heat from the helium lines. To further reduce radiation heat from the sample stage directly above the superconducting pickup coils the bottom side of the "EDM chip" is coated with a 1 μm thick layer of aluminum, decreasing emissivity to a minimum.

The design of this non-magnetic cooling by means of mixed helium gas flow is based on the requirements of an EDM measurement with the isotope ^{129}Xe. The melting and boiling point (at 1 atm) of xenon is 161.40 K and 165.03 K, respectively. In an EDM experiment using liquid hyper-polarized xenon we have to maintain the liquid phase during the measurement and deplete the sample in the gas phase to start a new measurement cycle. Gas that is hyper-polarized at room temperature has to be cooled and subsequently liquified in acceptable times governed by the longitudinal spin-relaxation time, which determines the cooling power needed.

Highly sensitive magnetic flux sensors

To detect magnetic flux changes external superconducting pickup coils are used, which are connected to highly sensitive SQUID current sensors (Magnicon) inside a superconducting shield. Operated in a flux-locked loop (FFL) mode these sensors exhibit an intrinsic noise level of $< 2\,\mathrm{fT}/\sqrt{\mathrm{Hz}}$ and a 1/f noise edge at 3 Hz. The sensors have an input inductance of 400 nH and an input coupling of $0.5\,\mu\mathrm{A}/\Phi_0$, with Φ_0 being the magnetic flux quantum. The sensitivity of the FLL feedback circuit is $42 - 44\,\mu\mathrm{A}/\Phi_0$ slightly varying for different channels.

Twelve turns of niobium wire (Goodfellow, $7\,\mu$m polyimide insulation, $50\,\mu$m diameter) on sapphire (2.0 mm diameter, 18 mm length) are prepared either as magnetometer or gradiometer (baseline 3-5 mm) pickup coils (see Fig. 23). The geometry of the coils is rather determined by the requirements for an EDM measurement than limited experimentally. In the current setup three coils mounted in line with a distance of 5 mm are connected to SQUID sensors. The connecting wire pairs of the coils are twisted to avoid pickup of stray fields, while they are mostly routed inside the SQUID's superconducting niobium capsule.

The input impedance of 400 nH can be matched very well with twelve windings. Inductances measured with a LCR meter (Standford Research SR720) are between 300 nH and 370 nH. The signal wires from the room temperature SQUID electronics (Magnicon) to the current sensors are attached to the thermal shield outside the magnetic shield and then routed down inside the thermal shield. Finally the cable manifold is attached to the end of the central copper rod to provide contact to the 4 K stage. The SQUID sensors as well as three pickup coils are thermally anchored to the cooled copper plate via sixteen little copper straps (2 mm diameter) of 40 mm length. The SQUID sensors are mounted roughly in the center axis, whereas the sapphire rods with the pickup coils have a position 40 mm off-axis and tilted at an angle of 45°. Due to the high mass temperature variations of the SQUID sensors are within 20 mK, cf. Fig. 24 (a). In principal, by implementing additional SQUID sensors the number of channels can easily be increased.

In FLL mode the externally induced current fed into the SQUID generates a magnetic flux in an internal loop, which is canceled by a field generated by a current in a feedback loop. This current controlled by the FLL electronics is measured as a voltage drop over a resistor of variable size ($1\,\mathrm{k}\Omega$ to $100\,\mathrm{k}\Omega$) in the feedback loop. The voltage data from the three SQUID channels is acquired with a fast 24-bit ADC card (National Instruments, NI-4662).

Calibration of the SQUID signal to a known magnetic field yields a conversion factor for the flux-to-voltage transformation of 23 nT/V and 46 nT/V for magnetometers and gradiometers, respectively (Fig. 28). This agrees very well with the specified input and mutual inductances.

Magnetic flux noise and mechanical vibrations

A main source of mechanical vibration is the piston in the coldhead, which moves at about 1 Hz. To reduce mechanical (and hence magnetic flux) vibrations to a minimum thermal connections are made of flexible copper straps. Installed parts inside the magnetic shield are made of non-magnetic materials and were screened at PTB Berlin to avoid magnetic contamination and gradients in the setup. However, in the measurements presented here, a magnetic silicon diode temperature sensor was mounted on the coldplate, which probably introduces strong magnetic noise due to vibrations.

Johnson-Nyquist noise

Another source of magnetic flux noise are current fluctuations in metallic parts due to thermal movement of electrons (Johnson-Nyquist noise). The current noise density of a resistor R is $i = \sqrt{4\pi k_\mathrm{B} T/R}$, with the temperature T and Boltzmann's constant k_B. At temperatures of 4 K and milliohm resistance Johnson-Nyquist noise accounts for a magnetic flux noise density of several $\mathrm{fT}/\sqrt{\mathrm{Hz}}$ in some millimeter distance. The superconducting pickup loops mounted on sapphire rods of 18 mm length are at a distance $> 10\,\mathrm{mm}$ to massive metallic parts at 4 K which yields Johnson-Nyquist noise of order $1\,\mathrm{fT}/\sqrt{\mathrm{Hz}}$. But, the the copper cooling tube and an aluminum part fixing the copper tube are at temperatures of order 100 K and the distance to the pickup loops is of order 5 mm. Measured noise levels of several tens of $\mathrm{fT}/\sqrt{\mathrm{Hz}}$ might arise from Johnson-Nyquist noise of these metallic parts and can currently be limiting the achievable noise levels.

Magnetic field coils

To perform an EDM experiment with a liquid Xenon sample we need to apply ultra-low field NMR techniques (e.g. control over nuclear spin orientation). Therefore, one cylindrical coil and two cosine-theta coils are implemented inside the magnetic shield to provide magnetic fields of up to 100 μT in all three spacial directions. These coils are printed on double-sided flexible circuit boards with 1 mm wide and 70μm thick copper conductors and non-magnetic tin (trough-)contacts. All three flexible circuit boards are attached to the outer surface of a rigid plastic tube of 350 mm length and an outer diameter of 224 mm. This tube is placed inside the innermost magnetic shielding cylinder and pushed over the vacuum system when assembling the magnetic shields (cf. Fig. 17).

The two equal cosine-theta coils have a height of 260 mm and provide perpendicular magnetic fields transverse to the axis of the magnetic shielding cylinders ($400\,\mu\mathrm{T/A}$). The use of printed flexible circuit boards assures a geometrically very accurate current distribution giving rise to good magnetic field homogeneity. With a current-canceling layout simulations of the generated magnetic fields show a relative homogeneity on a $< 10^{-4}$ level over a 1 cm^3 volume. This can be improved by introducing printed correction coils of nearly arbitrary shape placed on the field coils.

A cylindrical coil for generation of magnetic fields ($125\,\mu\mathrm{T/A}$) in the vertical direction consists of 34 windings with 20 mm separation exactly perpendicular to the coil axis. This avoids small tilt angles of the magnetic field when using wire-wound coils. The connection to the next-neighbour winding is done with two steps to cancel all vertical components of the magnetic field generated.

This magnetic field configuration allows for holding fields in all three spacial directions and rotating perpendicular magnetic fields, which are all very well aligned to each other due to the use of flexible circuits.

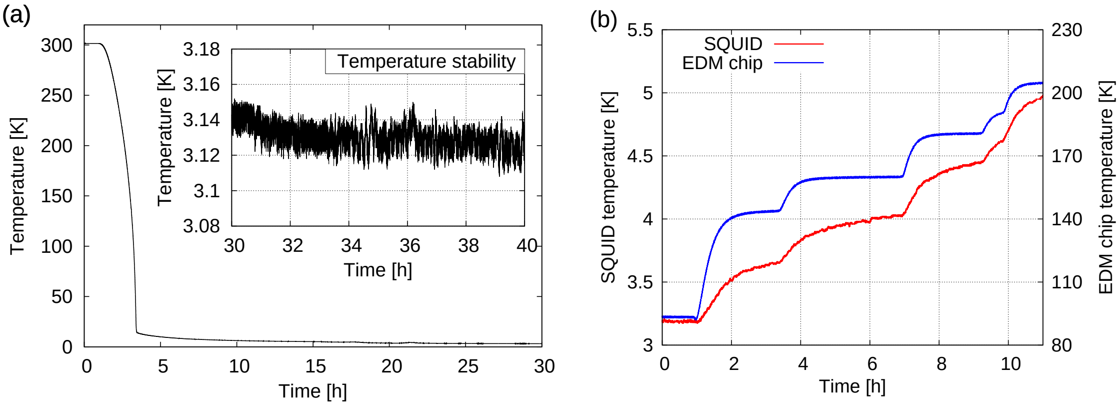

Fig. 24: (a) Cooldown of the coldplate, where the SQUID sensors are attached. The inset shows the temperature stability over 10 h after 30 h of cooling. (b) Temperature of the SQUID sensors while the sample stage temperature is varied from 90 K to 210 K.

Degaussing

To bring the μ-metal cylinders to a nearly non-magnetized equilibrium after exposure to magnetic fields, e.g. the earth magnetic field) a degaussing procedure is applied. The degaussing is usually done by applying a oscillating magnetic field to the μ-metal which has a slowly decreasing amplitude and a rather small frequency of several Hz. This basically runs the material through the hysteresis curve with ever decreasing remanent magnetization until only very little remains, which determines the residual magnetic field inside the shielding. The magnetic field for degaussing is generated by ten turns of ribbon cable, each ten wires of $0.5\,\mathrm{mm}^2$ cross section. These can carry up to 30 A when operating two adjacent turns in parallel. A sine wave usually oscillating at 10 Hz and decaying to zero within several hundred seconds is generated by a FPGA card (National Instruments, PXI-7853R). The bandpass (4 Hz width) filtered analog output from the FPGA card is connected to the analog input of a power amplifier (Kepco, BOP20-20M). To reduce residual DC currents due to slow drifts a transformer (Schmidbauer Transformatoren) optimized for 7-10 Hz separates the degaussing coils from the power amplifier.

5.2.3 Measurements

Temperature stability and sample temperature dependence

In these measurements two temperature related aspects of the setup are being addressed. First the temperature stability of the SQUID sensors is shown in Fig. 24 (a), as in our cryogen-free setup the SQUIDs are not emerged in a bath of liquid helium, which is rather temperature stable for low boil-off rates. The SQUID sensors are optimized for lowest noise level below 4.2 K. Fig 24 (a) shows a typical cooldown curve with the temperature measured with a silicon diode (Lakeshore, DT-670-SD) mounted on the niobium capsule of the SQUID sensors. This run was recorded without the glass tube and “EDM chip” mounted and demonstrates the performance when no additional heat-

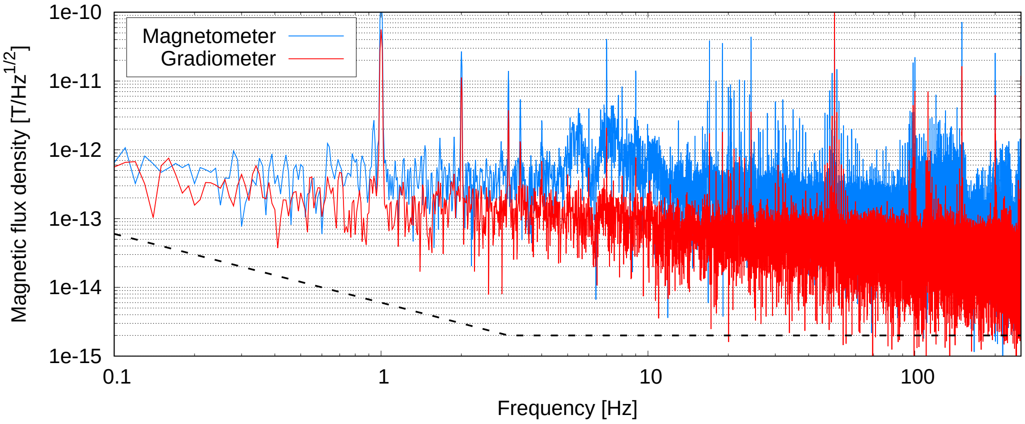

Fig. 25: Spectrum of magnetic flux noise density of a magnetometer (blue) and a gradiometer (red) coil with the dashed line indicate the intrinsic noise level of $2\,\mathrm{fT}/\sqrt{\mathrm{Hz}}$ above 3 Hz and $1/f$ behaviour below. The gradiometer of 4 mm baseline exhibits a noise floor of $85\,\mathrm{fT}/\sqrt{\mathrm{Hz}}$ at 10 Hz, decreasing to $48\,\mathrm{fT}/\sqrt{\mathrm{Hz}}$ above 50 Hz. Vibrations due to movement of the coldhead piston generate noise at 1 Hz and higher harmonics. Also several other vibrational peaks at low frequencies and particularly a 50 Hz peak from the power line is observed. The overall slope is attributed to Johnson noise from metallic parts. The magnetic shielding was not degaussed hence peaks might arise from magnetization of the magnetic shield.

ing is introduced by the helium cooling lines. Remarkably the minimum temperature of $< 3.16\,\mathrm{K}$ is only some hundred mK above the minimal temperature at the coldhead of 2.9 K, This demonstrates how well the cryostat works even in the tight space constrains due to magnetic shielding. At a temperature difference from coldhead to the SQUIDs of only 0.25 K the heat load on the 2nd stage can only be on the order of 50 mW. The temperature of the thermal shield reaches about 80 K within about 28 h. The temperature of the SQUID sensors is generally stable on a 20 mK level over many hours, as show in the inset of Fig. 24 (a).

The second aspect addresses the implementation of the glass tube, “EDM chip” and the helium cooling system. The cooling lines with helium gas at temperatures between 90 and 250 K introduces a significant heat load as this needs to be diverted into the thermal shield very close to the SQUIDs. The surface of 1/8″ tubing with a length of 350 mm radiates about 120 mW of power while for the “EDM chip” one gets roughly 150 mW, both at 160 K. The metal parts at 4 K are directly exposed to this heating sources. To minimize thermal radiation two main improvements were necessary. First. the emissivity of the “EDM chip” was significantly reduced by coating it’s bottom side with aluminum. And secondly an additional thin thermal shield made of aluminum was introduced between the helium lines and the 4 K rod. As this shield is thermally anchored to the thermal shielding cylinder it actually removes the radiative heat. With these two minor changes the SQUIDs are now operated at 4.2 K and pickup coils kept superconducting even at elevated sample temperatures of 160 K. Fig. 24 (b) shows the thermal influence of the sample stage on the SQUID temperature.

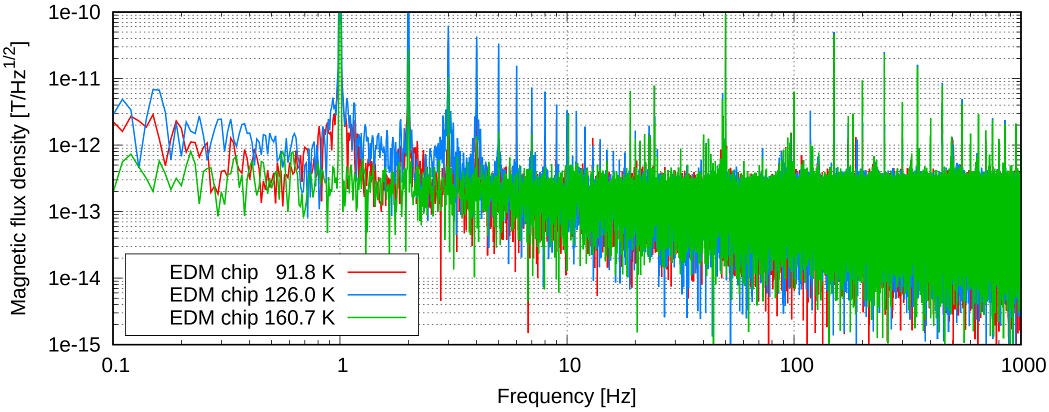

Fig. 26: Magnetic flux noise density spectra of a gradiometer for various sample stage temperatures of 92 K, 126 K and 161 K yield noise floor levels of 131 fT/$\sqrt{\text{Hz}}$, 135 fT/$\sqrt{\text{Hz}}$ and 144 fT/$\sqrt{\text{Hz}}$ in the frequency range of 50 to 90 Hz. The data show an increase in noise level of about a factor of two to four. At low frequencies the increased noise level at low “EDM chip” temperatures might be attributed to temperature fluctuations that depend on leakage from the helium cooling lines. Data was acquired after degaussing the magnetic shields.

Cooling the sample stage maximally to 90 K, the SQUID sensors can be kept as low as 3.2 K (see Fig. 24). Thus nearly no additional heat load is imposed. Even at 200 K sample temperature the SQUIDs can be used (e.g. the FLL lock works) while usually the pickup coils tend to become normal conducting already at lower temperatures around 180 K. The problem with the pickup coils arises as already a tiny part of the 50 μm that can't by cooled properly due to radiation renders the coil useless.

Magnetic flux noise sensitivity

The important figure for high precision measurements like the EDM search on ^{129}Xe is the sensitivity of detection. Since the dipolar signal of interest coming from a small droplet of hyper-polaized liquid xenon is only 1.5 mm away from one gradiometer side a baseline of 4 mm accounts for a signal-loss of only $(1.5/5.5)^3 = 2\%$.
Fig. 25 shows the spectral noise density of a magnetometer coil and a gradiometer coil. The spectrum is recorded without previous degaussing of the setup and shows some features arising from magnetization that are not observable after degaussing, cf. Fig. 26. The spectra show a dominant 50 Hz power line peak and some low-frequency peaks of 1 Hz and higher harmonics, which are mostly due to the mechanical vibrations caused by the moving piston in the coldhead. Noise can also be a result of magnetic contamination, particularly the temperature sensor mounted to the coldplate contains a highly magnetic nickel plating. However, the noise floor is demonstrated to be 165 fT/$\sqrt{\text{Hz}}$ and 48 fT/$\sqrt{\text{Hz}}$ above the 50 Hz peak for magnetometers and gradiometers, respectively. For NMR experiments the holding field can be chosen to detect spin precession in the frequency range above 50 Hz, where the noise floor is lower. However, improvements can still lead to lower magnetic flux noise levels.

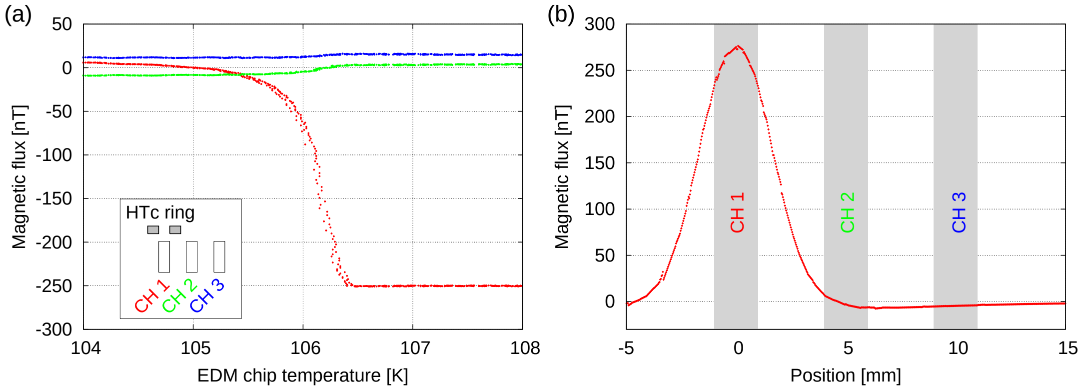

Fig. 27: Transition of a superconducting ring to the normal state. (a) With increasing temperature of the "EDM chip" the previously frozen magnetic flux in a superconducting ring made of Bi-2223 vanishes at the transition temperature around 108 K. The change in field amplitudes measured in the subjacent pickup coils is attributed to the geometrical arrangement of the pickup loops. (b) A simulation of the magnetic flux density component along the pickup loop axis (45° to the HTc ring axis). Plotted is the flux density generated by the supercurrent in the ring along a line connecting the three pickup loops. For a distance of the line to the ring center of 1.5 mm the field magnitude agrees with the measurement. Pickup coil positions are indicated by shaded areas.

As the temperature of the SQUIDs influences the intrinsic noise, the dependence of the magnetic flux noise level on the sample stage temperature has to be considered. The gradiometer noise density spectra of Fig. 26 were taken after degaussing the magnetic shields and show fewer individual noise peaks compared to Fig. 25. But, the level of the noise floor is increased roughly by a factor of two to four. Rather unexpected the highest sample temperature of 160.7 K apparently exhibits the lowest noise. This effect might be related to helium leaking the cooling tube connections, which depends on their expansion coefficients.

Phase transition of a superconducting ring and resolution

For demonstration of the variable temperature sample stage the magnetic field trapped in a superconducting ring was observed while increasing the temperature of the ring to $T > T_c$.

A ring made of Bi-2223 with dimensions of 5 mm outer diameter, 2 mm height and a 2 mm diameter central hole was placed on the "EDM chip" above the first pickup coil (CH1), cf. Fig. 27 (a). Bi-2223 is a high-temperature superconductor of the BSCCO system with composition $Bi_2Sr_2Ca_2Cu_3O_{10+x}$ and a transition temperature of $T_\mathrm{c} = 108\,\mathrm{K}$. The BSCCO ring was cooled from its normal state to $T < 90\,\mathrm{K}$ in a magnetic field B_z along the rings's axis. Then the magnetic field was switched of quickly yielding no signal change due to the trapped magnetic field. The ring was then warmed up to temperatures above T_c by introducing warm helium gas. After about five minutes the ring reached 140 K and the signal of the pickup coils showed an expected jump in magnetic field flux during

heating when the ring undergoes the transition from the superconducting state to the normal state (cf. Fig. 27). The transition occurred at $T \approx 106\,\mathrm{K}$ slightly above the quoted transition temperature, but could be due to a temperature offset between the ring and the position of the temperature sensor at the fringe of the "EDM chip", which is particularly large during warming (cf. Fig. A.2).
The small changes in flux in the SQUID channels 2 and 3 observed in Fig. 27 (a) can clearly be attributed to distance to the ring. The varying signs of magnetic flux changes become apparent when looking at the simulated flux density generated by the supercurrent in the ring, Fig. 27 (b). The component along the pickup loop axis is plotted along the connecting line of the pickup coils and one actually expects different signs for the flux change in the channels. Additionally from the simulation the distance of the pickup coil to the HTc ring center is determined to be 1.5 mm.
With this measurement the operation of the pickup coil and SQUID detection system was demonstrated, while being able to vary the temperature of our sample via the "EDM chip" cooling system. This is one of the essential technological advances for a future measurement of the EDM of ^{129}Xe.

5.2.4 Conclusion and outlook

With the successful operation of our setup, we have demonstrated that high magnetic field sensitivity on the order of $50,\mathrm{fT}/\sqrt{\mathrm{Hz}}$ can be achieved with SQUID current sensors cooled in a cryogen-free vacuum system. This cryogen-free approach enables easy operation and uninterrupted long-term operation. Most prominently introduced are noise peaks due to the moving coldhead parts at 1 Hz and harmonics and a peak arising from the power line frequency. Showing the working principle the detection scheme can easily be extended to more channels. This enables both high precision experiments with simultaneous multiple samples and new technological developments, e.g. a magnetic gradient pixel camera. Other examples of experimental perspectives with our setup are the search for spin-matter couplings or unknown forces at small distances, axion searches and EDM searches.

5.3 Pickup coils and SQUID signal calibration

In this section I want to provide a supplement to Sec. 5.2.2 of the above paper draft. The signal, e.g. voltage drop over the feedback resistor of the FLL loop, acquired from the SQUID electronics was calibrated to the magnetic flux density. In principle the data sheet of the SQUID sensors provides what is needed, namely the feedback sensitivity $1/M_\mathrm{f}$ (cf. Sec. 3.4.2) and input coupling $1/M_\mathrm{in}$ (cf. Sec. 3.4.3). Ideally the voltage output of the FLL electronics V is related to the current I^in the SQUID senses in the input loop via

$$V = R_\mathrm{f}\frac{M_\mathrm{in}}{M_\mathrm{f}}I^\mathrm{in}, \tag{5.10}$$

with the feedback resistor R_f. The law of induction and the pickup coil geometry yields the induced current in the superconducting coil due to a magnetic flux change at frequency ν,

$$I^\mathrm{in} = \frac{\pi r^2 N B^\mathrm{max}}{L^\mathrm{coil} + L^\mathrm{in}}\cos(2\pi\nu t), \tag{5.11}$$

where r is the pickup coil radius, N the number of turns, B^max the amplitude of the magnetic flux density and L^coil and L^in are the inductances of the pickup coil and the input loop, respectively. The input inductance of the current sensors used is 400 nH and the input coupling $0.5\,\mu\mathrm{A}/\Phi_0$. With the feedback sensitivity varying from 42.2 to $43.8\,\mu\mathrm{A}/\Phi_0$ an assuming a 12 turn pickup coil of 1 mm radius and a typical (measured) inductance of the pickup coils of 320 to 380 nH the expected magnetic flux density per voltage output is in the range $21.8 - 24.5\,\mathrm{nT/V}$ for a feedback resistor of $10\,\mathrm{k\Omega}$. However, very small deviations alter the conversion e.g. due to variations of up to 25% in the inductance of the hand-made pickup coils. A calibration of the response to a real magnetic flux was conducted (cf. Fig. 28 (b)) and yielded conversion factors of $22.2 - 24.8\,\mathrm{nT/V}$, in very good agreement with expectation from specifications.

The flux density to voltage ratio was calibrated by comparing the magnetic flux density measured at the position of the pickup loops with a fluxgate sensor (Bartington, MAG-03MC1000) to the signal acquired with a twelve-turn magnetometer pickup coil. Fig. 28 (b) shows the ratios of the fluxgate to the SQUID data.[31]. An initially surprising feature is the differing frequency dependence of fluxgate and SQUID signals. This can be attributed to the higher conductivity of the thermal shielding cylinder in the SQUID measurements. In that case the aluminum cylinder is cooled to about 80 K and larger Eddy currents are induced by the oscillating magnetic fields[32]. Differences for magnetic fields applied in B_y and B_z directions arise as the fields are transverse and axial to the aluminum cylinder, respectively. The differences in damping for the cold and warm metallic parts is shown in Fig. 28 (a).

From the calibration measurement using two different magnetic field coils (B_y and B_z, see Sec. 5.6) and three magnetometers an average conversion factor of $23.2\,\mathrm{nT/V} \pm 10\%$ for a pickup coil of twelve turns can be deduced. This translates to a calibration factor of

---

[31] The SQUID data needs to be corrected for a factor of $1/\sqrt{2}$ due to the 45° tilt of the pickup coils.

[32] In the fluxgate measurements all metallic parts were present but at room temperature

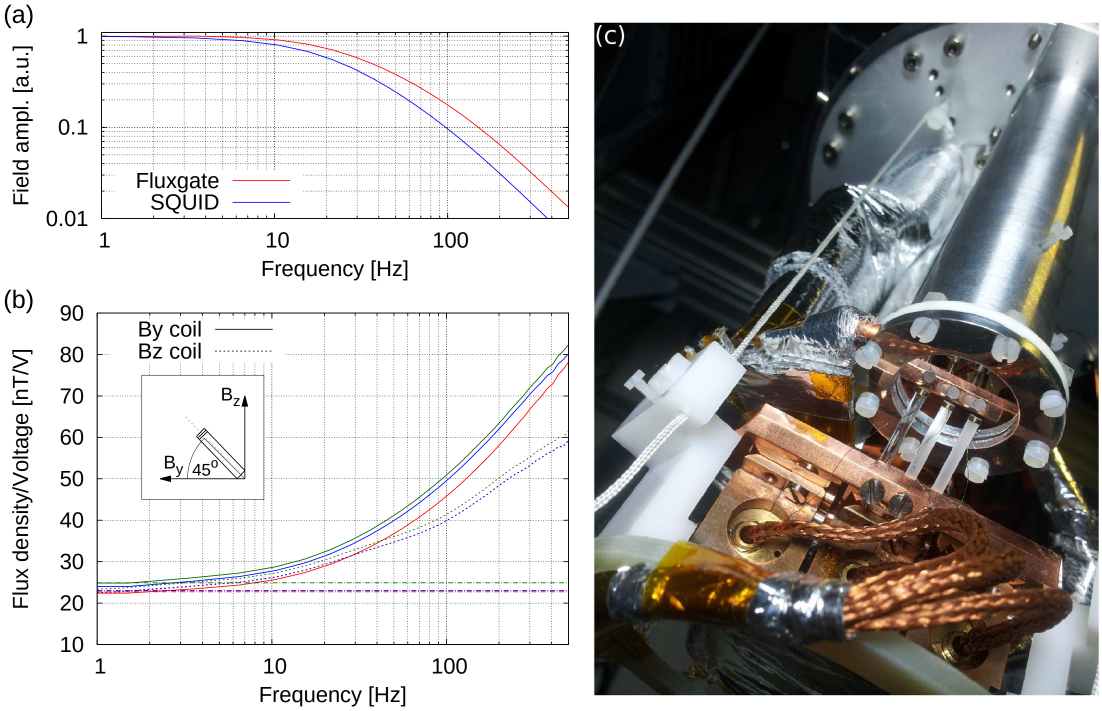

Fig. 28: (a) Damping of the transverse magnetic field (B_y) due to metallic parts of the setup. In the SQUID measurement damping is more effective due to cooled metal parts, see text. (b) Calibration of the voltage output of the FLL electronics to the magnetic flux density measured with a fluxgate sensor mounted at the pickup coil position. Plotted are measurements for fields in B_y (straight) and B_z (dashed) direction for the three SQUID channels (red, blue, green). The frequency dependence arises from increased damping for low temperatures, see text. Also indicated are the expected conversion factors from the specifications. (c) A view of the three pickup coils from the bottom. They are mounted to a copper coldplate and kept close to the metalized bottom of the EDM chip.

46.4 nT/V for a gradiometer having two counter-wound coils of six turns each. All data from SQUID measurements is scaled to magnetic flux density according to the quoted calibration factors.
Note, that each individual pickup coil (Fig. 23) has geometric imperfections and inductances from the length of the twisted wire. For example the twisted niobium wire connecting two coils of a gradiometer might have small but magnetic field sensitive loops, although thoroughly prepared.

5.4 Xenon polarizing setup

The EDM cryostat with highly sensitive magnetic flux detection ($< 50\,\mathrm{fT}/\sqrt{\mathrm{Hz}}$) was presented in the above paper draft. Another essential part of the liquid xenon EDM measurement is the production of a huge volume of polarized ^{129}Xe. This involves two setups (cf. Fig. 17), the polarizing setup described in this section and a cold trap for

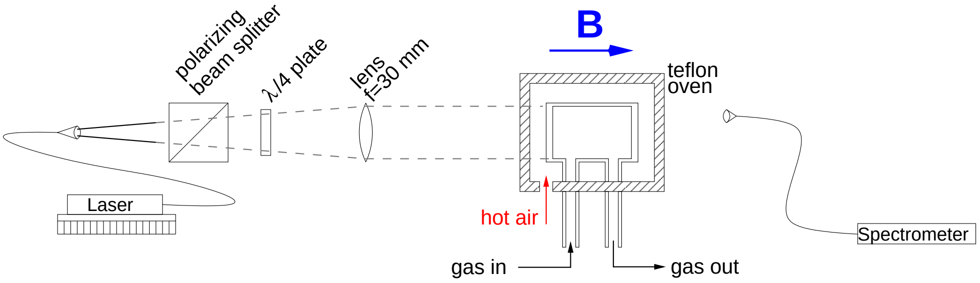

Fig. 29: Scheme of the SEOP setup. Light from the temperature controlled laser diode is circularly polarized and shines on the polarizing cell with optical quality windows. The cell is heated by hot pressurized air to 120 – 165° C. A spectrometer catches a light reflex from the cell to control the laser emmision frequency.

accumulation of a large volume of polarized xenon presented in the subsequent section. To polarize ^{129}Xe for the EDM experiment we use a SEOP setup as shown in Fig. 29. Rubidium is optically pumped in a magnetic field of some mT by several watts[33] of a 20 W laser diode (nLight, Pearl Series). To increase the rubidium density the polarizing cell is heated to 120 – 160° C by blowing hot pressurized air into the teflon oven enclosing the cell. The typical gas mixture used is $100-400\,$mbar of natural or enriched xenon, 100 mbar of nitrogen and $2000-3500\,$mbar of helium to pressure broaden the rubidium D1 line (cf. Sec. 3.2.1). The gas mixture is supplied by three flow-controllers (Natec sensors) either for filling the cell or flushing the system with a particular gas mixture.

After experiencing difficulties we replaced poor quality[34] spherical cells by cylindrical Borofloat cells with bonded optical quality windows (Hellma Analytics), that withstand elevated temperature and high pressures (Fig. 30). The polarizing cells have $28\pm0.8\,$mm cylindrical inner diameter and $30\pm0.02\,$mm inner length, hence a volume of $18.5\pm1.0\,\text{cm}^3$. For the liquid xenon EDM the amount of polarized liquid needed to fill up the "EDM chip" is $\approx 200-300\,\text{mm}^3$ per measurement, of which only a few mm^3 will actually be used after enclosing the liquid droplets. Additionally, the volume of the glass tube has to be filled with at least 0.8 bar of gas due to the xenon vapor pressure. To supply such an amount $\approx 400-600\,\text{cm}^3$ of gaseous xenon are necessary. For this amount a flow-through polarizing setup is required. Therefore the polarizing cell has an inlet an an outlet, where two non-magnetic high vacuum valves ($p < 10^{-6}\,$mbar) are attached that are operated remotely with pressurized air (Fig. 30). The actuator position (Festo, ADVU-25-10-A-P-A) is set by the state of a digital output which controls a 4/2 valve (Festo, VUVB-S-M42-AZD-QX-5WC1). Magnetic parts made of stainless steel were replaced by plastic parts. The glass portion of the high vacuum valve (Chemglass, CG-982-01)

---

[33] Typically $2-5\,$W of the available power were used to polarize rubidium to ≈ 100%. At 1 W the pumping rate at the front window of $\approx 6\,\text{cm}^2$ area is already $\approx 10^4\,\text{s}^{-1}$ (Sec. 3.2.1) competing with $\Gamma_{\text{Rb-Rb}} \approx 26\,\text{s}^{-1}$.

[34] Poor refers to cells that were obviously refracting and deflecting most of the light as could be judged by eye. As teflon is also highly reflective we assumed that the low intensity and back-reflections prevented buildup of a detectable polarization.

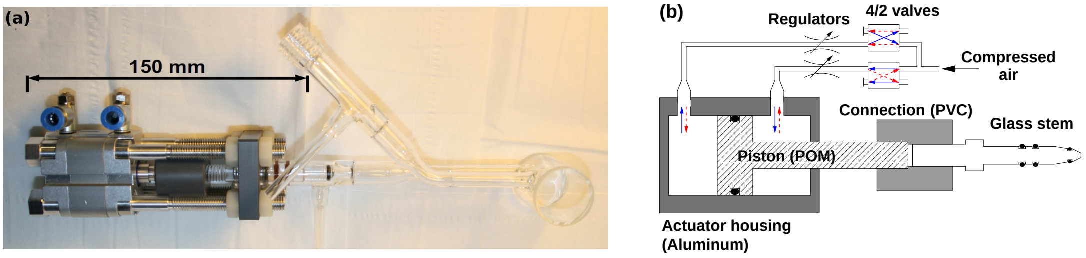

Fig. 30: (a) The polarizing cell made of Borofloat glass with optical quality windows, which maximize laser intensity in the cell. Attached to the polarizing cell is one of two non-magnetic and compressed air controlled high vacuum valves. (b) Materials and operating principle of the non-magnetic valve.

is fixed to the actuator with a 10 mm thick threaded PVC plate. The plate is mounted with eight nylon nuts (M8) allowing for positioning. The standard compressed air tube fittings on the actuator are currently containing magnetic stainless steel parts, but are about 150 mm away from the polarized gas. The connectors directly on the actuator can easily be replaced by plastic connectors with attached tubing using standard (magnetic) fittings only far away. Then the valve is basically free of magnetic contamination and well suited to be used even in magnetically shielded environments.

The polarizing cells were filled with a few hundred mg of natural rubidium (Sigma Aldrich) in a glove box under nitrogen atmosphere (flushed with nitrogen overnight). During the filling process the rubidium is covered by an oxide layer formed with residual oxygen[35]. To break free the rubidium the evacuated cells needed some heating either with an air gun or by mounting the cell in the oven and preheating it for 2-3 hours at 160° C. When heating with the heat gun it is very important to slowly heat up to 100° first, then slowly increase temperature o up to 250°. Slow heating avoids stress on the bonds of the windows and prevents bursts. After the heating procedure the rubidium should built a sliver layer on the inner cell surface. With fresh (and non-oxidized) rubidium the absorption is showing up in the laser spectrum quickly, even when flushing gas through the cell[36]. Flushing the polarizing cell with gas introduced significant cooling which made necessary much more heating power for the compressed air sent to the oven. To relax this a pre-heater for the gas mixture was installed close to the polarizing cell. With the gas pre-heated to ≈ 170° no increase in heating power for the hot air flushing the oven is needed.

To determine the degree of polarization an on-line NMR system is implemented in the polarizing setup. Additionally to the strong holding field (up to 24 mT) provided by a pair of Helmholtz coils of 18 cm diameter and 200 turns each a smaller B_1 coil is used to induce spin flips by generating an oscillating transverse magnetic field.

The precession tilted away from the holding field induces a voltage in a pickup coil (20 mm diameter) with ≈ 200 turns and an inductance of ≈ 1 mH. The pickup coil is part of a resonant circuit ($Q \approx 10$) with a parallel capacitor and tuned to the Larmor

---

[35] This actually facilitates getting the rubidium into the cylinder as it's not sticking on the glass so easily.

[36] If not, or its very shallow even at temperatures $> 160°$ C the rubidium needs to be replaced.

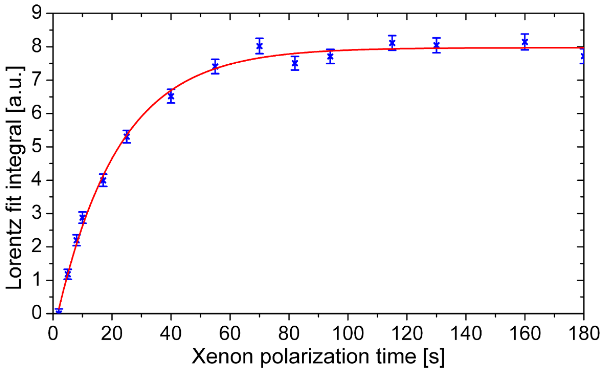

Fig. 31: Exponential buildup of ^{129}Xe polarization in the SEOP setup with a time constant of about 50 s. The exponential is fitted according to the model of Eq. (3.27).

frequency. The voltage on the capacitor ($\approx \mu$V) is pre-amplified (Standford Research, SR560) and digitized. Details on the home made NMR electronics, which basically consist of switching circuits to stop post-pulse oscillations of B_1, close the resonant pickup circuit and take care of the timing are already described elsewhere [150].

The degree of polarization was quantitatively deduced by a calibration of the NMR electronics to a known source of magnetization: the protons in a cell filled with water. A thermally polarized sample (Eq. (3.8)) of water in the cell generates a sufficient signal to be detected by averaging 2000 runs. The polarization is expected to be $P^{\mathrm{p}} \approx 2 \cdot 10^{-8}$ in a 6.0 mT holding field at 23° C. To minimize the influence of the on-line NMR electronics the signals of protons and ^{129}Xe need to be obtained at similar frequencies. The gyromagnetic ratio for protons (42.576 MHz/T) is a factor of 3.6 larger, so the ^{129}Xe NMR signal in a field of 21.7 mT can be calibrated against protons in 6 mT. The calibration data and fits are shown in Fig. 32. For calibration the polarizing cell contained 400 mbar of natural xenon which amounts to 4.7×10^{19} atoms of the isotope ^{129}Xe. The number of protons, two in each water molecule, is 1.1×10^{24}. Hence the ^{129}Xe polarization determined from the areas of the Lorentzian fit functions I_0^i (Fig. 32) is

$$P^{\mathrm{Xe}} = P^{\mathrm{p}} \frac{I_0^{\mathrm{Xe}}}{I_0^{\mathrm{p}}} \frac{N^{\mathrm{p}}}{N^{\mathrm{Xe}}} \frac{\gamma^{\mathrm{p}}}{\gamma^{\mathrm{Xe}}} \approx 43\%. \tag{5.12}$$

Due to errors, e.g. 5% on the cell volume, the xenon pressure and the magnetic field strength and the uncertainty in the temperature, which was not measured, the above result is a very rough estimate, with an error of probably 40%.

However, the goal was not to estimate the performance very accurately, as many other loss mechanisms are expected to dominate the accumulation and transport of the polarized gas. For the successful demonstration of the concept and sensitivity of an EDM search it is not yet essential to maximize the polarization and no optimization efforts were undertaken during this work.

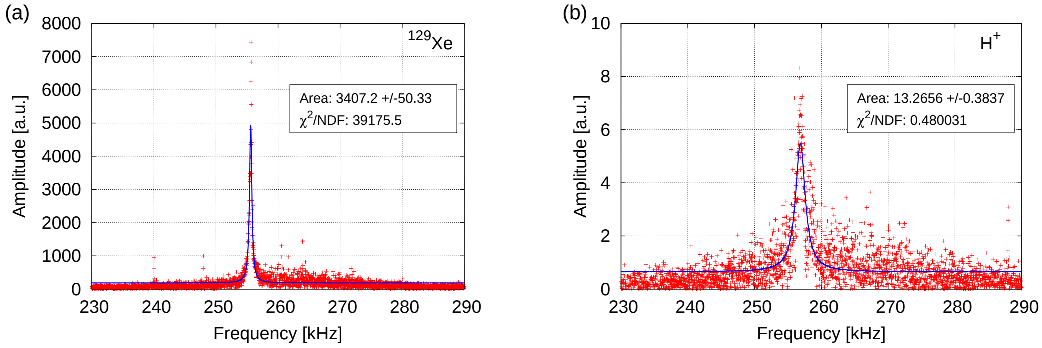

Fig. 32: (a) On-line NMR signal of ^{129}Xe spin-precession at a magnetic holding field of 21.7 mT in the polarizing setup. (b) Weak signal of thermally polarized protons ($\approx 10^{-6}\%$) in a water sample in 6.0 mT holding field. With this calibration measurement the polarization of ^{129}Xe in 400 mbar of natural xenon is determined to be on the order of 40%.

5.5 Accumulation and transfer of polarized xenon

As already pointed out in Sec. 3.3.2 sufficiently long longitudinal relaxation times were measured in frozen polarized xenon at liquid nitrogen temperatures when kept in magnetic fields of several tens of mT. When the accumulation period is finished and xenon ice is warmed up to the melting point or further for transfer in the gas phase the conditions of this process are crucial for preservation of polarization. When the temperature rises towards the liquid temperature of 161 K the longitudinal relaxation time is quickly decreasing due to temperature induced vacancy diffusion (cf. Sec. 3.3.2, particularly Eq. (3.50)). The relaxation this process generates strongly depends on the ambient magnetic field (cf. Fig. 11). Polarization losses can be suppressed by performing the phase transition to liquid or gas quickly and/or in magnetic fields of several hundred mT.
The position of the cold trap used for accumulation of polarized gas in the solid phase is depicted in Fig. 17 and Fig. 33 depicts a closer look.
Gas flowing out of the polarizer setup is diverted in a PFA tube to the cold trap were xenon is accumulated at liquid nitrogen temperature in a permanent magnetic field of about 240 mT. As indicated in Fig. 33 the gas mixture of Xe, N_2 and He is flown through a borosilicate glass bulb emerged in a liquid nitrogen dewar. The dewar sits on a platform that is remotely moved down for thawing. A separate intermediate volume which has an inlet at the top of the $\approx$ 300 mm long trap is flushed with room temperature air to prevent blockage of the inlet tube. The bulb has an outer diameter of 36 mm and exhibits an inner cold surface of $\approx 35\,\mathrm{cm}^2$.

To provide high magnetic fields four Halbach array rings surround the bulb. The permanent magnetic field in the center of this Halbach array is stronger than 240 mT throughout the volume of the bulb. Each Halbach ring consists of 32 neodymium cubes of 20 mm side length, each with a remanent magnetic field of 1.3 T. The cubes sit in a 3D printed holder imposing the correct orientation. Details on the Halbach array and

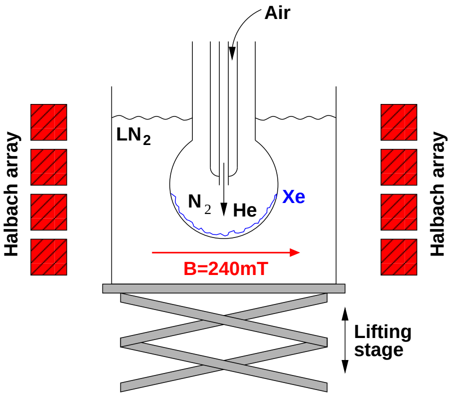

Fig. 33: The cold trap setup for accumulation of hyper-polarized xenon. The gas mixture enters a borosilicate bulb emerged in a movable liquid nitrogen dewar. Xenon freezes on the cold inner surface, while excess gas (N_2 and He) is finally flushed to atmosphere or pumped out. A magnetic field of $> 240\,\mathrm{mT}$ is provided by four Halbach array rings.

simulations can be found in Karsten Tells thesis [151].
By evacuating the trap while the bulb is kept in liquid nitrogen xenon can be easily separated from the excess gas. Quick thawing and evaporation is achieved by lowering the liquid nitrogen dewar and submerging the bulb with frozen xenon in warm water. During this process the pressure in the transfer line rises and reaches it's maximum within $\approx 50\,\mathrm{s}$.
On top of the cold trap the volume of the bulb is directly connected to a valve manifold made of borosilicate glass. The manifold has remote-controlled non-magnetic high vacuum valves[37] connecting to atmosphere, the vacuum pumping station or the EDM cryostat. Two valves are used at the inlet of the cold trap and to separate the trap from the pump stand, while evacuating the tubes to the EDM setup, cf. Fig. 17.

The performance of the trap was evaluated with a compact NMR system with a small probe bulb, cf. Fig. 34 (a). This probe system was attached to the tube connecting the polarizer and the cold trap. When the probe bulb was filled with gas from the polarizer cell containing 300 mbar ^{129}Xe a Lorentzian fit of the NMR signal from[38] 135 mbar ^{129}Xe in the bulb yields $A = 2.25 \pm 0.08$ for the area underneath the peak. For comparison the measurement was repeated with the probe bulb filled with xenon gas previously accumulated in the cold trap. The same gas mixture was flown through the trap for 5 minutes at a ^{129}Xe rate of 6.8 sccm. The excess gas was pumped out before thawing with warm water into vacuum ($< 10^{-4}$ mbar). The accumulated ^{129}Xe amounts to a pressure of about 490 mbar in the probe bulb. A fit gives 1.84 ± 0.10 for the area of the Lorentz function. A calculation of the loss factor κ due to accumulation in the cold trap and thawing gives

$$\kappa = \frac{2.25 \cdot 490\,\mathrm{mbar}}{1.84 \cdot 135\,\mathrm{mbar}} = 4.4 \pm 1.3. \tag{5.13}$$

---

[37] The valves are of the same type as in the polarizer, Fig. 30.
[38] Pressures herein are estimated from the volume ratios and probably accurate to 10%.

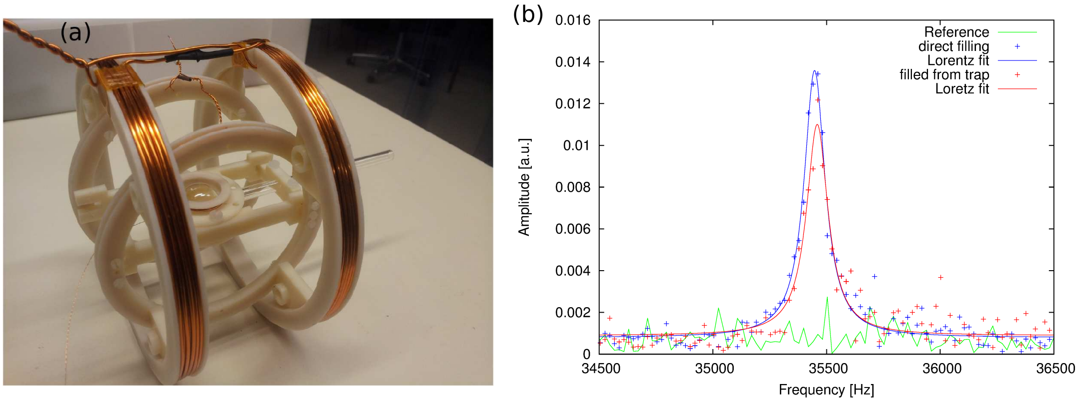

Fig. 34: (a) The polarization loss in the xenon trap was evaluated with a small NMR probe system. The probe bulb was connected between polarizer and cold trap and remained at this position for both measurements. (b) The NMR signal of 135 mbar polarized ^{129}Xe coming from the polarizing setup (blue) and of 490 mbarobtained after accumulating ^{129}Xe in the cold trap at 6.8 sccm for five minutes and thawing within 50 s using warm water (red). After accumulation about 23% of the initial polarization was recovered.

Hence about 77% of the initially polarized xenon is lost in the process. The expected loss only accounting for relaxation during accumulation yields (Eq. (3.29))

$$\frac{P_{\mathrm{Xe}}(t_{\mathrm{acc}})}{P_{\mathrm{Xe}}(0)} = \frac{T_1}{t_{\mathrm{acc}}} \left(1 - \exp^{-t_{\mathrm{acc}}/T_1}\right) \approx 0.97, \tag{5.14}$$

assuming the relaxation rate $\approx 2 \times 10^{-4}\,\mathrm{s}^{-1}$ at 77 K (Fig. 11).
For the EDM experiment these losses need to be reduced as recovery of nearly all polarized gas should be possible rather than only 20-25%. The losses are attributed to relaxation during transport, at the walls or at magnetic contamination. A thorough cleaning of the borosilicate trap and reducing losses during transport by providing guiding fields could improve on the losses. The demonstrated successful accumulation and thawing in the cold trap is an important accomplishment for the experiment and enables first polarized liquid xenon tests in the EDM cryostat, but the losses need to be studied and eliminated.

5.6 Generation and shielding of magnetic fields

Magnetic shielding cylinders and degaussing The environment for ultra-low field NMR ang long spin-precession times needs to be magnetically and electrically shielded from RF noise sources and dipolar fields. The magnetic shielding layers were described in Sec. 5.2.2. Magnetic noise spectra measured with gradiometers plotted in Fig. 35 show that degaussing with 20 A maximum current at 10 Hz with a decay duration of 100 s significantly reduces low frequency noise due to vibrations of magnetized domains in the μ-metal shield. The residual field inside the equilibrated magnetic shielding is about

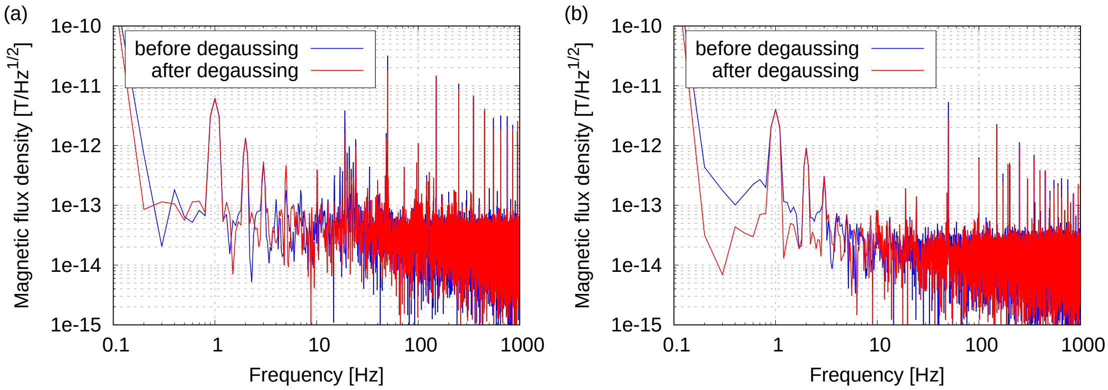

Fig. 35: Magnetic flux density spectra before (blue) and after (red) degaussing of the magnetic shields show a reduction of low frequency noise which is attributed to removal of mechanical vibration of residual magnetization in the magnetic shielding material. In the frequency range of interest, e.g. 10-100 Hz, both in the magnetometer (a) and gradiometer (b) only a marginal reduction of the noise level is observed.

3 nT. A definite result for the residual field and gradients in the setup can be obtained by observation of xenon spin precession.

Magnetic field homogeneity Here I want to include some remarks on the magnetic field coil system previously described (Sec. 5.2.2). The coil system based on flexible circuits was designed in the bachelor thesis of Max Newrzella [152]. The coils are printed on non-magnetic flexible circuits[39] (TopPrint Electronik, Ottobrunn) which makes them very thin (< 0.5 mm) and particularly the cos-theta coils are easy to mount accurately.

For the novel EDM experiment with several liquid xenon droplets (Sec. 5.1) the magnetic field simulations are helpful in choosing the preferred geometry. We have to deal with a highly non-symmetric problem. The droplets are placed 40 mm away from the central axis inside a field generated by a rather short coil (compared to its diameter). Additionally, the magnetic shielding which influences the gradients is much closer at the bottom than at the top. There are three options for generating the magnetic holding and B_1 fields (cf. Fig. 36):

- the cylindrical solenoid coil (B_z),
- a cosine theta coil with magnetic field aligned along the liquid droplets (B_x) and
- a cosine theta coil with magnetic field aligned perpendicular to the liquid droplets connection line (B_y).

The choice of field configuration influences the individual precession frequencies and flip angles of the three droplets. Let's first assume we don't use correction coils and

---

[39] The finish of contact pads and through contacts is tinn and not the standard gold layer, which has a nickel layer for adhesion.

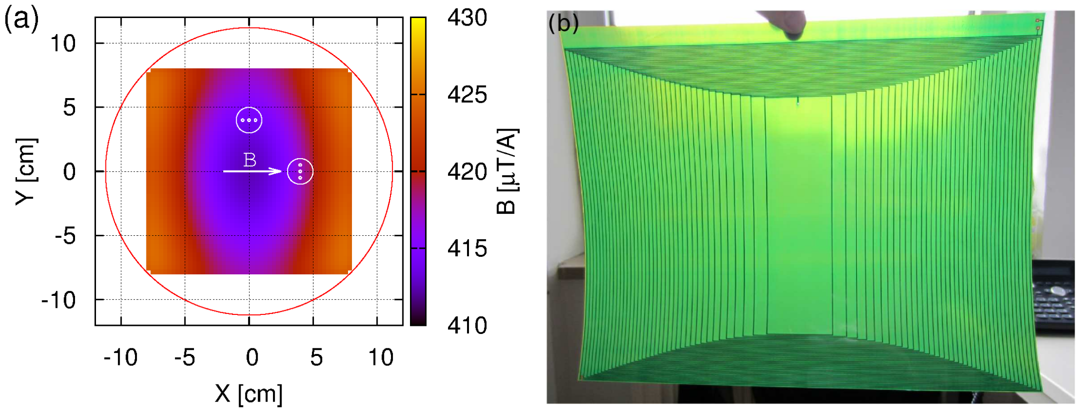

Fig. 36: (a) Magnetic fields generated by flexible printed-circuit coils of cosine theta current distribution simulated with Comsol Multiphysics (cf. [152]). Indicated are the relative orientations of the transverse magnetic fields ($B_\mathrm{x}, B_\mathrm{y}$ to the liquid xenon droplets, which are placed off-axis. The homogeneity of the magnetic field in 1 mm^3 improves by a factor of 10 and 2 for the B_x and B_y coil, respectively, when correction coils are employed (Tab. 5.2). (b) Fotograph of one half of a cosine theta coil as used for transverse fields B_x and B_y.

place droplets in the central plane of the coil ($z = 130\,\mathrm{mm}$). Table 5.2 summarizes the achievable field homogeneity between neighbouring droplets and inside droplets. Fig. A.1 shows all field components simulated for magnetic field coils $B_\mathrm{x}, B_\mathrm{y}, B_\mathrm{z}$ plotted along the three liquid samples separated by 5 mm. Implementation of correction coils yields an improvement of roughly a factor of 10 and 2 in homogeneity for the B_x and B_y fields, respectively. From the dependence of transverse spin-relaxation due to diffusion on gradients one can deduce the T_2^* limits from the holding field gradient inside a droplet. For a holding field of 10 μT a deviation of 10^{-4} over a 1 mm sized droplet yields a gradient of 100 nT/m, hence a $T_2^* < 10^4\,\mathrm{s}$ (cf. Fig. 12). Spin relaxation will not be limited by gradients. However, the deviations of magnetic fields imply errors in the flip-angle of the polarization vector due to either off-resonant spin-flips or amplitude deviations.

Variations in amplitude of the spin-flip pulse should in principle be as small as the accumulated phase angle in an EDM measurement, which is expected to be on the order of 10^{-7} for $d = 5 \times 10^{-30}\,e\mathrm{cm}$, cf. Eq. (5.2). However, after the free-precession period the polarization can also be tipped back to the initial direction cancelling the tip angle error[40].

A variation in Larmor frequency between droplets introduces a tip angle error due to off-resonant spin-flips. But the effect is expected to be small and can be compensated for by a broader pulse. And again it cancels by tipping the spins back to their initial direction.

---

[40] Systematic effects arising from misalignment of polarization vector and electric field vector during free-precession are supposed to be small for the quoted misalignment induced by magnetic field deviations (cf. Sec. 5.1.3).

Coil	Next droplet deviation	Inside droplet		Field strength [μT/A]
		Off-center position	Central position	
B_x	5.8×10^{-4}	1.8×10^{-4}	7.4×10^{-6}	403.5
B_x+Corr.	6.0×10^{-5}	2.0×10^{-5}	$< 5 \times 10^{-6}$	-
B_y	1.9×10^{-4}	7.5×10^{-5}	2.4×10^{-6}	412.7
B_y+Corr.	1.0×10^{-4}	4.0×10^{-5}	1.0×10^{-5}	-
B_z	4.0×10^{-5}	1.2×10^{-5}	$< 1 \times 10^{-6}$	123.8

Tab. 5.2: The simulated relative magnetic field deviations of the main field component of next-neighbour liquid droplets, the relative homogeneity through the droplets (off-center and central) and the generated field for each of the available coils. Also given is the improvement when implementing correction coils as calculated in [152]. Rather than using values in a volume of 2x2x10 mm as in [152] the numbers where deduced from field simulations along the central axis of the aligned droplets (Fig. A.1). The currents for the correction coils are determined by a least-squares method.

5.7 Development of the "EDM chip"

The structure housing the liquid xenon droplets has been roughly described in Sec. 5.1 and 5.2. However I want to include some more information and thoughts as the development of the "EDM chip" is an important challenge to be accepted by successive graduate students.
The choosing of an appropriate material has several prerequisites:

- high resistivity to reduce leakage currents
- low roughness surface to avoid breakthroughs
- machinability to impose the favoured microstructure
- spin-polarization preserving properties.

A material first chosen mainly for the in-house machinability was Macor ceramics. Macor has a resistivity of $> 10^{16}\,\Omega$cm at room temperature and can be polished to a roughness of < 13 nm. The prototype Macor chips were used for tests of the chip cooling system and temperature control, but is also a potential material for the "EDM chip".

In the bachelor thesis of David Wurm [153] temperature and heat-flow for a Macor chip were simulated particularly for the design and development of the chip cooling system, Fig. 37 (a). The thermal conductivity of Macor and other high resistivity materials is on the order of only 1 W/m K. Xenon is liquefied on the EDM chip onto an area of 254 mm^2 where the material thickness is as small as possible (< 0.5 mm) to put the pickup coils close to the sample. The simulations revealed that the cooling power of up to 4000 sccm helium flushed through circumferential copper tubes is sufficient to liquefy xenon gas and is not limited by the thickness of the center area. The temperature variation over the surface is expected to be within 1 K (cf. Fig. 37).

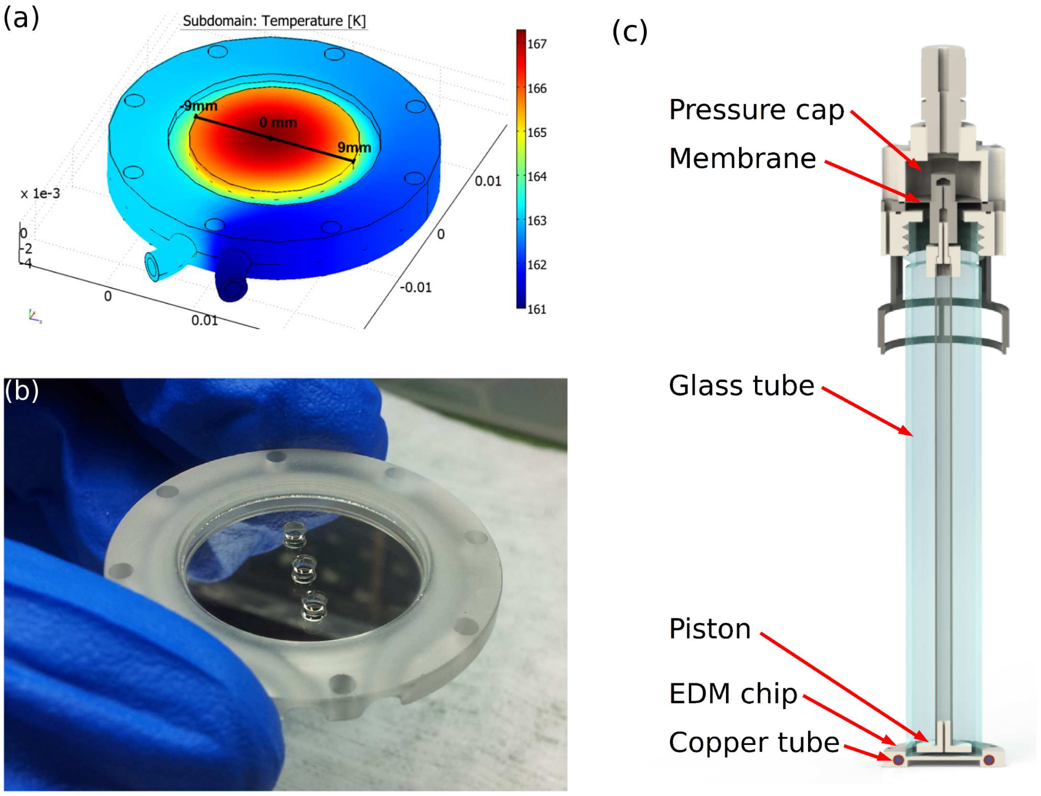

Fig. 37: (a) Simulation of the surface temperature of a Macor ceramics EDM chip [153]. (b) Prototype of an EDM chip made of fused quartz with polished tapped holes and a metalized bottom. (c) The glass tube with the EDM chip attached at the bottom. By pressurized air the piston can be moved down to seclude liquid samples. Meanwhile two electrodes on the piston and bottom of the EDM chip can be used to capacitively determine the liquid xenon level and to apply voltage.

To measure the temperature of the chip a non-magnetic PT-100 sensor with silver wires (IST AG, P0K1.520.4W.A.010) is mounted outside the glass tube close to the coolant tubes. The temperature difference of a sensor attached to the center of a Macor chip to the sensor close to the coolant tubes was measured to vary between $1 - 3\,\mathrm{K}$, with the variation exceeding $1.5\,\mathrm{K}$ only when warming up quickly (see Fig. A.2).

The spin-polarization preserving properties need to be determined first, but the Macor pieces were all tested to be non-magnetic. To avoid complications due to surface relaxation in first polarized xenon tests in the EDM cryostat we ordered prototypes made of fused quartz (Aachener Quarz-Glas Technologie Heinrich). The quartz surfaces are polished and three polished tapped blind holes are included positioned above the superconducting pickup coils (Fig. 37).

The fused quartz prototype is intended to be used in first tests of separating three cylindrical samples in the glass tube filled with liquid xenon. As the vapor pressure of xenon is $0.8\,\mathrm{bar}$ at the melting point the volume of the glass tube (Fig. 37) needs to be well sealed to the surrounding vacuum[41]. The EDM chip is glued to the glass tube end with epoxy glue (Hysol C1, Henkel), which is known to be non-magnetic and polarization preserving.

The three blind holes of the prototype chip can be secluded by a lid, whereas a more complicated development will follow for employing three spherical volumes as the shape of highest symmetry. With the pickup coils underneath individual spin precession of each separated volume can be studied. The mechanism to move a piston to later enclose samples is already developed and operable. It also serves the purpose of determining the amount of liquid xenon. In the thesis of Karsten Tell [151] the feasibility of a capacitive measurement of the liquid xenon level was demonstrated by using a movable electrode. Compressed air is used to deflect the piston attached to a membrane which was mounted on top of the glass tube, cf. Fig. 37 (c). The metalized bottom of the EDM chip acts as one electrode while the second electrode is the metalized bottom of the piston. The piston can be moved down with liquid xenon filled and hence close the liquid samples swamping out excess liquid. This mechanism is ready to be implemented in the EDM setup and enables observation of individual polarized liquid samples, which is easier to realize than spherical samples. Nevertheless, the influence on spin-relaxation times as to be determined.

The two electrodes are also available to apply voltage to a liquid sample and test the high voltage behaviour of the setup. For application of rotating electric fields electrodes surrounding each droplet need to be implemented in the “EDM chip”.

5.8 Summary of the liquid xenon EDM experiment

The new liquid xenon EDM experiment is now in a status of being ready to study spin-relaxation in liquid xenon and determine the sensitivity achievable in an EDM experiment.

The potential gain of using a liquid sample motivates the challenging R&D work. The paper draft presented in Sec. 5.1 describes the novel method introducing time-varying electric fields in an EDM search and several new subsequent systematic effects. Most of which seem to be in control, but predominantly AC leakage currents arising from the electrode capacitance seem to limit the sensitivity if the electric field is not perfectly aligned at 90° to the precessing polarization vector. Nevertheless, with a feasible alignment accuracy and a reference experiment the EDM sensitivity can be significantly improved over the current limit.

In the course of this work it turned out be be more difficult to reliably operate the detection system of superconducting pickup loops and SQUIDs in a cryogen free setup. Particularly with implementation of the “EDM chip” and it’s cooling system, which introduces a significant radiative heat source. Due to magnetic shielding space for feedthrough of the vacuum system and the cross-sectional area for thermal connection to

---

[41] It is actually not a trivial task to find the right glue as the epoxy seal has to withstand 1 bar of overpressure, while the temperature of the chip cycles between 90 K and 250 K. The thermal expansion coefficients of glass and typical epoxy glues deviate significantly.

the coldhead is very limited. However, all cryogenic issues were solved and the residual heat load was successfully removed to be marginal. Significant radiative heating comes from the "EDM chip" and helium cooling line which is now limiting the operating range of the superconducting pickup coils to $\lesssim 180\,\mathrm{K}$. Finally, in this range the noise floor of a gradiometer pickup coil is $144\,\mathrm{fT}/\sqrt{\mathrm{Hz}}$ above 50 Hz, even with a sample on the "EDM chip" at 162 K. The most dominant peaks are from vibration due to the moving coldhead piston and the power line frequency. The low frequency peaks from vibrations are of less concern in NMR measurements, whereas the strong 50 Hz signal is closer to spin-precession frequencies and potentially introduces spin-flips. One future task is finding and eliminating the sources of this peak and increasing the noise performance of the setup.

Parts of the liquid xenon EDM setup regarding production of large amounts of hyperpolarized xenon and transfer were built from scratch during this thesis. It was demonstrated that these components perform well and reliably deliver the polarized gas to be liquefied in the EDM setup. Improvements and optimizations of production parameters and reduction of losses during accumulation and transport need to be addressed in the future but are not limiting at this stage.

The possible approaches to deliver polarized liquid to the EDM setup have been evaluated. Accumulation of the polarized gas by freezing to the "EDM chip" suffers from severe polarization losses in elevated temperatures and low magnetic fields (cf. Sec. 3.3.2). As only small magnetic fields are available in the setup the warming and thawing needs to be done very quickly. However, due to the heat capacity and heat conductivity of the "EDM chip" material the heating process is slow (Fig. 24). Directly liquefying xenon from gas phase seems to be the best way and successful liquefaction on the "EDM chip" was already observed.

A major step to implementation of time-varying electric fields is the development of the "EDM chip" with electrodes introduced around the droplet cavities. But, already now an implementation of electrodes for a constant electric field along the magnetic holding field is nearly completed and a Ramsey-type EDM experiment is rather straightforward as soon as spin-precession can be observed.

The sensitivity will strongly depend on the preserved polarization and transverse spin relaxation times. These need to be experimentally determined in the setup to deduce an estimate on the EDM sensitivity accessible in the near future.

The setup now offers a rich playground probably for generations of graduate students to study spin-relaxation in low fields and explore the potential of novel methods of a liquid xenon EDM search.

6 A new EDM experiment using a He/Xe mixture and SQUID detection

As already pointed out earlier (cf. Sec. 2.5, Tab. 2.7) even slight improvements of d_{Xe} to about $10^{-28}\,e\mathrm{cm}$ will give enough information additional to the superior ^{199}Hg EDM measurement to get further insight and to better constrain several coefficients of $\mathcal{CP}$ violating interactions. This can potentially be achieved by improving the "conventional" method used in EDM searches with parallel electric and magnetic fields. Besides using a co-magnetometer as in [71] (cf. Sec. 4.1), two main features account for an expected improvement of EDM sensitivity. The use of a very low noise detection system yields a high signal-to-noise ratio even at low pressures. Observation time of ^{3}He spin precession at pressures of 1000 mbar is mostly limited by magnetic field gradients, while for 100 mbar of ^{129}Xe wall collisions are more dominant.

In an EDM measurement the electric field is sequentially reversed, while keeping the magnetic field, which cancels the Zeeman term in first order. However, a false EDM signal arises if an additional magnetic field is generated, that reverses sign with the electric field. The usually relevant geometric phase effect due to motional magnetic fields ($\propto \boldsymbol{v} \times \boldsymbol{E}$) is of no concern at high pressures, since the Larmor period τ_{L} is much larger than the correlation time τ_{c} (cf. [30]). The commonly most dominant effect due to leakage currents will be accounted for by the ^{3}He co-magnetometer that doesn't have an EDM[42].

The continuous operation of the He-Xe maser suffered mostly from instability of electronics and feedback loops as well as signal size. Our He-Xe clock comparison experiment is placed inside the Munich magnetically shielded room (MMSR) [154]. The room provides a very stable, RF shielded environment with very low magnetic field gradients ($\lesssim 1\,\mathrm{nT/m}$) and low residual fields ($\approx$ nT). Even more, with the inner shielding section installed it's expected to be the world's best magnetically and electrically shielded environment with a shielding factor of 10^6 at quasi-DC frequencies.

We aim to observe spin-precession in an applied electric field for several hundred seconds in each run. To improve statistics the collaboration is developing a gas system to continuously refill the EDM cell with freshly polarized gas while mounted inside the MMSR. This flowing gas concept brings some challenges, particularly for a system using such different species as ^{3}He and ^{129}Xe. But, it will make long-term operation feasible which could give a statistical improvement on the order of ≈ 1000 in one year (cf. (4.6)).

A question arising is the composition of the gas mixture. The only fixed pressure is the quenching gas, which will be about 100 mbar of N_2. The total pressure in the EDM cell (and the closed-cycle system) should be above one atmosphere, but not limiting

---

[42] Or at least one much smaller than the anticipated sensitivity.

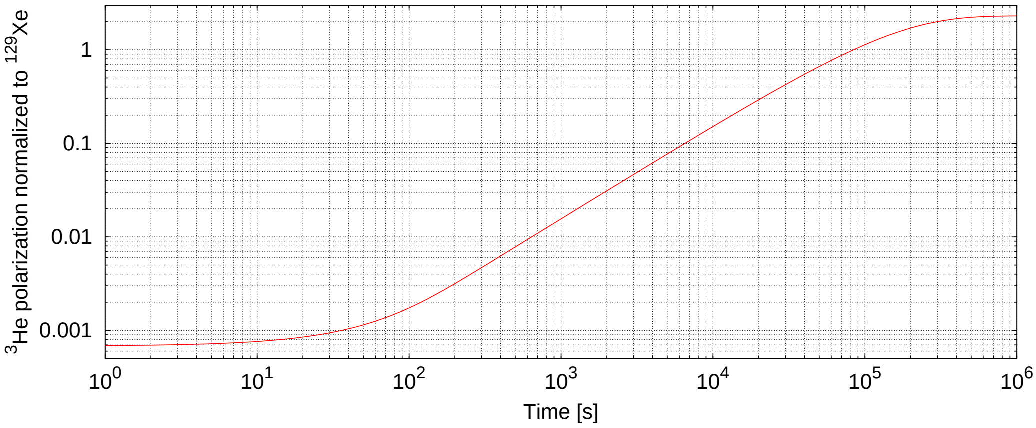

Fig. 38: The polarization buildup of ^{3}He in a typical SEOP setup, normalized to the simultaneous buildup of ^{129}Xe polarization in the same cell. Spin-exchange and destruction rates are the same as in Fig. 8.

the T_2 coherence time. Hence the ratio of ^{3}He to ^{129}Xe pressure $p^{\mathrm{He}}/p^{\mathrm{Xe}}$ needs to be determined, constrained by $p^{\mathrm{He}} + p^{\mathrm{Xe}} \approx 1.5\,\mathrm{bar}$ and, of course, the signal size to achieve the frequency sensitivity needed.

The sensitivity to magnetic field deviations in a frequency measurement of the ^{3}He co-magnetometer is a factor $\gamma_{\mathrm{He}}/\gamma_{\mathrm{Xe}}$ improved over ^{129}Xe. So, for monitoring the magnetic field the amplitude of ^{3}He precession can be roughly one third of the ^{129}Xe amplitude. One can set up a constraint for the ^{129}Xe pressure p^{Xe} from

$$P^{\mathrm{He}} p^{\mathrm{He}} \approx \frac{\gamma_{\mathrm{Xe}}}{\gamma_{\mathrm{He}}} P^{\mathrm{Xe}} p^{\mathrm{Xe}} \Rightarrow p^{\mathrm{Xe}} \approx p^{\mathrm{tot}} \left(\frac{\gamma_{\mathrm{Xe}}}{\gamma_{\mathrm{He}}} \left(\frac{P^{\mathrm{He}}}{P^{\mathrm{Xe}}} \right)^{-1} + 1 \right)^{-1}, \tag{6.1}$$

with total pressure p^{tot}, degrees of polarization $P^{\mathrm{Xe}}, P^{\mathrm{He}}$ and partial pressures $p^{\mathrm{Xe}}, p^{\mathrm{He}}$. With the help of Eq. (6.1) and the ratio of ^{3}He and ^{129}Xe polarizations evolving in a SEOP cell after starting to polarize (Fig. 38) we can estimate the noble gas pressures for the desired duration of simultaneous polarization.

From this very basic estimate the complications of a clock comparison using ^{3}He as co-magnetometer become apparent. Take for example 2000 s of polarization time, which is already much longer than the anticipated cycle duration of several hundred seconds. Then very little ^{3}He is polarized compared to ^{129}Xe, the ratio is about 0.03. So for a cell pressure of $\approx 1.5\,\mathrm{bar}$ we obtain a ^{129}Xe pressure of 114 mbar (Eq. (6.1)), equal to $N^{\mathrm{Xe}} = p^{\mathrm{Xe}} V / k_{\mathrm{B}} T \approx 2.8 \times 10^{19}$ ^{129}Xe atoms in an EDM cell of $10\,\mathrm{cm}^3$ volume.

Assume the magnetization $M = (PN\mu)/V$ is aligned in z-direction $(0, 0, M)$ and the pickup coil in the xy-plane is centered at $\boldsymbol{r} = (0, 0, z)$. Then the dipolar magnetic flux density[43] generated by the magnetization M only has a component

$$B_z(\boldsymbol{r}) = -\frac{\mu_0 M V}{2\pi z^3}, \tag{6.2}$$

---

[43] The dipolar field of a magnetization M equals $\boldsymbol{B}(\boldsymbol{r}) = \mu_0(3\boldsymbol{r}(\boldsymbol{M}.\boldsymbol{r}) - \boldsymbol{M}r^2)/(4\pi r^5)$.

where μ_0 is the magnetic permeability.
At a distance of e.g.[44] $z = 22.5\,\mathrm{mm}$ the polarized ^{129}Xe atoms generate a magnetic field density of

$$B_{\mathrm{z}}^{\mathrm{Xe}} \approx \frac{\mu_0 \cdot P \cdot 2.8 \times 10^{19} \cdot 3.9 \times 10^{-27}\,\mathrm{J/T}}{2\pi(22.5\,\mathrm{mm})^3} \approx P \cdot 2\,\mathrm{nT}, \tag{6.3}$$

which is roughly a factor of 1.7 less than assumed for the EDM sensitivity estimate with $P = 0.3$ (Eq. (4.6)).
Arguing from the other perspective, a ^{129}Xe precession signal of magnitude 1 nT assumes about 200 mbar of ^{129}Xe polarized to 30%. On the other hand 1200 mbar of ^{3}He yield a signal of $B_{\mathrm{z}}^{\mathrm{He}} \approx P \cdot 56\,\mathrm{nT}$, hence needs to be polarized for about 4000 s to yield $P \approx 0.02$ or 1 nT signal, cf. Fig. 38.
A solution to these complications arising from the slow spin-exchange of alkali metals to ^{3}He could be a polarized ^{3}He reservoir. Luckily enough the very slow interaction and resulting long T_1 times help storing polarized ^{3}He. For a refilling cycle of the EDM cell ($10\,\mathrm{cm}^3$) of 200 s and 4000 s of ^{3}He polarization time a storage volume of order $200\,\mathrm{cm}^3$ is sufficient to supply polarized ^{3}He. This could be realized by polarizing gases in two separated volumes and subsequent mixing. A dedicated volume for SEOP of ^{3}He would also allow higher temperature to speed up the polarization process. A SEOP volume for ^{129}Xe at lower temperatures avoids high Rb density related decrease of ^{129}Xe polarization.
Another gas-mixture related issue is the achievable breakdown voltage, as it may strongly depend on the composition. For EDM cells of 0.2 to 2 bar total pressure and cm size breakdown due to gas discharge is expected beyond 10 kV/cm.
Besides a refilling system for both ^{3}He and ^{129}Xe the development of a (valved) EDM cell with electrodes and T_2 relaxation times of several hundred seconds for both species is a major task. Progress regarding the EDM cell and first measurements with high voltage will be presented in Sec. 6.2.
An overview of the current (test) setup outside and inside the MMSR is shown in Fig. 39 and described in the following section.

6.1 The SQUID system and polarization setup

For the first measurement runs we temporarily used a SQUID system provided by PTB Berlin [155]. Six SQUID magnetometer are mounted on the sides of a cube (cf. Fig. 39) in a small liquid helium dewar. The warm-cold distance in this system is as long as $d = 70\,\mathrm{mm}$, which significantly downsizes the detected signals due to geometry. Development of a new system is underway and planned according to the requirements of the EDM experiment. The new SQUID system will have SQUID current sensors with external pickup coils[45] in only millimeter distance to the warm bottom of the dewar. The six channels (X1, Y1, Z1, X2, Y2, Z2) of the SQUID cube of 30 mm side length are connected to two FLL electronic boxes (Magnicon) and the FLL voltage output is acquired with a

---

[44] The distance chosen arises from the anticipated distance in the future helium dewar, see Sec. 6.2.3.
[45] A similar system with differently sized pickup coils is used in the liquid xenon EDM, cf. Sec. 5.

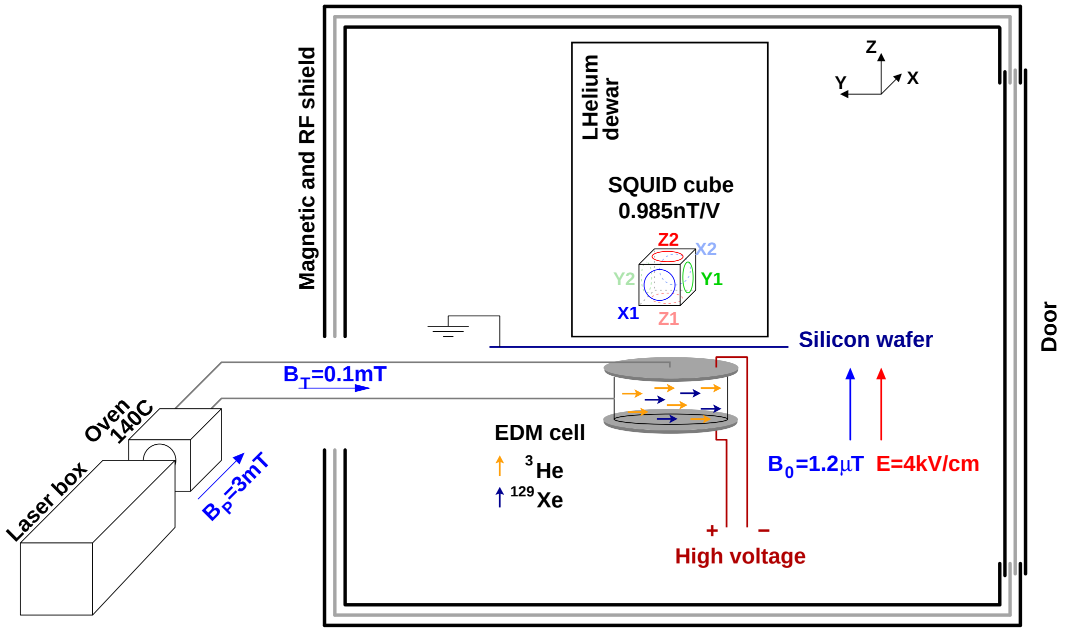

Fig. 39: Overview of the ^{3}He-^{129}Xe clock comparison EDM experiment. An EDM cell and the SQUID detection system is placed inside the Munich magnetically shielded room, which provides an environment of low magnetic field gradients ($\lesssim 1\,\mathrm{nT/m}$) and very low residual fields ($\approx 1\,\mathrm{nT}$). In the final version the polarized gas will be refilled to an EDM measurement cell through a closed flow system as indicated.

24-bit USB DAQ box (Data Translation, DT 9826-16 USB).

Another SQUID system intended as a magnetic field probe for magnetically shielded rooms was also developed throughout the course of this thesis, but is beyond the scope of this work and not further discussed. A cryogen-free system was shown to operate a three-axis SQUID magnetometer or gradiometer on the tip of a 3 m long copper rod and can be inserted into a magnetically shielded room through holes of only 50 mm diameter. The setup to polarize both ^{129}Xe and ^{3}He is close to the central hole at the back-side of the MMSR, Fig. 39. Due to the requirements for SEOP of ^{3}He previously described (Sec. 3.2.1) the setup is somewhat different to the one used in the liquid xenon EDM setup (Sec. 5.4). Since the spin-exchange of ^{3}He-Rb[46] is very slow, we implemented a 100 W laser diode array to maintain alkali polarization at 100 % even throughout higher volume pumping cells. In principle, a small fraction of the power could be used to polarize ^{129}Xe and the remaining power to polarize an optically thick Rb vapor at elevated temperatures in a second cell to speed up ^{3}He polarization buildup. The diode array is supplied by up to 100 A with it's emission wavelength controlled by the cooling water flow. The broad emission line is narrowed by reflecting back light from a grating which is oriented so that the reflected light preferentially stimulates diode emission at

---

[46] Spin-exchange is generally rather slow independent of the alkali metal used compared to spin-exchange of alkali metals with ^{129}Xe .

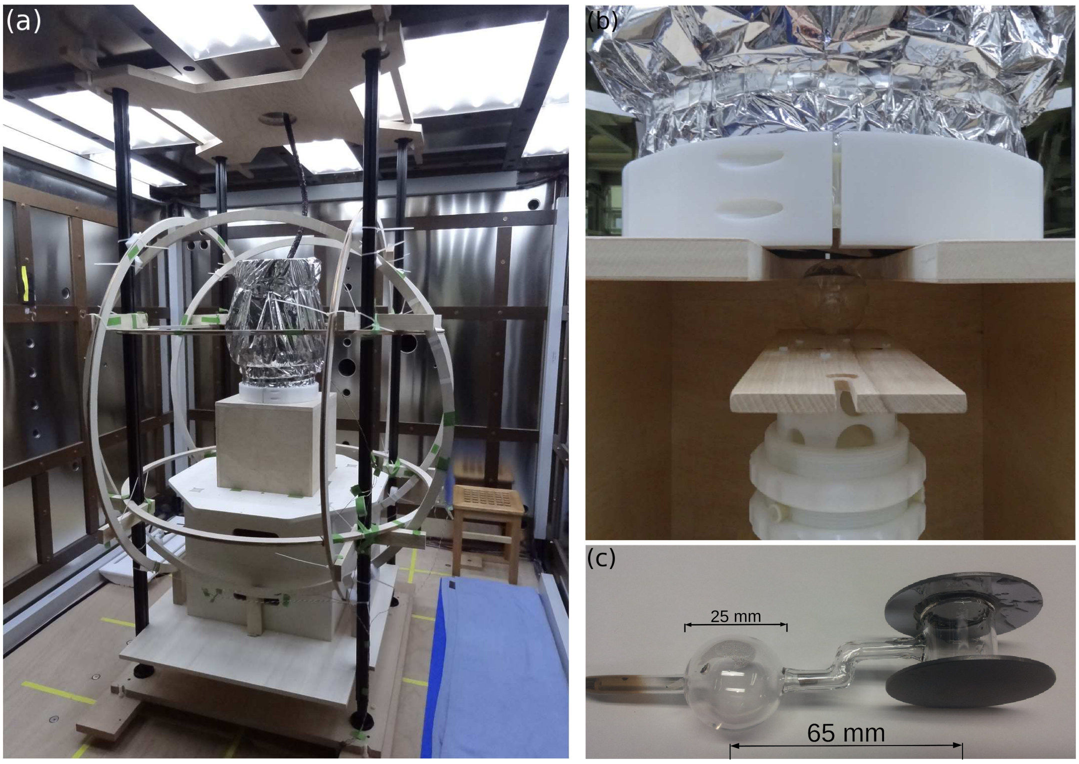

Fig. 40: (a) The setup of Helmholtz coils and SQUID dewar inside the magnetically shielded room used for test measurement runs. (b) The PTB glass bulb mounted underneath the SQUID dewar. (c) Prototype EDM cell with pumping and measurement chambers. Two silicon wafers as electrodes are bonded to a glass cylinder (GE180).

794.8 nm. The emitted light is sent through the usual optics to circularly polarize the photons and enters an oven in a round shape of about 60 mm diameter.
Typical magnetic fields used for SEOP and polarized gas transport are shown in Fig. 39.

6.2 Progress and test measurement results

In two test runs we made significant progress towards an upcoming EDM run. In the subsequently following sections I will present results and their implications on the way to an upcoming EDM run planned for 2015. First, I introduce some technical details on data analysis and the measurement procedure.

Data analysis and fitting

The spin precession data discussed was processed the following way. The FLL electronics provide outputs for six SQUIDs mounted on the SQUID cube (Fig. 39). As all the SQUID loops point inwards a gradiometer signal is obtained by summing SQUID channels of one axis. If not using the acquired lock-in signal the sum Z1+Z2 is calculated and bandpass filtered in software (Python, SciPy) with a width of 1 Hz and the appropriate center frequency. The fits processed in ROOT used exponentially decaying sine waves with a linearly drifting frequency

$$f([A, f_\mathrm{L}, \delta f, \varphi, T_2, b], t) = A \sin(2\pi(f_\mathrm{L} + (\delta f)t)t + \varphi)e^{-t/T_2} + b. \tag{6.4}$$

The signals from channels Z1 and Z2 are also simultaneously added and fed to two lock-in amplifiers referenced at 14.0 Hz and 40.0 Hz for ^{129}Xe and ^{3}He , respectively. An amplitude modulated decay function according to

$$f([A, f_\mathrm{M}, f_\mathrm{L}, \varphi, T_2, b], t) = A \sin(2\pi f_\mathrm{M} t) \sin(2\pi f_\mathrm{L} t + \varphi)e^{-t/T_2} + b \tag{6.5}$$

was used for the ^{3}He lock-in signal from two-chambered cells, as they show a strong beat signal. The fit parameter f_M yields the modulation or beat frequency.

The standard procedure for tests of sealed cells

In the first runs when the polarizing setup was not yet available at the MMSR cells were filled with polarized ^{129}Xe in the liquid xenon lab (Sec. 6.2.1) or ^{3}He cell polarized in Earl Babcock's lab upstairs of the MMSR (Sec. 6.2.2) and subsequently transported to the MMSR in appropriate holding fields. For measurements with prototype EDM cells (Fig. 40 (c)) in the second run the laser setup behind the MMSR was completed and used to polarize both noble gases via SEOP. The polarizing bulb was kept in the oven at ≈ 140 °C for at least 1 hour before it was slowly taken along the stray field of the polarizer. The cells were handed over into the degaussed MMSR through the magnetic field coil of the transporter, which was kept aligned to the hole and close to the wall. This provided a reasonable holding field through the two-layered wall of the MMSR where zero-crossings of the magnetic field need to be avoided. Before a spin-flip started spin precession the transport coil was slowly removed from the hole at the back wall. Precession was either started by non-adiabatically switching the magnetic field from the transport field B_y to B_x or by spin-flip pulses transverse to the transport field. Very stable (static) currents[47] were provided by a ultra-low noise current source from I-Test Systems (BE2100). Spin-flips were induced by a standard frequency generator (Agilent, 33220A).

6.2.1 A first spin-precession signal of ^{129}Xe

For first tests we transported polarized gas from the liquid xenon EDM lab (Sec. 5.4) over to the MMSR, which is roughly a 1 km car ride. The bulb of 60 mm diameter provided by PTB previously featuring $T_2^* \approx 4200\,\mathrm{s}$ in the Berlin magnetically shielded room was placed just below the SQUID dewar, cf. Fig. 40 (b). Fig. 41 shows one of the first ^{129}Xe precession signals in the MMSR ever acquired. The bulb contained a total pressure of 1.6 bar (±5%). The gases were mixed at ratios Xe:N$_2$:He=1:1:18, hence the

---

[47] After warm-up the drift of the current is on the order of 10 pT over 1000s.

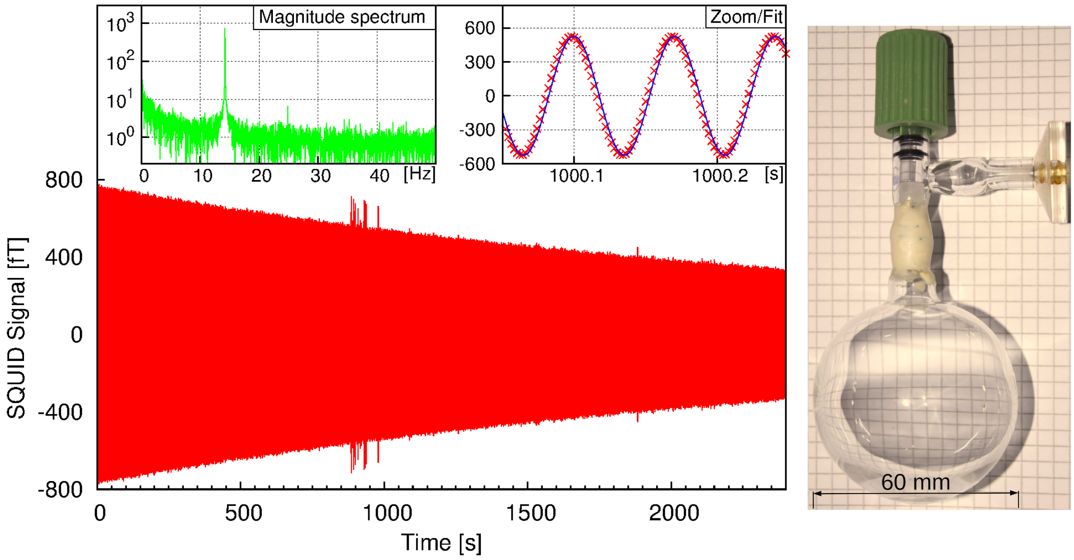

Fig. 41: One of the first precession signals of ^{129}Xe in the magnetically shielded room with $T_2^* = 2836\,\mathrm{s}$. A pure glass cell provided by PTB Berlin filled with 80 mbar of natural Xe from the polarizer of the liquid xenon EDM lab and transported to the MMSR by car. The signal has a signal-to-noise ratio of ≈ 300 at the precession frequency of 14.2 Hz. Deviations from the fit function arise from small non-linear drifts in the holding field that the fit doesn't account for.

cell contained $80.5 \pm 5\%$ mbar of natural xenon.

The cell was filled by expanding a 4 bar gas mixture used in the polarizing cell ($V \approx 18\,\mathrm{cm}^3$) to the evacuated glass bulb. At the same time the polarizer (Sec. 5.4) inlet valve was opened to push most of the polarized gas to the bulb with the line pressure. The tubing (PFA, Swagelok) followed the fringe field from the polarizer holding field coils generating 7 mT in the oven. Transport in the car was done in a transporter with a holding field of about $100\,\mu\mathrm{T}$ inside a 3-layer μ-metal shield.

From the observed signal size and Eq. 6.2 the remaining ^{129}Xe polarization in the MMSR can be estimated using

$$B_{Z1} - B_{Z2} = \frac{\mu_0}{2\pi} \frac{p^{\mathrm{Xe}} V^{\mathrm{cell}}}{k_{\mathrm{B}} T} \mu^{\mathrm{Xe}} \cdot P \cdot \left((100\,\mathrm{mm})^{-3} - (130\,\mathrm{mm})^{-3} \right) \approx P \cdot 0.1\,\mathrm{nT}, \tag{6.6}$$

which yields a degree of polarization of $P = 800\,\mathrm{fT}/(0.1\,\mathrm{nT}) = 0.8\%$. This result seemed very reasonable starting off with several ten percent polarization in the polarizing cell of the liquid xenon lab. The successful transport did prove, that we are able to easily hand a cell of polarized gas in the MMSR through a hole in the back without loosing more than one order of magnitude of polarized gas.

An exponentially decaying sine fit to the data yields a $T_2^* = 2836 \pm 0.2\,\mathrm{s}$ which is a factor of about 1.5 lower than previously obtained at PTB. However, at PTB the xenon partial pressure was only 50 mbar, hence the dependence of Eq. (3.41) on pressure accounts for this decrease since $80\,\mathrm{mbar}/50\,\mathrm{mbar} \approx 1.6$. From $T_2^* = 2836\,\mathrm{s}$ the magnetic

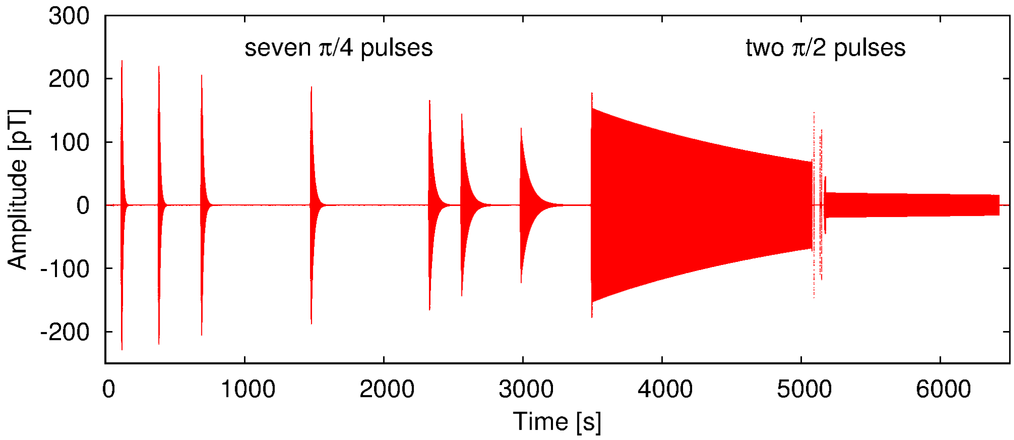

Fig. 42: A sequence of seven $\pi/4$ and two $\pi/2$ pulses applied to a sealed cell of 1 bar of highly polarized ^{3}He. The transverse relaxation time is rather short ($\approx 5-58\,\mathrm{s}$) as long as the longitudinal magnetization persists, particularly after $\pi/4$ pulses. See the text for a more detailed discussion.

field gradient in this measurement can be determined according to Eq. (3.41), using the adapted diffusion coefficient of ^{129}Xe in the gas mixture, Eq. (A.15). A limit on the magnetic field gradient in holding field direction (y) is obtained as

$$|\nabla B_{\mathrm{y}}| = \sqrt{\frac{175 \cdot 0.28\,\mathrm{cm}^2/\mathrm{s}}{8 \cdot (30\,\mathrm{mm})^4 \cdot (2\pi \cdot 11.777\,\mathrm{MHz/T})^2 \cdot T_2^*}} \approx 7\,\mathrm{nT/m}, \tag{6.7}$$

which can mostly be attributed to inhomogeneities due to imperfections in the field coils. The presented data of xenon spin-precession in the MMSR demonstrates the feasibility of the concept of introducing polarized gas through a hole in the wall. The observed transverse spin-relaxation times of xenon were highly encouraging for the EDM cell development. Measurements using EDM cells with silicon electrodes and obtained T_2^* are presented in Sec. 6.2.3.

6.2.2 Spin-flip sequence on highly polarized ^{3}He

In the EDM search approach with a co-magnetometer an effect that needs to be well studied is the self-interaction and coupling of both species, particularly at high pressures and polarizations.

To start these studies I'll discuss some features of the data, which is very rich in physics from a run with a ^{3}He cell called "Maya", that was polarized overnight. The type of cell with a ^{3}He pressure of 1 bar is usually used in polarized neutron experiments and is known to have longitudinal relaxation times of many hundreds of hours. The long polarization time in a high power laser beam and low spin-destruction rate yields a very high polarization of several ten percent.

In this run with the "Maya" cell containing 1 bar of highly polarized ^{3}He a sequence of seven $\pi/4$ and two $\pi/2$ spin-flip pulses was applied. In-between pulses the transverse magnetization was destroyed by applying a magnetic field gradient. Fig. 42 shows the bandpass filtered Z gradiometer signal of this run.

Off-resonant spin-flips

Clearly the T_2^* time grows as subsequent pulses are applied and is much longer after the last two $\pi/2$ pulses. Since the T_1 time is at least on the order of tens of hours the decrease in longitudinal magnetization due to relaxation can be neglected.

A first obvious feature of the data is, that the inital amplitudes only decrease slightly, although a loss of longitudinal magnetization of roughly $\sin(\pi/4) = 1/\sqrt{2}$ is expected for each spin-flip. In contrast to a perfectly spherical cell, the magnetization in the cylindrical cell ($\approx 100\,\mathrm{mm}$ diameter, $50\,\mathrm{mm}$ height) of $\approx 400\,\mathrm{cm}^3$ volume (10^{21} polarized atoms) generates an intrinsic local magnetic field of order $500\,\mathrm{nT}$. In a holding field of only $1.2\,\mu\mathrm{T}$ this amounts to 10%, which renders the spin-flip pulse off-resonant and inefficient.

The actual gradiometer signal expected after a $\pi/4$ flip is on the order of

$$S = \frac{1}{\sqrt{2}}\frac{\mu_0}{2\pi} \cdot 10^{21} \cdot \mu^{\mathrm{He}} \cdot \left((120\,\mathrm{mm})^3 - (150\,\mathrm{mm}^3)\right) \approx 400\,\mathrm{pT}. \tag{6.8}$$

From this rough estimate the spin-flip efficiency is about 1/2.

Spin-flip accuracy

From the two datasets following the $\pi/2$ pulses the accuracy of the spin-flips can be determined. The (small) error in flip-angle is $\delta\theta \approx \delta a/a_0$, where a_0 is the initial magnetization and δa_0 the remaining longitudinal magnetization. The ratio of the amplitudes of subsequent $\pi/2$ pulses gives the error in flip angle

$$\frac{a_1}{a_2} = \frac{a_0\sqrt{1+\delta\theta^2}}{\delta a\sqrt{1+\delta\theta^2}} = \frac{1}{\delta\theta}. \tag{6.9}$$

The amplitudes from the fitted decaying sine functions yield $\delta\theta = 0.13248\,(\pm 5.2 \times 10^{-5})$, hence an accuracy of an applied 90° pulse of 7.6° or about 10%.

Dipolar gradient limited transverse relaxation

Also clearly indicated is an increase of T_2^* as longitudinal magnetization is subsequently reduced and becomes much longer after the $\pi/2$ pulses. This indicates, that the gradient due to the dipolar field of the longitudinal magnetization vanishes and is not limiting T_2^* any more.

The initial amplitudes and precession frequencies of the free induction decays are obtained by fitting decaying sine functions (see Fig. 43 (b) for an example). The transverse relaxation time is expected to obey a inverse-square law dependence on the initial amplitude and frequency of the free induction decay (Fig. 43) as $T_2^{-1} \propto |\nabla B_z|^2 \propto B^2 \propto M^2$(Eq. (3.41)). The observed initial precession amplitudes and precession frequencies of

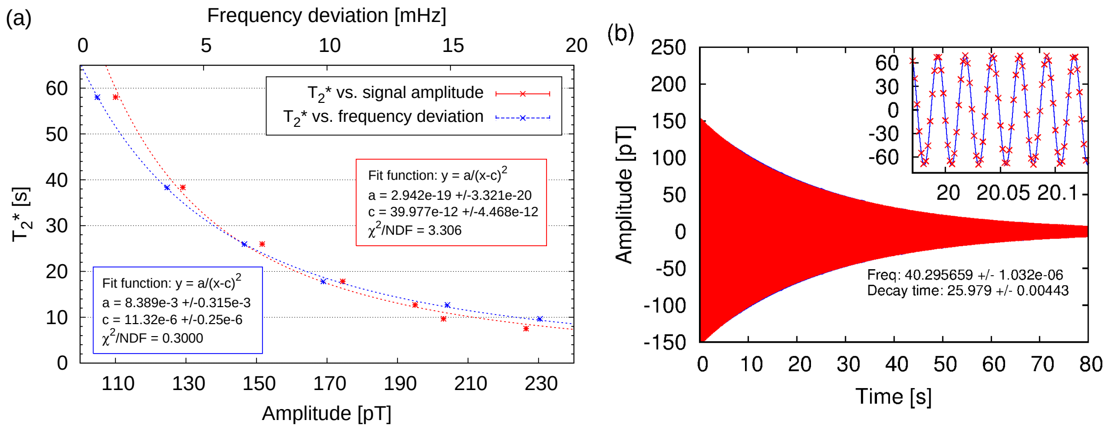

Fig. 43: (a) The transverse relaxation times T_2^* of highly polarized ^{3}He for a sequence of seven $\pi/4$ spin flips plotted depending on the initial amplitudes and the precession frequency deviation. Both show a similar decrease $\propto x^{-2}$ due to the gradients caused by longitudinal magnetization. (b) An example of a exponential decaying sine fit to the free induction decay signal following a $\pi/4$ pulse.

the free induction decays are directly proportional to the remaining longitudinal magnetization. Inverse square law fits qualitatively agree well with the data, but interpretation is difficult as the gradients strongly depend on geometry. However, the data represents the effect of the gradient of the intrinsic longitudinal dipole on the spin-coherence time of the transverse magnetization.
An estimate on the gradient can be obtained with the relation for a spherical cell[48] as

$$|\nabla B_{\mathrm{y}}| = \sqrt{\frac{175 \cdot 1.8\,\mathrm{cm}^2/\mathrm{s}}{8 \cdot (50\,\mathrm{mm})^4 \cdot (2\pi \cdot 32.434\,\mathrm{MHz/T})^2 \cdot T_2^*}}, \tag{6.10}$$

yielding average gradients for the $\pi/4$ sequence of $45\,\mathrm{nT/m}$ to $16\,\mathrm{nT/m}$ for T_2^* equal to $7.5\,\mathrm{s}$ and $58\,\mathrm{s}$, respectively. The expected order of magnitude of a gradient in the direction of a $100\,\mathrm{nT}$ dipolar field is of order $\partial B_{\mathrm{y}}/\partial y = 3rB_{\mathrm{y}} \approx 15\,\mathrm{nT/m}$ in a cell of radius $R = 50\,\mathrm{mm}$, which roughly agrees with obervations.

Free induction decay at reduced dipolar field gradient

The free induction decays after $\pi/2$ spin-flips yield $T_2^* \approx 1950\,\mathrm{s}$ and $T_2^* \approx 3200$, which corresponds to significantly reduced $\nabla B_{\mathrm{y}} \approx 3\,\mathrm{nT/m}$ and $\nabla B_{\mathrm{y}} \approx 2\,\mathrm{nT/m}$.

The decay after the first $\pi/2$ pulse clearly shows an increase in T_2^* (Fig. 44 (a)) and is not described by a single decay time (Fig. 44 (b)). Fits results are obtained by cutting the dataset of 1500 s into 250 ms intervals of ten Larmor precession periods and then fitting non-decaying sine functions. In Fig. 44 are plotted the fitted frequencies and amplitudes of the intervals. An exponential decay fit to the amplitude plot yields the T_2^* relaxation time.

---

[48] The “Maya” cell is actually of cylindrical shape.

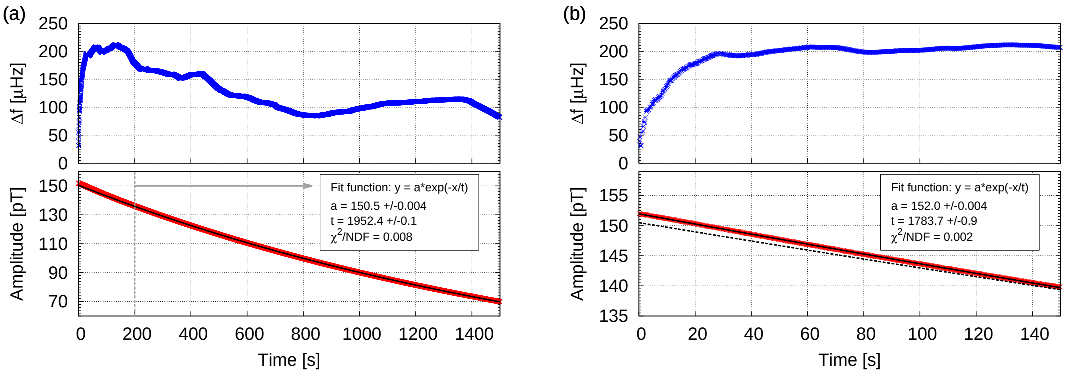

Fig. 44: (a) The frequency deviation Δf and amplitude of sequential fits to precession data following the first $\pi/2$ pulse. The spin-coherence time is significantly increased to 1952 s in the data after $t = 200$ s. Also plotted is the fitted frequency during the free induction decay showing magnetic field drifts in B_y direction of order 3 pT. (b) Zoom of the first 150 s of (a). In this data the decay deviates and an exponential fit (black line) yields $T_2^* = 1784$ s. For comparison the dashed line indicates the decay function of the subsequent data. The frequency deviation represents a change of the average magnetic field of 4.6 pT.

In the first about 100 s the decay is described by a spin-coherence time of 1784 s rather than 1952 s obtained in the remaining data. This suggests that two decay constants dominate the decay. If gradient dominated, the magnetic field gradient changes slightly from about 3.0 nT/m to 2.8 nT/m during that time. Presumably in the first 100 s a dipolar self-gradient generated by longitudinal magnetization vanishes due to spin-flips induced by the precessing transverse magnetization. At later times spin-coherence might be limited by the residual gradient of the Helmholtz coils[49].

The change in precession frequency indicates an initial magnetic field change of 4.6 pT or about 10^{-6} relative to the holding field, which might be representing a decay. The increase of magnetic field could indicate an equilibration process of the overall system, e.g. the magnetic shielding material. Details on the origin of these effects caused by ^{3}He self-interaction need to be clarified in further measurements.

This first superficial study shows the great importance of suppressing or well understanding ^{3}He self-interaction effects on spin precession. The presented measurements can be interpreted as a worst case scenario of self-interaction. A more careful study together with simulations is essential to determine the consequences on co-magnetometry in the (non-spherical) EDM cell.

6.2.3 Spin-precession of both species in an electric field

EDM cell development

A main design task in our clock-comparison approach for an EDM search is the development of a suitable measurement cell. With the high sensitivity detection scheme that SQUIDs provide any metallic surface can introduce noise due to randomly mov-

---

[49] The gradient may slightly deviate from the measurement in 6.2.1 due to cell position.

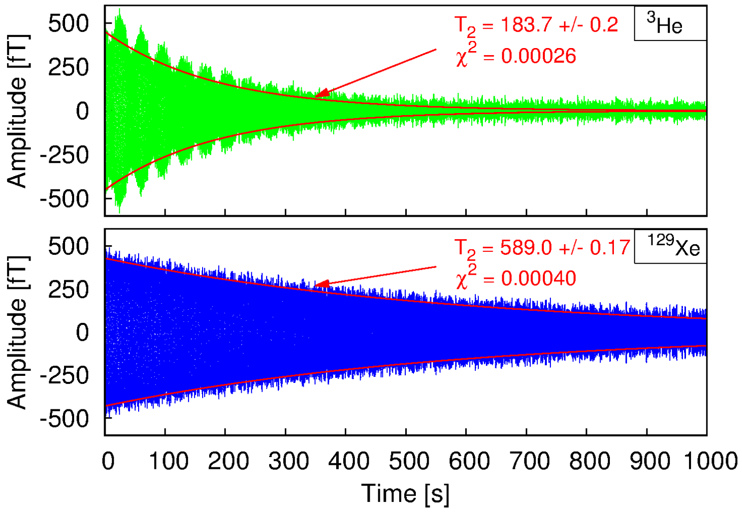

Fig. 45: Decaying precession signals of both ^{3}He and ^{129}Xe in a 12.3 cm^3 EDM prototype cell (F3) with no voltage applied acquired after a non-adiabatic field switch. The spin-precession shows transverse relaxation times of 184 and 589 s for ^{3}He and ^{129}Xe, respectively. One third of the total surface area of 29.5 cm^2 consists of the polished silicon electrodes. A beat frequency of about 27 mHz from spin-precession in the polarizing bulb is visible in the ^{3}He precession.

ing electrons (Johnson noise). If electrodes are placed above and below a glass cell the electric field in the cell is reduced due to the dielectric glass. For these reasons we aim to introduce silicon electrodes and successfully tested first sealed EDM prototype cells. The prototype cells used for the measurements discussed were made at the University of Michigan.

A bulb of 25 mm diameter filled with rubidium for SEOP is attached to a cylindrical EDM cell, cf. Fig. 40 (c). The EDM cell is made of a cylinder of 25 mm diameter and 25 mm height (GE180) with both ends closed by thick silicon wafers with rounded edges. The main challenge is the leak-tight bonding of silicon to GE180. We want to avoid any kind of glue as it might introduce issues with high voltage, like sparks or degradation that causes leakage of oxygen. Tests of bonding silicon electrodes to GE180 already yielded promising results, but were not yet available for an EDM cell. The prototype EDM cells are the results of first bonding tests of silicon to borosilicate (or pyrex) cylinders by Skyler Degenkolb. As the process still needs to be optimized glue (Hysol C1 and transparent UV curing glue) was applied for proper leak-tightness.

The sealed prototype cells contain 59 mbar of ^{129}Xe , 784 mbar of ^{3}He and 51 mbar of N_2, summing to 894 mbar total pressure. In the polarizing setup the bulb with rubidium was exposed to heated air and 794.8 nm laser light inside the oven, while keeping the EDM cell at room temperature. With an additional bend in the connecting tube the passage of rubidium vapor to the EDM cell is inhibited to avoid ^{129}Xe spin-destruction (cf. Tab. 3.1).

Data from a run with EDM prototype cell F3 (no high voltage applied) yields a transverse spin-relaxation time of ^{3}He and ^{129}Xe of 184 s and 589 s, respectively (Fig. 45). Yet no spin-relaxation rates of ^{129}Xe wall collisions with silicon have been reported. Without further studies we can set a limit on the relaxation rate from the observed T_2^*.

A limit on ^{129}Xe wall relaxation on silicon surfaces

In our cell of glass and silicon surfaces the polished silicon electrodes amount to $A_{\mathrm{Si}} \approx 9.8\,\mathrm{cm}^2$ at a total volume of the EDM cell and polarizing bulb of $V \approx 21.3\,\mathrm{cm}^3$. To set a limit on wall relaxation on silicon, the total transverse spin relaxation rate can be assumed to be dominated by the wall relaxation on silicon, hence

$$\Gamma^{\mathrm{tot}} = \Gamma^{\mathrm{grad}} + \Gamma^{\mathrm{glass}} + \Gamma^{\mathrm{Si}} \approx \Gamma^{\mathrm{Si}}, \tag{6.11}$$

where relaxation due to diffusion in gradients Γ^{grad} and wall relaxation on glass surfaces Γ^{glass} is neglected as both are assumed to be much smaller.
Under this assumption and scaling to the silicon surface area, volume and ^{129}Xe pressure a rough estimate on wall relaxation of a silicon surface of area A in a cell of volume V and a ^{129}Xe partial pressure of p is obtained as

$$\Gamma^{\mathrm{Si}} \lesssim \frac{1}{589\,\mathrm{s}} \frac{21.3\,\mathrm{cm}^3}{9.8\,\mathrm{cm}^2} \cdot 59\,\mathrm{mbar} \approx 2.2 \times 10^{-4} \frac{A}{V} \frac{1}{p} \frac{\mathrm{cm} \cdot \mathrm{bar}}{s}. \tag{6.12}$$

As can be seen in Fig. 45 the ^{3}He signal dephases very quickly, on the order of ten times faster than previously measured. The reason might not be depolarization on the polished silicon surface but rather cracks and rough surfaces at the interfaces of the GE180 cylinder and the silicon electrodes. This needs to be solved by improved bonding and further analyzed in the future. However, the long relaxation times observed for ^{129}Xe strongly motivate further studies of silicon electrodes and bonding techniques to improve on ^{3}He relaxation.

Beat frequency in the EDM cell

Another feature in Fig. 45 can be attributed to the geometry currently used prototype cells with two chambers of similar volumes. The ^{3}He precession exhibits a beat frequency in the EDM cell originating from ^{3}He precession in the polarizing bulb. The beat frequency is around 27 mHz and is not observable in ^{129}Xe precession. Due to higher pressure and gyromagnetic ratio the impact of precessing ^{3}He is a factor of ≈ 40 stronger than by ^{129}Xe. The beat frequency translates into a magnetic field deviation in z-direction of $27\,\mathrm{mHz}/(32.4\,\mathrm{Hz}/\mu\mathrm{T}) = 0.8\,\mathrm{nT}$ over the 65 mm between polarizing bulb and EDM cell. Hence a (linear) gradient $\partial B_{\mathrm{z}}/\partial z$ of order $13\,\mathrm{nT/m}$ can be estimated, which presumably originates from the magnetic field coils.

High voltage test runs

Prototype EDM cells F3 and F4 were both tested with high voltage applied to the electrodes using a high-voltage amplifier (Trek 610E). No sparks outside the cell were

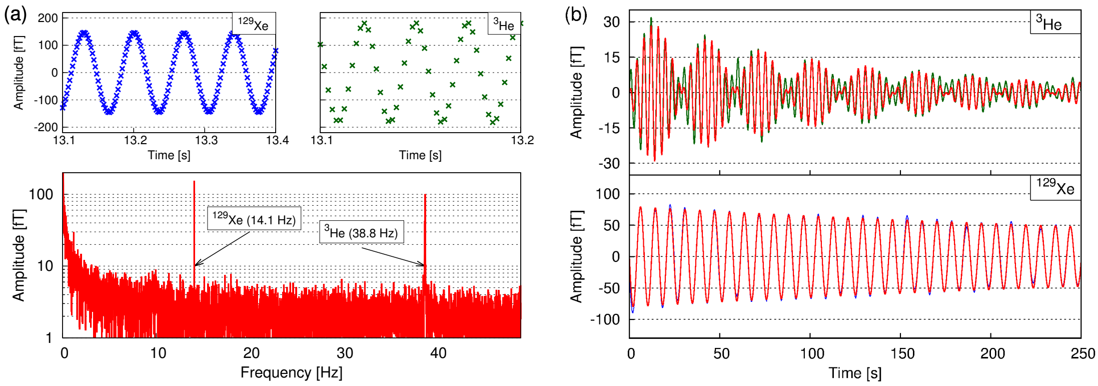

Fig. 46: (a) First simultaneous precession of ^{129}Xe and ^{3}He in a sealed EDM prototype cell (F3) with ±5 kV applied to silicon electrodes. The signals of both species in the measurement chamber show irregular beat frequencies of yet unknown origin, hence oscillating amplitudes. Fits to the data yield transverse relaxation times T_2^* of about 493 s and 160 s for ^{129}Xe and ^{3}He, respectively. (b) Lock-in detection of precession signals in a EDM prototype cell (F4) induced by a combined 45° spin-flip for ^{3}He (green) and ^{129}Xe (blue). From the fits (red line) the T_2^* times are deduced to be 478 s and 125 s for ^{129}Xe and ^{3}He , respectively. The ^{3}He signal exhibits a beat frequency of about 0.017 Hz supposed to originate from ^{3}He precessing in the polarizing bulb.

observed, but discharges typically appeared at 6-8 kV. The minimum breakdown voltages are presumably determined by the low-pressure xenon and not by structural effects of the EDM cells or the glue. These findings allowed for first high-voltage tests with polarized gas. To protect the SQUIDs from the threat of electric discharges a grounded silicon wafer of 150 mm diameter was placed between the EDM cell and the SQUID dewar (Fig. 39).

In two runs using different EDM prototype cells (F3, F4) simultaneous spin precession of ^{3}He and ^{129}Xe in an electric field was successfully observed. The EDM prototype cell was mounted in a vertical arrangement. In Fig. 46 (a) the frequency spectrum of a 90 s long run is shown with two clear peaks from ^{3}He and ^{129}Xe . The cell was polarized for about 1 hour in the polarizing setup behind the MMSR before being handed through the back wall. Due to the size of the electrodes (30 mm diameter) the cell was not placed as close to the dewar bottom as cells without electrodes. The peak amplitudes of ^{129}Xe and ^{3}He of 150 fT and 100 fT were observed at background noise levels of 5.5 fT and 4 fT, respectively. We found, that applying high-voltage did not significantly increase in the noise detected by the SQUIDs.

The insets in Fig. 46 (a) show the bandpass-filtered precession signals taken after a non-adiabatic field switch. Over the whole range beat signals of various frequencies disturb the signal. However, the fits yield reasonable results in agreement with an independent measurement with lock-in detection using cell F4. Fig. 46 (b) shows data after a $\pi/4$ spin-flip acquired using two lock-in amplifiers for ^{129}Xe and ^{3}He .

In the lock in data of ^{3}He the beat frequency corresponds to the observations of prototype EDM cells without high-voltage, Fig. 45.

The transverse decay times are deduced from decaying sine fits to both filtered gradiometer data using an adiabatic field switch and lock-in data using a $\pi/4$ spin flip. For ^{129}Xe two independent high voltage measurements yield $T_2^* = 493\,\mathrm{s}$ and $T_2^* = 478\,\mathrm{s}$. From the ^{3}He co-magnetometer data we obtain $T_2^* = 160\,\mathrm{s}$ and $T_2^* = 125\,\mathrm{s}$.

If faster dephasing is due to gradients introduced by the high-voltage setup, the magnitude of the gradients need to be on the order of[50] 760 nT/m for ^{129}Xe and 1000 nT/m for ^{3}He to appropriately limit T_2^*, which would indicate considerable magnetic contamination. More likely dephasing is caused by the coupling between EDM cell and polarizing bulb inducing permanent spin-flips. The origin of shorter spin relaxation times compared to the measurement without applied voltage (Fig. 45) needs to be clarified in further high-voltage tests and with improved prototype EDM cells.

In the lock-in data of precession at a tip angle of $\pi/4$ the remaining longitudinal polarization might decrease the T_2^* time due to dipolar gradients. In this case ^{3}He is of similar pressure but the degree of polarization is at least one order of magnitude smaller compared to the highly polarized cell in Sec. 6.2.2.

EDM sensitivity of high-voltage test runs

With the achieved observation time of 90 s the fundamental EDM sensitivity (Eq. (4.5)) of this run would yield an EDM sensitivity of

$$\sigma_\mathrm{d} = \frac{\hbar}{2 \cdot 10\,\mathrm{kV}/2.5\,\mathrm{cm}} \frac{2\,\mathrm{fT}/\sqrt{\mathrm{Hz}}}{(90\,\mathrm{s})^{3/2} \cdot 100\,\mathrm{fT}} \approx 1.9 \times 10^{-24}\, e\mathrm{cm} \tag{6.13}$$

in a single run. This is a great achievement for a non-optimized first electric field run. Under these conditions one day of data with 50% duty-cycle can statistically take the limit below $10^{-25}\,e$cm. Even more, some improvements are rather straightforward as will be discussed later. First, I want to give a simple discussion on the sizes of acquired precession signals.

Discussion of the precession signal amplitudes

In the present measurements the distance to the EDM cell center is about 95 mm[51], which is far from ideal.

A point under discussion is the generally weak signal even if considering the long distance to the pickup coil. For an order of magnitude estimation I will employ the simple calculation previously used (Eq. (6.2)).

The number of atoms N in an EDM cell of volume 12.3 cm^3 is

$$\begin{aligned} N^\mathrm{He} &= \frac{p^\mathrm{He} V}{k_\mathrm{B} T} \approx 2.3 \times 10^{20} \\ N^\mathrm{Xe} &= \frac{p^\mathrm{Xe} V}{k_\mathrm{B} T} \approx 1.8 \times 10^{19}. \end{aligned} \tag{6.14}$$

---

[50] Approximating the EDM cell to be spherical with radius 12 mm and using adapted diffusion coefficients for the gas mixture in the cells, $D^\mathrm{Xe} = 0.44\,\mathrm{cm}^2/\mathrm{s}$ and $D^\mathrm{He} = 1.68\,\mathrm{cm}^2/\mathrm{s}$ according to Sec. A.4 and Tab. A.2.

[51] This includes 70 mm cold-warm distance in the dewar and 25 mm imposed by the prototype cell geometry, when mounted in a vertical orientation below a grounded silicon wafer.

At the pickup coil the dipole of a magnetization $M = pN\mu$ - the sum of magnetic moments μ - placed in the center of the cell yields magnetic flux densities (Eq. (6.2))

$$\begin{aligned} B^{\mathrm{He}}(z = 95\,\mathrm{mm}) &\approx P^{\mathrm{He}} \cdot 580\,\mathrm{pT} \\ B^{\mathrm{Xe}}(z = 95\,\mathrm{mm}) &\approx P^{\mathrm{Xe}} \cdot 16.4\,\mathrm{pT}, \end{aligned} \tag{6.15}$$

where P^i denotes the degree of polarization. The difference in signal strength is due to the pressure and gyromagnetic ratios.

Due to the rejection of distant field sources the gradiometer signal is used for analysis. However in the current setup the ratio of gradiometer baseline to source distance (cf. Fig. 15 (b)) in the current SQUID dewar is far from ideal. The signal in the Z gradiometer is a factor of $(125\,\mathrm{mm})^3/(95\,\mathrm{mm})^3 \approx 2.3$ less than the real magnetic field density caused by the source. Additionally, in the data of the prototype EDM cells the effect of the second chamber is significant due to the geometry. The magnetization in the polarizing bulb, which is roughly the same volume and placed 65 mm away from the EDM cell, adds about $(95\,\mathrm{mm})^3/(160\,\mathrm{mm})^3 = 21\%$ to the Z1 signal, while adding about $(125\,\mathrm{mm})^3/(190\,\mathrm{mm})^3 = 28\%$ to Z2. Taking into account both of these factors, the degree of polarization P in a two-chambered EDM prototype cell is related to the Z gradiometer signal S^{grad} by

$$S^{\mathrm{grad}} = 1.21 B_{\mathrm{Z1}} - 1.28 B_{\mathrm{Z2}} = \left(1.21 - \frac{1.28}{2.3}\right) B_{\mathrm{Z1}} \approx \begin{cases} P^{\mathrm{He}} \cdot 380 & \mathrm{pT} \\ P^{\mathrm{Xe}} \cdot 10.7 & \mathrm{pT}. \end{cases} \tag{6.16}$$

For example, the initial ^{3}He and ^{129}Xe gradiometer amplitudes of $\approx 0.5\,\mathrm{pT}$ (Fig. 45) translate to degrees of polarization of 0.13% and 4.7%, respectively.

The estimated ^{129}Xe polarization is as expected and presumably reflects transport losses less than an order of magnitude. However the small ^{3}He polarization might need explanation. From the rate equations of SEOP (cf. Eq. (3.26), Fig. 8) one would typically expect a ^{3}He polarization of $\approx 1\%$ in a EDM prototype cell that was polarized for one hour. A study of polarization build up in the polarizing setup using an on-line NMR system needs to be taken out to actually determine the degree of polarization and to quantify the ^{3}He polarization losses during transport into the MMSR.

Improving EDM sensitivity

A main, very obvious improvement is a better suited sample to pickup loop distance and gradiometer baseline. In a new helium dewar currently developed particularly for this experiment the pickup coils will be mounted closer to the warm bottom. A dewar with a sapphire window can be set up with cold-warm distances of the pickup coil of several millimeters. A ground protection wafer of 1 mm thickness could be as close as 2 mm to the dewar and EDM cell. Even in air a 2 mm gap would withstand a voltage difference of 5 kV between EDM cell electrode and grounded wafer. However, for safety and higher electrode voltages a layer of high breakdown voltage gel could be applied. Assume a cold-warm distance of 5 mm and a horizontally oriented EDM cell (Fig. 39) of 25 mm height and 5 mm distance to the dewar. The signal will be increased by a

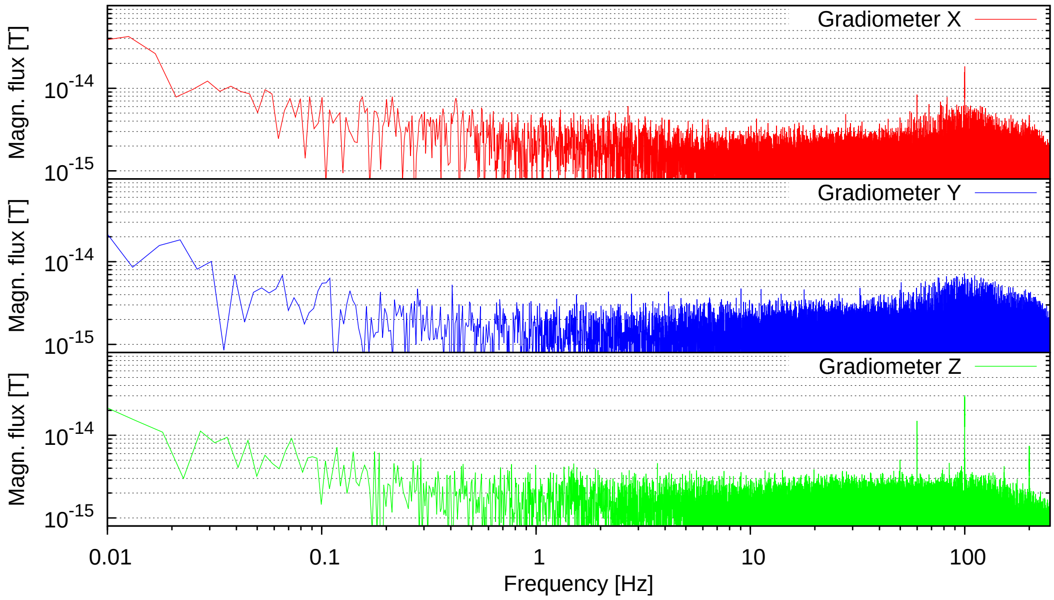

Fig. 47: Residual magnetic flux noise in SQUID gradiometers measured in the MMSR with the inner magnetic shielding installed. The He-Xe clock comparison experiment in this environment would benefit from a twofold improvement in sensitivity only due to the very high shielding factor.

factor of $(95\,\mathrm{mm})^3/(5\,\mathrm{mm}+5\,\mathrm{mm}+12.5\,\mathrm{mm})^3 = 75$.
Any decrease of precession signal due to subtraction by the second gradiometer coil can be neglected - e.g. is $\lesssim 1\%$ - if the gradiometer baseline exceeds 3.6 times the first coil's distance to the sample (cf. Fig 15 (b)). Assuming a EDM cell to pickup coil distance of 22.5 mm the gradiometer baseline should exceed 81 mm.
With a new dewar the improved geometry enhances the sensitivity of a single 90 s EDM run to $\sigma_\mathrm{d} \approx 3 \times 10^{-26}\,e\mathrm{cm}$.

Moreover the xenon signal size can be increased with higher ^{129}Xe pressure as long as the observation time and maximum degree of polarization is not affected. A factor of three seems feasible, by a moderate pressure increase to 180 mbar ^{129}Xe in the EDM cell. Furthermore reducing polarization losses by a conservative factor of two and prolonging the observation time to 250 s seem to be very reasonable. With these moderate and near future improvements, we aim to reach a single-run sensitivity level of $\sigma_\mathrm{d} \approx 1 \times 10^{-27}\,e\mathrm{cm}$, which translates into a statistical sensitivity per day (50% duty cycle) of

$$\sigma_\mathrm{d} \approx 8 \times 10^{-29}\,e\mathrm{cm}. \tag{6.17}$$

This corresponds to a nine-fold improvement on the current ^{129}Xe EDM limit. Note that the discussion is based on the fundamental sensitivity level (Sec. 4.2) and assumes a very good understanding of the systematic effects. The ^{3}He comagnetometer is perfect tool that can be thoroughly studied to account for these effects.

6.2.4 Potential of the magnetic shielding insert

Temporary installation of the inner shielding of the MMSR made possible a measurement of the noise floor in this highly shielded environment. The inner shield is a box of three layers of μ-metal and when installed yields a shielding factor of $\approx 10^6$ even at frequencies down to 100 mHz. The residual noise inside the inner shield measured with the X, Y, and Z gradiometers is shown in Fig. 47. Noise levels as low as 3 fT in the frequency range of interest are obtained . Assuming no other noise source, an EDM measurement would benefit by a factor of two higher sensitivity simply due to the reduction of background noise.

6.3 Summary of the He/Xe EDM search

This work presents a first overview of the most significant data taken in two test runs for the new He/Xe clock-comparison EDM experiment. The measurements show, that spin-precession in a high electric field can be successfully detected in prototype EDM cells of cylindrical shape with bonded silicon electrodes. In these cells wall relaxation of ^{129}Xe at the silicon surface was proven to be small enough to allow for several hundred seconds of observation time. The applied high voltage had no significant effect on spin-relaxation times and on the magnetic flux noise at the position of the SQUID cube in the current dewar. Under these conditions we showed that already now an EDM run can be performed with a sensitivity on the order of $\approx 10^{-24}\,e$cm for a single run of about 100 s.

Also a first study of self-interaction of polarized ^{3}He in a highly polarized cell gives first hints on the significance of these effects. Remaining longitudinal magnetization can strongly influence spin-precession in not perfectly spherical cells and introduce dipolar magnetic field gradients that limit transverse spin coherence times. Detailed studies of these self-interaction effects need to be carried out both experimentally and in simulations. A good understanding helps finding the optimal experimental parameters and can probably be used to account for this systematic in data analysis.

The co-magnetometer approach offers fast progress applying well known methods with now demonstrated improvements in EDM sensitivity well beyond current limits. An improved SQUID detection system adapted to the demands of this EDM experiment and very slight improvements will establish a sound basis for a single run sensitivity of $10^{-27}\,e$cm.

7 Conclusion and outlook

Limits on EDMs of fundamental systems have profound implications on interactions that violate $\mathcal{CP}$ symmetry. The best absolute EDM limit to date was obtained from the diamagnetic atom ^{199}Hg with the result $d_{\text{Hg}} \lesssim 3.1 \times 10^{-29}\,e$cm. These rather complex systems offer a wide range of coefficients of possible $\mathcal{CP}$ odd couplings that can be confined. However, further significant improvements in sensitivity are extremely challenging. Hence, in recent years the diamagnetic atom ^{129}Xe attracted interest, as it offers enhanced sensitivity to semileptonic $\mathcal{CP}$ odd couplings. Moreover, adding a new limit on the EDM of ^{129}Xe in the game improves current constraints on hadronic $\mathcal{CP}$ violating sources from the ^{199}Hg measurement by up to an order of magnitude.
Based on the distinguished nature of ^{129}Xe two complementary approaches to new exciting results were developed in the course of this thesis. With the demonstrated significant progress towards new EDM experiments ^{129}Xe can be used as a tool to study the different systematic effects as well as the particular physics reach. Both experiments potentially enhance the sensitivity on the current ^{129}Xe EDM limit of $\approx 10^{-27}\,e$cm by up to three orders of magnitude. The signal-to-noise ratio is significantly increased in very low magnetic holding fields by implementation of highly sensitive SQUID detection systems that exhibit noise levels in the fT range even at frequencies down to several Hz.
While the EDM experiment using a ^{3}He co-magnetometer is based on an established measurement technique and offers a moderate improvement in sensitivity on a short time scale, the liquid ^{129}Xe EDM experiment employs a novel method of time-varying electric fields requiring extensive R&D work, but featuring a high gain in sensitivity. Nevertheless, the systematic effects that commonly limit EDM sensitivities are utterly different in both experiments. Each of these approaches offers a certain balance between the time scale of expected results and the potential boost in EDM sensitivity. Combined they offer very powerful tools to cross-check results.

7.1 Progress towards a liquid ^{129}Xe EDM experiment

Progress and the achievement of milestones towards a liquid xenon EDM search which also employs a novel measurement technique is presented in Sec. 5. With this approach we intend to ultimately improve the sensitivity on the EDM of ^{129}Xe by two to three orders of magnitude to the $10^{-30}\,e$cm level, with even higher statistical sensitivity.
There are currently no efforts using liquid xenon in an EDM search other than ours[52]. However, due to the potential EDM sensitivity gain, the effort is worthwhile.

---

[52] An EDM experiment with liquid xenon based on a different approach than ours was proposed [130], but hasn't reappeared since several years.

Using a liquid sample of hyper-polarized ^{129}Xe offers a very high density, hence signal size, in a very small volume of sub-millimeter dimensions. This both improves field homogeneity, eases the application of high fields and makes simultaneous observation of many samples accessible. On the other hand large amounts of polarized ^{129}Xe gas need to be accumulated and liquefied, which is a rather difficult task experimentally. Particularly challenging is the implementation of a non-magnetic system to control the sample temperature ($< 180\,\mathrm{K}$), while keeping close-by niobium pickup coils in the superconducting state ($< 9\,\mathrm{K}$).

In this thesis the practicability and performance of such a complex cryogen-free SQUID system for highly sensitive detection of ^{129}Xe spin-precession was demonstrated. Background noise density levels of $< 50\,\mathrm{fT}/\sqrt{\mathrm{Hz}}$ above frequencies of 50 Hz were achieved. A sensitivity of $144\,\mathrm{fT}/\sqrt{\mathrm{Hz}}$ was reached in the cryogen-free EDM cryostat with the sample stage at 161 K and only a 1 mm gap to the superconducting pickup coils. The sample stage was found to increase the noise by a factor of two to four, which is attributed to Johnson noise, but independent of sample temperature.

The next milestone towards the realization of this experiment, a remotely operational flow-through and accumulation setup, was demonstrated to produce large amounts of highly polarized ^{129}Xe, that can be transfered to the EDM cryostat.

An “EDM chip” prototype made of quartz, where three liquid samples of millimeter size can be enclosed by a pressure-actuated piston was developed. The plate of quartz is polished on all surfaces in contact with polarized gas and can be used to test spin-precession in separated volumes detected by three pickup coils below the individual samples. The fabrication of cavities enclosing individual sub-millimeter liquid samples is not straightforward, particularly under the requirements imposed. Neither etching nor machining offers well suitable techniques. In the future the implementation of electrodes surrounding the individual droplets is the major challenging task and most probably a combination of milli- and micro-fabrication techniques will be necessary.

A first evaluation of the measurement concept and estimation of systematic limitations was taken out. The method offers on-line adjustment of individual electric field configurations of many simultaneous samples, hence providing a strong tool to study systematics. New systematic effects that arise from time-varying electric fields (Tab. 5.1) mostly modulate the holding field on a $\lesssim 10^{-6}$ level, which in contrast to the commonly used static electric field approach does not limit the EDM sensitivity. The most severe systematic effect is generated by AC leakage currents in conjunction with misalignment of the rotating electric field vector to the precessing polarization vector. This sensitivity limiting systematic effect is expected to be manageable on a level below $10^{-30}\,e\mathrm{cm}$. In preparation of an EDM experiment an extensive study of systematic effects is essential.

In the context of this quick summary of progress and status, the liquid xenon EDM experiment ultimately introducing time-varying electric fields is now set up for studies of spin precession in hyper-polarized liquid ^{129}Xe at very low magnetic fields ($< 100\,\mu\mathrm{T}$) and subsequently determine the accessible sensitivity of the novel method.

7.2 Status of the clock-comparison ^{129}Xe EDM search

Complementary to the liquid xenon EDM experiment, significant progress to a new EDM limit and a first look into systematic effects of a newly started EDM search using gaseous ^{129}Xe and a ^{3}He co-magnetometer is presented in Sec. 6. This alternative approach employs enhanced measurement methods that are well established and is performed in a unique highly shielded environment, which was particularly developed for low energy precision experiments.

In this EDM experiment we employ the method of parallel magnetic and electric fields and look for a deviation in Larmor precession frequency, while subsequently reversing the electric field direction. Most of the systematic effects can be accounted for by simultaneous detection of ^{3}He co-magnetometer precession, which yields the exact magnetic field that also ^{129}Xe is subject to.

First test measurements gave insight into systematic effects we need to take into account, like the self-interaction of a highly polarized ^{3}He sample. The magnetization of the sample in a non-spherical cell leads to several effects on spin-precession. We observed fast dephasing, off-resonant spin-flip pulses and precession frequency deviations due to the dipolar gradient, the strength of the intrinsic dipolar field and decay of the dipolar field, respectively. After a first study of these effects, the implications on the EDM experiment have to be determined by future tests in EDM-type cells. With a good understanding of this self-interaction alongside simulations their effect on spin-precession can presumably be accounted for in data analysis.

A main achievement towards application of electric fields was the observation of transverse spin-precession in prototype EDM cells with silicon electrodes. Spin-coherence times on the order of 500 s and 180 s were determined for ^{129}Xe and ^{3}He, respectively. The long spin-coherence of ^{129}Xe can be translated in an estimate on a limit of the wall relaxation rate of xenon on silicon surfaces, not yet reported in the literature. For a cell of volume V, xenon pressure p and silicon surface area A the wall relaxation rate Γ^{Si} can be limited to $\Gamma^{\mathrm{Si}} \lesssim 2.2 \times 10^{-4} \frac{A}{V} \frac{1}{p} \frac{\mathrm{cm \cdot bar}}{\mathrm{s}}$. A fast depolarization of ^{3}He is most likely due to interfaces of the silicon wafers to the GE180 cylinder as the bonding procedure needs to be optimized.

The major success of simultaneous detection of spin-precession of ^{129}Xe and ^{3}He in EDM prototype cells with voltages of up to 10 kV applied to the silicon electrodes was an impressive demonstration of fast progress. The data of this single run with an applied electric field of 4 kV/cm and an observation time of only 90 s translate to an EDM sensitivity of $2 \times 10^{-24}\,e$cm. Thus, during this thesis we already demonstrated a sensitivity of

$$\sigma_{\mathrm{d}} = 2.3 \times 10^{-26}\, \frac{e\mathrm{cm}}{\sqrt{\mathrm{week}}}, \tag{7.1}$$

which is only one order of magnitude away from the published state-of-the-art result. The main straightforward improvement for a competitive result, e.g. a SQUID dewar particularly designed for the EDM experiment[53] yielding a sensitivity gain of 75 is due

---

[53] In the currently used dewar for the first tests, the gradiometer baseline is far beyond the optimum and the distance of the cell to the SQUID sensor adds to about 95 mm.

for availability within the next six months. With additionally increased ^{129}Xe pressure (×3), optimizations in observation times (×2.5) and reduction of transport losses (×2) a total gain in sensitivity of roughly 1000 is expected.

Studies of systematic effects, e.g. self-interaction, and simulations are the most important near future tasks. With the past progress and high signal-to-noise ratios due to SQUID detection a new result on the EDM of ^{129}Xe is expected within a year time. Further suggested improvements are deploying the experiment inside the inner magnetic shielding box, which potentially reduces the background noise by a factor of two, and implementation of the circulating gas concept to obtain statistics more easily.

A Appendix

A.1 Analytical expressions of nuclear moments

Assuming a heavy nucleus, the $\mathcal{T},\mathcal{P}$ odd nucleon-nucleon interaction can be averaged over internal nucleons, thus simplifying to the effective Hamiltonian for a $\mathcal{T},\mathcal{P}$ odd interaction of an external (nonrelativistic) nucleon with spin $\boldsymbol{\sigma}$ and the internal core with nuclear density $\rho_A(\boldsymbol{r})$[54]

$$\mathcal{H}^{\cancel{\mathcal{T}}\cancel{\mathcal{P}}} = \frac{G_F}{\sqrt{2}}\frac{\eta_a}{2m_p}\boldsymbol{\sigma}\cdot\boldsymbol{\nabla}\rho_A(\boldsymbol{r}), \tag{A.1}$$

with Fermi's coupling constant G_F and the mass of the proton m_p. The dimensionless constant

$$\eta_a = \frac{Z}{A}\eta_{ap} + \frac{N}{A}\eta_{an} \tag{A.2}$$

characterizes the interaction strength of an external nucleon a with the core nucleons p, n.

The nuclear density and the nuclear potential $U(\boldsymbol{r})$ are of similar shape, hence $\rho_A(\boldsymbol{r}) = \frac{\rho_A(0)}{U(0)}U(\boldsymbol{r})$ is assumed and Eq. (A.1) can be rewritten in the form

$$\mathcal{H}^{\cancel{\mathcal{T}}\cancel{\mathcal{P}}} = \xi\boldsymbol{\sigma}\cdot\boldsymbol{\nabla}U(\boldsymbol{r}), \qquad \xi = \eta\frac{G}{2\sqrt{2}m_p}\frac{\rho_A(0)}{U(0)} \approx -2\times 10^{-21}\eta\,\mathrm{cm}. \tag{A.3}$$

The problem is now reduced to solving the Schrödinger equation $(\mathcal{H}+\widetilde{U})\widetilde{\psi} = E\widetilde{\psi}$ of a nucleon in a potential $\widetilde{U} = U + \xi\boldsymbol{\sigma}\cdot\boldsymbol{\nabla}U(\boldsymbol{r})$. Therefore, the perturbed wavefunction is

$$\widetilde{\psi} = (1+\xi\boldsymbol{\sigma}\cdot\boldsymbol{\nabla}U)\psi, \qquad \text{with } (\mathcal{H}+U)\psi = E\psi. \tag{A.4}$$

The electric dipole moment d, Schiff moment S and MQM M due to the excitation of the external nucleon interacting with the internal core with their characteristic values are

$$\begin{aligned}
d &= -e\xi\left(q-\frac{Z}{A}\right)t_I && \approx 10^{-8}\eta_a\,\mathrm{e\,fm}\\
S &= -\frac{eq}{10}\xi\left[\left(t_I+\frac{1}{I+1}\right)r_{ext}^2-\frac{5}{3}t_I r_q^2\right] && \approx 10^{-7}\eta_a\,\mathrm{e\,fm}^3\\
M &= \frac{e}{m_p}\xi(\mu-q)(2I-1)t_I && \approx 10^{-8}\eta_a\,\mathrm{e\,fm}
\end{aligned} \tag{A.5}$$

---

[54] The nucleon-nucleon interaction reduces to a single term, since all other terms contain the spin of the internal core nucleons, for which $\langle\boldsymbol{\sigma}\rangle = 0$.

$$\text{where } t_I = \begin{cases} 1, & I = l + 1/2 \\ -\frac{I}{I+1}, & I = l - 1/2. \end{cases} \tag{A.6}$$

In the above analytic results q is the charge and μ the magnetic moment of the nucleon, r_{ext}^2 and r_q^2 are the mean square radii of the external nucleon and the nuclear charge, respectively and l is the orbital angular momentum of the external nucleon.
While according to Eq. (A.5) in nuclei with an external proton there is a direct contribution to the Schiff moment, nuclei with an unpaired neutron can't directly contribute, as $q = 0$. Nevertheless, it has been shown [43, 44, 156] that paired protons virtually excited by the field of the external neutron contribute on a similar level, effectively yielding a nonvanishing Schiff moment with $q \approx \mathcal{O}(0.1)$, cf. Eq. (A.5).

A.2 The relations of electron-nucleon coupling coefficients

The coupling strengths of the $\mathcal{T}, \mathcal{P}$ odd electron-nucleon interaction can be related in the following way. An EDM contribution arises in third order perturbation theory and then C^{SP} can be related to the spin-dependent contribution C^{T} via [30, 157]

$$\left(\frac{Z}{A} C_p^{\mathrm{SP}} + \frac{N}{A} C_n^{\mathrm{SP}} \right) \frac{\boldsymbol{I}}{I} \leftrightarrow \frac{1.9 \times 10^3}{1 + 0.3 Z^2 \alpha^2} A^{-2/3} \mu^{-1} \left\langle C_p^{\mathrm{T}} \sum_p \boldsymbol{\sigma}_p + C_n^{\mathrm{T}} \sum_n \boldsymbol{\sigma}_n \right\rangle, \tag{A.7}$$

where α is the fine structure constant, μ the nuclear magnetic moment and the term $\langle\ \rangle$ denote averaging over the nuclear state. With the help of Eq. (A.7) an EDM measurement of a diamagnetic atom can also set a competitive limit on C^{SP}.

The weakest contribution from pseudoscalar-scalar terms C^{PS} can also be related to C^{T} by comparing the results of the matrix elements, thus obtaining [30, 157]

$$C^{\mathrm{PS}} \leftrightarrow 4.6 \times 10^3 \frac{A^{1/3}}{Z} C^{\mathrm{T}}. \tag{A.8}$$

Due to the above relations EDM searches using diamagnetic atoms can set limits on all three spin-dependent and spin-independent $\mathcal{T}, \mathcal{P}$ odd interactions of electrons with the nuclei, cf. Tab. 2.3.

A.3 A limit on the electon EDM from diamagnetic atoms

An electron EDM induces an atomic EDM of diamagnetic atoms due to polarization of the closed electron shell along the nuclear spin by the hyperfine interaction. In third order perturbation theory [30, 31]

$$\mathcal{H}_{\mathrm{hf}}^{\cancel{\mathrm{TP}}} = e \boldsymbol{\mu} \frac{\boldsymbol{r} \times \boldsymbol{\alpha}}{r^3}, \text{ with } \boldsymbol{\alpha} = \begin{pmatrix} 0 & \boldsymbol{\sigma} \\ \boldsymbol{\sigma} & 0 \end{pmatrix} \tag{A.9}$$

and the nuclear magnetic moment $\boldsymbol{\mu} = \frac{e\mu}{2m_p}\frac{\boldsymbol{I}}{I}$.
The second, more important contribution emerges from a direct interaction of the electron EDM with the magnetic moment of the nucleus $\boldsymbol{\mu}$:

$$\mathcal{H}_\mu^{\cancel{\mathrm{TP}}} = -id_e\boldsymbol{\gamma}\cdot\boldsymbol{B} = -id_e\boldsymbol{\gamma}\cdot\boldsymbol{\nabla}\times\left(\boldsymbol{\nabla}\frac{1}{r}\times\boldsymbol{\mu}\right) \quad \text{with } \boldsymbol{\gamma} = \begin{pmatrix} 0 & \boldsymbol{\sigma} \\ -\boldsymbol{\sigma} & 0 \end{pmatrix} \tag{A.10}$$

The total matrix element mixing $s_{1/2}$ and $p_{1/2}$ states in diamagnetic atoms is given in [30] as

$$\langle s_{1/2}|\mathcal{H}_\mu^{\cancel{\mathrm{TP}}} + \mathcal{H}_{\mathrm{hf}}^{\cancel{\mathrm{TP}}}|p_{1/2}\rangle = -d_e\frac{7}{3}\frac{e\mu}{m_p}\frac{Z^2\alpha(R-1)}{a^3(\nu_s\nu_p)^{3/2}}\frac{2\boldsymbol{j}\cdot\boldsymbol{I}}{I}, \tag{A.11}$$

where a is the Bohr radius and the relativistic enhancement factor

$$R = \frac{4}{\Gamma^2(2\gamma+1)}\left(\frac{a}{2ZR_0}\right)^{2-2\gamma}. \tag{A.12}$$

Here, $\gamma = \sqrt{(j+1/2)^2 - Z^2\alpha^2}$ and R_0 is the nuclear radius.
With this result the following relation can be established between the electron EDM d_e and the tensor interaction of electrons and nucleons (cf. Eq. (2.15))

$$d_e\frac{\boldsymbol{I}}{I} \leftrightarrow \frac{3}{7}\frac{G_F m_p e}{\sqrt{2}\pi\alpha\mu}\frac{R}{R-1}\left\langle C_p^{\mathrm{T}}\sum_p \boldsymbol{\sigma}_p + C_n^{\mathrm{T}}\sum_n \boldsymbol{\sigma}_n\right\rangle \tag{A.13}$$

With the help of this relation the numeric calculations of C^{T} can be used to set a limit on the electron EDM with measurements on diamagnetic atoms.

A.4 Diffusion in multi-component gas mixtures

In gas mixtures the diffusion coefficients of helium and xenon are altered according to

$$\frac{1}{D_{\mathrm{He}}} = \frac{p^{\mathrm{He}}}{D_{\mathrm{HeHe}}} + \frac{p^{\mathrm{Xe}}}{D_{\mathrm{HeXe}}} + \frac{p^{\mathrm{N2}}}{D_{\mathrm{HeN2}}} \tag{A.14}$$

and

$$\frac{1}{D_{\mathrm{Xe}}} = \frac{p^{\mathrm{Xe}}}{D_{\mathrm{XeXe}}} + \frac{p^{\mathrm{He}}}{D_{\mathrm{XeHe}}} + \frac{p^{\mathrm{N2}}}{D_{\mathrm{XeN2}}}, \tag{A.15}$$

where D_{ii} is the coefficient of self-diffusion and D_{ij} is the coefficient of diffusion of i in j. Appropriate binary diffusion coefficients are given in Tab. A.2.

A.5 Properties of relevant atoms

Property	Sym.	Atoms			Unit
		^{129}Xe	^{3}He	^{87}Rb	
nat. abundance		26.4	0.00014	27.8	%
nuclear charge	Z	54	2	37	e
electron configuration		$[\mathrm{Kr}]4d^{1}05s^{2}5p^{6}$	$1s^{2}$	$[\mathrm{Kr}]5s^{1}$	
nuclear spin	I	1/2	1/2	-3/2	$\hbar$
nucl. magnetic moment	μ_I	-3.93	-10.8	13.9	$10^{-27}\ \frac{\mathrm{J}}{\mathrm{T}}$
gyrom. ratio	γ	-11.777	-32.434	87.8	$\frac{\mathrm{MHz}}{\mathrm{T}}$
boiling point (1 atm)	T_{b}	165.2	4.15	961.2	K
melting point (1 atm)	T_{m}	161.4		312.5	K

Tab. A.1: Atomic data for isotopes ^{129}Xe , ^{3}He and ^{87}Rb.

Diffusion coeff. (1 atm, 300 K) [cm^2/s]		
	Xenon	Helium
Xenon	0.0576	0.6
Helium	0.79	1.8200
Nitrogen	0.21	0.77
Diffusion coeff. (liquid, 160 K) [cm^2/s]		
Xenon	3.9×10^{-5}	

Tab. A.2: Self-diffusion coefficients of helium, xenon and liquid xenon and binary diffusion coefficients of xenon, helium in nitrogen [115, 124, 158, 159]. Read as diffusion coefficient of row in column.

A.6 Supplemental data

A.6.1 Flexible circuits simulations

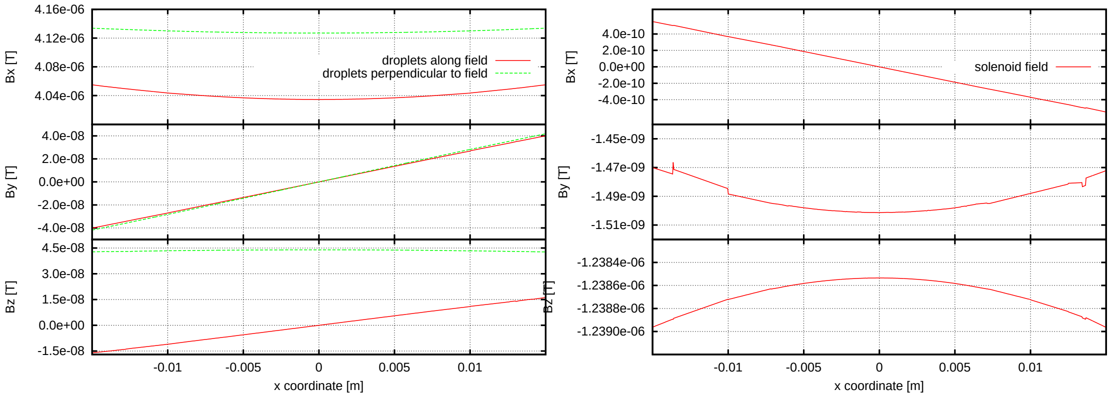

Fig. A.1: Components of magnetic fields generated by cosine theta coils (a) and the solenoid coil (b) simulated at currents of 10 mA. The plots are along the positions of three liquid xenon droplets.

A.6.2 EDM chip temperature difference

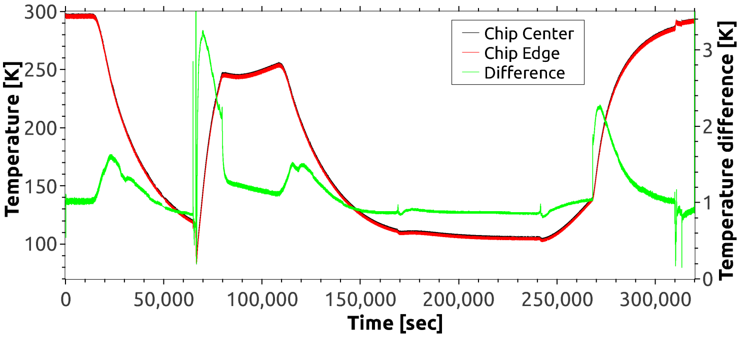

Fig. A.2: The deviation of the temperature measured in the center of a thin low thermal conductivity ($\approx 1\,\mathrm{W/mK}$) “EDM chip” to the permanently mounted sensor at the chip edge close to the coolant tubes.

A.6.3 Rubidium vapor pressure

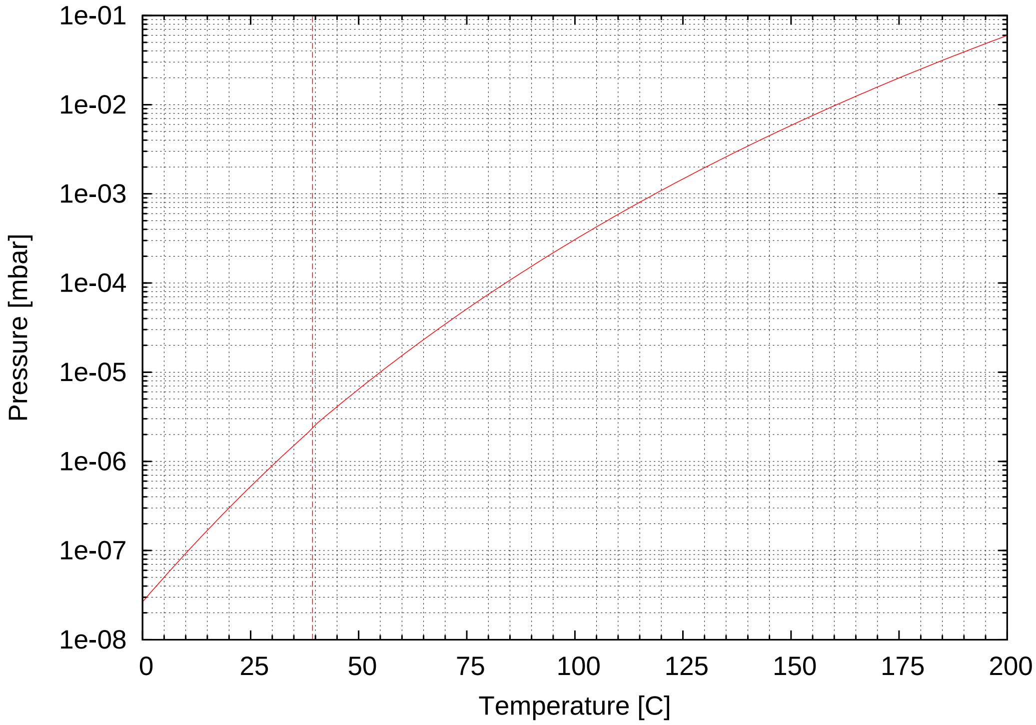

Fig. A.3: Vapor pressure curve of rubidium according to $\log_{10} p = 2.881 + 4.857 - \frac{4215}{T}$ below and $\log_{10} p = 2.881 + 4.312 - \frac{4040}{T}$ above the melting point at 39.31 °C (dashed line) [160]

List of Figures

List of Tables

Bibliography

[1] Georges Aad et al. “Observation of a new particle in the search for the Standard Model Higgs boson with the ATLAS detector at the LHC”. *Phys.Lett.* B716 (2012), pp. 1–29.
DOI: `10.1016/j.physletb.2012.08.020`. arXiv: `1207.7214 [hep-ex]`.

[2] Serguei Chatrchyan et al. “Observation of a new boson at a mass of 125 GeV with the CMS experiment at the LHC”. *Phys.Lett.* B716 (2012), pp. 30–61.
DOI: `10.1016/j.physletb.2012.08.021`. arXiv: `1207.7235 [hep-ex]`.

[3] G. Steigman. “Observational Tests of Antimatter Cosmologies”. *Annual Review of Astronomy and Astrophysics* 14 (1976), pp. 339–372.
DOI: `10.1146/annurev.aa.14.090176.002011`.

[4] F. W. Stecker. “On the nature of the baryon asymmetry”. *Nuclear Physics B* 252 (1985), pp. 25–36.
DOI: `10.1016/0550-3213(85)90423-7`.

[5] A. G. Cohen, A. De Rújula, and S. L. Glashow. “A Matter-Antimatter Universe?” *The Astrophysical Journal* 495 (1998), p. 539.
DOI: `10.1086/305328`. arXiv: `astro-ph/9707087 [astro-ph]`.

[6] C. L. Bennett et al. “First year Wilkinson Microwave Anisotropy Probe (WMAP) observations: Preliminary maps and basic results”. *Astrophys.J.Suppl.* 148 (2003), p. 1.
DOI: `10.1086/377253`. arXiv: `astro-ph/0302207 [astro-ph]`.

[7] P.A.R. Ade et al. “Planck 2013 results. XVI. Cosmological parameters”. *Astron.Astrophys.* (2014).
DOI: `10.1051/0004-6361/201321591`. arXiv: `1303.5076 [astro-ph.CO]`.

[8] Lawrence M. Krauss and Peter J. Kernan. “Big Bang Nucleosynthesis constraints and light element abundance estimates”. *Physics Letters B* 347 (1995), pp. 347–353.
DOI: `10.1016/0370-2693(95)00082-V`.

[9] G. Börner. *The Early Universe: Facts and Fiction.* 4th ed. Astronomy and Astrophysics Library. Springer, 2003.

[10] James M. Cline. *Baryogenesis.* arXiv: `hep-ph/0609145 [hep-ph]`.

[11] Laurent Canetti, Marco Drewes, and Mikhail Shaposhnikov. “Matter and antimatter in the universe”. *New Journal of Physics* 14 (2012), p. 095012.

[12] A. D. Sakharov. "Violation of CP Invariance, C Asymmetry, and Baryon Asymmetry of the Universe". *Pisma Zh.Eksp.Teor.Fiz.* 5 (1967), pp. 32–35.
DOI: `10.1070/PU1991v034n05ABEH002497`.

[13] Mark Trodden. "Electroweak baryogenesis". *Rev.Mod.Phys.* 71 (1999), pp. 1463–1500.
DOI: `10.1103/RevModPhys.71.1463`. arXiv: `hep-ph/9803479 [hep-ph]`.

[14] Michael Dine and Alexander Kusenko. "The Origin of the matter - antimatter asymmetry". *Rev.Mod.Phys.* 76 (2004), p. 1.
DOI: `10.1103/RevModPhys.76.1`. arXiv: `hep-ph/0303065 [hep-ph]`.

[15] Sacha Davidson, Enrico Nardi, and Yosef Nir. "Leptogenesis". *Physics Reports* 466 (2008), pp. 105–177.
DOI: `10.1016/j.physrep.2008.06.002`.

[16] G. 't Hooft. "Symmetry Breaking through Bell-Jackiw Anomalies". *Phys. Rev. Lett.* 37 (1976), pp. 8–11.
DOI: `10.1103/PhysRevLett.37.8`.

[17] V. A. Kuzmin, V. A. Rubakov, and M. E. Shaposhnikov. "On anomalous electroweak baryon-number non-conservation in the early universe". *Physics Letters B* 155 (1985), pp. 36–42.
DOI: `10.1016/0370-2693(85)91028-7`.

[18] V. Gribov and B. Pontecorvo. "Neutrino astronomy and lepton charge". *Physics Letters B* 28 (1969), pp. 493–496.
DOI: `10.1016/0370-2693(69)90525-5`.

[19] K. S. Hirata et al. "Observation of a small atmospheric vμ/ve ratio in Kamiokande". *Physics Letters B* 280 (1992), pp. 146–152.
DOI: `10.1016/0370-2693(92)90788-6`.

[20] Q. R. Ahmad et al. "Direct Evidence for Neutrino Flavor Transformation from Neutral-Current Interactions in the Sudbury Neutrino Observatory". *Phys. Rev. Lett.* 89 (2002), p. 011301.
DOI: `10.1103/PhysRevLett.89.011301`.

[21] C. S. Wu et al. "Experimental Test of Parity Conservation in Beta Decay". *Phys. Rev.* 105 (1957), pp. 1413–1415.
DOI: `10.1103/PhysRev.105.1413`.

[22] T. D. Lee and C. N. Yang. "Question of Parity Conservation in Weak Interactions". *Phys. Rev.* 104 (1956), pp. 254–258.
DOI: `10.1103/PhysRev.104.254`.

[23] L. Landau. "On the conservation laws for weak interactions". *Nuclear Physics* 3 (1957), pp. 127–131.
DOI: `10.1016/0029-5582(57)90061-5`.

[24] J. H. Christenson et al. "Evidence for the 2π Decay of the K_2^0 Meson". *Phys. Rev. Lett.* 13 (1964), pp. 138–140.
DOI: 10.1103/PhysRevLett.13.138.

[25] A. Abashian et al. "Measurement of the CP Violation Parameter $\sin 2\varphi_1$ in B_d^0 Meson Decays". *Phys. Rev. Lett.* 86 (2001), pp. 2509–2514.
DOI: 10.1103/PhysRevLett.86.2509.

[26] B. Aubert et al. "Measurement of *CP*-Violating Asymmetries in B^0 Decays to *CP* Eigenstates". *Phys. Rev. Lett.* 86 (2001), pp. 2515–2522.
DOI: 10.1103/PhysRevLett.86.2515.

[27] Nicola Cabibbo. "Unitary Symmetry and Leptonic Decays". *Phys. Rev. Lett.* 10 (1963), pp. 531–533.
DOI: 10.1103/PhysRevLett.10.531.

[28] Makoto Kobayashi and Toshihide Maskawa. "CP-Violation in the Renormalizable Theory of Weak Interaction". *Progress of Theoretical Physics* 49 (1973), pp. 652–657.
DOI: 10.1143/PTP.49.652. eprint: http://ptp.oxfordjournals.org/content/49/2/652.full.pdf+html.

[29] O. W. Greenberg. "*CPT* Violation Implies Violation of Lorentz Invariance". *Phys. Rev. Lett.* 89 (2002), p. 231602.
DOI: 10.1103/PhysRevLett.89.231602.

[30] Iosif B. Khriplovich and Steve K. Lamoreaux. *CP Violation Without Strangeness. Electric Dipole Moments of Particles, Atoms, and Molecules.* Springer Berlin Heidelberg, 1997.
DOI: 10.1007/978-3-642-60838-4.

[31] J.S.M. Ginges and V.V. Flambaum. "Violations of fundamental symmetries in atoms and tests of unification theories of elementary particles". *Physics Reports* 397 (2004), p. 63.
DOI: 10.1016/j.physrep.2004.03.005.

[32] Maxim Pospelov and Adam Ritz. "Electric dipole moments as probes of new physics". *Annals Phys.* 318 (2005), pp. 119–169.
DOI: 10.1016/j.aop.2005.04.002. arXiv: nucl-th/0304048 [hep-ph].

[33] Jonathan Engel, Michael J. Ramsey-Musolf, and U. van Kolck. "Electric Dipole Moments of Nucleons, Nuclei, and Atoms: The Standard Model and Beyond". *Prog.Part.Nucl.Phys.* 71 (2013), pp. 21–74.
DOI: 10.1016/j.ppnp.2013.03.003. arXiv: 1303.2371 [nucl-th].

[34] L. I. Schiff. "Measurability of Nuclear Electric Dipole Moments". *Phys. Rev.* 132 (1963), pp. 2194–2200.
DOI: 10.1103/PhysRev.132.2194.

[35] P. G. H. Sandars. "The electric dipole moment of an atom". *Physics Letters* 14 (1965), pp. 194–196.
DOI: 10.1016/0031-9163(65)90583-4.

[36] P.G.H. Sandars. “Enhancement factor for the electric dipole moment of the valence electron in an alkali atom”. *Physics Letters* 22 (1966), pp. 290–291.
DOI: 10.1016/0031-9163(66)90618-4.

[37] V. Spevak, N. Auerbach, and V. V. Flambaum. “Enhanced T-odd, P-odd electromagnetic moments in reflection asymmetric nuclei”. *Phys. Rev. C* 56 (1997), pp. 1357–1369.
DOI: 10.1103/PhysRevC.56.1357.

[38] J. Engel, J. L. Friar, and A. C. Hayes. “Nuclear octupole correlations and the enhancement of atomic time-reversal violation”. *Phys. Rev. C* 61 (2000), p. 035502.
DOI: 10.1103/PhysRevC.61.035502.

[39] L. P. Gaffney et al. “Studies of pear-shaped nuclei using accelerated radioactive beams”. *Nature* 497 (2013), pp. 199–204.
DOI: 10.1038/nature12073.

[40] V. V. Flambaum and V. G. Zelevinsky. “Enhancement of nuclear Schiff moments and time-reversal violation in atoms due to soft nuclear octupole vibrations”. *Phys. Rev. C* 68 (2003), p. 035502.
DOI: 10.1103/PhysRevC.68.035502.

[41] J. R. Guest et al. “Laser Trapping of Ra225 and Ra226 with Repumping by Room-Temperature Blackbody Radiation”. *Phys. Rev. Lett.* 98 (2007), p. 093001.
DOI: 10.1103/PhysRevLett.98.093001.

[42] E. R. Tardiff et al. “Polarization and relaxation rates of radon”. *Phys. Rev. C* 77 (2008), p. 052501.
DOI: 10.1103/PhysRevC.77.052501.

[43] V.V. Flambaum, I.B. Khriplovich, and O.P. Sushkov. “Limit on the constant of T-nonconserving nucleon-nucleon interaction”. *Physics Letters B* 162 (1985), pp. 213–216.
DOI: 10.1016/0370-2693(85)90908-6.

[44] V. V. Flambaum, I. B. Khriplovich, and O. P. Sushkov. “On the P and T Nonconserving Nuclear Moments”. *Nucl.Phys.* A449 (1986), p. 750.
DOI: 10.1016/0375-9474(86)90331-3.

[45] O. P. Sushkov, V. V. Flambaum, and I. B. Khriplovich. “Possibility of investigating P- and T-odd nuclear forces in atomic and molecular experiments”. *Sov. Phys. JETP* 60 (1984), p. 873.
DOI: 10.1103/PhysRevA.87.012102.

[46] V.A. Dzuba et al. “Electric dipole moments of Hg, Xe, Rn, Ra, Pu, and TlF induced by the nuclear Schiff moment and limits on time reversal violating interactions”. *Phys.Rev.* A66 (2002), p. 012111.
DOI: 10.1103/PhysRevA.66.012111. arXiv: hep-ph/0203202 [hep-ph].

[47] I. B. Khriplovich. “A bound on the proton electric dipole moment derived from atomic experiments”. *Sov. Phys. JETP* 44 (1976), p. 25.

[48] Martin Jung and Antonio Pich. "Electric Dipole Moments in Two-Higgs-Doublet Models" (2013). arXiv: `1308.6283 [hep-ph]`.

[49] Matthias Dall and Adam Ritz. "CP-violation and electric dipole moments". English. *Hyperfine Interactions* 214 (2013), pp. 87–95.
DOI: `10.1007/s10751-013-0801-1`.

[50] I.I. Bigi and N.G. Uraltsev. "Induced multi-gluon couplings and the neutron electric dipole moment". *Nuclear Physics B* 353 (1991), pp. 321–336.
DOI: `10.1016/0550-3213(91)90339-Y`.

[51] John Paul Archambault, Andrzej Czarnecki, and Maxim Pospelov. "Electric dipole moments of leptons in the presence of Majorana neutrinos". *Phys. Rev. D* 70 (2004), p. 073006.
DOI: `10.1103/PhysRevD.70.073006`.

[52] C. Jarlskog. "Commutator of the Quark Mass Matrices in the Standard Electroweak Model and a Measure of Maximal CP Nonconservation". *Phys. Rev. Lett.* 55 (1985), pp. 1039–1042.
DOI: `10.1103/PhysRevLett.55.1039`.

[53] R.J. Crewther et al. "Chiral estimate of the electric dipole moment of the neutron in quantum chromodynamics". *Physics Letters B* 88 (1979), pp. 123–127.
DOI: `10.1016/0370-2693(79)90128-X`.

[54] Maxim Pospelov and Adam Ritz. "Theta-Induced Electric Dipole Moment of the Neutron via QCD Sum Rules". *Phys. Rev. Lett.* 83 (1999), pp. 2526–2529.
DOI: `10.1103/PhysRevLett.83.2526`.

[55] C. A. Baker et al. "Improved Experimental Limit on the Electric Dipole Moment of the Neutron". *Phys. Rev. Lett.* 97 (2006), p. 131801.
DOI: `10.1103/PhysRevLett.97.131801`.

[56] R. D. Peccei and Helen R. Quinn. "CP Conservation in the Presence of Pseudoparticles". *Phys. Rev. Lett.* 38 (1977), pp. 1440–1443.
DOI: `10.1103/PhysRevLett.38.1440`.

[57] Jihn E. Kim and Gianpaolo Carosi. "Axions and the strong CP problem". *Reviews of Modern Physics* 82 (2010), p. 557.
DOI: `10.1103/RevModPhys.82.557`.

[58] Darwin Chang, Wai-Yee Keung, and Apostolos Pilaftsis. "New two loop contribution to electric dipole moment in supersymmetric theories". *Phys.Rev.Lett.* 82 (1999), pp. 900–903.
DOI: `10.1103/PhysRevLett.82.900`. arXiv: `hep-ph/9811202 [hep-ph]`.

[59] Toby Falk et al. "MSSM predictions for the electric dipole moment of the 199Hg atom". *Nuclear Physics B* 560 (1999), pp. 3–22.
DOI: `10.1016/S0550-3213(99)00471-X`.

[60] Timothy Chupp and Michael Ramsey-Musolf. "Electric Dipole Moments: A Global Analysis" (2014). arXiv: `1407.1064 [hep-ph]`.

[61] V.M. Khatsymovsky, I.B. Khriplovich, and A.S. Yelkhovsky. "Neutron electric dipole moment, T-odd nuclear forces, and nature of CP-violation". *Annals of Physics* 186 (1988), pp. 1–14.
DOI: 10.1016/S0003-4916(88)80015-0.

[62] Maxim Pospelov. "Best values for the CP-odd meson–nucleon couplings from supersymmetry". *Physics Letters B* 530 (2002), pp. 123–128.
DOI: 10.1016/S0370-2693(02)01263-7.

[63] Maxim Pospelov and Adam Ritz. "Neutron electric dipole moment from electric and chromoelectric dipole moments of quarks". *Phys. Rev. D* 63 (2001), p. 073015.
DOI: 10.1103/PhysRevD.63.073015.

[64] E. M. Purcell and N. F. Ramsey. "On the Possibility of Electric Dipole Moments for Elementary Particles and Nuclei". *Phys. Rev.* 78 (1950), pp. 807–807.
DOI: 10.1103/PhysRev.78.807.

[65] J. H. Smith, E. M. Purcell, and N. F. Ramsey. "Experimental Limit to the Electric Dipole Moment of the Neutron". *Phys. Rev.* 108 (1957), pp. 120–122.
DOI: 10.1103/PhysRev.108.120.

[66] Norman F. Ramsey. "Experiments with separated oscillatory fields and hydrogen masers". *Rev. Mod. Phys.* 62 (1990), pp. 541–552.
DOI: 10.1103/RevModPhys.62.541.

[67] W. Griffith et al. "Improved Limit on the Permanent Electric Dipole Moment of Hg199". *Physical Review Letters* 102 (2009).
DOI: 10.1103/PhysRevLett.102.101601.

[68] Bruce H. J. McKellar et al. "The neutron electric dipole moment in the standard KM model". *Physics Letters B* 197 (1987), pp. 556–560.
DOI: 10.1016/0370-2693(87)91055-0.

[69] J. Baron et al. "Order of Magnitude Smaller Limit on the Electric Dipole Moment of the Electron". *Science* 343 (2014), pp. 269–272.
DOI: 10.1126/science.1248213.

[70] Michael J. Booth. "The Electric dipole moment of the W and electron in the Standard Model" (1993). arXiv: hep-ph/9301293 [hep-ph].

[71] M. A. Rosenberry and T. E. Chupp. "Atomic Electric Dipole Moment Measurement Using Spin Exchange Pumped Masers of ^{1}29Xe and ^{3}He". *Phys. Rev. Lett.* 86 (2001), pp. 22–25.
DOI: 10.1103/PhysRevLett.86.22.

[72] T. G. Vold et al. "Search for a Permanent Electric Dipole Moment on the Xe129 Atom". *Phys. Rev. Lett.* 52 (1984), pp. 2229–2232.
DOI: 10.1103/PhysRevLett.52.2229.

[73] L. Bergmann et al. *Bestandteile der Materie: Atome, Moleküle, Atomkerne, Elementarteilchen*. Lehrbuch Series. Walter de Gruyter, 2003.

[74] F. Bloch. “Nuclear Induction”. *Phys. Rev.* 70 (1946), pp. 460–474.
DOI: 10.1103/PhysRev.70.460.

[75] H. C. Torrey. “Bloch Equations with Diffusion Terms”. *Phys. Rev.* 104 (1956), pp. 563–565.
DOI: 10.1103/PhysRev.104.563.

[76] Eiichi Fukushima and S.B.W. Roeder. *Experimental Pulse NMR: A Nuts and Bolts Approach*. Advanced book program. Addison-Wesley, 1993.

[77] F. Bloch and A. Siegert. “Magnetic Resonance for Nonrotating Fields”. *Phys. Rev.* 57 (1940), pp. 522–527.
DOI: 10.1103/PhysRev.57.522.

[78] F. D. Colegrove, L. D. Schearer, and G. K. Walters. “Polarization of He^3 Gas by Optical Pumping”. *Phys. Rev.* 132 (1963), pp. 2561–2572.
DOI: 10.1103/PhysRev.132.2561.

[79] M. A. Bouchiat, T. R. Carver, and C. M. Varnum. “Nuclear Polarization in He^3 Gas Induced by Optical Pumping and Dipolar Exchange”. *Phys. Rev. Lett.* 5 (1960), pp. 373–375.
DOI: 10.1103/PhysRevLett.5.373.

[80] B. C. Grover. “Noble-Gas NMR Detection through Noble-Gas-Rubidium Hyperfine Contact Interaction”. *Phys. Rev. Lett.* 40 (1978), pp. 391–392.
DOI: 10.1103/PhysRevLett.40.391.

[81] W. Happer. “Optical Pumping”. *Rev. Mod. Phys.* 44 (1972), pp. 169–249.
DOI: 10.1103/RevModPhys.44.169.

[82] Thad G. Walker and William Happer. “Spin-exchange optical pumping of noble-gas nuclei”. *Rev. Mod. Phys.* 69 (1997), pp. 629–642.
DOI: 10.1103/RevModPhys.69.629.

[83] Thad G Walker. “Fundamentals of Spin-Exchange Optical Pumping”. *Journal of Physics: Conference Series* 294 (2011), p. 012001.

[84] D. Steck. “Rubidium 87 D Line Data” (2010). eprint: http://steck.us/alkalidata/.

[85] Earl Babcock et al. “Hybrid Spin-Exchange Optical Pumping of ^{3}He”. *Phys. Rev. Lett.* 91 (2003), p. 123003.
DOI: 10.1103/PhysRevLett.91.123003.

[86] W. C. Chen et al. “Spin-exchange optical pumping of ^{3}He with Rb-K mixtures and pure K”. *Phys. Rev. A* 75 (2007), p. 013416.
DOI: 10.1103/PhysRevA.75.013416.

[87] Wenjin Shao, Guodong Wang, and Emlyn W. Hughes. “Measurement of spin-exchange rate constants between ^{129}Xe and alkali metals”. *Phys. Rev. A* 72 (2005), p. 022713.
DOI: 10.1103/PhysRevA.72.022713.

[88] G. D. Cates et al. “Rb$-^{129}$Xe spin-exchange rates due to binary and three-body collisions at high Xe pressures”. *Phys. Rev. A* 45 (1992), pp. 4631–4639.
DOI: 10.1103/PhysRevA.45.4631.

[89] M. V. Romalis, E. Miron, and G. D. Cates. “Pressure broadening of Rb D_1 and D_2 lines by ^{3}He, ^{4}He, N_2, and Xe: Line cores and near wings”. *Phys. Rev. A* 56 (1997), pp. 4569–4578.
DOI: 10.1103/PhysRevA.56.4569.

[90] M. E. Wagshul and T. E. Chupp. “Laser optical pumping of high-density Rb in polarized ^{3}He targets”. *Phys. Rev. A* 49 (1994), pp. 3854–3869.
DOI: 10.1103/PhysRevA.49.3854.

[91] M. S. Freeman, K. Emami, and B. Driehuys. “Characterizing and modeling the efficiency limits in large-scale production of hyperpolarized ^{129}Xe”. *Phys. Rev. A* 90 (2014), p. 023406.
DOI: 10.1103/PhysRevA.90.023406.

[92] Graham Norquay et al. “Optimized production of hyperpolarized 129Xe at 2 bars for in vivo lung magnetic resonance imaging”. *Journal of Applied Physics* 113, 044908 (2013), pp. –.
DOI: 10.1063/1.4776763.

[93] W. Happer et al. “Polarization of the nuclear spins of noble-gas atoms by spin exchange with optically pumped alkali-metal atoms”. *Phys. Rev. A* 29 (1984), pp. 3092–3110.
DOI: 10.1103/PhysRevA.29.3092.

[94] X. Zeng et al. “Experimental determination of the rate constants for spin exchange between optically pumped K, Rb, and Cs atoms and ^{129}Xe nuclei in alkali-metal˘noble-gas van der Waals molecules”. *Phys. Rev. A* 31 (1985), pp. 260–278.
DOI: 10.1103/PhysRevA.31.260.

[95] B. Driehuys et al. “High-volume production of laser-polarized 129Xe”. *Applied Physics Letters* 69 (1996), pp. 1668–1670.
DOI: 10.1063/1.117022.

[96] B. Chann et al. “Production of highly polarized 3He using spectrally narrowed diode laser array bars”. *Journal of Applied Physics* 94 (2003), pp. 6908–6914.
DOI: 10.1063/1.1621739.

[97] G. D. Cates, S. R. Schaefer, and W. Happer. “Relaxation of spins due to field inhomogeneities in gaseous samples at low magnetic fields and low pressures”. *Phys. Rev. A* 37 (1988), pp. 2877–2885.
DOI: 10.1103/PhysRevA.37.2877.

[98] N. Bloembergen, E. M. Purcell, and R. V. Pound. “Relaxation Effects in Nuclear Magnetic Resonance Absorption”. *Phys. Rev.* 73 (1948), pp. 679–712.
DOI: 10.1103/PhysRev.73.679.

[99] A. Abragam. *The Principles of Nuclear Magnetism.* International series of monographs on physics. Clarendon Press, 1961.

[100] N. R. Newbury et al. “Gaseous $^3-^3$He magnetic dipolar spin relaxation”. *Phys. Rev. A* 48 (1993), pp. 4411–4420.
DOI: 10.1103/PhysRevA.48.4411.

[101] R. L. Streever and H. Y. Carr. “Nuclear Magnetic Resonance of Xe^{129} in Natural Xenon”. *Phys. Rev.* 121 (1961), pp. 20–25.
DOI: 10.1103/PhysRev.121.20.

[102] H. C. Torrey. “Chemical Shift and Relaxation of Xe^{129} in Xenon Gas”. *Phys. Rev.* 130 (1963), pp. 2306–2312.
DOI: 10.1103/PhysRev.130.2306.

[103] E. R. Hunt and H. Y. Carr. “Nuclear Magnetic Resonance of Xe^{129} in Natural Xenon”. *Phys. Rev.* 130 (1963), pp. 2302–2305.
DOI: 10.1103/PhysRev.130.2302.

[104] B. Chann et al. “^{129}Xe − Xe Molecular Spin Relaxation”. *Phys. Rev. Lett.* 88 (2002), p. 113201.
DOI: 10.1103/PhysRevLett.88.113201.

[105] B. C. Anger et al. “Gas-phase spin relaxation of ^{129}Xe”. *Phys. Rev. A* 78 (2008), p. 043406.
DOI: 10.1103/PhysRevA.78.043406.

[106] W. A. Fitzsimmons, L. L. Tankersley, and G. K. Walters. “Nature of Surface-Induced Nuclear-Spin Relaxation of Gaseous He^3”. *Phys. Rev.* 179 (1969), pp. 156–165.
DOI: 10.1103/PhysRev.179.156.

[107] Steven R. Breeze et al. “Coatings for optical pumping cells and short-term storage of hyperpolarized xenon”. *Journal of Applied Physics* 87 (2000), pp. 8013–8017.
DOI: 10.1063/1.373489.

[108] X. Zeng et al. “Wall relaxation of spin polarized 129Xe nuclei”. *Physics Letters A* 96 (1983), pp. 191–194.
DOI: 10.1016/0375-9601(83)90702-8.

[109] B. Driehuys, G. D. Cates, and W. Happer. “Surface Relaxation Mechanisms of Laser-Polarized ^{129}Xe”. *Phys. Rev. Lett.* 74 (1995), pp. 4943–4946.
DOI: 10.1103/PhysRevLett.74.4943.

[110] Werner Heil et al. “Very long nuclear relaxation times of spin polarized helium 3 in metal coated cells”. *Physics Letters A* 201 (1995), pp. 337–343.
DOI: 10.1016/0375-9601(95)00243-V.

[111] R. E. Jacob et al. “Wall Relaxation of 3He in Spin-Exchange Cells”. *Phys. Rev. Lett.* 87 (2001), p. 143004.
DOI: 10.1103/PhysRevLett.87.143004.

[112] C. Gemmel et al. “Ultra-sensitive magnetometry based on free precession of nuclear spins”. English. *The European Physical Journal D* 57 (2010), pp. 303–320.
DOI: 10.1140/epjd/e2010-00044-5.

[113] Rodger L. Gamblin and Thomas R. Carver. “Polarization and Relaxation Processes in He^3 Gas”. *Phys. Rev.* 138 (1965), A946–A960.
DOI: 10.1103/PhysRev.138.A946.

[114] L. D. Schearer and G. K. Walters. “Nuclear Spin-Lattice Relaxation in the Presence of Magnetic-Field Gradients”. *Phys. Rev.* 139 (1965), A1398–A1402.
DOI: 10.1103/PhysRev.139.A1398.

[115] J. Kestin et al. “Equilibrium and Transport Properties of the Noble Gases and Their Mixtures at Low Density”. *Journal of Physical and Chemical Reference Data* 13 (1984), pp. 229–303.
DOI: 10.1063/1.555703.

[116] G. D. Cates et al. “Laser production of large nuclear-spin polarization in frozen xenon”. *Phys. Rev. Lett.* 65 (1990), pp. 2591–2594.
DOI: 10.1103/PhysRevLett.65.2591.

[117] M. Gatzke et al. “Extraordinarily slow nuclear spin relaxation in frozen laser-polarized ^{129}Xe”. *Phys. Rev. Lett.* 70 (1993), pp. 690–693.
DOI: 10.1103/PhysRevLett.70.690.

[118] William W. Warren and R. E. Norberg. “Nuclear Quadrupole Relaxation and Chemical Shift of Xe^{131} in Liquid and Solid Xenon”. *Phys. Rev.* 148 (1966), pp. 402–412.
DOI: 10.1103/PhysRev.148.402.

[119] Dinh M. TonThat et al. “SQUID detected NMR of laser-polarized xenon at 4.2 K and at frequencies down to 200 Hz”. *Chemical Physics Letters* 272 (1997), pp. 245–249.
DOI: 10.1016/S0009-2614(97)88016-5.

[120] R. J. Fitzgerald et al. “^{129}Xe spin relaxation in frozen xenon”. *Phys. Rev. B* 59 (1999), pp. 8795–8811.
DOI: 10.1103/PhysRevB.59.8795.

[121] N. N. Kuzma et al. “Fast Nuclear Spin Relaxation in Hyperpolarized Solid ^{129}Xe”. *Phys. Rev. Lett.* 88 (2002), p. 147602.
DOI: 10.1103/PhysRevLett.88.147602.

[122] Brian Patton. “NMR Studies of Angular Momentum Transfer and Nuclear Spin Relaxation”. PhD thesis. Princeton University, 2007.

[123] P. R. Granfors, A. T. Macrander, and R. O. Simmons. “Crystalline xenon: Lattice parameters, thermal expansion, thermal vacancies, and equation of state”. *Phys. Rev. B* 24 (1981), pp. 4753–4763.
DOI: 10.1103/PhysRevB.24.4753.

[124] W. M. Yen and R. E. Norberg. “Nuclear Magnetic Resonance of Xe^{129} in Solid and Liquid Xenon”. *Phys. Rev.* 131 (1963), pp. 269–275.
DOI: 10.1103/PhysRev.131.269.

[125] C A Sholl. “Nuclear spin relaxation by transitional diffusion in solids. XII. An analytical approximation”. *Journal of Physics C: Solid State Physics* 21 (1988), p. 319.

[126] K.L. Sauer, R.J. Fitzgerald, and W. Happer. “Laser-polarized liquid xenon”. *Chemical Physics Letters* 277 (1997), pp. 153–158.
DOI: 10.1016/S0009-2614(97)00876-2.

[127] M. V. Romalis et al. “New Limit on the Permanent Electric Dipole Moment of ^{199}Hg”. *Phys. Rev. Lett.* 86 (2001), pp. 2505–2508.
DOI: 10.1103/PhysRevLett.86.2505.

[128] K. L. Sauer et al. “NMR instabilities and spectral clustering in laser-polarized liquid xenon”. *Phys. Rev. B* 63 (2001), p. 184427.
DOI: 10.1103/PhysRevB.63.184427.

[129] J. Jeener. “Dynamical Effects of the Dipolar Field Inhomogeneities in High-Resolution NMR: Spectral Clustering and Instabilities”. *Phys. Rev. Lett.* 82 (1999), pp. 1772–1775.
DOI: 10.1103/PhysRevLett.82.1772.

[130] M. P. Ledbetter and M. V. Romalis. “Nonlinear Effects from Dipolar Interactions in Hyperpolarized Liquid ^{129}Xe”. *Phys. Rev. Lett.* 89 (2002), p. 287601.
DOI: 10.1103/PhysRevLett.89.287601.

[131] M. D. Swallows et al. “Techniques used to search for a permanent electric dipole moment of the 199Hg atom and the implications for CP violation”. *Phys. Rev. A* 87 (2013), p. 012102.
DOI: 10.1103/PhysRevA.87.012102.

[132] A. Yoshimi et al. “Nuclear Spin Maser Oscillation of 129Xe by Means of Optical-Detection Feedback”. English. *Hyperfine Interactions* 159 (2004), pp. 401–405.
DOI: 10.1007/s10751-005-9132-1.

[133] Tapani Ryhänen et al. “SQUID magnetometers for low-frequency applications”. English. *Journal of Low Temperature Physics* 76 (1989), pp. 287–386.
DOI: 10.1007/BF00681735.

[134] R. L. Fagaly. “Superconducting quantum interference device instruments and applications”. *Review of Scientific Instruments* 77, 101101 (2006), pp. –.
DOI: 10.1063/1.2354545.

[135] J. Clarke and A.I. Braginski. *The SQUID Handbook: Fundamentals and Technology of SQUIDs and SQUID Systems*. The SQUID Handbook. Wiley, 2004.

[136] M. Tinkham. *Introduction to Superconductivity: Second Edition*. Dover Books on Physics. Dover Publications, 2004.

[137] W. Buckel and R. Kleiner. *Supraleitung: Grundlagen und Anwendungen*. Lehrbuch Physik. Wiley, 2013.

[138] W. Meissner and R. Ochsenfeld. “Ein neuer Effekt bei Eintritt der Supraleitfähigkeit”. German. *Naturwissenschaften* 21 (1933), pp. 787–788.
DOI: `10.1007/BF01504252`.

[139] B.D. Josephson. “Possible new effects in superconductive tunnelling”. *Physics Letters* 1 (1962), pp. 251–253.
DOI: `10.1016/0031-9163(62)91369-0`.

[140] R.P. Feynman, R.B. Leighton, and M. Sands. *The Feynman Lectures on Physics: Quantum Mechanics*. Basic Books. Basic Books, 2011.

[141] A Yoshimi et al. “Nuclear spin maser with an artificial feedback mechanism”. *Physics Letters A* 304 (2002), pp. 13–20.
DOI: `10.1016/S0375-9601(02)01324-5`.

[142] A. Yoshimi et al. “Low-frequency 129Xe nuclear spin oscillator with optical spin detection”. *Physics Letters A* 376 (2012), pp. 1924–1929.
DOI: `10.1016/j.physleta.2012.04.043`.

[143] D. Budker and M. Romalis. “Optical magnetometry”. *Nature Physics* 3 (2007), pp. 227–234.
DOI: `10.1038/nphys566`.

[144] Yannis K. Semertzidis. “A Storage Ring proton Electric Dipole Moment experiment: most sensitive experiment to CP-violation beyond the Standard Model” (2011). arXiv: `1110.3378 [physics.acc-ph]`.

[145] Stephen E. Derenzo et al. “Electron avalanche in liquid xenon”. *Phys. Rev. A* 9 (1974), pp. 2582–2591.
DOI: `10.1103/PhysRevA.9.2582`.

[146] C. Ciofi et al. “Ultra low noise current sources”. *Instrumentation and Measurement Technology Conference, 1997. IMTC/97. Proceedings. Sensing, Processing, Networking., IEEE*. Vol. 2. 1997, pp. 1486–1489.
DOI: `10.1109/IMTC.1997.612447`.

[147] J. M. Pendlebury et al. “Geometric-phase-induced false electric dipole moment signals for particles in traps”. *Phys. Rev. A* 70 (2004), p. 032102.
DOI: `10.1103/PhysRevA.70.032102`.

[148] W. Feldmeier. “Numerical investigation of a new 129Xe EDM experiment”. Diploma thesis. TU München, 2010.

[149] F. Baudenbacher, N. T. Peters, and J. P. Wikswo. “High resolution low-temperature superconductivity superconducting quantum interference device microscope for imaging magnetic fields of samples at room temperatures”. *Review of Scientific Instruments* 73 (2002), pp. 1247–1254.
DOI: `10.1063/1.1448142`.

[150] B. Taubenheim. “Towards a New 129 Xenon EDM Experiment”. Diploma thesis. TU München, 2011.

[151] Karsten Tell. “Developments for efficient transport of hyperpolarized 129Xe”. Diploma thesis. TU München, 2014.

[152] Max Newrzella. “Calculation of a low-field NMR system for the XEDM experiment”. Bachelor thesis. TU München, 2011.

[153] David Wurm. “Development of a gas-flow cooling system for a new measurement of the electric dipole moment of 129Xe”. Bachelor thesis. TU München, 2012.

[154] I. Altarev et al. “A magnetically shielded room with ultra low residual field and gradient”. *Review of Scientific Instruments* 85, 075106 (2014), pp. –. DOI: `10.1063/1.4886146`.

[155] M. Burghoff et al. “A vector magnetometer module for biomagnetic application”. *Applied Superconductivity, IEEE Transactions on* 9 (1999), pp. 4069–4072. DOI: `10.1109/77.783920`.

[156] V.A. Dzuba, V.V. Flambaum, and P.G. Silvestrov. “Bounds on electric dipole moments and T-violating weak interactions of the nucleons”. *Physics Letters B* 154 (1985), pp. 93–95. DOI: `10.1016/0370-2693(85)90564-7`.

[157] V. Flambaum and I. Khriplovich. “New bounds on the electric dipole moment of the electron and on T-odd electron-nucleon coupling”. *Sov. Phys. JETP* 62 (1985), p. 872.

[158] K. C. Hasson et al. “Spin relaxation due to magnetic-field inhomogeneities: Quartic dependence and diffusion-constant measurements”. *Phys. Rev. A* 41 (1990), pp. 3672–3688. DOI: `10.1103/PhysRevA.41.3672`.

[159] R. H. Acosta et al. “Diffusion in binary gas mixtures studied by NMR of hyperpolarized gases and molecular dynamics simulations”. *Phys. Chem. Chem. Phys.* 8 (2006), pp. 4182–4188. DOI: `10.1039/B609316G`.

[160] C. B. Alcock, V. P. Itkin, and M. K. Horrigan. “Vapour Pressure Equations for the Metallic Elements: 298–2500K”. *Canadian Metallurgical Quarterly* 23 (1984), pp. 309–313. DOI: `10.1179/cmq.1984.23.3.309`.

Acknowledgements

I want to thank Prof. Dr. Peter Fierlinger, who trustfully received me in his very young group and got me into this fascinating field of physics. His enthusiastic character and inspiration feeds our work with new ideas and creates a productive and pleasant atmosphere.
I'm also particularly grateful to Jaideep Singh for guiding the last year of my thesis, his help in the lab and setting up most of the He/Xe equipment. Not to forget the night-shifts reading the thesis and sending comments.
The whole group needs to be thanked for the mutual support and humor, in particular the many students that contributed to the liquid xenon EDM: Wolfhart Feldmeier, Max Newrzella, Felix Rosenau, Stephanie Seidl, Ann-Katrin Straub, Bernd Taubenheim, Karsten Tell, David Wurm.
The great accomplishments of the He/Xe clock-comparison were only possible with the cooperation of many people from the University of Michigan, Michigan State, PTB Berlin and the MLZ in Garching, namely Tim Chupp, Skyler Degenkolb, Natasha Sachdeva, Fei Gong, Jaideep Singh, Wolfgang Kilian, Allard Schnabel, Silvia Knappe-Grüneberg, Jens Voigt, Isaac Fan, Earl Babcock, Martin Burghoff and the support of all our students, particularly Eva Krägeloh and Jonas Meinel.

A special thanks goes to staff at the mechanics workshop, particularly Michael Novotny and Thomas Deuschle and the glass blowing staff in the chemistry department. All of which did their best to produce urgently needed parts or fix broken glassware.
For their helpfulness in many aspects I want to thank the administration staff of the excellence cluster, Karin Frank and Rainer Stoepler.
A big thanks goes to Andi Weiss, who talked me into biking to Garching every day and supported urgent bike repairs any time.

I thank my partents and my sister for their lifelong support, motivation and kindness.
To conclude, I'm particularly grateful to Verena, who supported me with encouragement and patience throughout the last years.